19960729 038

MECHANICS AND PHYSICS OF LAYERED AND GRADED MATERIALS

Papers from the Engineering Foundation Conference on Mechanics and Physics of Layered and Graded Materials held in Davos, Switzerland, 21–25 August 1995

Guest Edited by
A. NEEDLEMAN and S. SURESH

N00014-95-1-1107

PERGAMON

AIMS AND SCOPE

Journal of the Mechanics and Physics of Solids. The Journal publishes papers reporting original research on the mechanics of solids. Emphasis is placed on the development of fundamental concepts of mechanics and novel applications of these concepts based on theoretical, experimental or computational approaches, drawing upon the various branches of engineering science and the allied areas within applied mathematics, materials science, structural engineering, applied physics and geophysics. The main purpose of the Journal is to foster scientific understanding of the processes of deformation and mechanical failure of all solid materials, both technological and natural, and the connections between these processes and their underlying physical mechanisms. In this sense, the content of the Journal should reflect the current state of the discipline in analysis, experimental observation and numerical simulation. In the interest of achieving this goal, authors are encouraged to consider the significance of their contributions for the field of mechanics and the implications of their results, in addition to describing the details of their work.

CONTENTS DIRECT

ContentsDirect delivers the table of contents of this journal, by e-mail, approximately two to four weeks prior to each issue's publication. To subscribe to this free service, complete and return the form at the back of this issue or send an e-mail message to p.mestecky@elsevier.co.uk

CONTENTS

MECHANICS AND PHYSICS OF LAYERED AND GRADED MATERIALS

PREFACE

The Engineering Foundation Conference on Mechanics and Physics of Layered and Graded Materials was held in Davos, Switzerland, 21–25 August 1995, with 86 participants representing academic institutions as well as government and industrial research laboratories. The objective of the Conference was to bring together scientists and engineers with different backgrounds and perspectives, but with a common interest in layered and graded materials. The Conference began with an Overview session; subsequent sessions were held on Processing and Characterization, Stress and Microscopic Deformation, Design and Applications, Thermomechanical Deformation, Coupled Mechanical/Electrical/Magnetic Phenomena, and Fracture and Fatigue. The conference format consisted of formal sessions in the morning and evening, with the afternoons free for informal discussion and relaxation. Presentations were of four kinds: 11 keynote lectures, 14 invited lectures, 32 contributed lectures and 11 poster contributions. These Proceedings contain the text of 10 of the keynote lectures.

It is a pleasure to thank the presenters for making their contributions accessible to participants with a wide range of backgrounds. We thank the Engineering Foundation and all participants for making this Conference such a pleasure to organize. Special thanks are due to Barbara Hickernell, Conferences Director of the Engineering Foundation for her invaluable assistance before, during and after the Conference, to Herman Bieber of the Engineering Foundation for being so helpful during the Conference and to Professor George Herrmann of Stanford University (and Davos, Switzerland) for providing local hospitality. We also thank Mr Jagi and his staff at the Cresta Hotel for their service and help above and beyond any call of duty. The result of all this was a warm and friendly atmosphere at the Conference that fostered scientific as well as personal interactions.

As can be seen from the list of sponsors, support came from a variety of sources, and this support is much appreciated. We are grateful to Professors L. B. Freund and J. R. Willis for devoting an issue of the *Journal of the Mechanics and Physics of Solids* to these Proceedings. The timely publication of this volume was made possible through the co-operation of authors in submitting the manuscripts.

These Proceedings provide a record of the formal part of the program. We hope that the interactions and collaborations that began during the Conference will serve as a further confirmation of its success.

S. Suresh   **A. Needleman**
MIT, Cambridge, MA   Brown University, Providence, RI
Conference Co-Chairs

ACKNOWLEDGEMENTS

PROCESSING–MICROSTRUCTURE–PROPERTY RELATIONSHIPS IN GRADED MATERIALS

B. ILSCHNER

Department of Materials, Swiss Federal Institute of Technology, Lausanne, Switzerland

ABSTRACT

The desired macroscopic properties of functionally graded components depend (1) directly on the local composition function $P(c)$ and (2) indirectly, because important microstructural parameters (porosity, grain size) that develop during processing are also strong functions of the local composition. These complex relationships are discussed for the case of functionally graded material (FGM) fabrication by powder compaction and sintering. The conclusion is that the real making of high quality graded components may be much more difficult than calculating an optimal composition profile $P(x)$.

DEFINITIONS AND INTRODUCTION

The title of this introductory paper contains a number of terms, the precise under-standing of which is considered to be essential for the following contributions. A few definitions may, therefore, be proposed and commented.

The term graded materials refers to solids having a well-defined geometrical shape (in particular, to components of technical systems), in which the characteristic compositional and microstructural parameters (P_c and P_μ) vary systematically over the cross section, in one or more dimensions. Functionally graded materials (FGM) shall be defined as graded materials, the parameter profile $P(x)$ of which has been deliberately designed and manufactured in order to optimize the functional value of that component.

Compositional parameters may be of two types: first, P_c can represent a chemical composition within a solid solution, including ordered structures with a stoichiometric composition range. Second, it can designate a volume fraction c_{vi} of species i of the $n = 2$ or > 2 phases that form a particular material; these phases are often mutually insoluble (such as Ni/alumina), in other cases not (WC–Co). In practical work, it is often difficult to distinguish between local composition changes $\delta c'$ that are due to the existence of a gradient and those, $\delta c''$ that are due to statistical fluctuations. Moreover, it is necessary to distinguish between average and local compositional parameters. As an example, the average porosity of a sintered gradient component may be 5%, while the local porosity varies between 2 and 8% within the gradient. In materials with polymer components, chain length and degree of reticulation are appropriate compositional parameters, in addition to chemical analysis.

Microstructural parameters P_μ in polycrystalline materials are obviously the grain size, grain or particle shape (aspect ratio), grain orientation and texture parameters,

647

including alignment of precipitates as often as observed. In polymer materials, crystallinity is to be considered as an additional parameter.

Properties comprise mechanical properties (modulus, strength, hardness, ductility, toughness, tribo-resistance), as well as chemical properties (resistance to corrosion, bio-compactibilty) and electromagnetic properties (including optical ones). As a general symbol for such properties, Y_i may be chosen. Again, as in the case of the compositional parameters P, one must distinguish between "global" or average values Y_{av}, describing the behavior of the whole component, and local values, $Y(x)$.

The term processing will be used in a very general sense, incorporating all procedures that are used to fabricate the graded material from its elemental or pre-alloyed constituents, as well as subsequent mechanical deformation, heat treatment, treatments for surface modification, or combinations of these.

Microstructure–property relationships are playing a central role in materials science and engineering. In fact, they represent the major breakthrough achieved in the period between 1955 and 1975 when it became obvious that, while chemical composition and crystallinity have certainly a primary influence on the macro-properties of materials, the microstructural parameters follow immediately as determining factors, in particular of the mechanical behavior. The Hall–Petch relation between grain size and yield strength, or the Orowan relation linking particle diameter and distance of precipitates to strength, are well-known examples.

In graded materials, the definition of such relationships becomes much more complex: even though global property values Y_{av} may well be defined (e.g. number of thermal shock events of a graded thermal barrier coating prior to intensive damage formation), they can no longer be meaningfully linked to global compositional or microstructural parameters. Instead, relations must be established between global properties and the functions $P(x)$ describing the parameter variation over the whole specimen or component. While the practical task can be simplified by choosing, for example, a power law $P(x)$ so that a single value of the exponent characterizes the function, the principal difficulty of dealing with global property values depending on functions of local parameters rests valid.

This difference between macroscopically homogeneous materials and graded ones becomes still more pronounced if the effect of processing is considered: not only have processing parameters (in the interpretation of the term as discussed above) together with chemical composition a decisive influence on the microstructure. In addition, this effect varies with the location within the gradient. Even a local property value $Y(x')$ at one given position will be influenced, not only by the neighboring volume elements in the gradient, having slightly different values of Y, but also by global effects like residual stresses caused by the existence of the macroscopic gradient. The establishment of meaningful processing–microstructure–property relationships of graded materials is thus a task demanding detailed and elaborate study of interconnected layers and their constitutive laws.

GRADIENT OR STEP FUNCTION

Among the numerous processes that are used for the fabrication (which is in general not yet going beyond laboratory scale) of graded materials, there are some that do

not really provide for smooth concentration gradients $P(x)$. Rather, they generate a sequence of stacked layers with discrete compositional parameters P_1, P, ... P_n, with n between 3 and about 8. This observation holds in particular for powder metallurgical process routes; here, the stacking before sintering of several thin layers that have been individually thoroughly mixed and homogenized is easier than designing and operating more sophisticated equipment for continuous gradient formation. The latter may also cause a higher risk of undesired excursions from the as-planned composition profile.

Likewise, in coating technology, the state of the art is characterized by one layer as a first step, then a bond coat layer and 1 or 2 additional interlayers, so that complex thermal barrier coatings with n layers are produced. These may be regarded as a "transient stage" on the way to the ultimate (and optimal) solution which is a continuously graded layer. In favor of the step function solution, which is often more economical, it may also be argued that the abrupt composition changes at the interfaces caused by the low temperature steps of the processing route will partially disappear by diffusion during subsequent high temperature sintering, HIP treatment, or service conditions.

While this is macroscopically true, at least for solid solutions, the situation may be different for two-phase aggregates without solid solubility, such as particle dispersion reinforced alloys. Let us consider a dense bi-layer material composed of a nickel matrix containing a dispersion of fine alumina particles; the size distribution of these particles may be identical in both parts of the bi-layer, only the volume fraction and, hence, the mean interparticle distance, differ by, e.g. a factor of two, as in Fig. 1. In
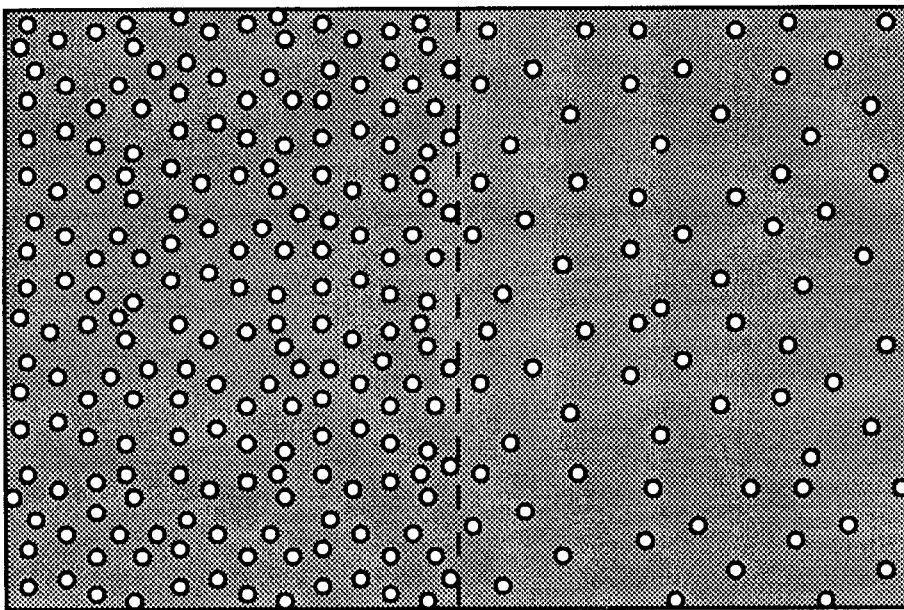
Fig. 1. Two-phase double layer, negligible solubility (like Ni/Al_2O_3), as an example for quasi-stable situation.

B. ILSCHNER

this case, there is practically no driving force for a diffusion process that might transform the step-function into a gradient, though, theoretically, there is more surface energy per volume element stored in the left part of the bi-layer than on the right-hand side.

The second example of non-homogenization concerns monophase alloys. In the case of thermodynamically ideal solid solutions (or of regular solutions without segregation tendency), existing concentration steps are obviously unstable and will smoothen, sufficient diffusivity being provided, Fig. 2(a). Thereby, true gradients will be formed, ultimately leading to large-scale homogenization. This is not the case, however, if the interaction terms within the Gibbs free energy $G(c)$ create a tendency for spinodal decomposition $(\partial^2 G/\partial c^2 < 0)$. Then, a graded transition between two concentration levels will form, see Fig. 2(b). This profile may be regarded as an extended step. The underlying principle is a balance of energies. On the one hand, the system tries to accommodate the bulk of atoms in low-energy positions and to restrict the "thermodynamic misfit" resulting from the Gibbs function to a small region, δ in Fig. 2(b). However, δ will not be squeezed too much either, as this would imply ever increasing gradients of composition where each atomic layer faces different compositions in neighboring planes. As Cahn (1968) and Hilliard (1970) have shown, this results in a specific gradient energy term, proportional to (grad c^2).

A gradient energy term may also be of mechanical origin, due to local variations
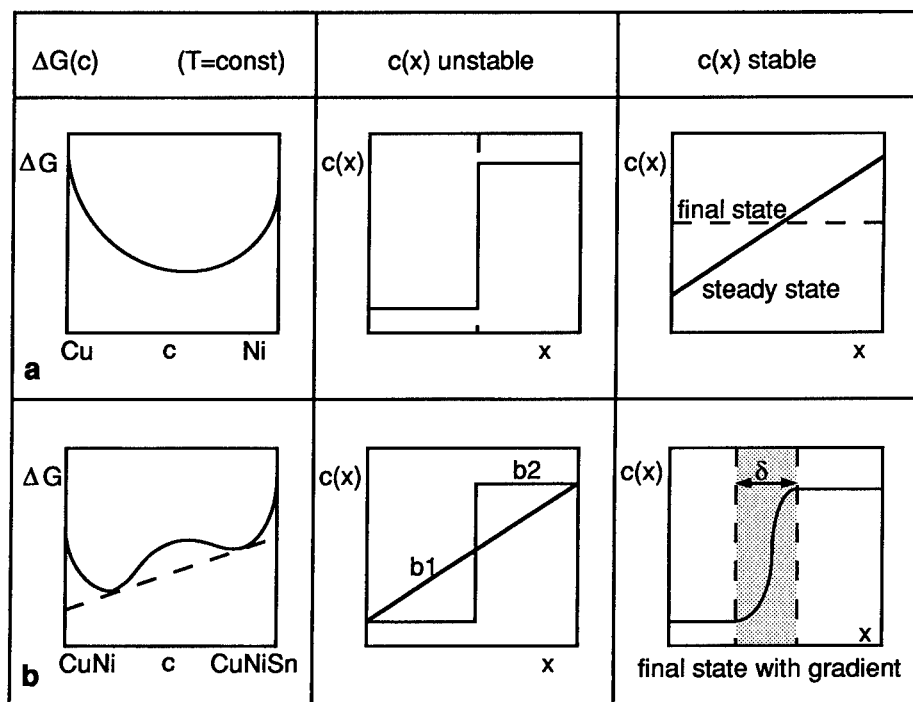
Fig. 2. Solid solution systems: stabilization of either homogeneous (a) or graded transition (b) due to concentration dependence of Gibbs free enthalpy, $G(c)$.

of thermal contraction during cooling of a graded material. As has been frequently discussed in the current literature, this additional thermoelastic energy can be minimized by avoiding abrupt transitions. A driving force will result, aiming at stress relaxation. However, this will normally take place by micromechanical processes (dislocation climb and glide) rather than by stress driven chemical diffusion creating smoother concentration gradients.

In conclusion, abrupt concentration changes originating from processing must be envisaged—unlike simple phase boundaries—as being associated to composition profiles as soon as at least a small solubility exists. Chemical as well as mechanical energy terms combine with diffusion in order to replace step functions gradually by smooth profiles. It appears, therefore, reasonable to aim in the same direction when one develops process routes for making gradient materials.

PROCESSING–MICROSTRUCTURE–PROPERTY RELATIONSHIPS; THE P/M ROUTE AS A CASE STUDY

This discussion will follow a sequence of simple processing steps, the objective being to produce a component with a concentration profile resulting from prior calculations of its functional effect.

Filling a mold with a dry powder mixture, the composition of which varies as the filling operation proceeds, implies several problems that will be addressed shortly. The process has aspects related to statistical physics even in the case of *one* powder species: falling with a certain velocity, each particle will eventually hit an already deposited one. Depending on the momentum transfer during primary impact, the arriving particle will either lose energy by pushing the "underdog" in a more stable position, or rebounce elastically and fall a second time. It is always being exposed to the probability of colliding with new particles, thus receiving subsequent impacts with resulting micromovements. Until a considerable number of covering layers has been accumulated on top of a given layer, it will be subject to statistical adjustments, with the "noise level" decreasing with increasing distance from the surface.

These adjustment processes may be modeled using critical angles of the center lines connecting neighboring grains. However, there are geometrical as well as physical factors to be considered: the geometrical factor concerns the deviations of particle shapes from the spherical model which is often used though some powders have very irregular shapes indeed. The physical factor is what is often termed *nano-tribology*: the atomic forces necessary to roll or slide one submicron particle over another one, driven by the short impact of the next falling grain. These processes become still more complex when two species are being filled simultaneously, each one with its different size, shape, mass and tribological characteristics. It is indeed difficult to fill a mold layer by layer in a dynamic mixing process, trying to establish a predetermined composition profile, without clustering, waviness of equi-composition surfaces which are supposed to be planar, and other defects.

Normally, further consolidation is being sought for by triggering local rearrangement events with the aim of obtaining higher "tapping densities". Vibrations may of course activate local disentanglements of grains—but again these movements are

subject to the statistics of contact points, free volume and micro-tribology. Clustering and segregation may be enhanced together with densification, so that the final micro-structure has a large-scale gradient, superimposed by fluctuations of considerable amplitude.

Next, cold compacting by static mechanical pressure (in some cases also by shock waves) is used in order to confer to the specimen a certain degree of mechanical stability, necessary for handling before sintering. Obviously, ductile and brittle powder particles behave in a very different manner during this operation: the first will develop increasing local stresses at the extremely small interparticle contact areas, going beyond the yield point and thus initiating local plastic deformation. This will result, by itself, in a small contribution to densification. More important is the welding effect between grains due to combined action of shear and compressive strain. Considerable "green strength" may thus be achieved by cold compaction. With brittle powders, increasing pressure will mainly result in the initiation and propagation of microcracks in adjacent grains, so that liquid or wax-like binders have to be added in order to achieve the desired stability during handling. Consequently, in a gradient of com-position (in particular one involving ductile and brittle powder fractions), the effect of cold compaction varies considerably with the position within the composition profile; it depends strongly on the probability for having like or unlike neighboring grains—and therefore, also on fluctuations (clusters) inherited from prior processing. Using prealloyed powders will in most cases increase the yield strength and, thus, the resistance to deformation of individual grains, as much as reducing their ductility.

Finally, the specimen is subjected to sintering; we begin by considering solid state sintering. The first guess is that due to thermal activation and the increased importance of entropy, existing local fluctuations will level off during sintering. This is not the case. In fact, sintering takes place at one temperature, T, which is the same in the whole specimen volume. On the other hand, sintering kinetics is determined by Arrhenius-type expressions, in which the activation energy $Q(c)$ is a function of composition and, therefore, of position within the concentration gradient. In a first approximation, the sintering rate between two points in the gradient will therefore vary with an Arrhenius function controlled by the difference of the activation energies of the two components. This ΔQ can be of the same order of magnitude as the individual Q values, which results in a very strong dependence of the sintering rate on composition and, hence, a very different rate of densification in different areas of the graded specimen. This may either lead to large differences in porosity, or to different shrinking rates of different layers, finally resulting in either strong bending of originally flat specimens, or in crack initiation in those parts of the specimen which, due to their composition, shrink faster. The processing–microstructure–property relationship is easily recognized.

With large differences in sintering rate due to composition gradients, it is not at all easy to compensate for this effect by using different powder grain sizes, carefully adjusted to the composition range. Moreover, this strategy demands for a new com-position variable (grain size in addition to composition) and, hence, more soph-isticated equipment and higher fabrication cost. Sintering additives are known to have a strong effect on the rate of densification; however, the same argument as before holds: they have to be added in different concentrations for each different level
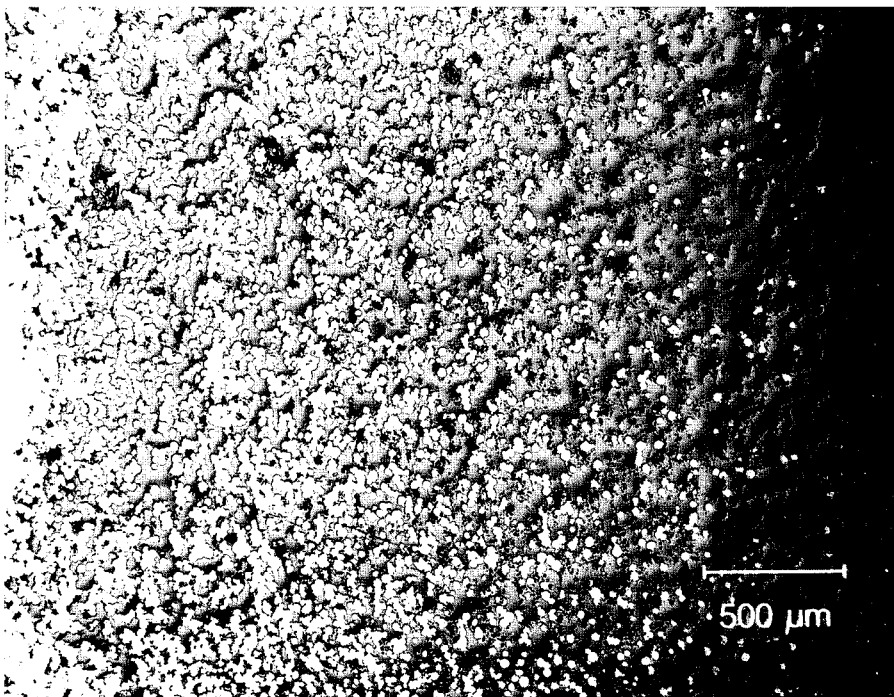
Fig. 3. Micrograph of graded transition between CrNi alloy and partially stabilized zirconia (PSZ).

of alloy composition. (In addition, they may have a negative influence on mechanical properties of the sintered part, due to grain boundary segregation.) Another strategy is to start sintering at a temperature adapted to the "fastest" constituent within the gradient and then slowly heating, until the "slow" layers are at an efficient temperature level. Of course, this will often cause recrystallization and grain growth in those layers that had sintered at the lowest temperature level; to correct for this, grain refining additives may be necessary, resulting in the same complications as mentioned above.

Liquid state sintering may be considered as very efficient, all of the necessary transport processes being transferred to a liquid phase that is present in all areas of the specimen, even in a gradient. In the manufacturing of cemented carbides of the type WC–Co ("hard metals"), liquid phase sintering is common industrial practice— for homogeneous parts. The application of this technique to graded parts is very often unable to yield the desired results: if, as usual, a certain degree of connected porosity is left in the structure at the moment when the binder phase becomes liquid, there will be a redistribution of the latter by capillary flow, partially or completely eliminating the gradient. If, as in the case of WC–Co, the solid phase has a high solubility in the liquid binder, an additional effect takes place: existing "bridges" between carbide particles, which have been formed during heating by solid state sintering, will be dissolved while approaching the eutectic temperature, thus weakening the cohesion of the whole structure. The pressure that is due to capillary forces in the porous structure is then able to blow up the "mushy" WC–Co structure in order to gain additional interface energy between solid carbide and liquid solution. Strong deformations of the geometrical shape as well as decohesions must be expected.

CONCLUDING REMARKS

The foregoing discussion was based on powder metallurgy and pressureless sintering techniques for the preparation of graded components. Similar thoughts can be presented for other process routes. Keeping all these interferences between processing, microstructure and the resulting properties in mind, it appears rather surprising that a considerable number of industrial and academic laboratories have nevertheless announced successful preparation of functionally graded components of reasonable microstructural quality, Fig. 3, and functional values corresponding to expectations. These results show that, by careful selection and preparation of starting materials, advanced mixing and feeding techniques, judiciously planned time–temperature cycles and mechanical "boosters" (HIP, sinter-rolling), it is indeed possible to obtain control over the generally adverse micro-processes that tend to object to the building of such unusual species as functionally graded materials. While the considerations presented here point, at the one hand, to the important challenges for applied scientific research in this field, the already reported success encourages, on the other hand, the perfection of processing routes in the direction of industrial production lines: low-cost, continuous, and reliable.

REFERENCES

Cahn, J. W. (1968) *Trans AIME* **242**, 166.
Hilliard, J. E. *Phase Transformations*, Ch. 12. ASM Metals Park, Ohio, 1970.

BIBLIOGRAPHY

Instead of listing a few individual references to published literature on functionally graded materials, it is felt to be more judicious to cite here the three proceedings volumes of the international FGM symposia in Sendai (1990), San Fransisco (1992) and Lausanne (1994):

Yamanouchi, M., Koizumi, M., Hirai, T. and Shiota. I. (eds) *Proc. 1st Int. Symp. on Functionally Gradient Materials*, Sendai, 1990.
Holt, B. (ed.) *Proc. 2nd Int. Symp. on Functional Gradient Materials*, San Fransisco, 1992 (*Ceramic Trans.* **34**).
Ilschner, B. and Cherradi, N. (eds), *Proc 3rd Int. Symp. on Structural and Functional Gradient Materials*, Lausanne, 1994. PPUR Lausanne, 1995.

STRESS AND GRAIN GROWTH IN THIN FILMS

CARL V. THOMPSON and ROLAND CAREL

Department of Materials Science and Engineering, Massachusetts Institute of Technology,
Cambridge, MA 02139, U.S.A.

ABSTRACT

The mechanical properties of polycrystalline thin films with thickness of 1 μm or less depend strongly on the grain geometry, the grain size, and the way in which the crystallographic orientations of the grains are distributed. Grain growth during film formation or during post-deposition annealing can play a dominant role in defining these microstructural characteristics, and therefore, the mechanical properties of films. Stress can suppress or promote grain growth. In the latter case, stress promotes texture evolution during grain growth. Grain growth can serve as a stress relief mechanism in both elastically isotropic and anisotropic materials, and can also promote plastic yielding.

INTRODUCTION

Polycrystalline thin films have highly constrained grain structures and as a result, they also have highly constrained, and often unusual, mechanical behavior. This affects the properties, performance and reliability of polycrystalline films in a wide variety of applications in electronic and magnetic devices and systems. In these applications, the term thin films is usually taken to apply to films with thicknesses of roughly 1 μm or less. Films with these thicknesses often have non-equiaxed grains that span the thickness of the film but have in-plane sizes ranging from much smaller than the film thickness to much larger than the film thickness. Polycrystalline films also often have bimodally-distributed grain sizes. The crystallographic orientation of the grains in polycrystalline films are also often non-random, even when they are deposited on amorphous substrates. Often films are "textured", in that the grains tend to have specific crystallographic planes parallel to the plane of the film.

The grain geometry, the average grain size, the grain size distribution and the distribution of grain orientations in polycrystalline films all strongly affect their mechanical as well as other properties. Specifically, the yield stress of polycrystalline thin films increases with decreasing grain size and film thickness, so that very thin, fine-grained films can have yield stresses of hundreds of MPa. This is due to specimen-size-induced constraints on dislocation generation mechanisms and dislocation motion. Also, the anisotropy of elastic properties and non-random texture of most films affect their elastic behavior.

Grain growth often occurs during deposition or post-deposition processing of thin films. As in bulk materials, grain growth in thin films leads to an increase in the

average grain size. However, in thin films, grain growth also leads to an evolution in the distribution of grain sizes and the distribution of grain orientations. As the excess volume associated with grain boundaries is redistributed during grain growth, a tensile stress can develop. Because of their high yield stresses, polycrystalline films can support very high strain energy densities, which can vary from grain to grain, so that stress can drive the preferred growth of grain subpopulations with low strain energy densities.

Grain growth can play a dominant role in defining the stress state and mechanical properties of films. These, in turn, affect the way in which grain growth proceeds. This coupling of stress and grain structure evolution in thin films is the focus of this paper.

FILM FORMATION

Most films do not wet their substrates, in that, in equilibrium, the energies of the film and substrate surfaces and the film–substrate interface are minimized when the film is in the form of an island as shown in Fig. 1. In this case, film formation initiates through the nucleation of islands, which then grow to cover the substrate surface and eventually coalesce to form a continuous film [Fig. 1(b–c)]. If nucleation and growth are the only processes that define the average in-plane grain size $\bar{d}$, $\bar{d}$ decreases with increasing nucleation rate, and increases with increasing growth rate (Thompson and Carel, 1995a).

As a thin film thickens during deposition, at least three fundamentally different types of microstructures can develop (Mouchan and Demichisin, 1969; Thornton, 1977; Grovenor et al., 1984), as illustrated in Fig. 2. Refractory metals tend to have structures of the type shown in Fig. 2(a) when deposited at temperatures below about 0.2–0.3 T_m (where T_m is the melting temperature in K), and structures of the type shown in Fig. 2(c) develop when $T_{dep} \geq T_m$. Semiconductors tend to be amorphous when $T_{dep} \leq 0.5\ T_m$, and have type 2a structures when $0.5\ T_m \leq T_{dep} \leq 0.9\ T_m$. Face-centered cubic materials tend to have 2c structures when $T_{dep} \geq 0.2–0.3\ T_m$.

In physical vapor-deposition processes (evaporative and sputter deposition), deposition is generally carried out under conditions of high supersaturation so that critical nuclei are small, the nucleation rate is high, and the nuclei spacing is small (Thompson and Carel, 1995a). These conditions might lead to the very fine grain sizes observed at the base of type 2a films. However, observation of type 2b structures probably indicates that grain boundary motion has occurred during coalescence (followed by expitaxial growth on the grains of the as-coalesced film). Clearly grain boundary motion during film coalescence and thickening plays a role in development of type 2c structures (Wong et al., 1986).

For 1 μm thick films with 2a structures, the in-plane grain size varies from at most a few thousand Ås at the top of the film, to 100 Å or less at the film–substrate interface. In both the 2a and 2b structures, the grains are highly non-equiaxed and have a largest dimension no greater than the film thickness. Only in the case of 2c structures are grains relatively equiaxed with in-plane sizes, roughly as large as the

$$\gamma_s$$

$$\theta$$

$$\gamma_i \qquad \gamma_{sub}$$
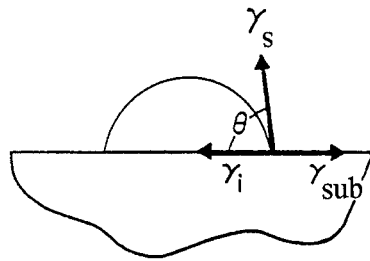
(a)
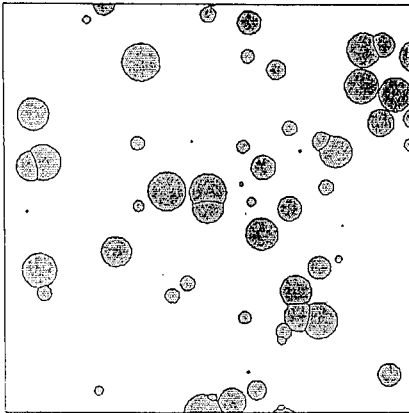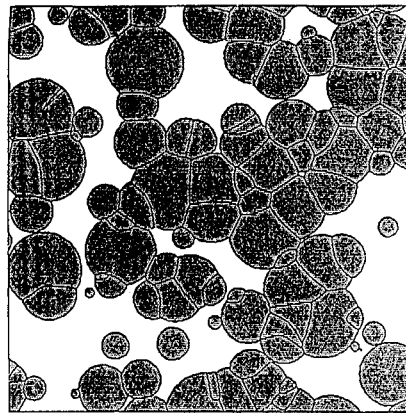
(b)   (c)

Fig. 1. (a) A spherical cap-shaped particle on a substrate that it partially wets. γ_s, γ_{sub}, and γ_i are the surface energies of the free surface of the particle, the surface of the substrate, and the particle–substrate interface, respectively. θ is the equilibrium contact angle. (b) and (c) Top views of a film forming through nucleation and growth of isolated particles or islands which grow together and coalesce to form a continuous film.

film thickness. When heated to sufficiently high temperatures, as deposited films with type 2a and 2b structures will evolve toward 2c structures, through a grain growth process that has both 3D and 2D character.
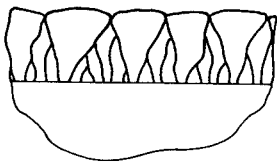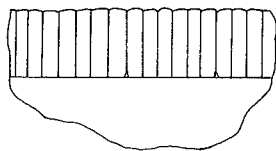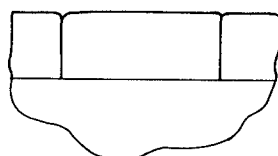
(a)   (b)   (c)

Fig. 2. Schematic cross-sectional views of possible grain structures of as-deposited thin films with thicknesses less than 1 μm.

MECHANICAL PROPERTIES OF POLYCRYSTALLINE FILMS

Polycrystalline films are often in a state of near biaxial strain, due to their attachment to generally much thicker substrates. Because of this, the stress and strain energy density vary from grain to grain, depending on the crystallographic orientations or textures, and therefore the effective biaxial moduli, of the grains (Thompson and Carel, 1995; Nix, 1989). Under plane-stress conditions, for a biaxial strain of magnitude ε the in-plane stress in a grain is given by

$$\sigma = M_{hkl}\varepsilon, \tag{1}$$

and the strain energy density is given by

$$F_\varepsilon = (M_{hkl})\varepsilon^2, \tag{2}$$

where M_{hkl} is the appropriate biaxial modulus, which for cubic materials can be determined as a function of the grain surface normal (hkl) and the stiffness constants $(C_{11}, C_{12},$ and $C_{44})$ as (Murikami and Chaudhari, 1977)

$$M_{hkl} = C_{11} + C_{12} + K - \frac{2(C_{12} - K)^2}{C_{11} + 2K}, \tag{3a}$$

where

$$K = (2C_{44} - C_{11} + C_{12})(h^2 k^2 + k^2 l^2 + h^2 l^2) \tag{3b}$$

and

$$h^2 + k^2 + l^2 = 1. \tag{3c}$$

The magnitudes of σ and F_ε therefore depend on the crystallographic orientation of the grains and on the elastic anisotropy of the material. The latter can be quantified in terms of the Zener anisotropy raio, $A = 2C_{44}/(C_{11} - C_{12})$. For all f.c.c. metals and most cubic metals A is greater than one. When this is the case, M_{hkl} has a minimum value for (100)-textured grains and a maximum for (111)-textured grains.

The yield stress of a polycrystalline film depends strongly on its average in-plane grain size and out-of-plane grain size, the latter being the film thickness, h, or less (Nix, 1989; Venkatraman and Bravman, 1992; Sanchez and Artz, 1992; Thompson, 1993). The yield stress σ_y increases with decreasing value of both h and d, and in the case of Al, has been shown to independently vary with the reciprocal of each (Venkatraman and Bravman, 1992), such that

$$\sigma_y = \frac{c_1}{d} + \frac{c_2}{h}. \tag{4}$$

It has been further argued that both c_1 and c_2 can be defined for individual grains, and that their values depend on the texture of a grain such that σ_y is high for grains with (111)-texture and low for grains with (210) and (110) textures (Sanchez and Artz, 1992; Thompson, 1993a,b; Carel and Thompson, 1995). This orientation dependence is predicted based largely on the magnitude of the resolved sheer stress.

Because of their anomalously high yield stresses, very high stresses are often mea-

sured in thin films. Venkatraman and Bravman (1992) measured yield stresses as high as 350 MPa in continuous films of pure Al, and stresses as high as 700 MPa have been inferred from electromigration experiments on thin film strips of Al imbedded in SiO_2 (Lloyd and Smith, 1983). Also, as will be discussed in the following section, Abermann and co-workers (Abermann *et al.*, 1978; Abermann and Koch, 1985; Abermann, 1990, 1992), as well as other groups, have also measured intrinsic stresses in as-deposited films ranging up to 1 GPa in a number of materials.

STRESSES IN THIN FILMS

Intrinsic stress

As-deposited films often have high intrinsic stresses. Abermann and co-workers (Abermann *et al.*, 1978; Abermann and Koch, 1985; Abermann, 1990, 1992) have studied intrinsic stresses during and after evaporative deposition of thin films. Measurements were made in the deposition system by monitoring the deflection of a cantilever on which the films were deposited. It was found that when films were deposited at room temperature, their behavior could be divided into two classes, as illustrated for Cr and Au in Fig. 3. Cr is typical of "type I", low mobility materials, while Au is an example of a "type II" material (of which Ag, Cu and Al are other examples). Type I materials typically have microstructures such as in Fig. 2(a). High tensile stresses in sputter-deposited as well as evaporatively-deposited thin films of type I materials have been observed by many other groups, including that of Hoffman and Thorton (1982). Hoffman (1976) proposed that tensile stresses develop as islands
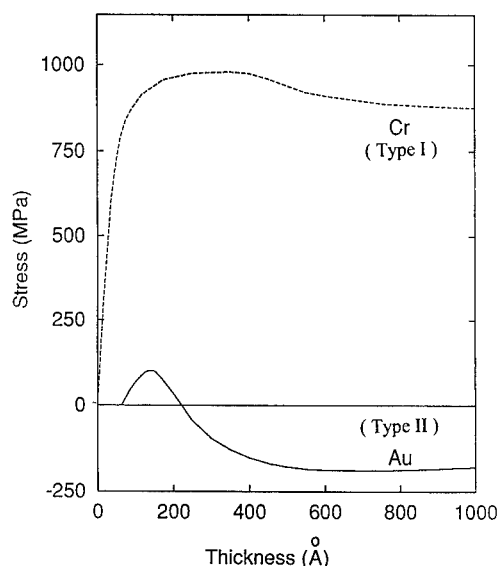
Fig. 3. *In situ* real-time measurements of stress in of Cr (type I) and Au (type II) films as a function of film thickness (based on Abermann and Koch, 1985).

coalesce, as a result of nearby islands elastically deforming to close up spaces in order to replace the two grain-free surfaces with one grain boundary. Nix (1994) has argued that the maximum strain that can result from this mechanism can be determined by balancing the resulting strain energy density with the change in the sum of the total surface and grain boundary energy. If the strain is elastically accommodated, Nix has shown that the resulting maximum stress is strongly dependent on the grain size at coalescence d_0 ($\sigma_{\max} \propto 1/d_0$), and that stresses of several GPa are possible when $d_0 \leqslant 100$ Å. This seems to provide a likely explanation for the tensile stresses observed by Abermann and others in type I materials.

Type II materials develop small tensile stresses as they coalesce, but this stress is relieved, and even appears to become compressive as the films thicken; Au provides an extreme example of this behavior. The relief of the "Hoffman" stress, or the failure to develop larger tensile stresses, is not likely to be due to plastic deformation, since, as discussed earlier, these films are expected to have high yield stresses. It seems more likely that the grain boundaries form and densify via surface and boundary atomic diffusion rather than by straining in these high mobility materials. The origin of the compressive stresses observed by Abermann and co-workers (Abermann et al., 1978; Abermann and Koch, 1985; Abermann, 1990, 1992) is ascribed by Abermann to surface stress effects.

Sputter-deposited thin films of type I materials can have either high tensile or compressive stresses, on the order of 1 GPa in either case (Ohring, 1992). Whether the stress is compressive or tensile most strongly depends on the pressure of the sputtering gas, with high compressive stresses usually occurring at low pressures and tensile stresses occurring at higher pressures. The transition occurs in the 1–10 mTorr range and can swing from 1 GPa compressive to 1 GPa tensile with a change of pressure of a few mTorr or less. Tensile stresses are likely to be due to the Hoffman mechanism. The origin of compressive stresses is less clear, but may be associated with shot-peening effects and sputtering gas incorporation (Ohring, 1992; d'Heurle, 1970).

Extrinsic stress

A common source for extrinsic stresses is differential thermal expansion. The biaxial strain resulting from differential thermal expansion of a thin film on a thick substrate is

$$\varepsilon_{\text{th}} = \int_{T_0}^{T} [\alpha_s - \alpha_f] \, dT \cong (\Delta\alpha)(\Delta T), \tag{5}$$

where T_0 is the zero stress-temperature, T is the actual temperature ($\Delta T \equiv T - T_0$), and α_s and α_f are the linear thermal expansion coefficients of the substrate and film, respectively. The strain due to differential thermal expansion can be large even for relatively small ΔTs. For example, for Al on Si (or Si covered with a thin oxide), $\alpha_f \cong 2.3 \times 10^{-5}$ and $\alpha_s \cong 2.6 \times 10^{-6}$ so that ΔT of 100°C results in a ε_{th} of 0.2%, or a stress of 50 MPa compressive for a (111) grain ($M_{111} = 115$ GPa).

Bending of substrates can also result in extrinsic strains and stresses. This allows the application of strains in films deposited on cantilevers, for example, when a force is applied to the unfixed end (Nix, 1989).

GRAIN GROWTH IN THIN FILMS

As discussed earlier, grain growth can play a dominant role in defining the texture and grain size distribution, and therefore the mechanical properties, of as-deposited f.c.c. metal films, and in other materials when they are deposited or annealed at temperatures sufficiently high to allow grain boundary motion. The current understanding of grain growth in thin films will now be briefly reviewed.

Normal grain growth

Grain growth in bulk materials has been studied for many years and has been the subject of a number of reviews (Atkinson, 1988). Discussion of grain growth in bulk systems tends to focus on what has come to be known as normal grain growth. Normal grain growth is taken to be a process in which the average grain size d changes with time t according to

$$d^2 - d_0^2 = ct, \tag{6}$$

where d_0 is the average grain size at $t = 0$ and c is time independent but strongly temperature dependent, such that $c = c_0 \exp(-Q/kT)$, and c_0 is weakly temperature dependent. Normal grain growth is also characterized by a "steady state" behavior for which the grain size distribution function $f(d)$ is monomodal and has a time-invariant shape. In normal grain growth, some grains grow and some grains shrink, as illustrated using a 2D computer simulation (Frost *et al.*, 1988) in Fig. 4. The resulting increase in the average grain size leads to a corresponding decrease in the total grain boundary area. This results in a decrease in the energy of the system due to the reduction of the excess free energy associated with grain boundaries, which will be discussed in terms of the excess energy per unit area of grain boundary, γ_{gb}. For

(a)   (b)
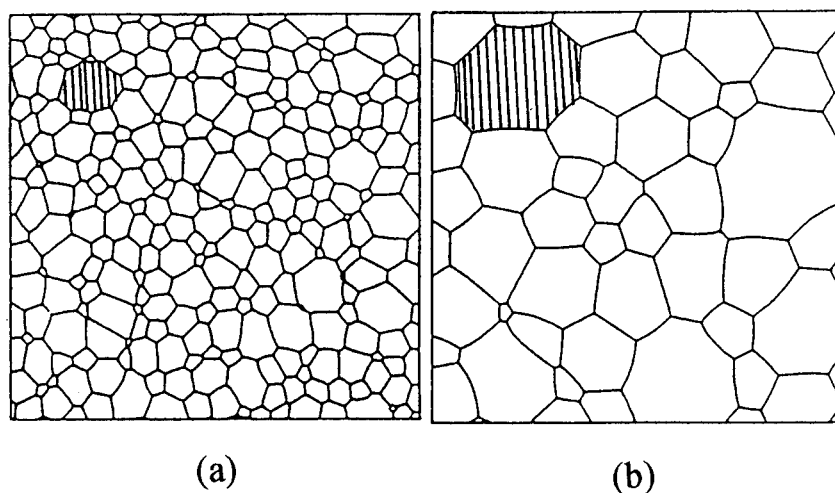
Fig. 4. Top view of a thin film undergoing normal grain growth. Large grains tend to grow larger and small grains tend to shrink and disappear, so that the average grain size increases over time. Output of a computer simulation of grain growth (Frost *et al.*, 1988).

the purposes of subsequent discussion, it will be assumed that it is adequate to consider all boundaries as having the same energy γ_{gb}, corresponding to the average over the system. Relaxation of this assumption in computer simulations is discussed elsewhere (Hayashi *et al.*, 1994). Normal grain growth is therefore driven by the reduction of the total energy associated with grain boundaries.

When grain growth leads to evolution from the grain structures represented in Fig. 2(a) and (b) to that of Fig. 2(c), a steady state is not obtained as the structure evolves from one having a fully 3D character with non-equiaxed grains to one with a quasi-2D structure as shown in the cross-section in Fig. 2(c), and as shown in top and perspective views in Figs 4 and 5, respectively. Once a quasi-2D structure develops, subsequent grain growth occurs primarily via grain boundary motion in directions lying in the plane of the film. In this case, steady state conditions and normal grain growth could in principle occur, and the energy change associated with a change in average in-plane grain size from d_0 to d would be

$$\Delta F_{gb} = \gamma_{gb}\left(\frac{2}{d_0} - \frac{2}{d}\right), \tag{7}$$

and (6) is expected to be obeyed. In a 2D system, grain growth can be modeled and simulated by considering local motion of boundaries with in-plane velocities v normal to the grain boundary, and proportional to the local in-plane curvature κ, such that

$$v = m\gamma_{gb}\kappa, \tag{8}$$

where m is the grain boundary mobility and has a temperature dependence given by $m = m_0\exp(-Q/kT)$. The simulation used to generate Fig. 4 was based on incremental application of this law to points on boundaries, along with application of force
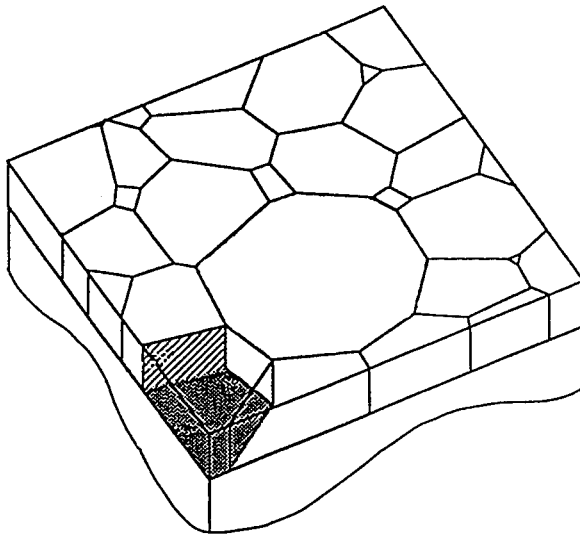
Fig. 5. Schematic perspective view of the grain structure of a film with equiaxed grains, and with most boundaries intersecting both surfaces of the film.

balances at grain boundary triple junctions in each time increment (Frost *et al.*, 1988). The resulting simulation obeys (6) [with $d = (4A/\pi)^{1/2}$ and $A =$ the in-plane grain area] and otherwise has the characteristics of normal grain growth.

Abnormal grain growth

While 2D normal grain growth is readily modeled and simulated and films with structures such as in Fig. 4 are attractive candidates for testing such models, normal grain growth rarely occurs even in films with equiaxed quasi-2D structures. There are two reasons for this:

(i) phenomena leading to grain boundary drag usually prevent steady state growth (or even lead to complete grain growth stagnation), and

(ii) there are almost always grain-orientation-specific driving forces for grain growth that favor subpopulations of grains and prevent steady state behavior until all favored grains are eliminated.

In both cases, the grain growth that occurs is considered abnormal grain growth.

A common source of grain boundary drag is the formation of grooves where grain boundaries intersect the surfaces of the film. Mullins (1958) has argued that if grain growth is driven by the elimination of grain boundary energy alone, groove formation can result in grain growth stagnation when the average in-plane size is approximately equal to the film thickness, $d \cong h$, as had often been observed in metallic sheet (Beck *et al.*, 1948), and as has subsequently been observed in thin films (Thompson, 1990). This result has also been obtained when 2D grain growth simulations are modified to allow for groove-induced stagnation (Frost *et al.*, 1988). Simulations have also shown that grain-boundary-groove-induced stagnation leads to lognormal grain size distributions, as is also often observed in thin films (Thompson, 1990; Frost *et al.*, 1990; Palmer *et al.*, 1987; Tracy *et al.*, 1988; Wu *et al.*, 1991). Solute drag has also been shown (Frost *et al.*, 1992) to result in transient, though persistent, lognormal grain size distributions.

Grain-orientation-specific driving forces for grain growth can arise from several sources. Thin films are not two-dimensional, and therefore have top and bottom surfaces that also have excess free energies per unit area, γ_s. For a film on a substrate, the bottom interface will have an excess energy per unit area, γ_i. Both γ_s (the energy of the free surface) and γ_i depend strongly on the orientation of a grain with respect to the plane of the film. For example, for f.c.c. metals on amorphous substrates (e.g. on oxidized Si), it is expected that both γ_i and γ_s are minimized for grains with (111) texture. This means that growth of grains with (111) texture is generally favored over growth of grains with other orientations. This can result in the development of bimodal grain size distributions (Frost *et al.*, 1992), as illustrated in Fig. 6(a), in which the large grains have γ_s and γ_i minimizing orientations. Eventually these grains will consume all other grains, resulting in a population of grains with a monomodal size distribution, but with highly restricted textures (Thompson, 1990).

Mullins (1958) argued that if the surface energies for grains meeting at a boundary are sufficiently different, the boundary can avoid groove-induced stagnation. In this case, low γ_s and γ_i grains can grow at the expense of an otherwise stagnant matrix of

(a)   (b)
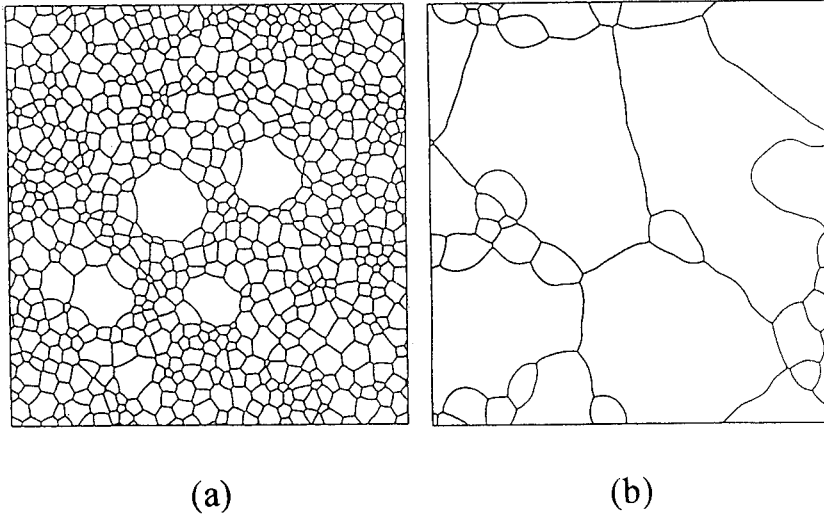
Fig. 6. (a) In abnormal and secondary grain growth, growth of a subpopulation of grains is favored so that bimodal grain sizes can develop. (b) Favored grains eventually consume unfavored grains, leading to large grains with monomodally distributed sizes. These figures are a result of computer simulations (Frost et al., 1992).

grains with other orientations. This mode of grain growth is often referred to as secondary grain growth (Thompson, 1985; Thompson, 1990). Stagnation of the matrix can result from groove formation or as a result of the presence of precipitates. Secondary grain growth can lead to striking examples of bimodally distributed grain sizes, in which the favored grains grow to sizes that can be many times the film thickness. For example, precipitate-induced secondary grain growth has been observed to lead to grain sizes as large as 1 mm in 1 μm thick Al films (Gangulee and d'Heule, 1972; Longworth and Thompson, 1991).

The change in energy associated with grain-growth-induced reductions in the average surface and interface energy of a film, γ_s and γ_i, respectively, can be shown to be given by

$$\Delta F_{s/i} = \frac{\Delta \bar{\gamma}}{h},\tag{9a}$$

where

$$\Delta \bar{\gamma} = [\bar{\gamma}_s - (\bar{\gamma}_s)_0] - [\bar{\gamma}_i - (\bar{\gamma}_i)_0],\tag{9b}$$

and where $\bar{\gamma}$ and $(\bar{\gamma})_0$ are the final and initial average energies, respectively (Thompson, 1992; Thompson and Carel, 1995). Because $\Delta F_{s/i}$ is an energy per volume, the relative contribution of $\Delta F_{s/i}$ to the total enery change accompanying grain growth is higher for thinner films. The effects of surface and interface energy minimization on grain growth and texture evolution are therefore strongest in very thin films.

Surface and interface energy minimization has been shown to lead to abnormal or secondary grain growth and texture evolution in a large number and wide variety of

experimental systems (Thompson, 1990; Carel and Thompson, 1995). Surface and interface-energy-driven abnormal or secondary grain growth in free-standing poly-crystalline films or films on amorphous substrates leads to dominance of grains with uniform or restricted textures, but with otherwise random orientations with respect to rotations around film normals. Grain growth in polycrystalline films on single crystal substrates can lead to epitaxial grain growth in which the dominating grains have three-dimensionally constrained, epitaxial orientations (Thompson *et al.*, 1990).

STRESS AND GRAIN GROWTH IN THIN FILMS

"Densification"

Grain boundaries have an excess free volume per unit area, Δa, when compared to single crystal material [for f.c.c. metals, $\Delta a \sim 1$ Å, Frost *et al.* (1982)]. As grains grow, this free volume is redistributed. In thin films attached to thick substrates and having high-traction interfaces, this results in a biaxial strain given by

$$\varepsilon_d = \Delta a \left(\frac{1}{d} - \frac{1}{d_0} \right). \tag{10}$$

(Note that this expression differs by a factor of 2 from that given by Doerner and Nix (1988), but its derivation is very similar to the one given by them, except that the value taken for the excess volume per grain is halved, to account for grain boundary sharing.) The "densification" strain can be quite high, depending strongly on d_0 which can again be taken to be the grain size when film coalescence occurs. If this strain is elastically accommodated, grain growth can therefore lead to a significant change in the average energy density,

$$\Delta F_d = \bar{M} \varepsilon_d^2, \tag{11}$$

where $\bar{M}$ is the average biaxial modulus that for now is assumed not to change during grain growth. As first pointed out by Chaudhari (1971), for sufficiently small d_0, ΔF_d can exceed ΔF_{gb} so that there is a limiting grain size d^*, as illustrated in Fig. 7(a).
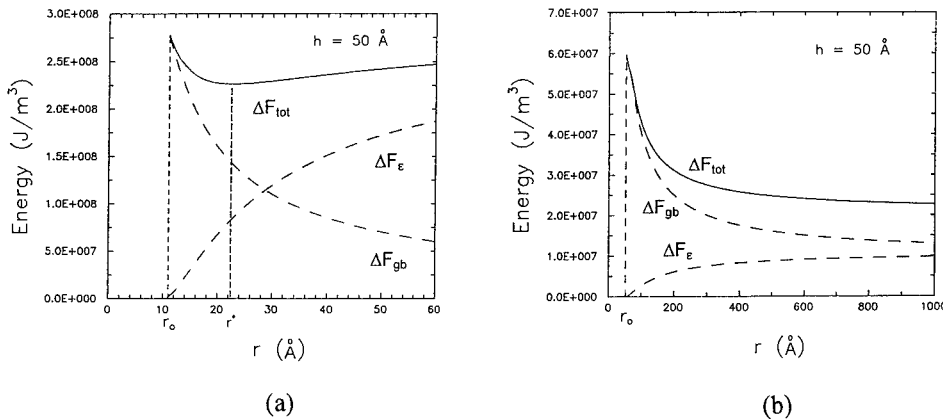
Fig. 7. (a) If the initial grain radius r_0 ($r_0 = d_0/2$) is less than about 20 Å, above r^*, the strain energy density due to "densification" will exceed the energy decrease due to reduction of the total grain boundary energy.
(b) For larger r_0s, strain will not stop grain growth and large strain energy densities can develop.
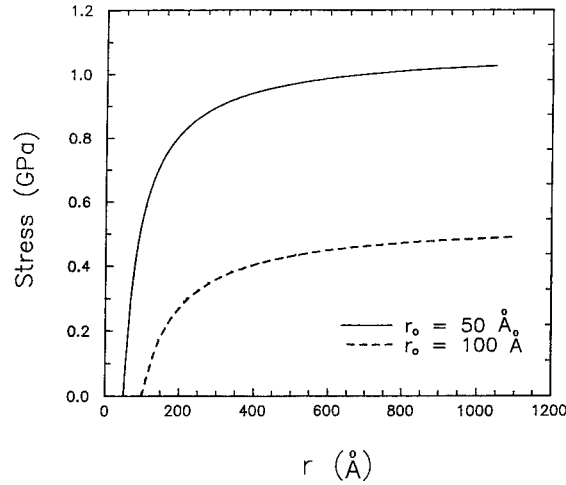
Fig. 8. Strain resulting from grain-boundary-energy-driven grain growth, as a function of two initial grain sizes.

However, this is only the case if $d_0 \lesssim 40$ Å. Otherwise, as shown in Fig. 7(b), the energy driving grain growth ($\Delta F_{s/i}$ as well as ΔF_{gb}) is high enough to overcome high changes in strain energy densities so that grain growth proceeds, leading to increased and potentially high strains (Fig. 8).

Strain-energy-driven abnormal grain growth

A more general form of (11) is

$$\Delta F_\varepsilon = (\bar{M} - \bar{M}_0)\varepsilon^2, \tag{12a}$$

where

$$\varepsilon = \varepsilon_{th} + \varepsilon_d + \varepsilon_i, \tag{12b}$$

and where ε_i is the intrinsic stress and ε_{th} is taken to be

$$\varepsilon_{th} = \int_{T_{dep}}^{T_{gg}} (\alpha_s - \alpha_f)\, dT, \tag{12c}$$

with T_{dep} being the deposition temperature and T_{gg} being the temperature at which grain growth occurs; and where $\bar{M}$ and $\bar{M}_0$ are the average effective biaxial moduli after and before grain growth. This expression allows for the fact that as texture evolves during grain growth, $\bar{M}$ will change (Floro *et al.*, 1994; Thompson and Carel, 1995a). In this case, the change in strain energy density can drive grain growth, but specifically favors the growth of grains with low M_{hkl} orientations, i.e. for f.c.c. metals, grains with (100) texture. Strain energy minimization, therefore, provides an orientation-specific driving force that can cause abnormal or secondary grain growth and texture evolution, just as surface and interface energy minimization does (Floro *et al.*, 1994; Carel *et al.*, 1994; Carel and Thompson, 1995; Thompson and Carel,

1995a). However, elastic strain energy minimization generally does not lead to the same texture as surface and interface energy minimization, so that $\Delta F_{s/i}$ and ΔF_{ε} compete in defining the final texture resulting from grain growth.

If we restrict our discussion to f.c.c. metals ("type II" materials) ε_i is expected to be small, and d_0 is relatively large, so that ε_d is small as well. In this case,

$$\Delta F_{\varepsilon} \cong (\Delta M)\varepsilon_{th}^2, \tag{13}$$

where $\Delta M = \bar{M} - \bar{M}_0$. For f.c.c. metals on amorphous substrates, we expect (100) strain-energy-minimizing textures to dominate when $\Delta F_{\varepsilon} > \Delta F_{s/i}$, and (111) surface and interface energy minimizing textures to dominate otherwise. This allows prediction of a "texture map" (Carel and Thompson, 1995; Thompson and Carel, 1995), as illustrated in Fig. 9, where the transition from (111) to (100) texture as a function of $\Delta T = T_{gg} - T_{dep}$ and the film thickness h, is found by setting $\Delta F_{\varepsilon} = \Delta F_{s/i}$, or requiring that

$$\Delta M(\Delta\alpha\Delta T)^2 \cong \frac{\Delta\gamma}{h}, \tag{14}$$

where $\Delta\gamma$ and ΔM are defined in terms of the difference for (111) and (100) grains. This expected behavior has been confirmed in a variety of systems, including Ag films undergoing grain growth on both single crystal substrates (Floro et al., 1994) and amorphous substrate (Carel and Thompson, 1995; Thompson and Carel, 1995b), as shown in Fig. 10(a) and (b). This behavior is also quantitatively consistent with more detailed simulations of grain growth that are based on modifications of the 2D simulation discussed earlier (Carel et al., 1994). Differences in strain energy density
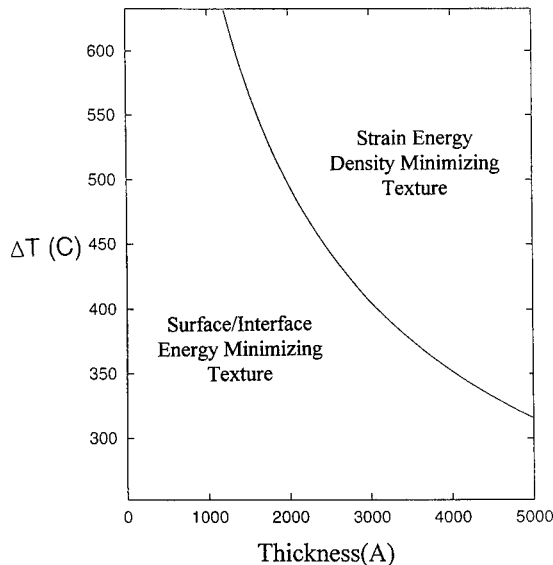
Fig. 9. A texture map for the texture resulting from grain growth at temperatures T_{gg} in films of thickness h deposited at T_{dep}. The thermal strain scales with $\Delta T \equiv T_{gg} - T_{dep}$. At low ΔT and h, surface- and interface-energy-minimizing textures are favored. At high ΔT and h, strain-energy-minimizing textures are favored.

can therefore be seen to drive grain growth and texture evolution in some cases, and oppose grain growth in others. When strain-energy-density-minimization dominates over surface- and interface-energy-minimization, grain growth can be a strain relief mechanism.

The effects of yielding

In the discussion so far, it has been assumed that the yield stresses of all the grains are sufficiently high that thermal strains are elastically accommodated. However, if grain growth continues, the yield stress of individual grains will decrease so that their advantage will diminish and eventually disappear. Therefore, even at high ΔT, surface and interface energy minimization will eventually dominate in the latter stages of growth, assuming that grain growth stagnation does not "lock-in" strain-energy-minimizing orientations.

It should be noted that as discussed previously, grains with (110) or (210) orientation are expected to have lower yield stresses than (111) or (100) grains, so that, for grains of equal initial sizes, (110) grains will yield before (100) or (111) grains, and may therefore have an energetic advantage for further growth. Yielding therefore favors the growth of low yield stress grains. This can lead to strain energy minimizing textures other than (100), even in nearly elastically isotropic materials (Sanchez and Artz, 1992; Thompson, 1993b), as has been suggested as an explanation for observation of (110) textures resulting from precipitate-induced secondary grain growth in Al alloys at anomalously high T_{gg}s. Again, strain energy minimization associated with

(a)   (b)
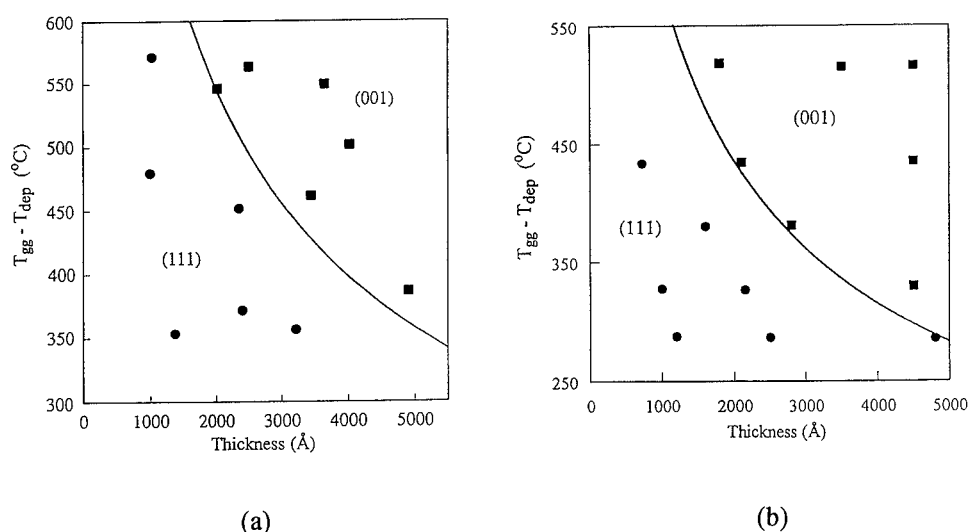
Fig. 10. (a) An experimental texture map for polycrystalline Ag films deposited and annealed on single crystal (100)Ni films on (100)Ag on (100)MgO. The line is calculated based on known values of $\Delta\gamma$ and ΔM. Squares and circles correspond to films with (100) (111) textures, respectively (Carel and Thompson, 1995; Thompson and Carel, 1995b). (b) An experimental texture map for polycrystalline Ag films deposited on (100) MgO substrates coated with amorphous SiO_2 (Carel and Thompson, 1995; Thompson and Carel, 1995b).

yielding of a subpopulation of grains can drive grain growth, so that grain growth can be a strain-relief mechanism, and, in this case, assist yielding.

SUMMARY AND CONCLUSIONS

In polycrystalline thin films, the grain size perpendicular to the plane of the film is similar to the film thickness. However, the in-plane grain sizes can be much smaller than the film thickness, e.g. when refractory materials are deposited at or near room temperature; can be comparable to the film thickness (e.g. in as-deposited f.c.c. metals); or can be many times the film thickness, when abnormal or secondary grain growth occurs during film formation or as a result of post-deposition annealing.

Both the small grain sizes and the small thickness of polycrystalline thin films constrain yielding mechanisms and lead to very high yield stresses up to the order of GPas. As a result, thin films can, and do, support very high intrinsic and extrinsic stresses. Intrinsic tensile stresses of order 1 GPa can develop during evaporative or sputter deposition of low mobility materials (refractory materials at or near room temperature). Intrinsic compressive stresses of order 1 GPa can develop during sputter deposition of low mobility materials. High mobility materials (e.g. pure f.c.c. metals) tend to have low intrinsic stresses when deposited at or near room temperature, but can support high extrinsic stresses.

Grain growth can play a dominant role in defining the grain size and texture of as-deposited films of high mobility materials, and of annealed films of any polycrystalline material. Grain growth in films is almost always abnormal, in that growth of sub-populations of grains with specific crystallographic orientations is favored either by surface- and interface-energy-minimization or by strain-energy-density-minimization. This often leads to bimodal grain size distributions, and also leads to texture evolution during grain growth. Strain-energy-minimizing textures are favored when films are deposited at temperatures well below grain growth temperatures and in thicker films. Surface and interface energy minimizing textures are favored at low strains and in thinner films.

Because there is excess free volume associated with grain boundaries, grain growth can lead to the development of a tensile strain, the final magnitude of which increases sharply with decreasing initial grain size. Because strains in films are generally biaxial, they lead to grain-to-grain differences in strain energy densities in elastically aniso-tropic materials, as well as in isotropic materials in which yielding has occurred. These differences can drive or suppress grain growth depending on whether or not strain-energy-density-minimization dominates over surface- and interface-energy-mini-mization. When differences in strain energy densities dominate in driving grain growth, grain growth can provide a mechanism for stress relief and can promote plastic yielding.

Because of the strong dependence of grain growth behavior on mechanical proper-ties and the dependence of mechanical properties on microstructure, grain structure evolution, mechanical properties and mechanical deformation are highly coupled in thin films.

ACKNOWLEDGEMENTS

REFERENCES

Abermann, R. (1990) *Vacuum* **41**, 1279.
Abermann, R. (1992) *Mater. Res. Soc. Symp. Proc.* **239**, 25.
Abermann, R. and Koch, R. (1985) *Thin Solid Films* **129**, 71.
Abermann, R., Kramer, R. and Mäser, J. (1978) *Thin Solid Films* **52**, 215.
Atkinson, H. V. (1988) *Acta Metall.* **36**, 469.
Beck, P. A., Kremer, J. C., Dember, L. J. and Holzworth, M. L. (1948) *Am. Inst. Min. (Metall.) Engng* **75**, 372.
Carel, R., Thompson, C. V. and Frost, H. J. (1994) *Mater. Res. Soc. Symp. Proc.* **343**, 49.
Carel, R. and Thompson, C. V. (1995) Ph.D. Thesis, Department of Materials Science and Engineering, Massachusetts Institute of Technology.
Chaudhari. (1971) *J. Vac. Sci. Tech.* **9**, 520.
d'Heurle, F. M. (1970) *Metall. Trans.* **1**, 725.
Doerner, M. F. and Nix, W. D. (1988) *CRC Critical Rev. in Sol. State and Mater. Sci.* **14**, 225.
Floro, J. A., Thompson, C. V., Carel, R. and Bristowe, P. D. (1994) *J. Mater. Res.* **9**, 94.
Frost, H. J., Hayashi, Y., Thompson, C. V. and Walton, D. T. (1994) *Mater. Res. Soc. Symp. Proc.* **317**, 431.
Frost, H. J., Spaepen, F. and Ashby, M. F. (1982) *Scripta Metall.* **16**, 1165.
Frost, H. J., Thompson, C. V., Howe, C. L. and Whang, J. (1988) *Scripta Metall.* **22**, 65.
Frost, H. J., Thompson, C. V. and Walton, D. T. (1990) *Acta Metall. Mater.* **38**, 1455.
Frost, H. J., Thompson, C. V. and Walton, D. T. (1992) *Acta Metall.* **40**, 779.
Gangulee, Q. A. and d'Heurle, F. M. (1972) *Thin Solid Films* **12**, 399.
Grovenor, C. R. M., Hentzell, H. T. G. and Smith, D. A. (1984) *Acta Metall.* **32**, 773.
Hayashi, Y., Frost, H. J., Thompson, C. V. and Walton, D. T. (1994) *Mater. Res. Soc. Symp. Proc.* **317**, 485.
Hoffman, D. W. (1976) *Thin Solid Films* **34**, 185.
Hoffman, D. W. and Thorton, J. A. (1982) *J. Vac. Sci. Tech.* **20**, 355.
Lloyd, J. R. and Smith, P. M. (1983) *J. Vac. Sci. Technol.* **A1**, 455.
Longworth, H. P. and Thompson, C. V. (1991) *J. Appl. Phys.* **69**, 3929–3940.
Mouchan, B. A. and Demichisin, A. V. (1969) *Fiz. Met.* **28**, 83.
Mullins, W. W. *Acta Metall.* **6**, 414 (1958).
Murikami, M. and Chaudhari, P. (1977) *Thin Solid Films* **46**, 109.
Nix, W. D. (1989) *Met. Trans.* **20A**, 2217.
Nix, W. D. (1994) Private communication.
Ohring, M. (1992) *The Materials Science of Thin Films*, Ch. 9. Academic Press, Boston.
Palmer, J. E., Thompson, C. V. and Smith, H. I. (1987) *J. Appl. Phys.* **62**, 2494.
Sanchez, J. E. and Artz, E. (1992) *Scripta Metall. Mater.* **27**, 285.
Thompson, C. V. (1985) *J. Appl. Phys.* **58**, 763.
Thompson, C. V. (1990) *Ann. Rev. Mater. Sci.* **20**, 245.
Thompson, C. V. (1992) *Proceedings of the International Conference on Grain Growth in Polycrystalline Materials*, Trans. Tech. Publications, Pt. I, 245.
Thompson, C. V. (1993a) *J. Mater. Res.* **8**, 237.
Thompson, C. V. (1993b) *Scripta Metall. Mater.* **28**, 167.
Thompson, C. V. and Carel, R. (1995a) *J Mater. Sci. Engng* **32B**, 211.
Thompson, C. V. and Carel, R. (1995b) to be published in the *Proceedings of the 2nd International Conf. on Grain Growth*, Kitakyushu, Japan.
Thompson, C. V., Floro, J., Smith, H. J. (1990) *J. Appl. Phys.* **67**, 4099.

Thornton, J. A. (1977) *Ann. Rev. Mater. Sci.* **7,** 239.

Tracy, Davies, P. W., Fanger, D. and Gartman, P. (1988) *Microstructural Science for Thin Film Metallizations in Electronic Applications* pp. 157–167 TMS.

Venkatraman, R. and Bravman, J. C. (1992) *J. Mater. Res.* **7,** 2040.

Wong, C. C., Smith, H. I. and Thompson, C. V. (1986) *Appl. Phys. Lett.* **48,** 335.

Wu, K., Baerg, W. and Jupiter, P. (1991) *Appl. Phys. Lett.* **58,** 1299–1301.

Pergamon

PII S0022–5096(96)00005–1

SUBSTRATE CURVATURE RESULTING FROM THE CAPILLARY FORCES OF A LIQUID DROP

FRANS SPAEPEN

Division of Applied Sciences, Harvard University, Cambridge, MA 02138, U.S.A.

ABSTRACT

The difference between interfacial tension and interface stress is illustrated by considering a hemispherical liquid drop on a solid substrate. The equilibrium shape is determined by minimizing the total interfacial free energy, which leads to the Young equation for balance of the interfacial tensions. The curvature of the substrate is determined by the interfacial stresses. Two contributions are calculated: one arising from the hydrostatic pressure in the drop, the other from the imbalance of the interfacial stresses.

INTRODUCTION

The surface of a solid (or the interface between a solid and a fluid) is characterized by two thermodynamic quantities (Gibbs, 1906; Shuttleworth, 1950; Herring, 1951; Cahn, 1980; Cammarata, 1994): the surface (or interfacial) tension, γ, which is a scalar equal to the work required to create a unit area of new interface at constant strain in the solid, and the surface (or interface) stress, f_{ij}, which is 2×2 tensor such that the surface work required to strain a unit surface elastically by $d\varepsilon_{ij}$ is $f_{ij} d\varepsilon_{ij}$.†

The following argument, due to Shuttleworth (1950) and illustrated in Fig. 1, shows the relation between the two quantities. Splitting a strain-free solid in two parts (I → II) creates two new surfaces of area A, and requires an amount of work $2A\gamma$. Straining the two parts by $d\varepsilon_{ij}$ (II → IV) requires dW_{bulk} to strain the bulk solids (as for I → III) and $2Af_{ij} d\varepsilon_{ij}$ to strain the two surfaces. Splitting the strained solid into the same two parts (III → IV) creates two new (strained) surfaces of area $A + dA = A(1 + d\varepsilon_{ij})$, and requires an amount of work $2A(d\varepsilon_{ij})\gamma(d\varepsilon_{ij}) = 2A\gamma + 2d(A\gamma)$. The first law of thermodynamics now demands

$$Af_{ij} d\varepsilon_{ij} = d(\gamma A). \tag{1}$$

Since

$$d(\gamma A) = A \, d\gamma + \gamma \, dA = A \, d\gamma + \gamma A \, d\varepsilon_{ii}, \tag{2}$$

(1) becomes

---

† There is no uniformity in the nomenclature for the two quantities. Some authors refer to the surface tension, as defined here, as the surface energy or free energy, or to the surface stress, as defined here, as the surface tension. The nomenclature used here is common at the present time, but not unique.

F. SPAEPEN
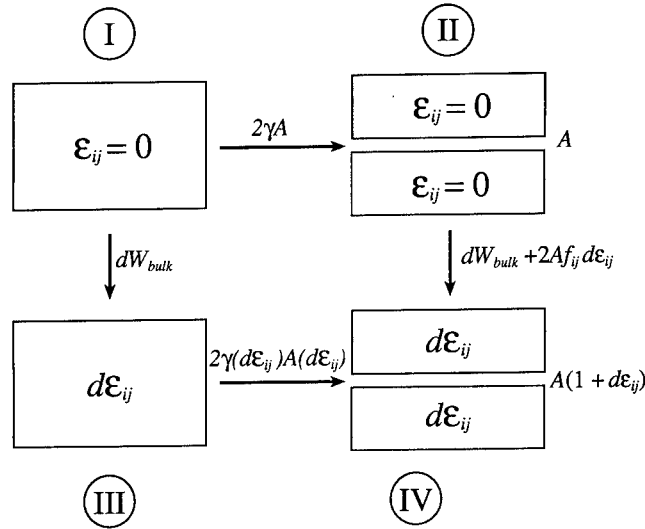
Fig. 1. Transformations in the derivation of the relation between the surface tension, γ, and the surface stress, f_{ij}. After Shuttleworth (1950).

$$f_{ij} = \gamma \delta_{ij} + \frac{\mathrm{d}\gamma}{\mathrm{d}\varepsilon_{ij}}. \tag{3}$$

The first term on the right-hand side simply reflects the change in the Eulerian area of the surface. The second term arises from the presence between the atoms at or near the surface of forces that are different from those in the bulk. For fluid surfaces or fluid–fluid interfaces this second term is zero, since no elastic shear stresses can be applied. In that case f is identical to γ. If a solid phase is present, the elements of f_{ij} can be quite different from γ; even their sign, unlike that of γ, which is always positive for stable interfaces, is not *a priori* known. Note that even though f is called a "stress", it has the same dimensions as γ, i.e. force per length (not force per area).

To illustrate the importance of the difference between the two quantities, the curvature of a substrate as a result of the presence of a liquid drop placed on it is calculated. It will be shown that the shape of the drop is determined by the balance of the surface and interface tensions, γ_{ab}. The elastic curvature of the substrate, however, results from the forces exerted by the surfaces and interface, and hence from the surface and interface stresses, f_{ab}.

Figure 2 shows the droplet on a solid surface, surrounded by a vapor phase. For simplicity, the problem is kept two-dimensional (i.e. a cylindrical droplet, with quantities computed per unit length perpendicular to the page). Associated with the three types of interfaces are the tensions γ_{lv}, γ_{sv}, and γ_{sl}, and the stresses f_{lv} ($=\gamma_{lv}$), f_{sv} and f_{sl} (corresponding to the only applicable strain, ε_{11}, in the direction of the interface). To avoid complications from surface segregation, the three phases consist of the same single element. This problem is also of interest for the analysis of *in situ* curvature measurements during the early stages of condensation experiments.
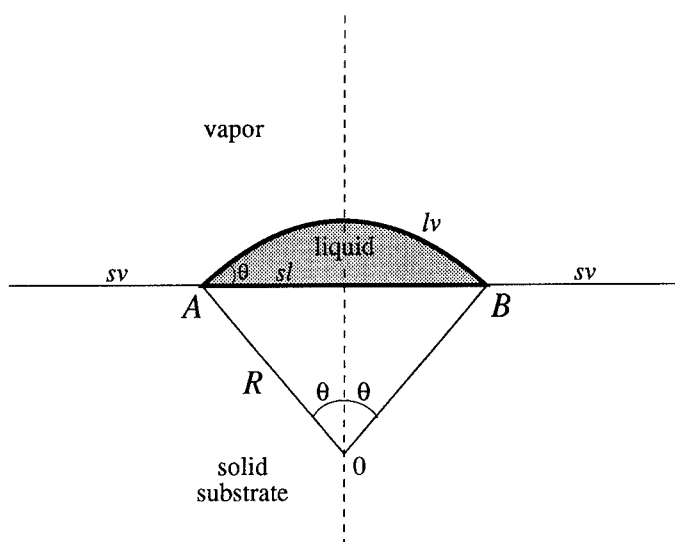
Fig. 2. Diagram of the droplet on the substrate, indicating the relevant interfaces and quantities.

EQUILIBRIUM SHAPE OF THE DROPLET

Consistent with γ_{lv} being isotropic, the liquid–vapor interface is considered semi-circular, with radius of curvature R. Let the angle between the radii to the end points, OA and OB, be 2θ. The equilibrium shape of the droplet of a given volume is determined by the minimum in the free energy of the system with respect to θ or R. Placing the droplet on the substrate replaces solid–vapor interface by solid–liquid interface over an area A_{sl}, and creates an area A_{lv} of liquid–vapor interface. The associated changes in free energy are

$$\Delta F = A_{sl}(\gamma_{sl} - \gamma_{sv}) + A_{lv}\gamma_{lv}, \tag{4}$$

or, from the geometry of Fig. 2

$$\Delta F = 2R\sin\theta(\gamma_{sl} - \gamma_{sv}) + 2\theta R\gamma_{lv}. \tag{5}$$

To minimize this free energy at constant volume $V = R^2(\theta - \sin\theta\cos\theta)$, a Lagrange multiplier, λ, is introduced

$$F = 2R\sin\theta(\gamma_{sl} - \gamma_{sv}) + 2\theta R\gamma_{lv} + \lambda R^2(\theta - \sin\theta\cos\theta). \tag{6}$$

Minimization gives the conditions

$$\frac{\partial F}{\partial R} = 2\sin\theta(\gamma_{sl} - \gamma_{sv}) + 2\theta\gamma_{lv} + 2\lambda R(\theta - \sin\theta\cos\theta) = 0, \tag{7a}$$

$$\frac{\partial F}{\partial \theta} = 2R\cos\theta(\gamma_{sl} - \gamma_{sv}) + 2R\gamma_{lv} + \lambda R^2(1 - \cos^2\theta + \sin^2\theta) = 0. \tag{7b}$$

Equating λR found from both equations gives

$$-\lambda R = \frac{(\gamma_{sl}-\gamma_{sv})\cos\theta+\gamma_{lv}}{\sin^2\theta} = \frac{(\gamma_{sl}-\gamma_{sv})\sin\theta+\gamma_{lv}\theta}{\theta-\sin\theta\cos\theta}. \tag{8}$$

Putting the last equality on a common denominator gives for the numerators, after dividing by γ_{lv} and collecting terms in θ to one side

$$\theta\left(\frac{\gamma_{sl}-\gamma_{sv}}{\gamma_{lv}}\cos\theta-\sin^2\theta+1\right) = \sin\theta\cos\theta+\frac{\gamma_{sl}-\gamma_{sv}}{\gamma_{lv}}\sin\theta\cos^2\theta+\frac{\gamma_{sl}-\gamma_{sv}}{\gamma_{lv}}\sin^3\theta,$$

$$\tag{9}$$

or, simplifying the trigonometric functions

$$\theta\cos\theta\left(\frac{\gamma_{sl}-\gamma_{sv}}{\gamma_{lv}}+\cos\theta\right) = \sin\theta\left(\frac{\gamma_{sl}-\gamma_{sv}}{\gamma_{lv}}+\cos\theta\right). \tag{10}$$

Equation (10) can only be satisfied in two ways: $\theta = 0$ (complete wetting, which requires $\gamma_{sl}+\gamma_{lv} < \gamma_{sv}$, or, more interestingly

$$\cos\theta = -\frac{\gamma_{sl}-\gamma_{sv}}{\gamma_{lv}}, \tag{11}$$

which is the well-known equation of Young for the equilibrium wetting angle, θ. This scalar equation has an equally well-known vector representation, shown in Fig. 3. Although in this diagram the interfacial tensions are formally represented as vectors that are horizontally equilibrated, it should be kept in mind that these vectors are not forces. The formal equilibration at A simply arises from requirement that the change in total interfacial free energy upon a virtual displacement of A (horizontal—the only possible direction consistent with the problem) to be zero (Herring, 1951).

Insertion of (11) into (8) gives the value of the Lagrange multiplier in equilibrium

$$\lambda = -\frac{\gamma_{lv}}{R}, \tag{12}$$

which is the pressure difference between the liquid and vapor across the curved interface, as discussed below.
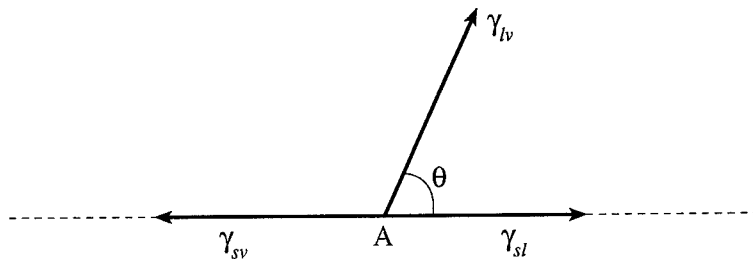
Fig. 3. Vector diagram showing the horizontal balance of the interfacial tensions that yields the wetting angle, θ.
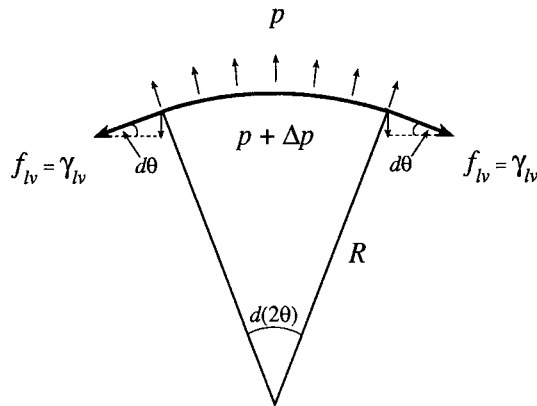
Fig. 4. Portion of the liquid–vapor interface, indicating the relevant quantities for Laplace's calculation of the pressure difference between liquid and vapor.

CURVATURE OF THE SUBSTRATE

Having established the shape of the droplet from the relation between the tensions, we can now consider the strains in the substrate that result from the forces exerted by the droplet and its interfaces. Since the displacements under consideration here are elastic ones, the interfacial stresses are the relevant quantities.

The stress inside the droplet is hydrostatic. The pressure exceeds that in the vapor by Δp, which is found by the well-known Laplace force equilibrium, illustrated in Fig. 4 on a small portion of the liquid surface. The component of the force normal to the surface is balanced by the components of f_{lv} in that direction:

$$2R\,\mathrm{d}\theta \Delta p = 2f_{\mathrm{lv}}\,\mathrm{d}\theta, \qquad (13)$$

or, since for the liquid $f_{\mathrm{lv}} = \gamma_{\mathrm{lv}}$

$$\Delta p = \frac{\gamma_{\mathrm{lv}}}{R} \qquad (14)$$

A free body diagram of the vertical forces on the substrate is shown in Fig. 5. The
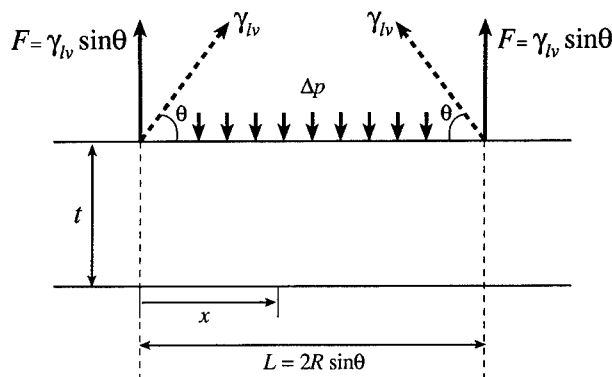
Fig. 5. Free body diagram of the substrate with the vertical capillary forces.

F. SPAEPEN

vertical components of the capillary forces, $2\gamma_{lv}\sin\theta$, spaced a distance $L = 2R\sin\theta$ apart, are balanced by the force from the hydrostatic pressure $\Delta p\ 2R\sin\theta$. The substrate curvature resulting from this load is estimated using simple beam bending, with a strain that varies linearly through the thickness. It can be used if the thickness of the substrate, t, is less than L. Left and right of the droplet the curvature is zero. Under the droplet, the curvature varies, being maximum in the middle, and going to zero at the ends. We are interested in calculating an average curvature, since that is the one measured in condensation experiments. Standard balancing of forces and moments gives for the strain in the top surface

$$\varepsilon_0(x) = \frac{6Fx}{Et^2}\left(\frac{x}{L} - 1\right),\tag{15}$$

where E is Young's modulus of the substrate. The total elongation of the top fiber is then

$$\Delta L = \int_0^L \varepsilon_0(x)\,\mathrm{d}x = -\frac{FL^2}{Et^2},\tag{16}$$

which translates into an average curvature of

$$\kappa_1 = \frac{2\Delta L}{tL} = -\frac{2FL}{t^3E} = -\frac{4\gamma_{lv}R\sin^2\theta}{t^3E}.\tag{17}$$

The free body diagram for the horizontal forces on the substrate is shown in Fig. 6. When balancing forces for the system to one side of a cut AA', the capillary contributions are: the horizontal component of the liquid–vapor interfacial tension, $\gamma_{lv}\cos\theta$, the interface stress f_{sl} from the solid–liquid interface at the top, and the interface stress f_{sv} from the solid–vapor interface at the bottom. The interface stress at the bottom is taken the same as that at the top–vapor interface; otherwise the substrate outside the droplet would have a net curvature.

The curvature under droplet is constant in this case, and is obtained directly
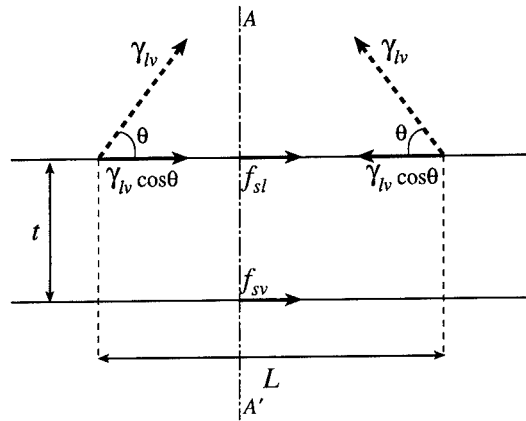
Fig. 6. Free body diagram of the substrate with the horizontal capillary forces.

from the well-known Stoney equation (Nix, 1989), which applies exactly for the infinitesimally thin surfaces in which the forces on either side of the substrate act

$$\kappa_2 = \frac{6(f_{sv} - f_{sl} - \gamma_{sl} \cos \theta)}{t^2 E}.$$

(18)

Note that having f_{sv} acting at the bottom is equivalent to having $-f_{sv}$ acting at the top. This contribution to the curvature is an essential result of the action of interface stresses insteads of tensions. The factor in parentheses would be zero by the Young equation, (11), if interfacial tensions were used.

ACKNOWLEDGEMENTS

REFERENCES

Cahn, J. W. (1980) Surface stress and the chemical equilibrium of small crystals—I. The case of the isotropic surface. *Acta Metall.* **28,** 1333–1338.
Cammarata, R. C. (1994) Surface and interface stress effects in thin films. *Prog. Surf. Sci.* **46,** 1–38.
Gibbs, J. W. (1906) *The Scientific Papers of J. Willard Gibbs,* Vol. I, p. 55. Longmans-Green, London.
Herring, C. (1951) Surface tension as a motivation for sintering. *The Physics of Powder Metallurgy* (ed. W. E. Kington), pp. 143–179. McGraw-Hill, New York.
Nix, W. D. (1989) Mechanical Properties of thin films. *Met. Trans. A* **20,** 2217–2245.
Shuttleworth, R. (1950) The surface tension of solids. *Proc. Phys. Soc. London* **A63,** 444–457.

SMALL AND LARGE DEFORMATION OF THICK AND THIN-FILM MULTI-LAYERS: EFFECTS OF LAYER GEOMETRY, PLASTICITY AND COMPOSITIONAL GRADIENTS

M. FINOT and S. SURESH

Department of Materials Science and Engineering, Massachusetts Institute of Technology, Cambridge, MA 02139, U.S.A.

ABSTRACT

The thermomechanical response of multi-layered materials subjected to small and large deformation during temperature excursions is examined in this paper. General bilayer and trilayer plates with comparable layer thicknesses, as well as the limiting cases of thin films on thicker substrates with and without compositionally graded interfaces are examined, all within the context of the classical Kirchoff theory for thin plates. Closed-form analytical formulations for small elastic deformation are presented whereby explicit expressions for stress/curvature relations are obtained for any general bilayer or graded trilayer with isotropic elastic properties, but anisotropic strains. The effects of the variation of Poisson ratio through the thickness of layered and compositionally graded materials on the evolution of multiple curvatures are analyzed. New theoretical results are presented on the effects of layer geometry, plastic flow and compositional gradation on large deformation (small strains and small rotations) in bilayer and trilayer systems comprising thick or thin-film layers. It is shown that the small deformation theory predictions for the generalized plane strain state provide an upper bound for curvature evolution among all the cases considered. By recourse to analytical methods and three-dimensional finite element modeling involving shell elements, particular attention is devoted to the occurrence of bifurcation in the solution for curvature evolution and the associated geometry changes in the thermoelastoplastic response of layered materials during thermal excursions. The model systems chosen for analyses include Ni–Al$_2$O$_3$ layers with a sharp or compositionally graded interfaces, Al/Si thin-film bilayers and a compositionally graded interlayer sandwiched between layers in In$_{0.12}$Ga$_{0.88}$As and GaAs for applications in microelectronics and optoelectronics, and a carbon/epoxy laminated composite.

NOTATION

a	Half thickness of the graded layer
$\hat{a}$	Non-dimensional thickness ($=2a/h_2$)
α	Coefficient of thermal expansion
$[\mathbf{A}, \mathbf{B}, \mathbf{D}]$	Reduced stiffness matrices of the layered plate
$[\mathbf{C}]$	Relation between the applied moments/loads and the curvatures of the plate
γ_{xy}	Shear strain
$\Delta\gamma_{xy}$	Mismatch shear strain between two layers
$\Delta\varepsilon$	Mismatch normal strain between two layers
ΔT	Temperature change from a stress-free state
$\widehat{\Delta T}$	Normalized temperature change
ΔT_1	Critical temperature change to induce plasticity as defined in Suresh *et al.* (1994)

ΔT_{b} Critical temperature change for bifurcation

ε° Strain at $z = 0$

$\varepsilon_{xx}, \varepsilon_{yy}$ Normal strains in the x and y direction

ε^{m} Mean normal strain

$[\mathbf{E}]$ Relation between the strain mismatch, $\vec{\Delta}\varepsilon$, and the overall strain at $z = 0$

$E_{(i)}$ Young's modulus of layer (i)

E_{bi} Biaxial modulus equal to $E/(1-v)$

$\hat{E}_{\mathrm{Bi}}$ Ratio of the biaxial moduli of layer 1 and layer 2

$h_{(i)}$ Thickness of layer (i)

$\hat{\kappa}$ Normalized curvature for small deformation $(=\kappa\lambda)$

κ_1 Curvature at the critical temperature variation, ΔT_1

κ_{b} Critical curvature for bifurcation

λ Characteristic length equal to $(h_1 + h_2)^3/6h_1 h_2$

$[\mathbf{M}]$ Matrix relating the mismatch strain, $\vec{\Delta}\varepsilon$, to the normalized curvature, $\hat{\kappa}$

$\vec{M}$ Resultant moments on the plate with respect to the plane $z = 0$

$\mu(i)$ Shear modulus of layer (i)

$\hat{\mu}$ Ratio of the shear moduli of layer 1 and layer 2

$\vec{N}$ Resultant forces on the plate

$v_{(i)}$ Poisson's ratio of layer (i)

v_{κ} Coupling effect between the curvatures in the x and y directions

ρ Ratio of the thicknesses of layer 1 and layer 2 $(=h_1/h_2)$

ρ_{a} Non-dimensional thickness of the graded layer $(=2a/(h_1 + h_2))$

$[\mathbf{S}]$ Stiffness matrix of each layer

σ_{xx}, σ_{yy} In-plane stresses in the x and y directions

$[\Sigma(z)]$ Matrix relating to the curvatures, $\vec{\kappa}$, to the stress, $\vec{\sigma}(z)$

τ Shear stress

$\vec{q}$ Vectorial notation of a tensor of order 2, q, (q_{xx}, q_{yy}, q_{xy}) such as κ, ε, σ and α

q^{inel} Variable depending on the inelastic strain

q^{m} Mean value of the tensor $\vec{q}$ equal to $(q_{xx} + q_{yy})/2$

1. INTRODUCTION AND OVERVIEW

The mechanics and micromechanics of the evolution of thermal stresses, plastic strains, geometry changes (including bending and stretch/contraction), instability and failure in multi-layered materials are of considerable interest in a wide variety of engineering applications. Examples include ceramic thermal-barrier coatings on metallic substrates, passivation and metallization thin films on Si substrates in microelectronic devices, thin-film coatings used in magnetic storage devices, inorganic or organic composite laminates used in load-bearing structures, and ceramic/metal multi-layer stacks of controlled porosity and compositional gradation in solid oxide fuel cells.

1.1. *Elastic response*

Stresses and deformation in multi-layered plates are commonly analyzed by recourse to linear models within the context of classical beam or plate theories. In this approach, which is predicated upon small deformation analyses, the following assumptions are usually invoked: (i) the through-thickness stresses within all the layers are small compared to the in-plane stresses, and out-of-plane deflections are

small compared to the plate thickness, (ii) the displacements vary continuously across the layers, (iii) the normals to the interfaces remain undeformed during thermo-mechanical deformation, (iv) the strains vary linearly with displacements, and (v) the size of the region in which multi-axial stresses prevail (i.e. very close to the free edges) is small compared to the in-plane dimensions. Extensions and modifications of the small deformation elasticity theory to account for the deformation of "thick" multi-layers including thick, orthotropic laminates (e.g. Timoshenko and Woinowsky-Krieger, 1959) and for the stresses near free edges (e.g. Bogy, 1971) have been reported.

The small deformation theory is adequate for determining the through-thickness fields for many applications. There also exist, however, a number of practical situations where large elastic deformations, which are accompanied by marked geometry changes, occur. An example of this phenomenon is the curling of unsymmetric laminates of reinforced plastics, thin-film/substrate systems (e.g. Ta film on polycarbonate substrate with use in microelectronic and optical applications), and unsymmetric laminated tapes of sintered ceramics. In addition, curvature measurements, which are widely used to assess thermal stresses in thin films on substrates, can be made with enhanced precision if the experimental conditions are designed to promote large rotations.

The subject of large rotations of elastic laminates has received increasing attention within the past 15 years. Hyer (1981a, b, 1982), Harper and Wu (1990), Masters and Salamon (1993, 1994) and Salamon and Masters (1995) extended the classical plate/laminate theories to include geometrical non-linearities for situations where the out-of-plane deflections are on the order of many plate thicknesses (while the strains are still very small). In these analyses, the out-of-plane deflections and the mid-plane normal strains are approximated by second-order polynomials whose unknown coefficients are determined by minimizing the total strain potential energy and by identifying the equilibrium shapes of the multi-layers. An outcome of this exercise is the realization that while the classical plate theory predicts a single shape with a unique curvature at low stresses (which arise as a result of the isotropic thermal mismatch between the layers), a bifurcation in the solution can occur at higher stresses. Here, three equilibrium shapes are feasible after the bifurcation stress or temperature. The single shape at low stresses is a spherical geometry for isotropic thin films on substrates (Salamon and Masters, 1995) and a saddle shape for unsymmetric (anisotropic) laminates (Hyer, 1981). The post-bifurcation configurations for the isotropic thin-film/substrate case at higher stresses are an unstable (nearly) spherical case and two stable ellipsoidal shapes with two different non-zero curvatures along the two mutually orthogonal in-plane coordinate (x and y) axes. For the unsymmetric laminate, the corresponding post-bifurcation configurations are an unstable saddle shape and two stable cylindrical shapes which can be snapped from one to the other by small perturbations in applied force or moment. All these shapes predicted by the non-linear theories have been observed experimentally (Hyer, 1981a; Fahnline et al., 1991). In subsequent studies, Masters and Salamon (1994) systematically released the following restrictive assumptions of the foregoing models: (i) the mid-plane normal strains vary only in one direction, and (ii) the mid-plane shear strains vanish. Releasing the first simplification did not affect the solutions significantly; however, allowing the

mid-plane shear strains to vary and approximating the mid-plane normal stresses by a sixth-order polynominal (instead of a second-order polynominal) markedly improved the solution. This was especially true in the vicinity of the bifurcation in the solution, as verified by comparing the analytical formulations with non-linear finite element simulations. The large deformation elasticity analyses of laminates and thin-film/substrate systems have focused on square plate geometry for the multi-layers. The critical conditions identified for the bifurcation in the solution and for the occurrence of multiple shapes in the post-bifurcation equilibrium configuration are very specific to the square layer geometry.

In the present paper, we begin with a discussion of a new generalized formulation for the coupled bending response within the context of small deformation elasticity theory. We then show, within the context of the classical (thin) plate theory, that the geometric shapes and stability conditions reported for the square layer geometry do not have general validity for rectangular multi-layers where the in-plane edge lengths are unequal. In this context, we explore the changes in the conditions governing large deformation as the length to the width ratio and the length to the thickness ratio of the layers are systematically varied for both "thick" and "thin" multi-layers.† In addition, as discussed in the following sections, we consider the effects of plasticity or compositional gradations in one of the layers of the multi-layered structure on the evolution of curvature and stability during large deformation. The analytical formulations are checked with non-linear finite element analyses involving shell elements (without incorporating edge effects), wherever appropriate.

1.2. *Plastic response*

The aforementioned theories for small and large deformation responses provide reliable results only when each layer in a multi-layer stack exhibits an elastic response. In many engineering structures and devices employing metallic layers, plastic strains can evolve even during cool down from the processing or deposition temperature, and the plastic strains may accumulate during subsequent thermal or mechanical loading/cycling. Examples of applications where such plastic deformation is of considerable interest for failure analyses include thermal-barrier and tribological coatings of ceramics adhered with metallic bondcoats on metallic substrates, metallization films deposited on semiconductor layers in electronic devices, piezoelectric detectors, and alloy solders used in integrated circuits. The development of plastic flow can drastically alter the deformation characteristics, the fracture response, and the service lifetime of multi-layers, thereby rendering the commonly-employed linear-elastic analyses unreliable. The estimation of both elastic stresses and elastoplastic defor-

---

† Throughout this paper, "thick" multi-layers refer to those for which the thickness of each layer is substantially greater than the appropriate microstructural size scale, such as the grain size, and for which no layer is significantly thicker than any other. "Thin" film refers to a layer in a multi-layer stack wherein at least one layer is significantly thicker than the others and the thickness of the layer may be comparable to the characteristic microstructural dimensions. For both cases, the continuum formulations described in this paper are expected to hold because (i) the in-plane dimensions are significantly larger than the microstructural size scale and (ii) the plates are subjected primarily to a state of biaxial stress. In all cases, we employ the thin plate theory where the overall thickness of the plate is much smaller (less than 2%) than the smaller of the two in-plane dimensions.

mation in thin ductile films deposited on thick elastic substrates usually involves experimental measurements of curvature which is then converted to an average film stress on the basis of the classical Stoney's formula (Stoney, 1909) or its appropriate modifications. In this approach, the average stress in the thin-metal film deposited on a substrate is related to the change in overall (spherical) curvature, for a state of equal biaxial stress (see the discussion in Section 2.2.1).

The Stoney equation is simple to implement and provides a measure of the average stresses and small deformation response of thin ductile layers (deposited on substrates) exhibiting elastic/plastic deformation. There are, however, some serious drawbacks. (1) It is not amenable for directly predicting the variation of curvature with temperature fluctuations, especially for the general multi-layered systems (with more than two layers) of arbitrary layer thicknesses, and temperature-dependent physical and mechanical properties commonly encountered in microelectronic devices and structural coatings. Such predictions are necessary for direct comparisons with experimentally determined curvature changes. (2) In addition, the variation of stresses along the thickness of the layer cannot be estimated; this may be necessary for identifying the failure origins in multi-layered systems. (3) As shown later in the present article, the evolution of plastic deformation, in conjunction with the in-plane anisotropic response and/or large deformation, can induce an overall mechanical response of the multi-layer that can differ markedly from that predicted by the simple Stoney approximation.

In an attempt to overcome these limitations of conventional approaches, detailed elastoplastic analyses for two-layered and three-layered systems subjected to thermal cycling have been reported (Suresh et al., 1994; Shen and Suresh, 1995a). These analyses also reveal that there exists a direct link between the spread of plastic flow in one or more ductile layers of multi-layered systems (depending on certain combinations of layer properties and thicknesses) and the occurrence of specific geometry changes, such as the reversal of curvature (Shen and Suresh, 1995a).

The aforementioned elastoplastic analyses for small deformation can also be implemented into simple numerical programs amenable for use with personal computers (e.g. Finot and Suresh, 1994). Here the effects of (i) in-plane anisotropy, (ii) plastic flow with strain hardening, (iii) thermal heat conduction across layers, (iv) variation of physical and mechanical properties with temperature, (v) plastic strain accumulation in one or more layers during thermomechanical cycling, and (vi) compositional gradients on the evolution of stresses, plastic strains, multiple curvatures, and failure at any location can be estimated (without incorporating edge effects) for a general multi-layered system with arbitrary numbers of well-bonded metal and ceramic layers, each of arbitrary thickness. In the present paper, we extend earlier analyses of elastoplastic deformation in multi-layered systems to include certain specific cases of large deformation, within the context of small strain plate theory.[†] For this purpose, we choose two model systems: (i) a bilayer comprising an aluminum

---

[†] More comprehensive, fully three-dimensional, thick plate analyses of elastoplastic bifurcation including large strains and rotations reveal overall trends of elastoplastic response which are qualitatively similar to those presented in this paper (Giannakopoulos and Suresh, 1995). The onset of bifurcation and the conditions governing its dependence on thermal loading, however, may depend on the level of details incorporated in the analyses.

thin film deposited on a Si single crystal substrate, and (ii) a thick Ni layer bonded to a thick alumina ceramic substrate.

1.3. *Compositional gradients*

Multi-layered structures with gradients in composition, microstructure and properties across the thickness of one or more layers are of much research attention because of current or potential applications in a variety of engineering applications. Examples include case-hardening of steels for tribological protection, thermally-sprayed zirconia-metal graded coatings for thermal-barrier protection in ground-vehicle engines, and Si/Ge and InGaAs graded layers in microelectronics and optoelectronics. Intentionally grading the composition and/or microstructure of materials can offer the possibility for improvements in performance and damage tolerance on account of the following considerations.

- A compositionally graded interlayer between two dissimilar solids with a large thermal expansion mismatch "smoothens" the distribution of thermal stresses across the thickness of the layer and can be used to diminish the magnitude of thermal stresses at critical locations.
- The magnitude of the thermal stresses can be altered by the proper choice of layer thickness and geometry, as well as of the profile of the compositional gradient in the layer.
- Compositional gradation can mitigate the spread of plastic flow in ductile layers, or the onset of cracking at the interface and within the brittle layers (depending on the stability of the microstructure during service and on the geometry of the graded layer).
- Graded semiconductor layers, synthesized by molecular beam epitaxy or chemical vapor deposition, can be used to control the population, distribution or kinetics of misfit and threading dislocations in heteroepitaxial structures (Fitzgerald *et al.*, 1992).
- Compositionally graded interfaces in multi-layered structures can minimize or even fully eliminate stress concentrations and singularities at free edges, thereby improving the tolerance of the structure to the onset of cracking (Erdogan *et al.*, 1991).
- The joining of "thick" layers (typically 0.5 mm or more in thickness) of dissimilar solids, such as metals and ceramics, subject to large excursions in temperature necessarily requires an interface with a step-wise or a gradual change in composition to maintain the mechanical integrity of the interface.

Thermoelastic (Kroupa *et al.*, 1993; Williamson *et al.*, 1993; Freund, 1993; Giannakopoulos *et al.*, 1995) and thermoelastoplastic (Williamson *et al.*, 1993; Giannakopoulos *et al.*, 1995; Finot *et al.*, 1996) responses of compositionally graded multilayers under small deformation conditions have been addressed both theoretically and experimentally. In addition, engineering diagrams providing graphical representations of the effects of layer geometry and compositional gradation on the onset of deformation and failure have been formulated (Finot *et al.*, 1996; Giannakopoulos *et al.*, 1995). In Section 5 of this paper, we present an analysis of the effects of

compositional gradation on the large deformation response of compositionally graded elastic multi-layers. Two applications involving tri-layer systems are considered: (i) a compositionally graded thin-film layer sandwiched between thin-film layers of $In_{0.12}Ga_{0.88}As$ and GaAs, and (ii) a compositionally graded Ni/alumina composite sandwiched between thick layers of homogeneous alumina and Ni.
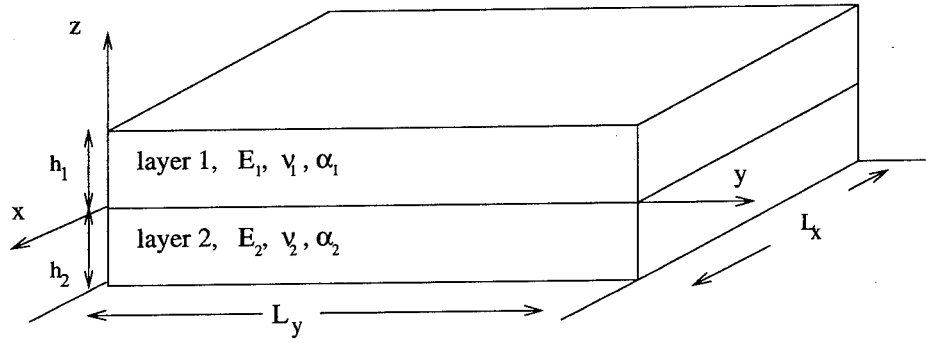
2. THEORY

We first present in this section a new general formulation, in closed form, on the evolution of stresses and curvature due to strain mismatch among the different layers in a multi-layer stack, within the context of small deformation elasticity theory. Explicit expressions are presented for the stress/curvature relations for a bilayer plate with isotropic in-plane elastic properties, but with an anisotropic inelastic strain mismatch. It is shown that the elastic bilayer is fully characterized by the ratio of the layer thicknesses, and by two elastic mismatch parameters: (i) the ratio of the biaxial Young's moduli of the layers and (ii) the ratio of the shear moduli of the layers. It is demonstrated that the two principal curvatures of the bilayer due to strain mismatch are uncoupled only if the two layers have the same Poisson's ratio. In the general case relevant to the vast majority of practical applications, these exists a coupling between the curvatures along two in-plane orthogonal directions if there is a variation of the Poisson's ratio through the thickness. This coupling is quantified with closed-form solutions. New solutions are also presented for the direct determination of the elastic stress variations through the thickness of the multi-layer in terms of the two principal curvatures and the orientations of the principal curvature directions. Extensions of this method to layered plates with compositionally graded interlayers are also discussed.

2.1. *Nomenclature and review of standard methods*

Consider a layered stack of dissimilar solids whose in-plane reference coordinates are denoted by x and y axes, and the layer thickness direction is along the z-axis, as shown in Fig. 1(a) and (b). The in-plane shape of the general multi-layer analyzed in this work is a rectangle whose dimensions are L_x and L_y along the x and y axes, respectively. The plate is assumed to have a uniform thickness and a uniform temperature (at all times during thermal excursions).

Let the multi-layer be flat (zero curvature) and stress-free at the reference state (such as the sintering, bonding or curing temperature for laminates, or the deposition temperature for thin films). Consider the application of uniform forces $\vec{N} = (N_{xx}, N_{yy}, N_{xy})$, uniform moments $\vec{M} = (M_{xx}, M_{yy}, M_{xy})$, and internal inelastic strain, $\vec{\varepsilon}^{inel}$. Here $\vec{\varepsilon}^{inel}$, which is a function of z only, is the inelastic strain which may result from plasticity, thermal expansion, epitaxial strains, differential shrinkage of powders during sintering, or transformation strain. For such loading, the transverse components of strain can be assumed to be negligible in the plate except within a distance equal to the thickness from the edge of the plate, in accordance with the

M. FINOT and S. SURESH

(a)
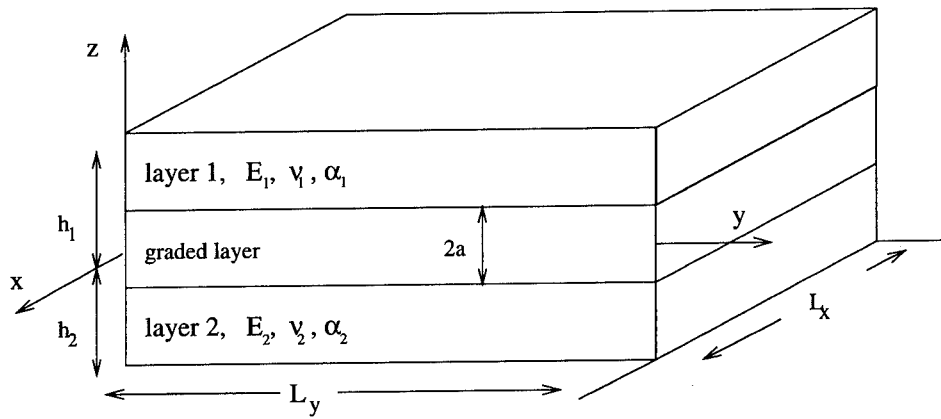
(b)

Fig. 1. Schematic of the geometry of the layered plate and the associated nomenclature. (a) Bilayer and (b) graded trilayer.

classical Kirchoff plate theory. The relevant total strain components can then be written as

$$\varepsilon_{xx} = \varepsilon_{xx}^{\circ} - z\frac{\partial^2 w}{\partial x^2} = \varepsilon_{xx}^{\circ} + \kappa_{xx}z,$$

$$\varepsilon_{yy} = \varepsilon_{yy}^{\circ} - z\frac{\partial^2 w}{\partial y^2} = \varepsilon_{yy}^{\circ} + \kappa_{yy}z,$$

$$\gamma_{xy} = \gamma_{xy}^{\circ} - 2z\frac{\partial^2 w}{\partial x \partial y} = \gamma_{xy}^{\circ} + 2\kappa_{xy}z, \tag{1}$$

flat plate $\kappa_x = \kappa_y = 0$
$\kappa_{xy} = 0$

κ_{xy}

sphere $\kappa_x = \kappa_y$
$\kappa_{xy} = 0$

κ_x, κ_y

saddle shape $\kappa_x = -\kappa_y$
$\kappa_{xy} \neq 0$

cylinder $\kappa_x = 0 , \; \kappa_y \neq 0$
(or) $\kappa_y = 0 , \; \kappa_x \neq 0$
$\kappa_{xy} \neq 0$
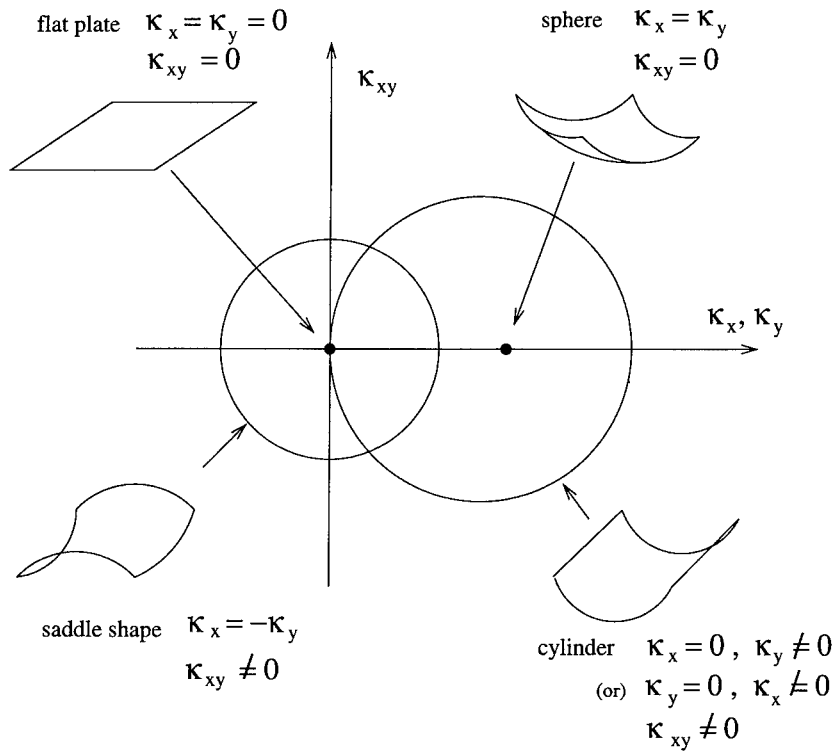
Fig. 2. Schematic of the Mohr's circle representation of the shape of a plate. The x and y directions are the principal directions of curvature.

where w is the out-of-plane displacement. In the case of small deformation, i.e. when w is small compared to the thickness of the plate, the curvatures and the strains at $z = 0$ can be assumed to be constant in the plate. (The large deformation case is considered in Section 2.6.) The degrees of freedom for the small deformation case are: (i) the two curvatures, κ_{xx} and κ_{yy}, along the x and y directions, respectively, and the twist curvature, κ_{xy}, and (ii) the strains at $z = 0$, ε_{xx}°, ε_{yy}° and γ_{xy}°.

It is convenient to use the Mohr's circle representation of the curvatures to visualize the shapes of the layered plate (see Fig. 2). As discussed in Hyer (1981a), the shape of a layered plate can be represented as a circle with a center at $\frac{1}{2}(\kappa_x + \kappa_y)$ and a radius equal to $\frac{1}{2}(\kappa_x - \kappa_y)$ in the $\kappa_x/\kappa_y - \kappa_{xy}$ space; here, κ_x and κ_y are the principal curvatures. Examples of different shapes are illustrated in Fig. 2. The total strains can be written in vectorial form as

$$\vec{\varepsilon} = \vec{\varepsilon}^{\circ} + z\vec{\kappa} = \begin{pmatrix} \varepsilon_{xx} \\ \varepsilon_{yy} \\ \gamma_{xy} \end{pmatrix} = \begin{pmatrix} \varepsilon_{xx}^{\circ} + z\kappa_{xx} \\ \varepsilon_{yy}^{\circ} + z\kappa_{yy} \\ \gamma_{xy}^{\circ} + 2z\kappa_{xy} \end{pmatrix}, \qquad (2)$$

where the variables, such as $\vec{\varepsilon}$ or $\vec{\kappa}$, represent three-dimensional vectors. The consti-

tutive response at any location, z, through the thickness depends on the stiffness matrix [S], in the general orthotropic elastic case, as

$$[\mathbf{S}(z)] = \begin{bmatrix} S_{11} & S_{12} & 0 \\ S_{12} & S_{22} & 0 \\ 0 & 0 & S_{66} \end{bmatrix}. \tag{3}$$

The stress distribution through the thickness is

$$\vec{\sigma} = \begin{pmatrix} \sigma_{xx}(z) \\ \sigma_{yy}(z) \\ \sigma_{xy}(z) \end{pmatrix} = [\mathbf{S}](\vec{\varepsilon} - \vec{\varepsilon}^{\,\text{inel}}). \tag{4}$$

In the present analysis, we consider the thermal expansion strain given by

$$\vec{\varepsilon}^{\,\text{inel}} = \vec{\varepsilon}^{\,T} = \begin{pmatrix} \alpha_x \\ \alpha_y \\ \alpha_{xy} \end{pmatrix} \Delta T, \tag{5}$$

where α is the coefficient of thermal expansion (CTE). Combining (4) and (1), the resultant force and moment due to the stress distribution through the thickness are

$$\vec{N} = \int_h \vec{\sigma}(z)\,\mathrm{d}z = [\mathbf{A}]\vec{\varepsilon}^{\,\circ} + [\mathbf{B}]\vec{\kappa} - \vec{N}^{\text{inel}}, \quad \text{and} \tag{6}$$

$$\vec{M} = \int_h \vec{\sigma}(z)z\,\mathrm{d}z = [\mathbf{B}]\vec{\varepsilon}^{\,\circ} + [\mathbf{D}]\vec{\kappa} - \vec{M}^{\text{inel}}, \tag{7}$$

where [A], [B] and [D] are the classical reduced stiffness matrices of the plate (Tsai, 1988) defined as

$$[\mathbf{A}] = \int_h [\mathbf{S}]\,\mathrm{d}z, \quad [\mathbf{B}] = \int_h [\mathbf{S}]z\,\mathrm{d}z \quad \text{and} \quad [\mathbf{D}] = \int_h [\mathbf{S}]z^2\,\mathrm{d}z. \tag{8}$$

$\vec{N}^{\text{inel}}$ and $\vec{M}^{\text{inel}}$ are the resultant forces and moments induced by the inelastic strains

$$\vec{N}^{\text{inel}} = \int_h [\mathbf{S}](z)\vec{\varepsilon}^{\,\text{inel}}\,\mathrm{d}z \quad \text{and} \quad \vec{M}^{\text{inel}} = \int_h [\mathbf{S}](z)\vec{\varepsilon}^{\,\text{inel}}z\,\mathrm{d}z. \tag{9}$$

Equations (6) and (7) show a system of six linear equations for the six degrees of freedom given by

$$\begin{pmatrix} \vec{N} + \vec{N}^{\text{inel}} \\ \vec{M} + \vec{M}^{\text{inel}} \end{pmatrix} = \begin{bmatrix} [\mathbf{A}] & [\mathbf{B}] \\ [\mathbf{B}] & [\mathbf{D}] \end{bmatrix} \begin{pmatrix} \vec{\varepsilon} \\ \vec{\kappa} \end{pmatrix} = [\mathbf{C}] \begin{pmatrix} \vec{\varepsilon} \\ \vec{\kappa} \end{pmatrix}. \tag{10}$$

A simple inversion of the 6×6 matrix [C] provides the value of the curvatures, κ_{xx}, κ_{yy} and κ_{xy}, and the strains, ε_{xx}°, ε_{yy}° and γ_{xy}°, as a function of the applied force and moment, $\vec{M}$ and $\vec{N}$, and as a function of the internal force and moment, $\vec{N}^{\text{inel}}$ and $\vec{M}^{\text{inel}}$.

$$\begin{pmatrix} \vec{\varepsilon} \\ \vec{\kappa} \end{pmatrix} = [\mathbf{C}]^{-1} \begin{pmatrix} \vec{N} + \vec{N}^{\text{inel}} \\ \vec{M} + \vec{M}^{\text{inel}} \end{pmatrix}. \tag{11}$$

The stress distribution through the thickness can be computed by (4). It is important to note that a uniform inelastic strain $\vec{\varepsilon}^{\text{inel}}$ through the thickness does not generate any stress. Therefore, this uniform inelastic strain does not alter the curvature; instead, it increases the strains at $z = 0$ by $\vec{\varepsilon}^{\text{inel}}$.

2.2. General formulation for isotropic elastic bilayers under internal loading

The approach developed here is generally applicable to any multi-layer stack, with interfaces that are mechanically bonded with or without compositional gradients, wherein the elastic properties have in-plane isotropy, but the internal mismatch strains may be anisotropic. The layered solid is free of external constraints. In order to derive simple closed-form solutions and to keep the algebra to a minimum, the following discussion centers around bilayer plates. It is convenient to define a normalized curvature for the bilayer,

$$\vec{\hat{\kappa}} = \frac{(h_1 + h_2)^3}{6h_1 h_2} \vec{\kappa} = \lambda \vec{\kappa}, \tag{12}$$

where h_1 and h_2 are the thicknesses of the two layers.† With this normalization, the curvature has a finite, non-zero value when h_1 or h_2 goes to zero in the thin-film limit. We assume that the inelastic strain is uniform in layers 1 and 2, and is equal to $\vec{\varepsilon}_1^{\text{inel}}$ and $\vec{\varepsilon}_2^{\text{inel}}$, respectively. Only the case where $\vec{\varepsilon}_1^{\text{inel}} = -\vec{\varepsilon}_2^{\text{inel}} = \Delta\vec{\varepsilon}/2$ needs to be addressed.

Since the two layers are isotropic, the response of the plate is solved by considering two basic problems: (i) pure equal biaxial internal normal strains, $\Delta\varepsilon^m = \Delta\varepsilon_{xx} = \Delta\varepsilon_{yy}$ and $\Delta\gamma_{xy} = 0$, and (ii) pure shear internal strains, $\Delta\varepsilon_{xx} = -\Delta\varepsilon_{yy}$.

2.2.1. *Equal biaxial loading*. For an isotropic material under equal biaxial loading, the deformation is characterized by the mean curvature, $\hat{\kappa}^m$ and the mean strain ε^m at $z = 0$. The mismatch strain is a pure equal biaxial mismatch equal to $\vec{\Delta\varepsilon} = (\Delta\varepsilon, \Delta\varepsilon, 0)$. In this case, the geometry of the two layers at any point of deformation is fully specified by the ratio of the two thicknesses, $\rho = h_1/h_2$, and by the ratio of the two biaxial moduli, $\hat{E}_{\text{Bi}} = E_1(1 - v_2)/\{E_2(1 - v_1)\}$. From (11) the normalized curvature and the strain at $z = 0$ are

$$\hat{\kappa}^m = \hat{\kappa}_{xx} = \hat{\kappa}_{yy} = f(\hat{E}_{\text{Bi}}, \rho)\Delta\varepsilon \quad \text{and} \quad \varepsilon^m = \varepsilon_{xx}^\circ = \varepsilon_{yy}^\circ = \varepsilon^{\text{ave}} + g(\hat{E}_{\text{Bi}}, \rho)\Delta\varepsilon, \tag{13}$$

$$f(\hat{E}_{\text{Bi}}, \rho) = \frac{(1 + \rho)^4 \hat{E}_{\text{Bi}}}{1 + 2\hat{E}_{\text{Bi}}\rho(2 + 3\rho + 2\rho^2) + \hat{E}_{\text{Bi}}^2 \rho^4}, \tag{14}$$

$$g(\hat{E}_{\text{Bi}}, \rho) = \frac{-1 + 4\hat{E}_{\text{Bi}}\rho(1 - \rho^2) + \hat{E}_{\text{Bi}}^2 \rho^4}{2(1 + 2\hat{E}_{\text{Bi}}\rho(2 + 3\rho + 2\rho^2) + \hat{E}_{\text{Bi}}^2 \rho^4)}. \tag{15}$$

---

† The normalization in (12) involves a factor of six in the denominator because it provides a link to the commonly used "Stoney" formula [see (17)].

M. FINOT and S. SURESH

$$f(\hat{E}_{Bi}, \rho) = \kappa(h_1 + h_2)^3/(6h_1 h_2 \Delta\varepsilon)$$

$$\hat{E}_{Bi} = \frac{E_1(1-\nu_2)}{E_2(1-\nu_1)}$$
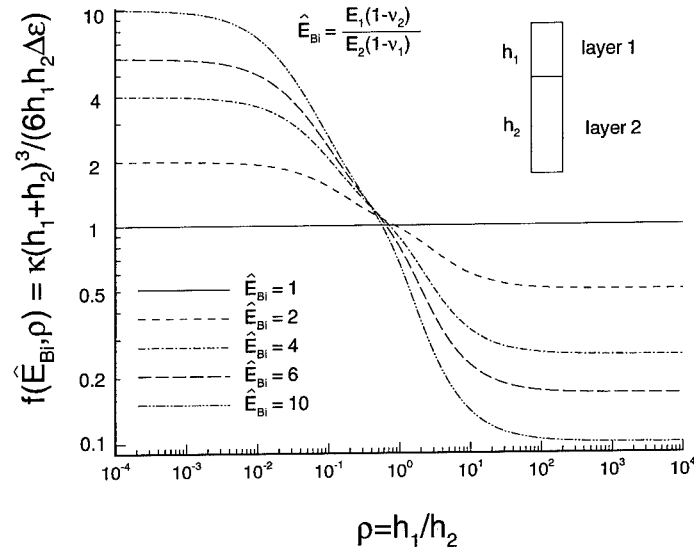
Fig. 3. Representation of the function f in terms of the thickness ratio, $\rho = h_1/h_2$, for different values of the bi-axial modulus ratio, $\hat{E}_{Bi}$.

$$g(\hat{E}_{Bi}, \rho) = (\varepsilon^o - \varepsilon^{ave})/\Delta\varepsilon$$

$$\hat{E}_{Bi} = \frac{E_1(1-\nu_2)}{E_2(1-\nu_1)}$$
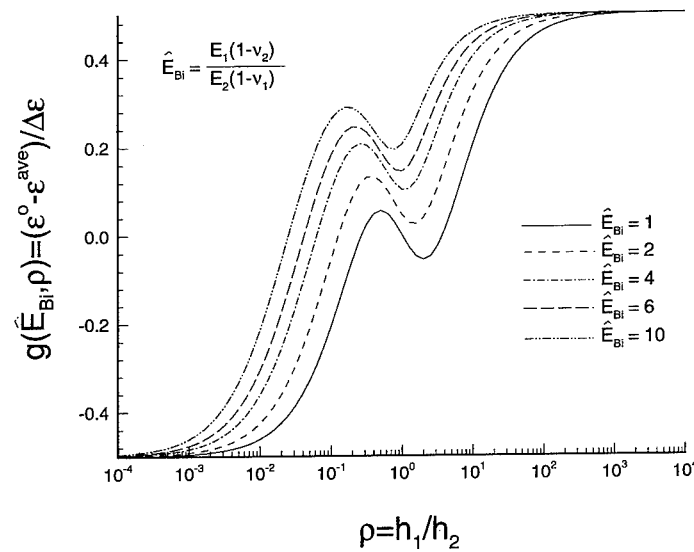
$$\rho = h_1/h_2$$

Fig. 4. Representation of the function g in terms of the thickness ratio, $\rho = h_1/h_2$, for different values of the bi-axial modulus ratio, $\hat{\mu}$.

The functions f and g are plotted against ρ in Figs 3 and 4, respectively, for different values of $\hat{E}_{Bi}$. When $\rho \to 0$, $f \to \hat{E}_{Bi}$ and $g \to -0.5$; when $\rho \to \infty$, $f \to 1/\hat{E}_{Bi}$ and $g \to 0.5$. If the interface is at $z = 0$, the stress distribution through the thickness is

$$\sigma^m(z) = \frac{E_1}{1-v_1}(g(\hat{E}_{Bi},\rho)-\tfrac{1}{2}+zf(\hat{E}_{Bi},\rho)\lambda^{-1})\Delta\varepsilon, \quad \text{in layer 1,}$$

$$\sigma^m(z) = \frac{E_2}{1-v_2}(g(\hat{E}_{Bi},\rho)+\tfrac{1}{2}+zf(\hat{E}_{Bi},\rho)\lambda^{-1})\Delta\varepsilon, \quad \text{in layer 2,} \tag{16}$$

where λ is the length defined in (12).

From these equations, we can recover stress/curvature relations derived by Stoney (1909) for the thin-film limit

$$k(h_1 \to 0) = 6\frac{h_1}{h_2^2}\hat{E}_{Bi}\Delta\varepsilon = 6\frac{h_1}{h_2^2}\frac{(1-v_2)}{E_2}\sigma_f^m, \quad \varepsilon^\circ(h_1 \to 0) = \varepsilon_2^{inel}. \tag{17}$$

This Stoney approximation for the average stress in the film, σ_f^m, is represented by the plateau regions (i.e. f independent of ρ) in the left and right extremes of Fig. 3 for different $\hat{E}_{Bi}$. For $\rho \approx 10^{-2}-10^2$, the Stoney formula becomes invalid, and (13) provides accurate results.

2.2.2. *Pure shear loading.* Another extreme situation pertinent to the present problem is pure shear loading for which $\Delta\vec{\varepsilon} = (0, 0, \Delta\gamma_{xy})$. In this case, the appropriate elastic mismatch parameter is the ratio of the shear moduli of the two layers, $\hat{\mu} = \mu_1/\mu_2 = E_1(1+v_2)/\{E_2(1+v_1)\}$. The twist curvature and the shear strain at the interface, $z = 0$, are then written as

$$\hat{\kappa}_{xy} = f(\hat{\mu},\rho)\frac{\Delta\gamma_{xy}}{2}, \quad \gamma_{xy}^\circ = \gamma_{xy}^{ave}+g(\hat{\mu},\rho)\Delta\gamma_{xy}, \tag{18}$$

where the functions f and g are defined in (14) and (15). The shear stress distribution is

$$\tau(z) = \mu_1(g(\hat{\mu},\rho)-\tfrac{1}{2}+zf(\hat{\mu},\rho)\lambda^{-1})\Delta\gamma_{xy} \quad \text{in layer 1,}$$

$$\tau(z) = \mu_2(g(\hat{\mu},\rho)+\tfrac{1}{2}+zf(\hat{\mu},\rho)\lambda^{-1})\Delta\gamma_{xy} \quad \text{in layer 2.} \tag{19}$$

2.2.3. *General normal and shear loading.* Consider next both normal and shear thermal strain mismatch, $\Delta\varepsilon_{xx}$, $\Delta\varepsilon_{yy}$, and $\Delta\gamma_{xy}$. The three curvature values for the bilayer plate, $\hat{\kappa}_{xx}$, $\hat{\kappa}_{yy}$ and $\hat{\kappa}_{xy}$, are

$$\vec{\kappa} = \begin{pmatrix} \hat{\kappa}_{xx} \\ \hat{\kappa}_{yy} \\ \hat{\kappa}_{yx} \end{pmatrix} = [\mathbf{K}]\Delta\vec{\varepsilon} = \begin{bmatrix} b+s & b-s & 0 \\ b-s & b+s & 0 \\ 0 & 0 & s \end{bmatrix} \begin{pmatrix} \Delta\varepsilon_{xx} \\ \Delta\varepsilon_{yy} \\ \Delta\gamma_{xy} \end{pmatrix}, \tag{20}$$

$$b = \tfrac{1}{2}f(\hat{E}_{Bi},\rho) \quad \text{and} \quad s = \tfrac{1}{2}f(\hat{\mu},\rho). \tag{21}$$

The strains at $z = 0$, $\vec{\varepsilon}^\circ$, are equal to

$$\vec{\varepsilon}^\circ = \vec{\varepsilon}^{ave}+[\mathbf{E}]\Delta\vec{\varepsilon}, \tag{22}$$

where the matrix $[\mathbf{E}]$ has the same form as the matrix $[\mathbf{K}]$ with b and s given as

$$b = \tfrac{1}{2}g(\hat{E}_{Bi},\rho) \quad \text{and} \quad s = \tfrac{1}{2}g(\hat{\mu},\rho). \tag{23}$$

Fig. 5. Representation of the Poisson effect characterized by $v_k = \kappa_{yy}/\kappa_{xx}$ as a function of the thickness ratio, $\rho = h_1/h_2$, for different values of the biaxial modulus ratio, $\hat{E}_{Bi}$, and shear modulus ratio, $\hat{\mu}$.
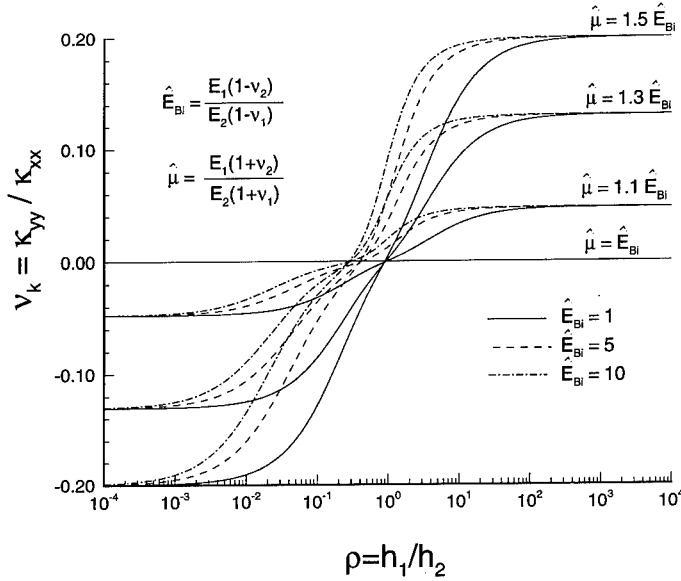
It is interesting to note that this matrix is very similar to the stiffness matrix of an isotropic material. With similarity to the Dundurs' parameters for elastic bilayers (Dundurs, 1969), the above problem is fully formulated in terms of two dimensionless material parameters, $\hat{E}_{Bi}$ and $\hat{\mu}$, and the relative thickness, ρ.

2.2.4. *Coupling between curvatures along in-plane orthogonal directions.* One can further characterize the curvature coupling effect between the in-plane orthogonal directions by the ratio $v_\kappa = (b-s)/(b+s) = \kappa_{yy}/\kappa_{xx}$, which represents the "Poisson effect". This effect, in the present context, refers to the strain mismatch in one direction due to the curvature in the other direction. The factor v_κ is defined in terms of $\hat{E}_{Bi}$ and $\hat{\mu}$ in the following way

$$v_\kappa = \frac{(\hat{E}_{Bi} - \hat{\mu})(1 - \hat{\mu}\hat{E}_{Bi}\rho^4)}{(\hat{E}_{Bi} + \hat{\mu})(1 + \hat{\mu}\hat{E}_{Bi}\rho^4) + 4\hat{\mu}\hat{E}_{Bi}\rho(2 - 3\rho + 2\rho^2)}. \tag{24}$$

When $h_1 \to 0$, v_κ approaches a limit independent of E_1 and E_2 and is given by the simple expression

$$v_\kappa(h_1 \to 0) = \frac{\hat{E}_{Bi} - \hat{\mu}}{\hat{E}_{Bi} + \hat{\mu}} = \frac{v_1 - v_2}{1 - v_1 v_2}. \tag{25}$$

The variation of v_κ as a function of $\rho = h_1/h_2$ is plotted in Fig. 5 for $\hat{\mu} = 1\text{--}15$. An increase in $\hat{\mu}/\hat{E}_{Bi}$ causes a marked increase in $|v_\kappa|$, which is independent of ρ in the thin-film limit ($\rho \leqslant 10^{-2}$ or $\rho \geqslant 10^2$). For $10^{-2} < \rho < 10^2$, $|v_\kappa|$ is sensitive to both ρ and $\hat{E}_{Bi}/\hat{\mu}$ as shown in Fig. 5.

The results of Fig. 5 clearly show that the Poisson ratio mismatch across the layer

thicknesses can cause an appreciable coupling effect in some cases. Consider, for example, the bilayer for which $\hat{E}_{Bi} = 5$ and $\hat{\mu} = 1.3\ \hat{E}_{Bi}$. For this combination, $|v_\kappa| \approx 13\%$, or $\kappa_{yy} \approx \pm 0.13\ \kappa_{xx}$ even when the two layers are elastically isotropic. This non-zero value of v_κ caused the bilayer plate to assume a saddle shape or an ellipsoidal shape instead of a spherical shape during small elastic deformation.

2.2.5. *Stress/curvature relations*. Curvature changes during layer deposition or thermal cycling are commonly monitored in many structural coatings and thin-film applications to estimate the evolution of thermal and intrinsic stresses in multi-layers. The Stoney approximation for thin films, (17), which relates the average biaxial stress in the film to the curvature, is commonly used to approximate the film stress. In this section, we present general expressions for determining the variation of stresses through the thickness of each layer in a bilayer with arbitrary layer thicknesses directly as a function of the measured curvature (and independently of the origin or magnitude of the strain mismatch between the layers).

The stress distribution through the thickness is given by

$$\vec{\sigma}(z) = [\mathbf{S}_1](\mathbf{E} - \tfrac{1}{2} + \mathbf{K}z\lambda^{-1})\Delta\vec{\varepsilon} \quad \text{in layer 1,}$$

$$\vec{\sigma}(z) = [\mathbf{S}_2](\mathbf{E} + \tfrac{1}{2} + \mathbf{K}z\lambda^{-1})\Delta\vec{\varepsilon} \quad \text{in layer 2} \tag{26}$$

where [S] is the stiffness matrix defined in (3) and λ is the length defined in (12).

It is important to note that the stress distribution depends only on the strain mismatch between the two layers. Therefore, if the matrix **K** is not singular, the stress distribution through the thickness varies linearly with curvature. There exists a matrix $[\Sigma(z)]$, independent of the loading conditions, such that

$$\vec{\sigma}(z) = [\Sigma(z)]\vec{\kappa}, \tag{27}$$

where

$$[\Sigma(z)] = [\mathbf{S}_1](\lambda(\mathbf{E} - \tfrac{1}{2}) + \mathbf{K}z)\mathbf{K}^{-1} \quad \text{in layer 1,}$$

$$[\Sigma(z)] = [\mathbf{S}_2](\lambda(\mathbf{E} + \tfrac{1}{2}) + \mathbf{K}z)\mathbf{K}^{-1} \quad \text{in layer 2.} \tag{28}$$

This is a generalization of the Stoney formula to an elastic bilayer with arbitrary layer thicknesses. Explicit expressions of the mean stress and the shear stress can be found in Section (2.5).

The previous analysis can easily be generalized for n layers in a multi-layer stack. However, in most cases, the relation between the stress and the curvature is not unique since the number of independent variables to determine the internal deformation will be larger than three which is the number of variables characterizing the curvature. However, in the case of a three-layered plate with a graded layer inbetween two homogeneous layers, this stress/curvature relation can easily be written in closed form, as discussed in Section 2.4.

The curvature matrix can be derived in a straightforward manner for the orthotropic bilayers as well using the procedure discussed above. For orthotropic materials, it can be shown that the matrix has the following general form

$$\mathbf{K} = \begin{bmatrix} K_{xx} & N_{xy} & 0 \\ N_{xy} & K_{yy} & 0 \\ 0 & 0 & G \end{bmatrix}. \tag{29}$$

2.3. A particular case of generalized plane strain

The assumption of a generalized plane strain state allows us to examine the case where the plate is constrained to deform as a cylinder. In this state, we invoke the condition that the plate has a zero curvature in the y direction. The problem now has four unknowns which are: the principal curvature, $\kappa = \kappa_{xx}$, the two principal strains at $z = 0$, ε_{xx}^{o} and ε_{yy}^{o}, and the resulting moment in the y direction.

The problem is solved by noting that the resulting forces, N_{xx} and N_{yy}, and the resulting moment, M_{xx}, are zero. These three conditions lead to the following linear system of equations

$$\begin{bmatrix} A_{11} & A_{12} & B_{11} \\ A_{12} & A_{22} & B_{12} \\ B_{11} & B_{12} & D_{11} \end{bmatrix} \begin{pmatrix} \varepsilon_{xx}^{o} \\ \varepsilon_{yy}^{o} \\ \kappa \end{pmatrix} = \begin{pmatrix} N_{xx}^{\text{inel}} \\ N_{yy}^{\text{inel}} \\ M_{xx}^{\text{inel}} \end{pmatrix} \tag{30}$$

where the matrices [A], [B] and [D] are defined in Section 2.1. The expression for the resulting moment in the y direction, M_{yy}, is given by

$$M_{yy} = B_{12}\varepsilon_{x}^{o} + B_{22}\varepsilon_{y}^{o} + D_{12}\kappa - M_{yy}^{\text{inel}}. \tag{31}$$

For the isotropic bilayer presented in Section 2.2, the curvature in the x direction is simply equal to $(f(\hat{E}_{\text{Bi}}, \rho) + v_{\kappa})\Delta\varepsilon$ where f and v_{κ} are defined in (14) and (24).

2.4. Graded layer

Consider the thermoelastic response of a three-layered system, with a compositionally graded layer between two layers of homogeneous compositions, subject to a uniform change of temperature. Giannakopoulos et al. (1995) and Finot et al. (1996) studied the elastic and plastic behavior (small deformation) of such a trilayer plate, and Freund (1993, 1996) has considered the small deformation elastic response of compositionally graded thin films. In the present work, we consider the large deformation of the compositionally graded material subject to thermal loading.

We assume a linear variation of biaxial modulus, the shear modulus and the coefficient of thermal expansion in the graded layer such that

$$P = P_1 \quad \text{for } a \leqslant z \leqslant h_1,$$

$$P = \frac{P_1 + P_2}{2} + \frac{P_2 - P_1}{2} \frac{z}{a} \quad \text{for } -a \leqslant z \leqslant a,$$

$$P = P_2 \quad \text{for } -h_2 \leqslant z \leqslant -a, \tag{32}$$

where P is any material property that in the present context is the biaxial modulus,

E_{Bi}, the shear modulus, μ, or one of the coefficients of thermal expansion (α_x, α_y, α_{xy}). With these assumptions, the previous analyses of Giannakopoulos *et al.* (1995) and Finot *et al.* (1996) can easily be extended to compute the mean and shear curvatures, with an additional dimensionless parameter which is the ratio of the thickness of the graded layer to the total thickness of the trilayered solid: $\rho_a = 2a/(h_1 + h_2)$. We have found that there is still a direct link between the curvatures of the plate and the stress distribution through the thickness, analogous to the results presented for the sharp interface case in Section 2.2. (Full details are not presented here because of space restrictions.) Using the analytical results of Section 2.1 of this paper, and Section 2.1 in Giannakopoulos *et al.* (1995) and assuming small deformation theory, the mean curvature and the shear curvature can be expressed as

$$\hat{\kappa}^m = f(\hat{E}_{Bi}, \rho, \rho_a)\Delta\alpha^m\Delta T, \quad \hat{\kappa}_{xy} = f(\hat{\mu}, \rho, \rho_a)\Delta\alpha_{xy}\Delta T, \tag{33}$$

where the expression for f can be found in the Appendix of Giannakopoulos *et al.* (1995) and the dimensionless parameters $\hat{E}_{Bi}$, ρ, ρ_a and $\hat{\mu}$ are defined in Section 2.1. Here, $\Delta\alpha^m$ and $\Delta\alpha_{xy}$ are the mismatch of mean CTE and the mismatch of shear CTE. Explicit expressions for the stress/curvature relations for a general, compositionally graded trilayer are given in the Appendix of the present paper.

2.5. *Plasticity*

Suresh *et al.* (1994) studied the conditions governing the onset and spread of plasticity in an isotropic bilayer subject to cyclic thermal loading. They defined a set of critical temperature changes to characterize plastic deformation in one or both layers. Shen and Suresh (1995a) extended this problem to some specific geometries of a general metal/ceramic trilayer system, and established a direct link between the spread of plasticity and the occurrence of reversals in curvature. Giannakopoulos *et al.* (1995) considered the effect of a graded interlayer on the critical temperature for the initiation and spread of plastic flow, within the context of small deformation theories.

Consider a metal/ceramic bilayer in which layer 1 is a metal undergoing plastic flow and layer 2 is a ceramic (elastic material). It is possible to define a critical temperature change beyond which layer 1 yields. For the isotropic bimaterial case subject to general anisotropic loading, the problem can be considered as a superposition of a mean equal axial stress field, $\sigma^m(z)$ and a pure shear field, $\tau(z)$ (Hill, 1950). The effective stress is simply given by

$$(\sigma^e)^2 = (\sigma^m)^2 + 3\tau^2. \tag{34}$$

The effective stress is always a maximum at the interface between the two layers because both the mean stress and the shear stress assume extreme values there. The mean stress and the shear stress in layer 1 at the interface are given by

$$\sigma_1^m = \frac{E_1}{1 - v_1}(g(\hat{E}_{Bi}, \rho) - \tfrac{1}{2})\Delta\varepsilon^m \quad \text{and} \quad \tau_1^m = \mu_1(g(\hat{\mu}, \rho) - \tfrac{1}{2})\Delta\gamma, \tag{35}$$

where g is defined in (14) and (15), $\Delta\varepsilon^m$ is the mean strain mismatch and $\Delta\gamma$ is the shear mismatch. A plot of the loading, which equates the effective stress to the yield

strength of layer 1 in the plane $(\Delta\varepsilon^m, \Delta\gamma)$, defines the yield locus beyond which layer 1 starts to yield. Since there is a uniqueness between the stress field and the curvatures, it is possible to define a critical shape change at which plastic yielding has occurred. This is accomplished by linking the mean stress to the mean curvature, and the shear stress to the twist curvature.

$$\sigma_1^m = -\frac{E_1}{1-\nu_1}\frac{1+\hat{E}_{Bi}\rho(3+4\rho)}{\hat{E}_{Bi}(1+\rho)^4}\kappa^m \quad \text{and} \quad \tau_1 = -2\mu_1\frac{1+\hat{\mu}\rho(3+4\rho)}{\hat{\mu}(1+\rho)^4}\hat{\kappa}_{xy}. \quad (36)$$

2.5.1. *A special case for thermal loading.* For thermal loading, the mean strain mismatch and the shear strain mismatch are

$$\Delta\varepsilon^m = \frac{\Delta\alpha_x + \Delta\alpha_y}{2}\Delta T \quad \text{and} \quad \Delta\gamma_{xy} = (\Delta\alpha_x - \Delta\alpha_y)\Delta T. \quad (37)$$

As defined in Suresh *et al.* (1994) for isotropic bimaterials, the first critical temperature, ΔT_1, is the temperature change required to induce plasticity in the ductile layer. If layer 1 has a yield strength equal to σ_1, the critical temperature and the corresponding critical curvature for the onset of yielding, respectively, are given by

$$\Delta T_1 = \frac{2\sigma_1(1-\nu_1)}{E_1\Delta\alpha^m(2g(\hat{E}_{Bi},\rho)-1)}, \quad \hat{\kappa}_1 = \frac{2\sigma_1(1-\nu_1)f(\hat{E}_{Bi},\rho)}{E_1(2g(\hat{E}_{Bi},\rho)-1)}, \quad (38)$$

where g and f are defined in Section 2.2. Note that the critical curvature does not depend on the CTE mismatch. If the CTE mismatch is not isotropic, the difference in curvatures between the two principal directions is given by

$$\hat{\kappa}_x - \hat{\kappa}_y = f(\hat{\mu},\rho)(\Delta\alpha_x - \Delta\alpha_y)\Delta T. \quad (39)$$

2.6. *Large deformation and bifurcation*

When the out-of-plane deflection of the plate is comparable to the thickness, the strain and the curvature throughout the plate are no longer uniform. Following the work of Hyer (1981a, b, 1982) for orthotropic laminates and Masters and Salamon (1993, 1994, 1995) for thin films, we extend the analysis of the large deformation problem for bilayer materials (of arbitrary layer dimensions) subject to thermal excursions. Certain aspects of this problem have been considered as far as five decades ago (e.g. Panov, 1947, Writtick, 1953) in the context of the stability of bimetallic disk for thermostats.

The displacements $(u^\circ, v^\circ, w^\circ)$ along the axes x, y and z, respectively, and the strains at the mid-plane, $z = 0$, are related by (von Kármán, 1910; Timoshenko and Woinowsky-Krieger, 1959).

$$\varepsilon_{xx}^\circ = \frac{\partial u^\circ}{\partial x} + \frac{1}{2}\left(\frac{\partial w}{\partial x}\right)^2$$

$$\varepsilon_{yy}^\circ = \frac{\partial v^\circ}{\partial y} + \frac{1}{2}\left(\frac{\partial w}{\partial y}\right)^2$$

$$\gamma_{xy}^{\circ} = \frac{\partial u^{\circ}}{\partial y} + \frac{\partial v^{\circ}}{\partial x} + \left(\frac{\partial w}{\partial x}\right)\left(\frac{\partial w}{\partial y}\right). \tag{40}$$

The main assumption of the model is to consider the deformations of the plate with constant curvatures. Therefore, the deflection $w(x, y)$ is given by

$$w(x, y) = -\tfrac{1}{2}(\kappa_{xx}x^2 + \kappa_{yy}y^2 + 2\kappa_{xy}xy), \tag{41}$$

assuming that w is small compared to the dimensions of the plate, L_x and L_y.

The in-plane displacements u and v, are considered as polynomials in x and y of different orders. In their studies of the departures in the bending responses of laminated plates and thin films on substrates from the classical Kirchoff plate theory predictions, Hyer (1981b) used polynomials of order two, while Salamon and Masters (1995) used polynomials of order up to six in an attempt to consider the in-plane shear and the boundary conditions at the edges. The curvatures were then computed by minimizing the strain energy of the system using the Rayleigh/Ritz energy minimization approach.

It was found in the above studies that the curvature was not linear during thermal excursions (as a consequence of large elastic deformation). In addition, at a certain imposed load or temperature change, a bifurcation of the solution was observed, resulting in the possibility of several equilibrium shapes some of which were stable beyond the point of bifurcation. The main drawback of this formulation is the assumption that the curvature is uniform in the plate. In many cases, this assumption may result in the bifurcation of the solution.

Analytical expressions of the critical curvature and critical strain mismatch can be found for bilayered isotropic plates with $L_x = L_y = L$. In the case of large deformation, the curvature, κ, is no longer a linear function of the strain mismatch. However, the critical radius of curvature for bifurcation can be expressed by the ratio $L^2/(h_1 + h_2)$, as noted in Masters and Salamon (1993). This is equivalent to considering the bifurcation phenomenon as a ratio of the critical defection of the plate, w_c, to the total thickness of the plate. The critical curvature and the critical deflection are given by

$$\kappa_c = \frac{h}{L^2} \hat{\kappa}_c(\text{material distribution}) \quad \text{and} \quad w_c = \frac{L^2}{4}\kappa_c = \frac{h}{4}\hat{\kappa}_c(\text{material distribution}) \tag{42}$$

where $\hat{\kappa}_c$ is a dimensionless curvature depending on the material distribution (e.g. compositional grading).

If we consider a second order strain approximation with a non-zero midplane shear strain, the normalized curvature, $\hat{\kappa}_c$, can be expressed as

$$\hat{\kappa}_c^2 = 24\left(1 + \frac{5}{1 + A_{12}/A_{11}}\right)\left(\frac{A_{66}D_{66} - B_{66}^2}{A_{66}^2}\right), \tag{43}$$

where $[A]$, $[B]$ and $[D]$ are the reduced stiffness matrices. Note that $\hat{\kappa}_c$ depends only on the shear modulus distribution and on the coefficient A_{12}/A_{11}.

For example, for a bilayered plate with the same Poisson's ratio, v, for both layers, (which implies that $A_{12}/A_{11} = v$), the square of $\hat{\kappa}_c$ is given by

$$\hat{\kappa}_c^2 = \frac{24(6+v)(1+\hat{\mu}\rho(4+6\rho+4\rho^2)+\hat{\mu}^2\rho^4)}{(1+v)(1+\hat{\mu}\rho)^2(1+\rho)^2} \qquad (44)$$

For the thin-film limit, i.e. as $\rho \to 0$, $\hat{\kappa}_c$ is simply equal to

$$\hat{\kappa}_c = \sqrt{\frac{24(6+v)}{(1+v)}}, \qquad (45)$$

as expressed in Salamon and Masters (1995).

2.7. Finite element calculations

Finite element calculations have been carried out in this study to check the accuracy of the analytical formulation, and to extend the large deformation problem to elasto-plastic bimaterials. The general purpose finite element program ABAQUS (1994) was used. An 8×8 regular mesh of 8-noded general shell elements with 17 integration points through the thickness was used with a non-linear geometry integration scheme. The convergence of the mesh has been checked by increasing the number of degrees of freedom. In the case of a bifurcation in the solution (square plate for example), possible solutions were computed by introducing an initial perturbation before the temperature change. This perturbation was a moment distributed on the edge of the plate. This moment, which depended on the geometry of the plate and the material distribution (i.e. grading), was reduced to be of the least possible value in an attempt to achieve converge towards the exact bifurcation behavior predicted by the theory. The simulations were done on a multi-layered rectangular plate free of external constraints under uniform temperature change. Only one quarter of the plate was modeled assuming that the deformation preserves the two symmetric in-plane axes. (In some cases, however, the development of shear loading may lead to the rotation of the principal axes.) The ratio of the in-plane length of the plate to the thickness was chosen to be always greater than 50 such that the effect of the singularity of the field at the free edge could be considered negligible in order to use the shell elements. In the case of a graded region, each integration point through the thickness was given a linear interpolation between the two homogeneous layers as presented in Section 2.4. The plastic behavior of the metallic layers was modeled as conforming to the J_2 flow theory. We considered a wide variety of numerical simulations incorporating different degrees of internal constraints on the plate in an attempt to simulate the analytically predicted trends. On the basis of these computations, the following observations can be made.

(1) When a perfect square plate was modeled, the post-bifurcation shape revealed five main eigenmodes corresponding to two cylindrical shapes oriented along the x and y axes, two cylindrical shapes oriented along the directions of the diagonals of the square, and a 4-fold symmetry shape. In the present paper we focus only on the first two modes which are the lowest energy shapes.

(2) When the symmetry of the plate is lost by increasing the size in one direction,

the finite element calculation does not reveal any abrupt bifurcation which is predicted by the analytical methods. This is so because the plate gradually curves more in the longer direction.

(3) The freezing of the out-of-plane shear or membrane shear did not affect the deformation history. This results from the fact that the aspect ratio L_x/h is large for the cases examined, and that the thermal loading induces localized moments and forces which are uniform over the plate. Thus, the imposition of temperature changes causes a large deformation bifurcation response of the plate which is markedly different from that resulting from an externally applied force or moment on the edge of the plate.

(4) The analytical solution presented in Section 2.6 was recovered by constraining the plate to keep a uniform curvature. This was achieved by linking all the out-of-plane displacements with a quadratic form in x and y such as (41). The main result of this constraint is to create a bifurcation point in the case of rectangular plates.

(5) As noted by Salamon and Masters (1995), the curvature of the plate is not at all uniform over the length or the width of the plate. The corners have the curvature equal to the small deformation theory. However, the center of the plate has a much lower curvature due to the constraints resulting from the large deformation. In the present paper, all the curvature values reported for large deformation (pre- and post-bifurcation) are taken at the center of the plate in order to compare the values for different shapes on a common basis. These center-point curvatures were computed from the deflection of the nodes neighboring the center of the plate. Therefore, the curvatures presented in the following figures underestimated the average curvatures of the plate if one considers the deflection of the edges.

3. LARGE THERMOELASTIC DEFORMATION OF BILAYERS

In this section, the effects of (i) layer dimensions, (ii) in-plane thermal and elastic anisotropy, and (iii) geometric imperfections on the evolution of curvature in bilayers are addressed. Attention is confined to a consideration of the thermoelastic response and large deformation in each layer under uniform temperature change.

3.1. *Model systems*

In an attempt to illustrate the geometry dependence of large deformation in bilayers, we consider two model systems. (1) A 1-mm-thick layer of polycrystalline Ni bonded (e.g. by diffusion bonding) to a 1-mm-thick layer of polycrystalline Al_2O_3. (2) An unsymmetric, two-ply $[O_1/90_1]_T$ C-epoxy laminated composite with a ply thickness of 1 mm.

This Ni/Al_2O_3 bilayer is of rectangular geometry with $L_x = 100$ mm and $L_y = L_x$, $1.5L_x$, $2.0L_x$, or $5.0L_x$. The Ni layer has the following properties, which were considered isotropic and constant over the range of temperatures analyzed: $E_{Ni} = 214$
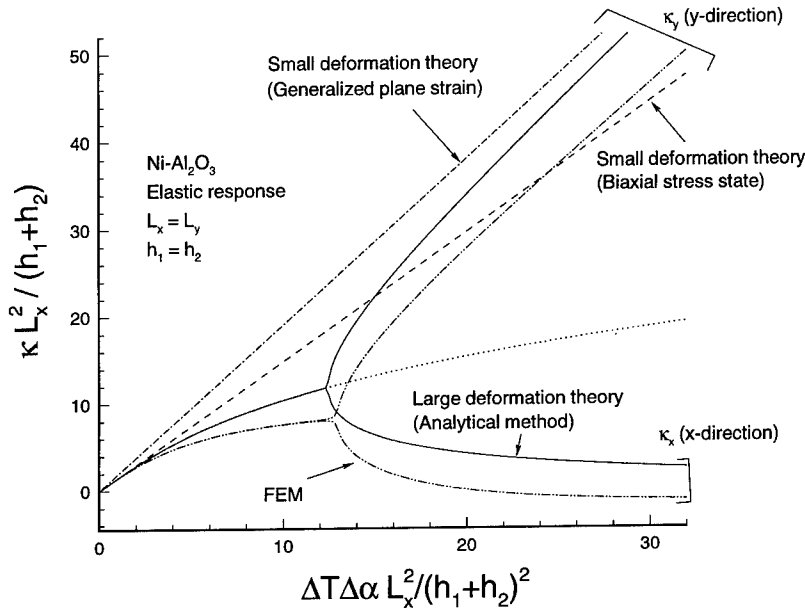
Fig. 6. Comparison of different models to predict the curvature of a square bilayered plate as a function of the normalized temperature change. The aspect ratio of the plate, $L_x/(h_1 + h_2)$, is assumed to be larger than 50. The model system is a Ni/Al_2O_3 bilayer with equal layer thickness. The Ni layer is permitted to undergo only elastic deformation.

GPa, $v_{Ni} = 0.31$, and $\alpha_{Ni} = 15.4 \times 10^{-6}$ $1/^\circ C$. The properties of the isotropic alumina layers are: $E_{Al_2O_3} = 380$ GPa, $v_{Al_2O_3} = 0.25$, and $\alpha_{Al_2O_3} = 7.4 \times 10^{-6}$ $1/^\circ C$.

The in-plane geometry of this orthotropic bilayer is a 200 mm × 200 mm square. The C-epoxy composite plate is an orthotropic material wherein layer has a thickness equal to 1 mm and is taken to be linear elastic with the following properties: $E_1 = 181$ GPa, $E_2 = 10.3$ GPa, $v_{12} = 0.28$, $G_{12} = 7.17$ GPa, $\alpha_1 = -0.106 \times 10^{-6}/^\circ C$ and $\alpha_2 = 25.6 \times 10^{-6}/^\circ C$. Finite element analyses were conducted with the purpose of simulating the evolution of bending in the plate under a positive change of temperature from 0 to 200°C.

3.2. Predictions based on different theories for different stress states

Consider first the effect of large deformation, arising from thermal excursions from the initial (stress-free) temperature, on the evolution of curvature in the $Ni–Al_2O_3$ bilayer with in-plane isotropy. The metal layer is permitted to undergo only thermoelastic deformation. Figure 6 shows the variation of the normalized curvature, $\hat{\kappa} = \kappa L_x^2/(h_1 + h_2)$, as a function of the normalized temperature change, $\widehat{\Delta T} = \Delta T \Delta \alpha$ $L_x^2/(h_1 + h_2)^2$, for the Ni/Al_2O_3 bilayer. This normalization of curvature and temperature is chosen because it enables a representation of results which are independent of the particular choice of $L_x/(h_1 + h_2)$ when the edge effects are not significant. As anticipated, the small deformation theory for an equal biaxial state of stress in the bilayer plate shows a linear variation of $\hat{\kappa}$ with $\widehat{\Delta T}$ (the dashed line in Fig. 6). For a

state of generalized plane strain, the small deformation theory (Section 2.3) predicts a curvature which is higher than that evolving in a biaxial stress state. The small deformation, equal biaxial stress state predicts a spherical shape with a unique curvature ($\kappa_x = \kappa_y$), whereas a state of generalized plane strain produces a cylindrical shape (see Section 2.3).

The theory for large elastic deformation (Section 2.6) predicts an initial curvature evolution at low $\widehat{\Delta T}$ (the solid line in Fig. 6) which is coincident with that seen for the small deformation biaxial state. At a critical temperature change, $\widehat{\Delta T}_{cr} = \widehat{\Delta T} \approx 2$, the two curves begin to deviate. The large deformation theory predicts a single spherical curvature which is smaller than that for small deformation. At another critical temperature change, $\widehat{\Delta T}_b = \widehat{\Delta T} \approx 11.5$, a bifurcation in the solution is predicted. In the post-bifurcation regime, three different equilibrium shapes are possible: a stable ellipsoidal shape with a large curvature in one direction (along the y axis) and a small curvature along the other (x axis), shown by the solid lines in Fig. 6, a stable shape identical to the first one where the x and y curvatures are "flipped" (not shown in Fig. 6 for the purpose of clarify), and an unstable spherical shape which is a continuation of the initial curvature line prior to $\widehat{\Delta T}_b$, shown by the dotted line. With increasing $\widehat{\Delta T}$, the ellipsoidal shape continues to change whereby $\hat{\kappa}_y$ increases while $\hat{\kappa}_x$ decreases. For $\widehat{\Delta T} > 14.5$, $\hat{\kappa}_y$ becomes larger than the small deformation spherical curvature for the biaxial stress state at the same temperature.

The three-dimensional finite element analyses (the dotted lines in Fig. 6) for the Ni/Al_2O_3 plate reveal curvature evolution trends which are similar to those predicted by the large deformation elastic theory. The curvature values for large deformation seen in the computations, however, are lower than the analytical predictions. Note that the critical temperature at which the curvatures for small and large deformation begin to deviate, $\widehat{\Delta T}_{cr}$, and the critical temperature at which bifurcation occurs, $\widehat{\Delta T}_b$, are predicted to be essentially the same by the large deformation theory and the finite element analyses. The maximum values of the post-bifurcation curvature corresponding to the ellipsoidal shape during large thermoelastic deformation ($\widehat{\Delta T} \gg \widehat{\Delta T}_b$) asymptotically approach the cylindrical curvature estimated for small deformation under generalized plane strain.

3.3. The effects of in-plane geometry on bifurcation

For fixed thicknesses of Ni and Al_2O_3 layers, we explore the effects of changes in in-plane dimensions of the rectangular Ni/Al_2O_3 plate on the occurrence of bifurcation. For this purpose, finite element analyses were carried out with $L_x = 100$ mm, $h_1 = h_{Ni} = 1$ mm, and $h_2 = h_{Al_2O_3} = 1$ mm. The ratio L_y/L_x was varied from 1.0 to 5.0.

The evolution of normalized curvature $\hat{\kappa}$ with the temperature change ΔT is plotted in Fig. 7 for the above conditions from the finite element analyses. For the square plate, $L_x = L_y$, a bifurcation in the solution is predicted at $\Delta T \approx 160°C$ from the initial stress-free temperature. When $L_y/L_x > 1.0$, however, a sharp bifurcation in the solution leading to abrupt shape changes is not predicted by the present analysis. Instead, a more gradual evolution of the transition from a single spherical curvature at the early stages of thermal excursions to an ellipsoidal shape with two distinctly different curvatures along the x and y axes is seen for $L_y/L_x = 1.5$. Thermal loading
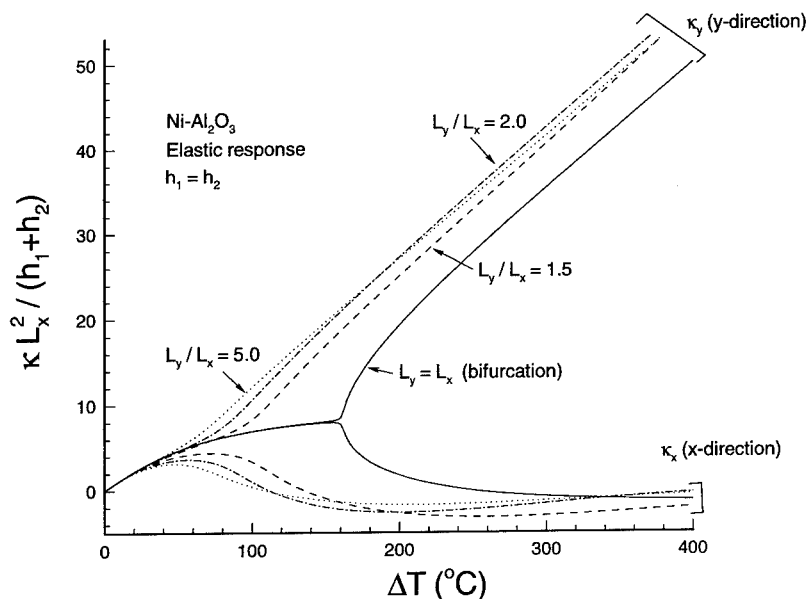
Fig. 7. Effect of the ratio of the two principal lengths of the plate, L_x and L_y on curvature evolution under thermal loading. The model system is a Ni/Al$_2$O$_3$ bilayer with equal layer thicknesses (1 mm). $L_x = 100$ mm. The Ni layer is permitted to undergo only elastic deformation.

causes the rectangular plate to gradually bend more and more in the longer side of the plate (y direction); a progressively smaller curvature evolves in the orthogonal direction (along the x axis). An increase in L_y/L_x from 1.5 to 5.0 causes a reduction in the temperature at which the transition from a unique spherical curvature to an ellipsoidal shape commences.

The results of Fig. 7 thus show that curvature evolution during large elastic deformation and the concomitant bifurcation are strongly sensitive to the in-plane aspect ratio of the rectangular bilayer plate, when the small strain (thin) plate theory analysis is employed.

3.4. Curvature evolution in orthotropic bilayer composites

The stable room-temperature shapes of cured, unsymmetric organic laminates have been studied in detail by Hyer (1981, 1982). In his work, layers of equal thicknesses of laminated square plates ($L_x = L_y$) were examined for a variety of $[0_n/90_n]_T$ composites. In this section, we illustrate how minor perturbations in geometry result in large variations in the room-temperature shapes of a $[0_1/90_1]_T$ composite which is cooled from a curing temperature of 200°C. Figure 8 shows the finite element predictions of the evolution of κ_x and κ_y for the organic composite as its temperature is dropped (uniformly through the bilayer) by ΔT from the curing temperature. For $L_x = L_y$ and $h_1(=h_0) = h_2(=h_{90})$ (with $L_x = 100(h_1+h_2)$), a unique saddle shape ($\kappa_x = -\kappa_y$) evolves prior to the bifurcation temperature, $\Delta T_b \approx 110°C$. Beyond ΔT_b, κ_x gradually assumes a cylindrical shape; κ_y has the same magnitude but opposite sign. Small fluctuations in applied loads or moments can "snap" the laminate from
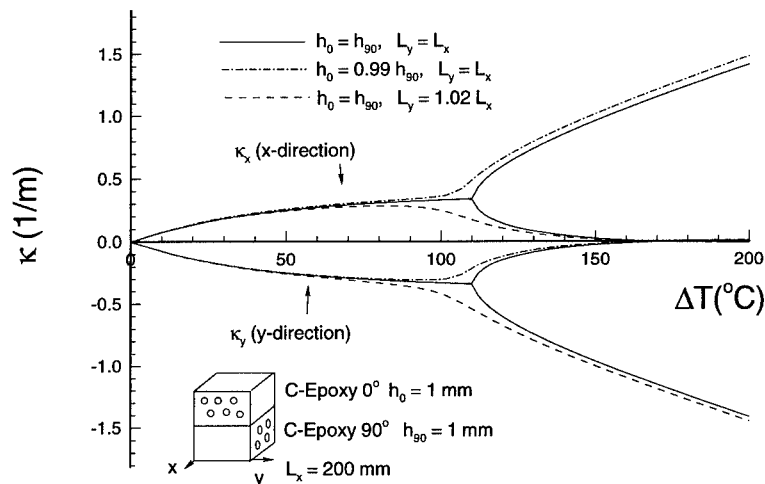
Fig. 8. FEM predictions of the curvature of a two-ply [$0_1/90_1$] C-epoxy laminate as a function of temperature change. The plate is a 200 mm × 200 mm square of total thickness equal to 2 mm. The effects of a thickness imperfection and a size imperfection are shown by the two dashed curves.

one cylindrical shape (say, $\kappa_x \neq 0$ and $\kappa_y = 0$) to another ($\kappa_y \neq 0$ and $\kappa_x = 0$), as noted in Hyer (1981).

While a sharp bifurcation temperature exists for the square plate with $h_1 = h_2$, minor geometric imperfections cause large variations in the manner in which the saddle shape evolves into an equilibrium cylindrical shape for large ΔT. Consider first the situation where the square geometry is preserved ($L_x = L_y$), but the thicknesses of the two layers are slightly different with $h_0 = 0.99h_{90}$. In this case, around $\Delta T \approx 100°C$, the saddle shape gradually changes to a stable cylindrical shape with a curvature only in the x or y direction. In other words, a 1% difference in the layer thickness erases the sharp bifurcation. Similarly, a 2% difference in side length ($L_y = 1.02\ L_x$) produces a gradual transition from a saddle shape to a cylindrical shape. The results presented in Sections 3.2–3.4 collectively reveal the sensitivity of curvature evolution, during large deformations induced by thermal excursions, to the aspect ratio of the rectangular geometry, and to the layer thickness.

4. EFFECTS OF PLASTICITY ON LARGE DEFORMATION

When a metal/ceramic bilayer plate is subject to temperature changes, the thermal stresses arising from differential thermal expansion between the layers can induce the onset of plastic flow at the interface at a certain critical temperature; the plastic zone spreads outward into the ductile layer eventually causing the entire metallic layer to be fully yielded. Consider a metal layer of thickness h_1 perfectly bonded to a ceramic layer of thickness h_2 at some initial stress-free temperature. For this large bilayer plate subject to an equal biaxial state of stress, the temperature change at which plasticity commences at the interface [see (38)] is given by Suresh et al. (1994).

When both the metal and the ceramic layer undergo elastic deformation, the unique spherical curvature which evolves under small deformation conditions varies linearly with temperature. Upon the onset of plastic flow in the metal layer at $\Delta T = \Delta T_1$, the $\kappa - \Delta T$ plot begins to show a non-linear response. For a state of equal biaxial stress, the curvature at which plasticity commences in the ductile layer at $\Delta T = \Delta T_1$ is given by (38).

In this section, we examine the effects of plasticity in one of the layers of the bilayer on curvature evolution and geometry dependence of large deformation of the bilayer. Since this is a topic of much complexity, we confine attention only to situations involving small strains and small rotations of bilayer plates. In an attempt to extract some general trends for a broad range of applications, two model systems are selected. (1) The bilayer system comprising "thick" polycrystalline layers of Ni and Al_2O_3 whose elastic properties were described in Section 3.1. The thicknesses of the Ni and Al_2O_3 layers are $h_1 = 0.2$ mm and $h_2 = 0.8$ mm, respectively; a square geometry $(L_x = L_y)$ is considered with several different values of the ratio, $L_x/(h_1 + h_2)$. For the purposes of the simulations presented here, the Ni layer is assumed to exhibit an elastic/perfectly plastic response, with a temperature-independent yield strength of 150 MPa. (Full details of the small deformation thermoplastic response of the Ni/Al_2O_3 bilayer, including the effects of temperature dependence of thermal and plastic properties, and isotropic strain hardening can be found in Suresh *et al.*, 1994.) (2) An Al thin film deposited on an elastic Si single crystal substrate (with in-plane isotropy).

The Si layer has in-plane isotropic properties, with $E_{Si} = 130$ GPa, $\nu_{Si} = 0.28$, and $\alpha_{Si} = 3.0 \times 10^{-6}$ 1/°C. The aluminum layer is considered to be elastic/perfectly plastic with the following isotropic properties: $E_{Al} = 70$ GPa, $\nu_{Al} = 0.33$ and $\alpha_{Al} = 23.5 \times 10^{-6}$ 1/°C, and (thin film) yield strength, $\sigma_y = 200$ MPa.

4.1.   Ni/Al_2O_3 bilayer

Figure 9 shows the finite element results of the evolution of curvature κ as a function of temperature change ΔT for different $L_x/(h_1 + h_2)$ ratios of the square plate of the Ni/Al_2O_3 bilayer. Here the curvature is normalized by the value of curvature κ_1 for the temperature change $\Delta T = \Delta T_1$ at which plasticity begins in the Ni layer during small deformation, and the temperature change is normalized by ΔT_1. For $L_x/(h_1 + h_2) = 50$, the curvature increases linearly from $\Delta T = 0$ to $\Delta T = \Delta T_1$ at which a plastic zone starts to spread outward from the interface in the Ni layer. The entire Ni layer yields before $\kappa/\kappa_1 \approx 1.08$; beyond this point, the curvature remains essentially unchanged with ΔT. Small deformation elastoplastic analyses reveal that for an elastic/perfectly plastic metal bonded to an elastic substrate, the curvature reaches a constant saturated value when the metal is fully yielded. The results for $L_x/(h_1 + h_2) = 50$ are the same as those predicted by the small deformation elastoplastic theory (Suresh *et al.*, 1994), as evident from the linear variation of κ with ΔT up to ΔT_1.

An increase in $L_x/(h_1 + h_2)$ to higher values causes a significantly different response than what can be anticipated from the small deformation elastoplastic analyses. The following observations can be made from Fig. 9.

- The curvature increases linearly with ΔT up to $\Delta T/\Delta T_1 = 0.4$, beyond which a non-linear variation occurs.
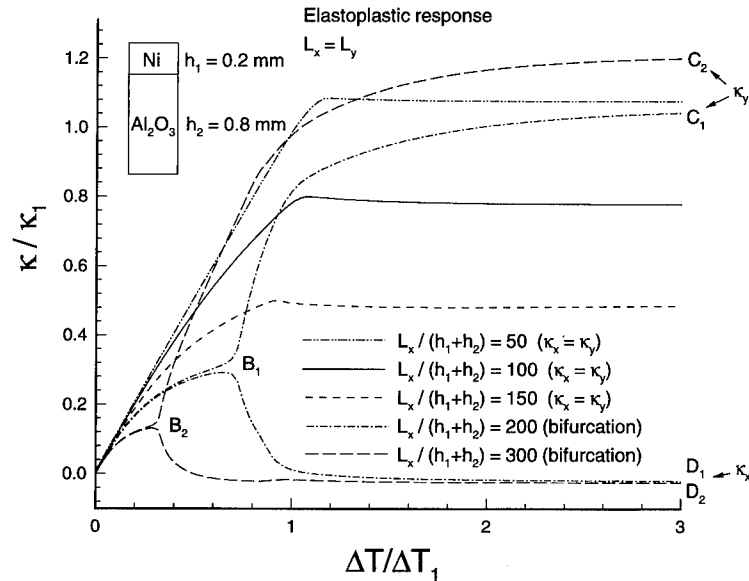
Elastoplastic response

Fig. 9. FEM predictions of the evolution of a Ni/Al_2O_3 square plate as a function of the temperature change for different sizes of the plate. Here, the Ni layer is assumed to be elastic/perfectly plastic with a yield strength of 150 MPa (independent of temperature). The curvature and the temperature are normalized by the critical curvature $\Delta\kappa_1$ and the critical temperature change, ΔT_1, to initiate plastic yielding in the nickel layer as defined in Suresh et al. (1994) for equal biaxial stress state (small deformation).

- The saturated value of curvature κ/κ_1 corresponding to the full yielding of the Ni layer decreases from a value of about 1.07 for $L_x/(h_1+h_2) = 50$ to about 0.76 for $L_x/(h_1+h_2) = 100$. In both cases, however, a single spherical curvature evolves during both elastic and plastic deformation in the Ni layer.

- A further increase in $L_x/(h_1+h_2)$ to 150 causes a further reduction in the saturated value of the curvature ($\kappa/\kappa_1 = 0.48$). Notice also the significantly more marked non-linearity in curvature for $\Delta T/\Delta T_1 < 1.0$.

- An additional increase in $L_x/(h_1+h_2)$ to 200 causes a pronounced reduction in the ΔT range over which a unique spherical curvature results. At $\Delta T/\Delta T_1 \approx 0.7$ (the location marked B_1 in Fig. 9), a bifurcation in the solution occurs causing an abrupt change from a single spherical curvature to two stable cylindrical shapes both of which are equally likely to occur above the bifurcation temperature. The finite element solutions shown in Fig. 9 exhibit the typical "pitchfork bifurcation", as was also seen in the thin-film elastic analyses of Masters and Salamon (1993).

- An increase in $L_x/(h_1+h_2)$ from 200 to 300 causes a greater degree of non-linearity in the $\kappa - \Delta T$ plot prior to bifurcation, a more substantial reduction in the bifurcation temperature and curvature (from the location marked B_1 to B_2 in Fig. 9), and a higher value of the cylindrical curvature along the y axis.

- Although the bifurcation temperature, the corresponding curvature (just prior to the point of bifurcation), and the saturation curvature for complete plastic
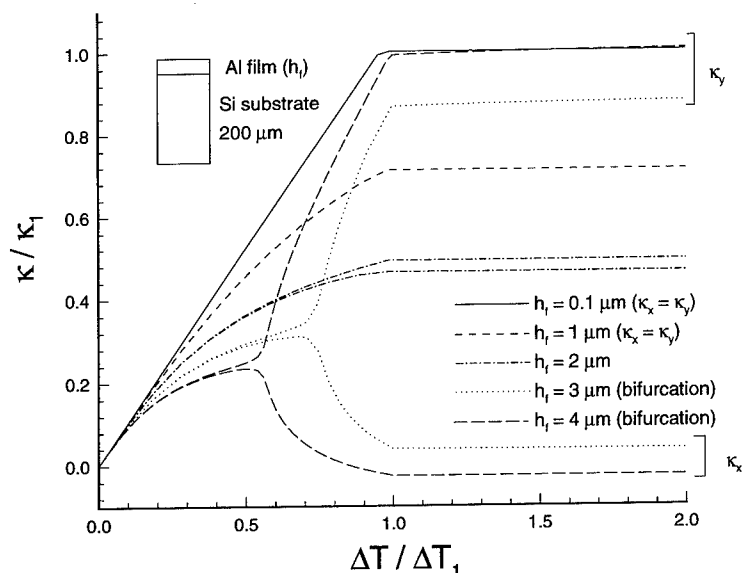
M. FINOT and S. SURESH

Fig. 10. FEM predictions of the evolution of the curvature of Si/Al 100 mm × 100 mm square plate as a function of a temperature change. The temperature and curvature are normalized by the corresponding values at the onset of plastic flow during small deformation (biaxial stress state). The aluminum thin-film layer is assumed to be elastic/perfectly plastic with a yield strength equal to 200 MPa (independent of temperature). The effect of the Al film thickness is indicated.

yielding of the metal layer are strongly influenced by $L_x/(h_1 + h_2)$ for large deformation, the temperature at which plastic yielding begins in the metal is insensitive to $L_x/(h_1 + h_2)$. For $h_{Ni}/h_{Al_2O_3} = 1/4$, plasticity begins at the Ni/Al$_2$O$_3$ interface at $\Delta T \approx \Delta T_1$ for all the values of $L_x/(h_1 + h_2)$ considered in Fig. 9.

4.2. Si/Al bilayer

We now consider the effect of geometry and plastic flow on curvature evolution during small and large deformation in a bilayer comprising a Si single crystal and an Al thin film. The bilayer is a 100 mm × 100 mm square plate.† The Si thickness is fixed at 200 μm. We begin with a consideration of the effect of Al film thickness (h_f) on large deformation, assuming that the Al thin film exhibits an elastic/perfectly plastic response. For the purpose of the present computations, the yield strength of the Al film (with in-plane isotropic properties) is taken to be 200 MPa (over the temperature range 0–200°C), which is typical of the value reported for Al films approximately 1 μm in thickness (Nix, 1989; Shen and Suresh, 1995b).

4.2.1. Perfect plasticity in the Al film. Figure 10 presents the computational results of curvature evolution during uniform thermal excursions in the Al/Si bilayer, as a

† Si single crystal circular wafers, typically 75–100 mm in diameter, are commonly used in microelectronic applications. The results presented here for square plates of Si/Al also hold for circular wafers of Si with Al films deposited on them. Recent advances in wafer design call for larger diameters of Si, i.e. up to 300 mm. With such larger dimensions, the issues of large deformation during thermal and/or mechanical loading would be expected to become more significant.

function of the Al film thickness which was varied from 0.1–4 μm, with all the other dimensions fixed. κ and ΔT are normalized by κ_1 and ΔT_1, respectively. For $h_f = 0.1$ and 1.0 μm, temperature variations ΔT of up to 200°C from the initial stress-free temperature induce a unique spherical curvature. For $h_f = 0.1$ μm, both the Al and Si layers undergo only small thermoelastic deformation for the entire range of temperatures considered here; this is reflected as a linear variation of κ with ΔT in the elastic regime. Beyond this point, the Al layer becomes fully plastic and the perfect plasticity of the thin Al layer results in a constant value of curvature beyond $\Delta T = \Delta T_1$. This result for plastic response is the same as that predicted by the small deformation biaxial stress model and by the small deformation generalized plane strain model. Increasing the Al film thickness to 1 μm causes a slightly non-linear variation of κ with ΔT, even in the elastic regime that persists up to the onset of plastic flow, beyond which κ is independent of ΔT. A further increase in h_f to 2 μm causes a greater degree of non-linearity in elastic bending, although ΔT for the onset of plastic flow in the Al layer is unaffected. A small asymmetry in curvature develops between the x and y directions in the vicinity of ΔT at which plastic flow initiates. A further increase in h_f to 3 μm causes dramatic changes in the bending response of the bilayer. The thermoelastic curvature evolution shows a greater degree of non-linearity. A bifurcation occurs at $\Delta T/\Delta T_1 \approx 0.6$, beyond which the spherical geometry of the bilayer is replaced by an ellipsoidal/cylindrical geometry. Note that despite the large changes induced in the thermoelastic response for $h_f = 3$ μm (as compared to $h_f < 2$ μm), the plastic response is relatively unaffected. Specifically, the temperature at which the Al film becomes plastic is unchanged. A still further increase in h_f to 4 μm moves the ΔT value at which bifurcation occurs down to about $0.5\Delta T_1$, and increases the differences between the curvatures along the x and y directions in the post-bifurcation regime.

4.2.2. *Strain hardening in the Al film.* The effects of isotropic, linear strain hardening ($d\sigma/d\varepsilon = H = 4$ GPa) in the Al layer on the geometry changes induced during the thermoelastoplastic deformation of the Al/Si bilayer are presented in Fig. 11 for $h_f = 1$, 2, and 3 μm for ΔT up to 400°C. The solid lines in this figure correspond to the elastic/perfectly plastic response of the Al layer. The following trends can be extracted from Fig. 10.

- For $h_f = 1$ μm, the small deformation solution is adequate in both the thermoelastic and thermoplastic regimes. For this geometry, strain hardening in the Al film merely serves to increase slightly the magnitude of the spherical curvature in the bilayer.
- For $h_f = 2$ μm, the strain hardening of the Al film causes an increase in the anisotropy in the curvatures between the in-plane coordinate directions. When the film yields, the curvature of the plate is just below the bifurcation temperature. The hardening tends to increase the curvature.
- For $h_f = 3$ μm, the bifurcation occurs prior to the yielding. The hardening induces a non-saturation of the curvature beyond yielding.

The results of Fig. 11 thus illustrate that strain hardening in the ductile thin film can have a significant effect on large deformation and on the equilibrium shapes of the bilayer.
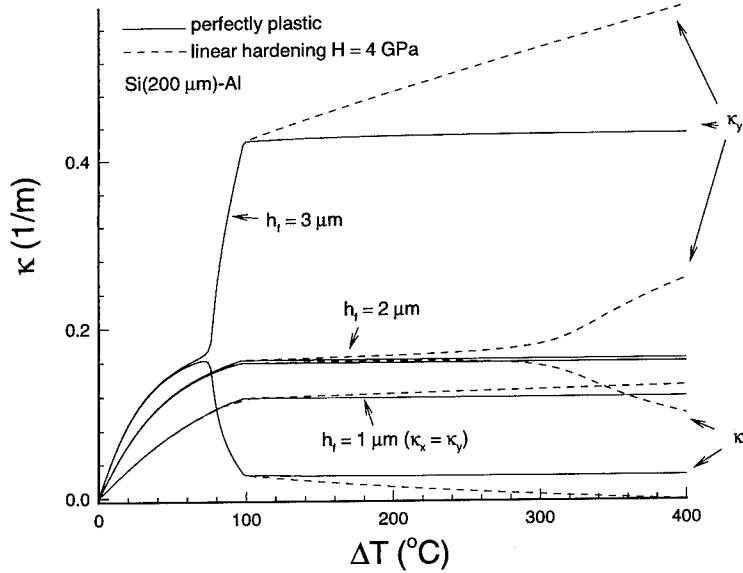
M. FINOT and S. SURESH

Fig. 11. FEM predictions of the effect of the plastic behavior of the Al thin film on the evolution of curvature in the Si/Al bilayer (100 mm × 100 mm square plate) as a function of temperature change. The substrate thickness is equal to 200 μm. The aluminum layer is considered either perfectly plastic (solid) or with a linear, isotropic hardening equal to 4 GPa (dashed).

5. EFFECTS OF COMPOSITIONAL GRADIENTS ON LARGE DEFORMATION

As discussed in Section 1.3, the introduction of compositional gradients between two layers offers the possibility to control the thermomechanical deformation of layered structures. In this section, we examine the effects of compositional gradients on the large thermoelastic deformation of two model systems. (1) A Ni/Al_2O_3 layered structure with a composite layer (also referred to as a functionally graded material layer or FGM) sandwiched between the layers of homogeneous Ni and homogeneous Al_2O_3. The relative volume fraction of Ni varies linearly within the gradient layer. The trilayered $Ni/Gradient/Al_2O_3$ plate analyzed here is of square shape with $L_x = L_y = 100$ mm. The relative thicknesses of the three layers were systematically altered in an attempt to examine the effects of layer thickness on large deformation. (2) A thin-film trilayer system comprising a compositionally graded layer of $In_{0.12}Ga_{0.88}As$ and GaAs (wherein the volume fraction of the GaAs varies linearly from one end of the layer to the other along the thickness direction) which is sandwiched between a homogeneous GaAs layer (thickness $= 10$ μm) and a homogeneous $In_{0.12}Ga_{0.88}As$ layer (thickness $= 100$ μm). The in-plane dimensions of the trilayer plate are 30 mm × 30 mm. Several different thicknesses of the graded layer were analyzed. The thermoelastic properties of Ni and Al_2O_3 were listed in Section 4. For the purposes of the simulations here, the Ni layer were assumed to be elastic/perfectly plastic with an yield strength of 150 MPa for the entire range of temperatures
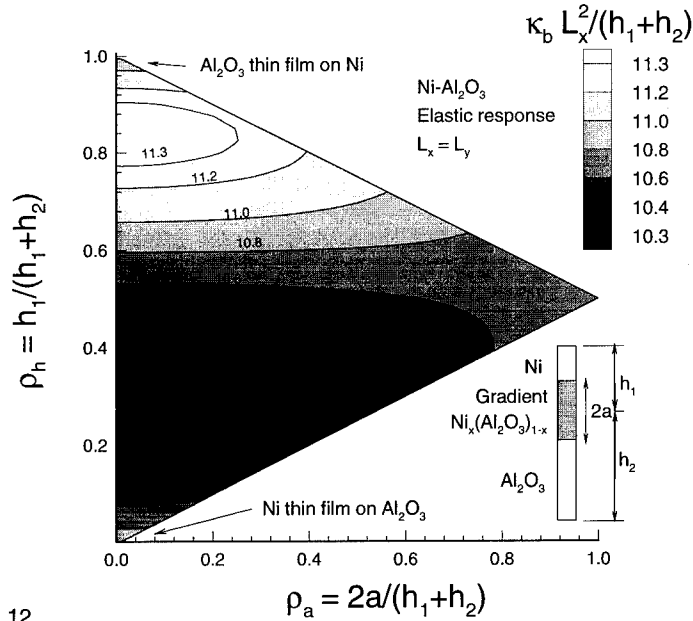
Fig. 12. Contours of constant normalized curvature to induce bifurcation in the tri-layered system, Ni/ Gradient/Al$_2$O$_3$, as a function of the material distribution through the thickness. For this calculation, the large deformation theory for elastic multilayers, Section 2.6, was used.

examined. Both the Ni and Al$_2$O$_3$ layers were assumed to be isotropic, with the same temperature at all locations during temperature excursions. The properties of the InGaAs system are: Young's modulus, $E = 86$ GPa, Poisson's ratio, $v = 0.31$, and the coefficient of thermal expansion, $\alpha = 6.9 \times 10^{-6}/°C$. The properties of GaAs are: $E = 81$ GPa, $v = 0.3$, $\alpha = 8.0 \times 10^{-6}/°C$. Both materials were modeled as isotropic, and the thermoelastic properties were considered to be constant over the range of temperatures analyzed in the study. In the graded region, the effective properties for E, α and v were linearly interpolated over ten steps of equal increments.

5.1. A graded layer between Ni and Al$_2$O$_3$ layers

Consider first the thermoelastic response of the Ni/Gradient/Al$_2$O$_3$ trilayer system focusing on the occurrence of bifurcation during large deformation. Consider arbitrary thicknesses of the three layers, Fig. 12, with $h_2 - a$, $2a$, and $h_1 - a$ denoting the thickness of the Ni, gradient and Al$_2$O$_3$ layers, respectively. The following two non-dimensional parameters

$$\rho_a = \frac{2a}{h_1 + h_2}, \quad \rho_h = \frac{h_2}{h_1 + h_2} = \frac{1}{\rho + 1} \tag{46}$$

define the full range of relative thicknesses of the three layers. The ordinate ($\rho_a \to 0$) corresponds to the Ni/Al$_2$O$_3$ bilayer; $\rho_h \to 0$ refers to the limiting case of a thin Ni
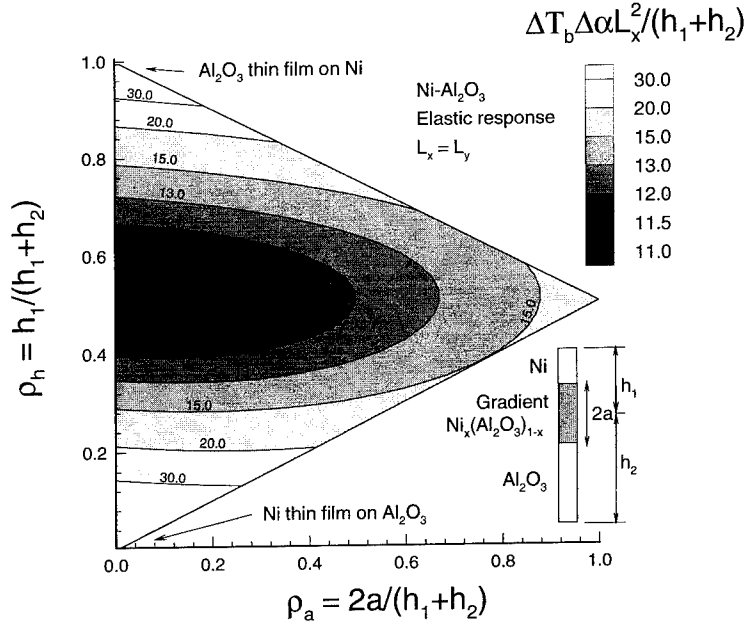
13

Fig. 13. Contours of constant normalized temperature to induce bifurcation in the tri-layered system, Ni/Gradient/Al_2O_3, as a function of the material distribution through the thickness. For this calculation, the large deformation theory for elastic multilayers, Section 2.6, was used.

film on a thick Al_2O_3 substrate, $\rho_h \to 1$ and $\rho_a = 0$ corresponds to a thin Al_2O_3 film on a thick Ni substrate, and $\rho_h = 0.5$ and $\rho_a = 0$ corresponds to the case of a Ni/Al_2O_3 bilayer where the two layers are of equal thickness. $\rho_a = 1$ and $\rho_h = 0.5$ is the limiting case where the entire composite is a single graded layer (with no homogeneous layers of Ni or Al_2O_3) whose composition varies linearly from $z = 0$ to $z = 2a = (h_1 + h_2)$. The sides of the triangle with corners at $(\rho_a = 0.0, \rho_h = 0.0)$, $(\rho_a = 1.0, \rho_h = 0.5)$, and $(\rho_a = 0.0, \rho_h = 1.0)$ contain within them all possible relative thicknesses of the three layers.

Figure 12 shows the numerically predicted contours of constant curvature $\kappa = \kappa_b$ (at which bifurcation occurs during large thermoelastic deformation) in a square plate of the Ni/Gradient/Al_2O_3 trilayer for arbitrary variations in the relative thicknesses of the three layers. Here the normalized curvature, $\hat{\kappa}_b = \kappa_b L_x^2/(h_1 + h_2)$ is used because this normalization holds for any L_x. It is seen that for thick multilayers with graded interfaces, vast changes in relative thicknesses of the layers promote only small changes in $\hat{\kappa}_b$ (about 10% for the conditions of the simulations described in Fig. 12). The maximum and minimum values of $\hat{\kappa}_b$ occur near the regions of $(\rho_h \approx 0.9, \rho_a < 0.15)$ and $(\rho_h \approx 0.3, \rho_a < 0.3)$, respectively. This results from the fact that bifurcation arises as a consequence of a geometric incompatibility.

The temperature change needed to cause bifurcation, ΔT_b, for the trilayer system, however, is more sensitive to compositional gradation. Figure 13 shows contours of constant temperature ΔT_b at which bifurcation occurs in the thermoelastic solution
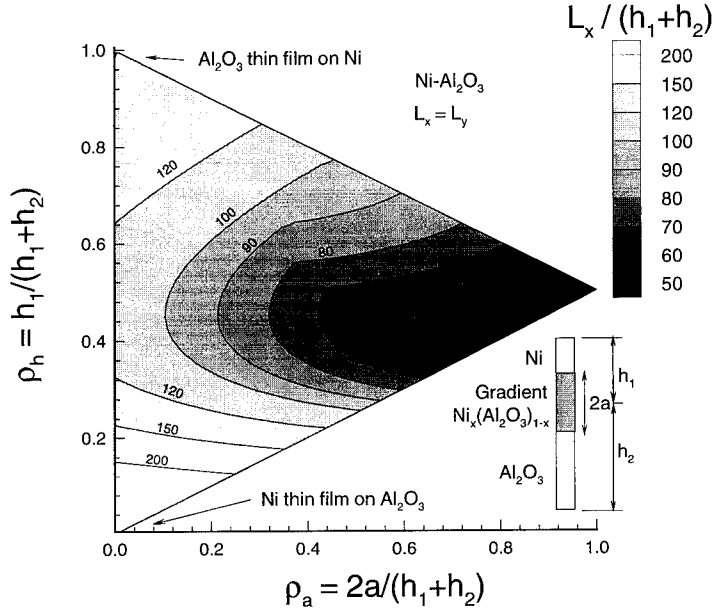
Fig. 14. Contours of constant critical aspect ratio of the plate, $L_x/(h_1 + h_2)$, for which the temperature of bifurcation predicted by the large deformation elasticity theory (Section 2.6) and the critical temperature for the onset of yielding as predicted by the small deformation elastoplasticity theory (Suresh et al., 1994) are equal. The triangle shape represents any material distribution of the tri-layered system, Ni/Gradient/ Al$_2$O$_3$.

for a wide range of relative thicknesses. Here the normalized bifurcation temperature, $\widehat{\Delta T_b} = \Delta T_b \Delta \alpha L_x^2/(h_1 + h_2)^2$, is plotted so that the indicated trends are valid for any L_x. For the conditions of the simulations, $\widehat{\Delta T_b}$ is the lowest for a Ni/Al$_2$O$_3$ bilayer of comparable layer thickness (with no graded interlayer). $\widehat{\Delta T_b}$ is increased by more than a factor of two if a gradient layer replaces the homogeneous Ni and Al$_2$O$_3$ (with $h_1 + h_2$ fixed). The maximum values of $\widehat{\Delta T_b}$ are seen near the corners of the triangular plot with (ρ_h, ρ_a) coordinates at (0,0) and (1,0)

We consider next the conditions governing the onset of plastic flow in the Ni/ Gradient/Al$_2$O$_3$ trilayer. For this purpose, we specifically seek those geometrical combinations of the three layers for which the temperature for the occurrence of bifurcation during large deformation, ΔT_b (which is predicted from the analytical formulation presented in Section 2.6), is equal to the temperature for the onset of plastic yielding, ΔT_1, which is the temperature for the onset of plastic flow during small deformation, as described in Giannakopoulos et al. (1995). Contours of constant $L_x/(h_1 + h_2)$ for which $\Delta T_b = \Delta T_1$ are plotted in Fig. 14. It is clearly evident that the geometry of the trilayer strongly influences the competition between instability and plastic flow. As the thickness of the graded layer, $2a$, increases (for a fixed total thickness of all layers), bifurcation occurs at a lower value of $L_x/(h_1 + h_2)$. For the Ni/ Al$_2$O$_3$ bilayer, especially near the limiting case of a Ni or Al$_2$O$_3$ thin film, the $L_x/(h_1 + h_2)$ ratio needed to cause bifurcation increases by nearly four times.
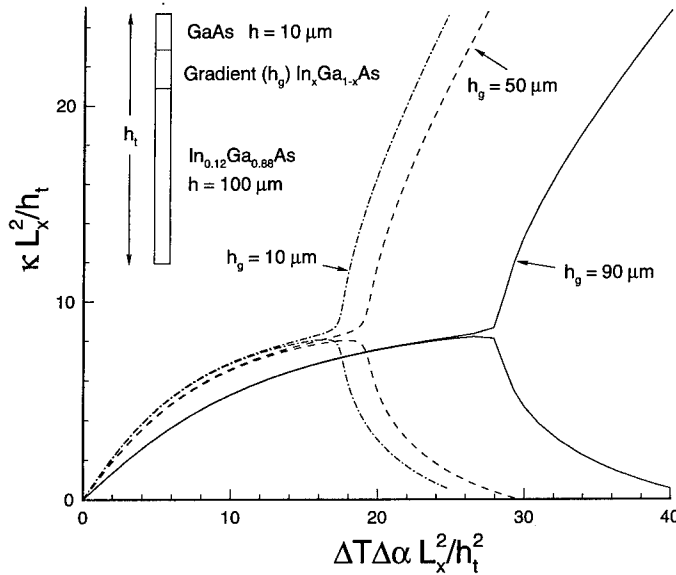
Fig. 15. FEM predictions of the normalized curvature as a function of the normalized temperature change for three different geometries of the tri-layered system, $In_{0.12}G_{0.88}As/Gradient/GaAs$. Three values of the thickness of the gradient are considered : 10, 50 and 90 μm.

5.2.   A graded layer between $In_{0.12}Ga_{0.88}As$ and GaAs thin films

Figure 15 shows the finite element predictions of the normalized curvature $\kappa L_x^2/h_t$ as a function of the normalized temperature change, $\Delta T \Delta \alpha L_x^2/h_t^2$ for the graded trilayer system : $In_{0.12}Ga_{0.88}As/Gradient/GaAs$. Here three different thickness levels of the graded layer are considered for fixed thicknesses of GaAs (10 μm) and $In_{0.12}Ga_{0.88}As$ (100 μm). These results are normalized such that they hold for any specific value of L_x; the finite element calculations were performed for a square plate with dimensions 30 mm × 30 mm.

Figure 15 indicates that increasing the gradient layer thickness causes a significant increase in the temperature for the onset of bifurcation. This increase is more pronounced for the higher thickness levels (i.e. from 50–90 μm). Increasing the gradient layer thickness also produces increased non-linearity in the curvature/temperature plot at a lower temperature level, and reduces the curvature in the pre-bifurcation regime. As with the results presented for Ni/Al_2O_3 and Si/Al, it is evident from Fig. 15 that compositional gradation does not suppress the occurrence of bifurcation.

6.   CONCLUSIONS

(1) In this work, closed form expressions have been derived for the deformation of a bilayer plate with isotropic elastic properties that is subjected to general anisotropic loading, (e.g. non-equibiaxial strain mismatch), within the context of small deformation elasticity theory. The deformation of the bilayer plate is fully characterized

by the ratio of the two thicknesses h_1/h_2, and two elastic mismatch parameters, which are the ratio of the biaxial moduli,

$$\frac{E_1(1-v_2)}{E_2(1-v_1)},$$

and the ratio of the shear moduli,

$$\frac{E_1(1+v_2)}{E_2(1+v_1)},$$

for the two layers. The principal curvatures, for a given strain mismatch between the layers, are independent only if the two layers have the same Poisson's ratio. In general, for a multi-layered material there is coupling between the two orthogonal (in-plane) curvatures if the Poisson ratio varies through the thickness (in the case of a non-equibiaxial strain mismatch). This coupling is quantified by means a parameters, v_κ (which is the ratio of curvatures measured along the two in-plane coordinate axes), as a function of the elastic constants and thicknesses of the two layers.

(2) The main advantage of the classical Stoney (1909) formula is that a direct link can be established between the curvature of a substrate and the stress in the thin-film (deposited on the substrate). In this approach, one assumes isotropic responses for the substrate and the thin film, isotropy of the strain mismatch, and a constant stress in the thin film. A knowledge of the origin or the magnitude of the strain mismatch for small deformation is not required. In this paper, we have presented a new general extension of the Stoney approach to any isotropic bilayered plate with arbitrary layer thicknesses or a trilayer with a graded interface (under anisotropic strain mismatch). With this extension, the measurement of the two principal curvatures and the orientation of the principal directions uniquely provide the stress field at any location through the thickness for small elastic deformation. This result has also been generalized for a three-layered plate which contains a compositionally graded layer inbetween two homogeneous layers. The analysis for this latter case requires a knowledge of the strain mismatch variation in the graded layer and the elastic property variation through the thickness.

(3) For small deformation, an elastic bilayer subject to temperature variations under generalized plane strain conditions exhibits a larger curvature than under a state of equal biaxial stress. Curvature evolution during thermoelastic small deformation under generalized plane strain also constitutes an upper bound for all possible stress states (small or large deformation with small strains) of bilayer plates.

(4) For large thin plates, the small deformation theory can deviate significantly from the exact solution when the deflection of the edge of the plate is of the same order as the thickness. Analytical formulations can provide accurate descriptions of curvature in large deformation. It is shown that as a general rule of thumb, the geometric non-linearity of the curvature with respect to the strain mismatch occurs for a critical size of the plate L larger than $\sqrt{Rh_t}$, where h_t is the thickness and R is the radius of curvature. This result is not sensitive to the stress distribution through the thickness since the phenomenon is mainly driven by a geometric incompatibility

introduced by the curvature. The non-linearity can result in a bifurcation in the solution for curvature evolution in some specific cases where the geometry of the plate has a high symmetry or the material properties have certain non-isotropic variations (e.g. square, equilateral triangle, circle shapes of the plate for isotropic layered materials, and asymmetric distribution of properties for orthotropic materials). For $L > 6\sqrt{Rh_t}$, the solution of the generalized plane strain problem gives a good approximation for the curvature in the longer direction of the plate.

(5) Thermoelastic bending of bilayer plates with in-plane thermal and elastic isotropy produces a unique spherical curvature during small deformation. For certain geometries (e.g. square shape of the layered plate), a bifurcation occurs in the solution for curvature. The post-bifurcation equilibrium shapes during large elastic deformation of the layered plate are ellipsoidal (or in the limiting case, cylindrical), with a larger and a smaller principal curvature. The occurrence of such bifurcation, however, is sensitive to the in-plane dimensions (specifically, the length to width ratio) of the bilayer. The plate theory predicts that the bifurcation can be eliminated, in some cases, by simply changing the geometry from a square plate to a rectangular plate with slightly different side lengths ($L_x \neq L_y$).

(6) The stable configuration for small elastic deformation in orthotropic bilayer composite laminates is a saddle shape, which upon bifurcation transforms into two different cylindrical shapes. Small variations in the relative thicknesses of the layers can completely suppress the existence of such bifurcation; they may instead produce a gradual transition from an equilibrium saddle shape at small deformation to an equilibrium cylindrical shape at large deformation.

(7) The temperature at which bifurcation occurs, the curvature just prior to the onset of bifurcation, and the saturation curvature corresponding to perfect plastic yielding of the entire metal layer in a bilayer are strongly influenced by the length to thickness ratio, $L_x/(h_1 + h_2)$, during large deformation. However, the temperature at which plastic yielding initiates in the metal is relatively insensitive to $L_x/(h_1 + h_2)$. This temperature is nearly the same as that predicted from the small deformation elastoplastic theory (Suresh *et al.*, 1994). The magnitude of the saturation curvature, however, is sensitive to the extent of large deformation and, hence to $L_x/(h_1 + h_2)$. The maximum value of curvature attainable upon complete yielding of the metal layer in a metal/ceramic bilayer system is the same for small deformation biaxial stress and generalized plane strain. This limiting curvature is also the same during large deformation (small strains).

(8) For thin films on substrates, increasing the metal film thickness (for a fixed substrate thickness) can enhance the propensity for non-linear elastic deformation and bifurcation at lower ΔT. Beyond bifurcation, strain hardening in the yielded film induces an increase in the anisotropy between curvatures along the in-plane principal axes (i.e. the shape of the film/substrate system is made more ellipsoidal).

(9) The presence of a graded layer inbetween two homogeneous layers can significantly change the in-plane stresses due to thermal strain mismatch and delay the onset of plastic flow. However, for these geometries, bifurcation is not minimized significantly or erased by compositional gradation because curvature evolution is not altered markedly by the graded layer. Larger deformations are accommodated by graded materials before failure or yielding since the stresses are lower.

ACKNOWLEDGEMENTS

REFERENCES

ABAQUS (1994) ABAQUS, Version 5.3, General Purpose Finite-Element program. Providence, RI.

Bogy, D. B. (1971) Two edge-bonded elastic wedges of different materials and wedge angles under surface tractions. *ASME, J. Appl. Mech.* **38**, 377–386.

Drake, J. T., Williamson, R. L. and Rabin, B. H. (1993) Finite-element analysis of thermal residual-stresses at graded ceramic-metal interfaces. 2. Interface optimisation for residual-stress reduction. *J. Appl. Phys.* **74**, 1321–1336.

Dundurs, J. (1969) Edge-bonded dissimilar orthogonal elastic wedges. *ASME, J. Appl. Mech.* **36**, 650–652.

Erdogan, F., Kaya, A. C. and Joseph, P. F. (1991) The crack problem in bonded non-homogeneous materials. *Trans. ASME* **58**, 410–418.

Fahnline, B. D., Masters, C. B. and Salamon, N. J. (1991). *J. Vac. Sci. Technol.* **A9**, 2483–2487.

Finot, M. and Suresh, S. (1994) MultiTherm, Software for Thermomechanical Analysis of Multilayered and Graded materials, Version 1.3. Copyright MIT, Cambridge, MA.

Finot, M., Suresh, S., Bull, C. and Sampath, S. (1996) Curvature changes during thermal cycling of a compositionally graded Ni–Al$_2$O$_3$ multi-layered material. *Mater. Sci. Engng A* **205**, 59–71.

Fitzgerald, E. A., Xie, Y.-H., Monroe, D., Silverman, P. J., Kuo, J.-M., Kortan, A. R., Thiel, F. A., Weir, B. E. and Feldman, L. C. (1992) Relaxed Ge$_x$Si$_{l-x}$ structures for III–V integration with Si and high mobility two-dimensional electron gases in Si and high mobility two-dimensional electron gases in Si. *J. Vac. Sci. Technol.* **B10**, 1807–1819.

Freund, L. B. (1993) The stress distribution and curvature of a general compositionally graded semiconductor layer. *J. Crystal Growth* **132**, 341–344.

Freund, L. B. (1996) Some elementary connections between curvature and mismatch strain in compositionally graded thin films. *J. Mech. Phys. Solids* **44**, 723–736.

Giannakopoulos, A. E., Suresh, S., Finot, M. and Olsson, M. (1995) Elastoplastic analysis of thermal cycling: Layered materials with compositional gradients. *Acta Metall. Mater.* **43**, 1335–1354.

Giannakopoulos, A. E. and Suresh, S. (1995) Unpublished results, MIT, Cambridge, MA.

Harper, B. D. and Wu, C. P. (1990) A geometrically nonlinear model for predicting the intrinsic film stress by the bending–plate method. *Int. J. Sol. Struct.* **25**, 511–525.

Hill, R. (1950) *The Mathematical Theory of Plasticity*. Clarendon Press, Oxford, U.K.

Hyer, M. W. (1981a) Calculation of the room-temperature shapes of unsymmetric laminates. *J. Comp. Mater.* **15**, 296–310.

Hyer, M. W. (1981b) Some observation on the curved shape of thin unsymmetric laminates. *J. Comp. Mater.* **15**, 175–194.

Hyer, M. W. (1982) The room-temperature shape of four-layer unsymmetric cross-ply laminates. *J. Comp. Mater.* **16**, 318–340.

Kroupa, F., Knesl, Z. and Valach, J. (1993) Residual stresses in graded thick coatings. *Acta Technica CSAV* **38**, 29–74.

Masters, C. B. and Salamon, N. J. (1993) Geometrically nonlinear stress-deflection relations for thin film/substrate systems. *Int. J. Engng Sci.* **31**, 915–925.

Masters, C. B. and Salamon, N. J. (1994) Geometrically nonlinear stress-deflection relations for thin film/substrate systems with a finite element comparison. *ASME, J. Appl. Mech.* **61**, 872–878.

Nix, W. D. (1989) mechanical properties of thin films. *Metall. Trans. A* **20A**, 2217–2245.

Panov, D. V. (1947) On the stability of a bimetallic membrane on heating. *Prikl. Mat. i Mekh.* **11**, 603–610.

Salamon, N. J. and Masters, C. B. (1995) Bifurcation in isotropic thin film/substrate plates. *Int. J. Solids Structures* **32**, 473–481.

Shen, Y.-L. and Suresh, S. (1995a) Elastoplastic deformation of multilayered materials during thermal cycling. *J. Mater. Res.* **10**, 1200–1215.

Shen, Y.-L. and Suresh, S. (1995b) thermal cycling and stress relaxation response of Si–Al and Si–Al–SiO$_2$ layered thin films. *Acta Metall. Mater.* **43**, 3915–3926.

Stoney, G. G. (1909) The tension of metallic films deposited by electrolysis. *Proc. R. Soc. Lond. Ser. A* **82**, 172–175.

Suresh, S., Giannakopoulos, A. E. and Olsson, M. (1994) Elastoplastic analysis of thermal cycling: layered materials with sharp interfaces. *J. Mech. Phys. Solids* **42**, 979–1018.

Timoshenko, S. and Woinowsky-Krieger, S. (1959) *Theory of Plates and Shells.* McGraw-Hill, New York.

Tsai, S. W. (1988) *Composites Design*, 4th edition. Think Composites, Dayton, OH.

von Kármán, T. (1910) *Encyklopedie der Mathematischen Wissenschaften*, Vol. 4, U. Berlin.

Williamson, R. L., Rabin, B. H. and Drake, J. T. (1993) Finite-element analysis of thermal residual-stresses at graded ceramic-metal interfaces. 1. Model description and geometric effects. *J. Appl. Phys.* **74**, 1310–1320.

Wittrick, W. H. (1953) Stability of a bimetallic disk. *Quart. J. Mech. Appl. Math.* **6**, Part I, 15–26.

APPENDIX

The stress/curvature for the graded trilayer geometry described in Section 2.4 can be given in a simple way in terms of the three dimensionless parameters

$$\rho = \frac{h_1}{h_2}, \quad \hat{a} = \frac{a}{h_2}, \quad \hat{E}_{\text{Bi}} = \frac{E_1(1-\nu_2)}{E_2(1-\nu_1)}, \tag{A.1}$$

where a is equal to half of the thickness of the graded layer as shown in Fig. 1(b).

The mean stress field through the thickness is

$$\sigma_1^m = E_{\text{Bi}}(F + \Delta F + z\lambda^{-1})\kappa^m \quad \text{in layer 1,}$$

$$\sigma_g^m = E_{\text{Bi}}(z)\left(F + \Delta F\frac{t}{a} + z\lambda^{-1}\right)\kappa^m \quad \text{in the graded layer,}$$

$$\sigma_2^m = E_{\text{Bi}}(F - \Delta F + z\lambda^{-1})\kappa^m \quad \text{in layer 2,} \tag{A.2}$$

where

$$F = \frac{3\rho}{\beta}(-3 + 8\hat{a} - 6\hat{a}^2 + \hat{a}^4 + \hat{E}_{\text{Bi}}(-8\hat{a} + 12\rho - 12\rho^3 + 8\hat{a}\rho^3) + \hat{E}_{\text{Bi}}^2(-\hat{a}^4 + 6\hat{a}^2\rho^2 - 8\hat{a}\rho^3 + 3\rho^4)), \tag{A3}$$

$$\Delta F = \frac{3\rho}{\beta}(-3-6\hat{a}^2+\hat{a}^4+\hat{E}_{\text{Bi}}(6\hat{a}^2-2\hat{a}^4-12\rho-18\rho^2+6\hat{a}^2\rho^2-12\rho^3)+\hat{E}_{\text{Bi}}^2(\hat{a}^4-6\hat{a}^2\rho^2-3\rho^4)),$$

$$(A4)$$

and

$$\beta = 2(1+\rho)^3(3\hat{a}-\hat{a}^3+\hat{E}_{\text{Bi}}(-3\hat{a}-3\hat{a}^2+2\hat{a}^3+9\rho-3\hat{a}^2\rho+9\rho^2-3\hat{a}\rho^2)+\hat{E}_{\text{Bi}}^2(-\hat{a}^3+3\hat{a}\rho^2)).$$

$$(A.5)$$

The shear stress resulting from a twist curvature $\hat{\kappa}_{xy}$ is given by the same expressions by replacing the biaxial modulus E_{bi} by the shear modulus and the ratio $\hat{E}_{\text{Bi}}$ by $\hat{\mu}$.

Pergamon

PII S0022–5096(96)00008–7

SOME ELEMENTARY CONNECTIONS BETWEEN CURVATURE AND MISMATCH STRAIN IN COMPOSITIONALLY GRADED THIN FILMS

L. B. FREUND

Division of Engineering, Brown University, Providence, RI 02912, U.S.A.

ABSTRACT

A thin film structure with through-the-thickness variation of properties and/or mismatch strain is considered. The relationship of the overall curvature of the film to the variation of properties and mismatch strain is reviewed. It is shown that, if the material properties are known, the mismatch strain distribution in the film can be expressed in terms of the dependence of curvature on film thickness. In addition, the case of film growth under conditions for which the mismatch strain of deposited material depends on the local strain conditions of the growth surface is considered. By means of an illustration, it is shown that the final state of strain within a free film following growth depends on the constraint conditions that were imposed on the film during its growth.

INTRODUCTION

Thin film structures with through-the-thickness variations in composition and/or mismatch strain are in wide use in microelectronics and other applications. In thin metal films, the grain structure of the material varies as the film grows, from random at the nucleation surface to textured columnar for substantial amounts of growth. In epitaxial strained layer semiconductor materials, a layer with continuously graded composition can provide a transition in lattice parameter from one material to another in a way that minimizes the tendency for formation of dislocations or other defects. Grading can also suppress the tendency for island formation during growth in material systems with large mismatch in lattice parameter. In general, the variations in composition may be abrupt or graduated, monotonic or periodic. The internal (residual) stress associated with this compositional variation provides a driving force for various failure modes in these material systems, so methods for measuring this stress and for controlling its effects are of interest. Also, characterization of the mechanical state of layered material systems is frequently based on measurements made by means of the wafer curvature method, so knowledge of the connections between curvature and mismatch strain are central to interpretation of data (Flinn, 1989).

The physical system being considered here is a thin, plate-like structure. The total thickness h is much less than the lateral dimensions, and the details of the mechanical fields very near the lateral edges are ignored. The remote lateral edges of the layer are

free of applied loading, in the sense that the resultant bending moment, twisting moment and extensional force all vanish. An elastic mismatch strain which varies in a general way through-the-thickness direction of the film is present. This strain may arise from thermal expansion mismatch, epitaxy with lattice parameter mismatch, chemical reaction with volume and/or phase change, or microstructural evolution. the mismatch strain can have any piecewise continuous variation, so either abrupt interfaces with jumps in mismatch strain, smoothly graded mismatch strain distributions, or any combination of the two, can be taken into account. The properties of the material, namely the elastic constants and coefficient of thermal expansion, can vary across the thickness. Temperature may also vary across the thickness in a general way, but this is assumed to be reflected implicitly in the mismatch strain. Mechanical fields are referred to a rectangular coordinate system oriented as shown in Fig. 1, so that the z direction is normal to the plane of the layer with $z = 0$ lying in the bottom face of the layer. The conditions imposed on mechanical fields by equilibrium, material behavior and compatibility are considered to obtain elementary formulas for the relationship between curvature and mismatch strain.

   Two other issues are addressed within this elementary framework. It is well-known that the distribution of mismatch strain through the thickness of such a film at its final thickness cannot be determined from knowledge of the final curvature of the film. However, if the distribution of material properties across the layer is known, it can be shown that the mismatch strain distribution can be expressed in terms of curvature as a function of film thickness as the thickness increases. Thus, if curvature can be measured continuously during film growth, this measurement can provide information on the distribution of mismatch strain. Such observations are currently being carried out by Spaepen and coworkers (1996).

   The second issue concerns film growth in cases when the development of mismatch strain depends on local strain conditions on the growth surface. If this is the case, then the mismatch strain distribution that evolves may depend on the constraint
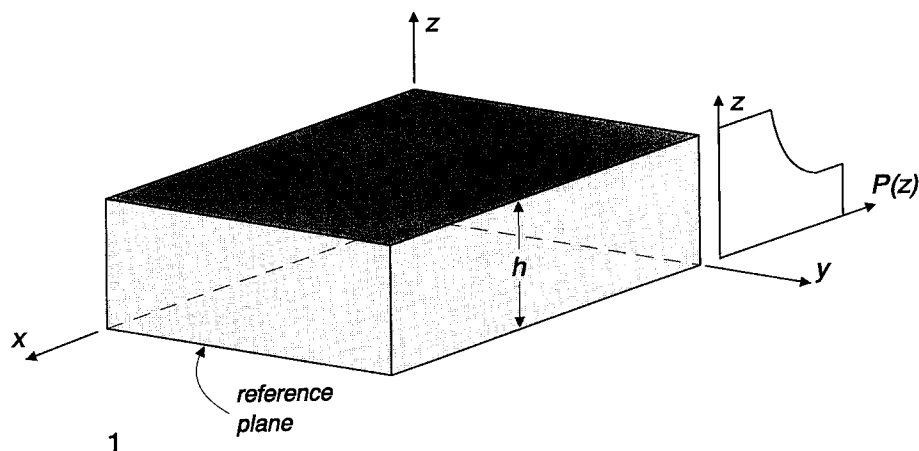

Fig. 1. Orientation of the rectangular coordinate system with respect to the layer, which has total thickness h. The face $z = 0$ is the reference plane for mismatch strain. $P(z)$ represents the variation of any system parameter across the thickness.

conditions on the film during its growth. The idea is illustrated for film growth with a local relative strain deposition criterion.

GENERAL CURVATURE EXPRESSIONS

Both the top surface $z = h$ and the bottom surface $z = 0$ of the layer are free of applied traction. Under the stated conditions, the layer is invariant under translation in either the x or y direction. It follows that all fields are independent of x and y, and that three stress components vanish identically, namely

$$\sigma_{zz} = \sigma_{xz} = \sigma_{yz} = 0. \tag{1}$$

If the film is cut by any plane normal to the layer surface, then the absence of any externally applied loading implies that the net force, bending moment and twisting moment due to the traction on that cut must be zero, that is

$$\int_0^h \sigma_{ij}(z)\,\mathrm{d}z = 0, \quad \int_0^h z\sigma_{ij}(z)\,\mathrm{d}z = 0 \quad \text{for} \quad i,j = x,y. \tag{2}$$

The mismatch strain is defined in the following way. The bottom surface $z = 0$ is identified as the reference plane for mismatch strain. The mismatch strain on any intermediate plane at z is then the elastic strain which must be imposed to render it compatible with the mismatch strain; the in-plane components of mismatch strain are denoted by $\varepsilon_{xx}^{(m)}(z)$, $\varepsilon_{xy}^{(m)}(z)$ and $\varepsilon_{yy}^{(m)}(z)$. For example, if the mismatch strain is due to epitaxy and the mean lattice parameter in a certain direction varies as $a(z)$, then the mismatch extensional strain in that direction at z is $-[a(z) - a(0)]/a(z)$. It is noted in passing that the strain defined in this way is equal but opposite to Eshelby's stress-free transformation strain (Eshelby, 1957). The remaining components of the mismatch strain array $\varepsilon_{ij}^{(m)}$ are implied by (1).

The total strain in the film is not compatible, in general. However, the incompatibility is represented by $\varepsilon_{ij}^{(m)}(z)$. Thus, the total strain can be written as the sum of the incompatible part plus a compatible part,

$$\varepsilon_{ij}(z) = \varepsilon_{ij}^{(m)}(z) + \varepsilon_{ij}^{(c)}(z). \tag{3}$$

The second term on the right side of (3) is subject to the compatibility equations which, in this case, reduce to the three uncoupled equations

$$\frac{\partial^2 \varepsilon_{ij}^{(c)}}{\partial z^2}(z) = 0, \quad i,j = x,y. \tag{4}$$

Thus, the condition imposed on the strain by compatibility is that

$$\varepsilon_{ij}^{(c)}(z) = -z\kappa_{ij} + \varepsilon_{ij}^{(r)}, \quad i,j = x,y. \tag{5}$$

The quantity $\varepsilon_{ij}^{(r)}$ is the strain of the reference layer $z = 0$, κ_{xx} is the curvature of a reference plane coordinate line in the x direction, κ_{yy} is the curvature of a reference plane coordinate line in the y direction, and $\pm\kappa_{xy}$ is the curvature of the line $x = \pm y$

on the reference plane, resulting in zero mean curvature of that plane for this component of deformation.

Finally, the response of the material is linearly elastic

$$\sigma_{ij}(z) = C_{ijkl}(z)\varepsilon_{kl}(z). \tag{6}$$

Although the results reported here can be obtained for an anisotropic material of arbitrary orientation, only the relatively simple and transparent results for the case of elastic isotropy with constants E, v are included.

If stress is now expressed in terms of the mismatch strain and the geometrical parameters κ_{ij} and $\varepsilon_{ij}^{(r)}$, then the result of imposing the equilibrium equations (2) is a system of linear equations for the geometrical parameters. For the case of uniform Poisson ratio v but general variation in modulus $E(z)$, the solution is

$$\kappa_{ij}(h) = \frac{I^{(1)}J_{ij}^{(0)} - I^{(0)}J_{ij}^{(1)}}{I^{(1)2} - I^{(0)}I^{(2)}}, \quad \varepsilon_{ij}^{(r)}(h) = \frac{I^{(2)}J_{ij}^{(0)} - I^{(1)}J_{ij}^{(1)}}{I^{(1)2} - I^{(0)}I^{(2)}}, \quad i,j = x,y, \tag{7}$$

where

$$I^{(k)}(h) = \int_0^h z^k \bar{E}(z)\,dz, \quad J_{ij}^{(k)}(h) = \int_0^h z^k \bar{E}(z)\varepsilon_{ij}^{(m)}(z)\,dz, \tag{8}$$

$$\bar{E}(z) = \begin{cases} E(z)/(1-v^2) & i = j \\ E(z)/2(1+v) & i \neq j \end{cases} \tag{9}$$

Thus, given the mismatch strain and the material properties, these formulas provide expressions for the curvature and strain of the reference plane within the film. The curvature or strain of any other plane can be found from these. Similar formulas have been reported recently by Freund (1993) and by Kroupa (1993).

The formulas (7) provide a generalization of some of the well-known special results for problems in this class, such as plate bending with a temperature gradient (Boley and Weiner, 1960) or the Stoney formula for curvature of a substrate due to a relatively thin strained layer on its surface (Stoney, 1909). The Stoney formula is obtained on the assumption that the thickness of the uniformly strained layer, say h_2, is infinitesimally small compared to the thickness of the substrate, say h_1. It is a straightforward matter to determine the correction to the Stoney formula when this condition is relaxed somewhat. For a uniform equi-biaxial mismatch strain $\varepsilon^{(m)}$ in a layer of thickness h_2 and biaxial modulus $M_2 = E_2/(1 - v_2)$ bonded to a substrate of thickness h_1 and biaxial modulus $M_1 = E_1/(1 - v_1)$, the distance of the neutral plane from the reference plane is found to be

$$\bar{z} = \frac{h_1}{3} + \frac{h_1}{6}\frac{h_2}{h_1} \tag{10}$$

and the curvature of the neutral plane is

$$\kappa = \frac{6\varepsilon^{(m)}}{h_1}\frac{h_2}{h_1}\frac{M_2}{M_1} + \frac{6\varepsilon^{(m)}}{h_1}\left(\frac{h_2}{h_1}\right)^2\frac{M_2(M_1 - 4M_2)}{M_1^2}. \tag{11}$$

For equal biaxial moduli $M_1 = M_2$, the ratio of the second term to the first term in the curvature result has magnitude $3h_2/h_1$. Thus, when $h_2/h_1 = 0.1$, neglect of the second term results in a 30% error in the estimate of curvature based on the Stoney formula.

A second illustration of the use of the general formulas is provided by the category of bimaterial systems with a region of linear compositional gradation of thickness h_2 between homogeneous regions of thickness h_1 for material 1 and thickness h_3 for material 3. The composite structure is considered at a temperature differing from the reference temperature by the spatially uniform ΔT. All other system parameters vary with z as

$$
P(z) = \begin{cases} P_1 & \text{for } 0 < z < h_1 \\[2mm] P_1\left(\dfrac{h_1+h_2-z}{h_2}\right)+P_3\left(\dfrac{z-h_1}{h_2}\right) & \text{for } h_1 < z < h_1+h_2 \\[2mm] P_3 & \text{for } h_1+h_2 < z < h_1+h_2+h_3 \end{cases} \tag{12}
$$

where P_1 and P_3 are constants. Here again, $P(z)$ represents any system parameter (modulus, thermal expansion coefficient, epitaxial mismatch strain). A common special case occurs when the thickness h_2 of the intermediate region is zero.

Under these circumstances, the integrals appearing in (8) are readily evaluated to yield

$$2I_0 = M_1(2h_1+h_2)+M_3(h_2+2h_3),$$

$$6I_1 = M_1(3h_1^2+3h_1h_2+h_2^2)+M_3(3h_1h_2+2h_2^2+h_1h_3+h_2h_3+3h_3^2),$$

$$\begin{aligned}12I_2 = {}& M_1(4h_1^2+6h_1^2h_2+4h_1h_2^2+h_2^3)+M_3(6h_1^2h_2+8h_1h_2^2+3h_2^3 \\ &+12h_1^2h_3+24h_1h_2h_3+12h_2^2h_3+12h_1h_3^2+12h_2h_3^2+4h_3^3),\end{aligned}$$

$$\begin{aligned}6J_0 = {}& M_1[-\varepsilon_3^{(m)}h_2+\Delta T(12\alpha_1h_1+4\alpha_1h_2+\alpha_3h_2)] \\ &+M_3[-2\varepsilon_3^{(m)}(h_2+2h_3)+\Delta T(\alpha_1h_2+2\alpha_3h_2+\alpha_3h_3)],\end{aligned}$$

$$\begin{aligned}12J_1 = {}& M_1[-\varepsilon_3^{(m)}h_2(2h_1+h_2)+\Delta T(6\alpha_1h_1^2+4\alpha_1h_1h_2+2\alpha_3h_1h_2-\alpha_1h_2^2+\alpha_3h_2^2)] \\ &+M_3[-\varepsilon_3^{(m)}(4h_1h_2+3h_2^2+12h_1h_3+12h_2h_3+6h_3^2) \\ &+\Delta T(2\alpha_1h_1h_2+4\alpha_3h_1h_2+\alpha_1h_2^2+3\alpha_3h_2^2+12\alpha_3h_1h_3+12\alpha_3h_2h_3+6\alpha_3h_3^2)],\end{aligned}$$

where the association of subscripts with the three regions is obvious, and $\varepsilon_1^{(m)} = 0$. These simple algebraic expressions are exact. As an illustration, these formulas have been applied to the case of a GaAs/In$_x$Ga$_{1-x}$As/In$_{0.12}$Ga$_{0.88}$As ternary epitaxial structure, using the material parameters given by Nakajima (1991). The system is illustrated in Fig. 2 and the stress distribution is shown in Fig. 3. The strong influence of the thickness of the intermediate graded layer on the magnitude of the stress in the top layer is evident from this figure. If the results obtained by the above formulas are compared to the computational results of Nakajima (1992), it is observed that the stresses computed here exceed those reported earlier by a factor of $1/(1-v)$ because
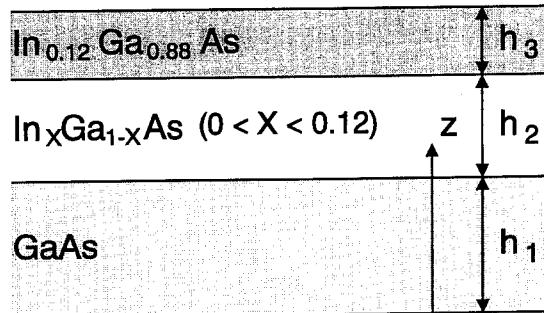
L. B. FREUND

Fig. 2. A compositionally graded crystalline layer with a homogeneous GaAs portion of thickness h_1, a linearly graded portion of thickness h_2, and a homogeneous $In_{0.12}Ga_{0.88}As$ portion of thickness h_3.

this factor was erroneously omitted from the elastic stress–strain relation for biaxial states of stress [see equation (3) in Nakajima (1992), for example].

DEPENDENCE OF MISFIT STRAIN ON CURVATURE HISTORY

In this section, it is demonstrated that the misfit strain distribution through the thickness of a strained layer can be expressed in terms of the dependence of curvature on film thickness as the film is formed. This is done under the conditions that the material properties are known and that the film formation process is time independent.
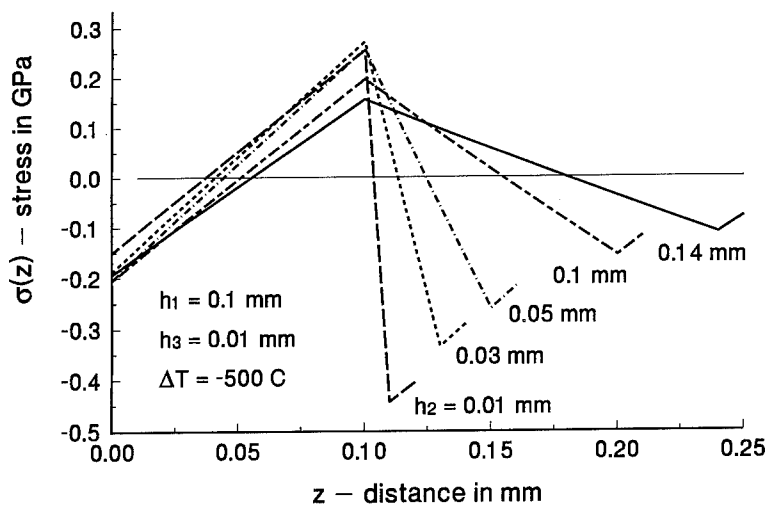
Fig. 3. Stress distribution across the thickness of the layer depicted in Fig. 2 due to the epitaxial mismatch plus a temperature change of $\Delta T = -500°C$ for five values of the thickness of the intermediate graded portion of the composite film.

For purposes of illustration, the simple situation with

$$\varepsilon_{xx}^{(m)} = \varepsilon_{yy}^{(m)} = \varepsilon^{(m)}, \quad \varepsilon_{xy}^{(m)} = 0 \tag{13}$$

and

$$\bar{E}(z) = \text{constant} \tag{14}$$

is considered. In this case, the curvature expression in (7) reduces to

$$\kappa(h) = -\frac{6}{h^2} \int_0^h \varepsilon^{(m)}(z)\,dz + \frac{12}{h^3} \int_0^h z\varepsilon^{(m)}(z)\,dz. \tag{15}$$

This expression can be inverted to solve for $\varepsilon^{(m)}(z)$ by first multiplying through by h^3 and then differentiating with respect to h several times. Finally, an integration is required to obtain the desired result. A constant of integration arises in this step, but it can be shown to be zero by noting that $\kappa(h)$ is continuous in h if $\varepsilon^{(m)}$ is bounded, so that $\kappa(h_1) = 0$ for arbitrary $h_1 \geqslant 0$ if $\varepsilon^{(m)}(z) = 0$ for $0 \leqslant z \leqslant h_1$. The result is

$$\varepsilon^{(m)}(h) = \tfrac{2}{3}h\kappa(h) + \tfrac{1}{6}h^2\kappa'(h) + \frac{1}{3}\int_0^h \kappa(z)\,dz. \tag{16}$$

This is the desired expression for the strain distribution in terms of the history of the curvature of the film. For the case when $\varepsilon^{(m)}(z) = 0$ for $0 \leqslant z \leqslant h_1$, several strain–curvature pairs are shown in Fig. 4. This analysis, which can also be applied for unequal biaxial mismatch strains or other cases, seems to provide a generalization of some residual stress formulas given in Baldwin *et al.* (1955).

MISMATCH STRAIN DEPENDING ON LOCAL DEPOSITION CONDITIONS

Suppose that the process of growth of a thin film takes place by successive addition of infinitesimally thin layers of material to the growth surface of the film to increase its thickness. The magnitude of the local mismatch strain is determined by the physics of the attachment process. For example, if the materials are single crystals and the attachment process is epitaxial, then the mismatch strain is determined by the relative mean lattice parameters, independent of other factors, including the state of strain of the growth surface. In contrast, consider a growth process whereby a thin layer is deposited as a melt. Due to the loss of heat, it subsequently solidifies with no residual stress. Then, due to further cooling and/or shrinkage a mismatch strain with respect to the original deposition surface develops. Under such conditions, the magnitude of the mismatch depends on the state of strain of the deposition surface prior to addition of the layer. The purpose in this section is to derive a differential equation for the mismatch strain as a function of position through the thickness for such a situation. Again, attention is limited to the simplest case of equi-biaxial extensional mismatch strain.

L. B. FREUND

Suppose that an unstrained substrate layer with thickness h_1 is clamped, and additional material is added layer-by-layer onto its surface in the manner described above. If the clamping prevents both bending and extension, then each layer is added
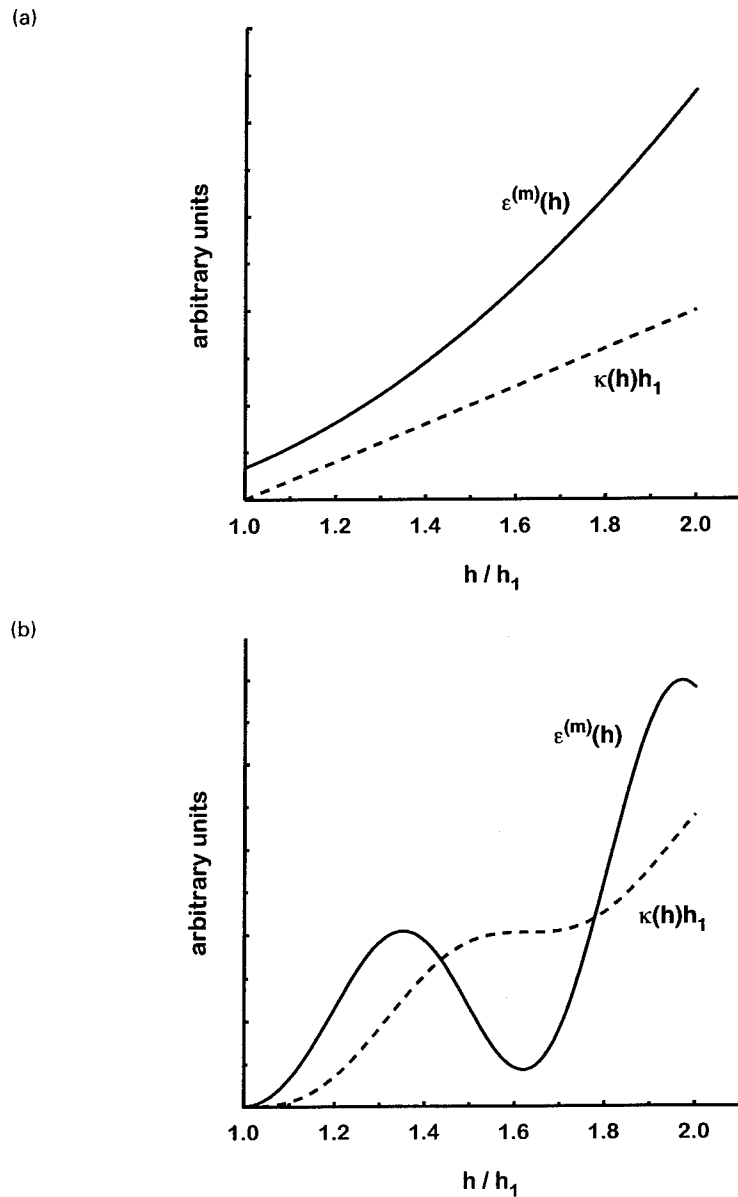
(a)

(b)

Fig. 4. Examples of curvature–mismatch strain pairs according to (16). (a) Curvature increasing linearly, (b) curvature increasing with oscillations, and (c) curvature increasing to a plateau level.
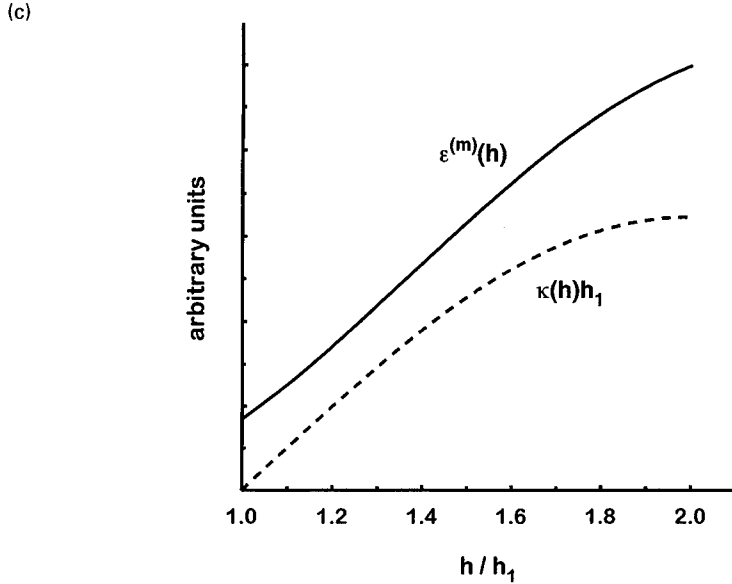
(c)

Fig. 4. (Continued).

under identical conditions and its mismatch strain is some constant, say

$$\varepsilon^{(m)}(z) = \begin{cases} 0, & 0 \leqslant z < h_1 \\ \varepsilon_*, & h_1 \leqslant z < h \end{cases}.$$ (17)

If the film is then released at some final thickness h, it will take on the curvature given by (7), namely

$$\kappa(h) = \frac{6}{h_1} \frac{h_1^2}{h^2}\left(1 - \frac{h_1}{h}\right).$$ (18)

The uniform strain distribution and the dependence of curvature on total film thickness for this case are shown in Figs 5 and 6, respectively, in the graphs labeled "clamped". The complete strain distribution following relaxation of the clamping constraint is given for five values of final thickness in Fig. 7.

Now, instead of the substrate being clamped, suppose that the film is free from constraints. The first strained lamina is added with mismatch strain ε_*. This induces slight bending and extension of the whole film, however, so that the conditions on the growth surface are modified for addition of the next lamina. If the mismatch strain is ε_* with respect to the surface on which it grows that it must satisfy the condition

$$\varepsilon^{(m)}(h) = \varepsilon_* + \kappa(h)h - \varepsilon^{(r)}(h),$$ (19)

where $\kappa(h)$ and $\varepsilon^{(r)}(h)$ are given in terms of $\varepsilon^{(m)}(z)$ in (7). If material properties are uniform through the entire thickness of the film, this condition reduces to
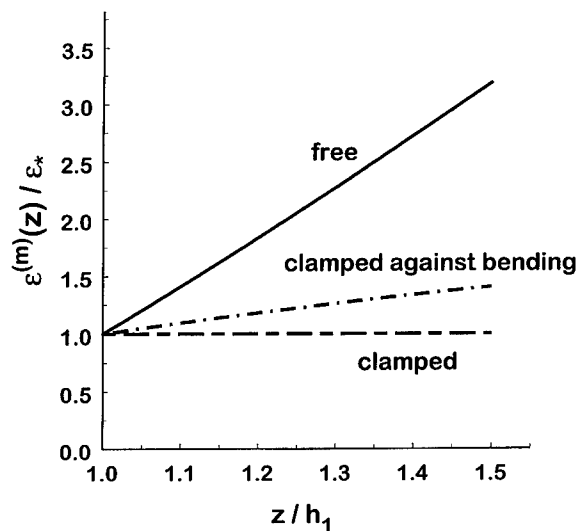
L. B. FREUND

Fig. 5. Mismatch strain distribution in the film for several possible constraint conditions during growth
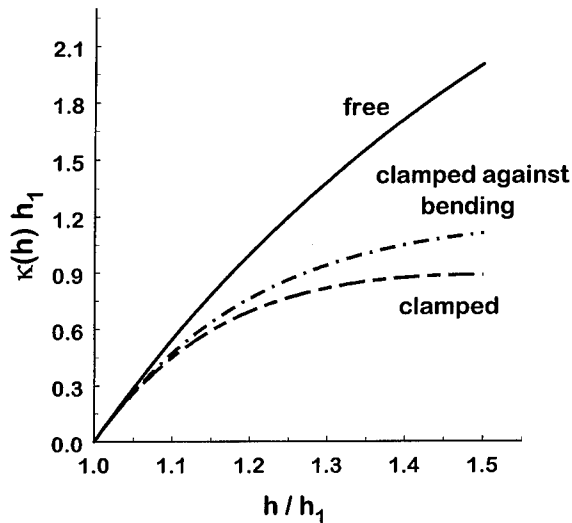according to a local strain growth condition.

Fig. 6. Curvature versus film thickness for several possible constraint conditions during growth according
to a local strain growth condition, corresponding to mismatch strain in Fig. 5.

$$\varepsilon^{(m)}(h) - \varepsilon_* + \frac{2}{h}\int_0^h \varepsilon^{(m)}(z)\,\mathrm{d}z - \frac{6}{h^2}\int_0^h z\varepsilon^{(m)}(z)\,\mathrm{d}z = 0. \qquad (20)$$

Multiplication by h^2 and differentiation with respect to h leads to the ordinary differential equation
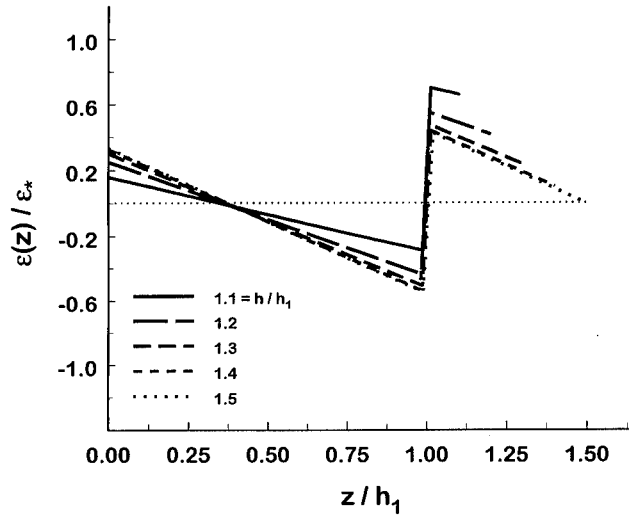
Fig. 7. Distribution of total elastic strain in the film for growth according to a local strain criterion under clamped conditions, followed by release of the constraint after growth, for five values of film thickness.

$$\frac{d^2 \varepsilon^{(m)}}{dh^2}(h) = \frac{2\varepsilon_*}{h^2}. \tag{21}$$

An obvious boundary condition on the strain distribution is that

$$\varepsilon^{(m)}(h_1) = \varepsilon_*. \tag{22}$$

A second boundary condition

$$\frac{d\varepsilon^{(m)}}{dh}(h_1) = \frac{4\varepsilon_*}{h_1} \tag{23}$$

follows from the expression obtained by differentiating (21) once with respect to h, and evaluating the result at $h = h_1$. Integration of (21) subject to these conditions yields the solution

$$\varepsilon^{(m)}(z) = \begin{cases} 0, & 0 \leqslant z < h_1 \\ -2\varepsilon_* \ln \dfrac{z}{h_1} + \varepsilon_*\left(6\dfrac{z}{h_1} - 5\right), & h_1 \leqslant z \leqslant h \end{cases}. \tag{24}$$

This expression gives the variation of mismatch strain due to the changing mechanical conditions on the growth surface. The distribution is shown as the curve labeled "free" in Fig. 5. As is evident from the equation itself, the distribution is nearly linear in z with a fairly large slope. Thus, the mismatch strain can differ significantly from its initial value, even for quite a thin film on an unstrained substrate. For the particular case when the added layer is thin compared to the substrate, that is, when $h - h_1 \ll h_1$, the mismatch strain varies linearly according to
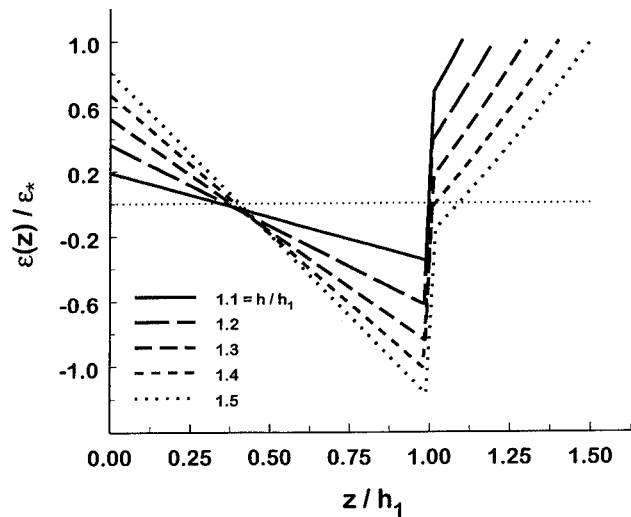
L. B. FREUND

Fig. 8. Distribution of total elastic strain in the film for growth according to a local strain criterion under unconstrained conditions, for five values of film thickness.

$$\varepsilon^{(m)}(z) = \varepsilon_* \left(1 + 4\frac{z - h_1}{h_1}\right), \quad h_1 \leqslant z \leqslant h. \tag{25}$$

The corresponding curvature, found from (7), is given by

$$\kappa(h) = \frac{6}{h_1}\left(1 - \frac{h_1}{h}\right), \quad h_1 \leqslant h \tag{26}$$

and it is shown in Fig. 6 as the curve labeled "free". The strain of the reference plane for this case is

$$\varepsilon^{(r)}(h) = 2\varepsilon_* \ln\frac{h}{h_1}, \quad h_1 \leqslant h. \tag{27}$$

The complete strain distribution across the thickness of the film is shown in Fig. 8 for five values of final thickness. Note that the total strain at the growth surface in each case is ε_*, but that the mismatch strain is something different from that value, depending on the local growth conditions. For purposes of comparison, the complete strain distributions for the clamped and free cases are both shown in Fig. 9 for the particular case of $h/h_1 = 1.2$. The plot illustrates the difference which may be expected in the total strain in the film due to constraint conditions.

As a situation intermediate between the cases of a completely free film and a rigidly clamped film, the case of a film clamped against bending but free to undergo in-plane extension can be considered. The result of doing so is the mismatch strain distribution

$$\varepsilon^{(m)}(z) = \begin{cases} 0, & 0 \leqslant z < h_1 \\ \varepsilon_* \ln\frac{z}{h_1} + \varepsilon_*, & h_1 \leqslant z \leqslant h \end{cases} \tag{28}$$
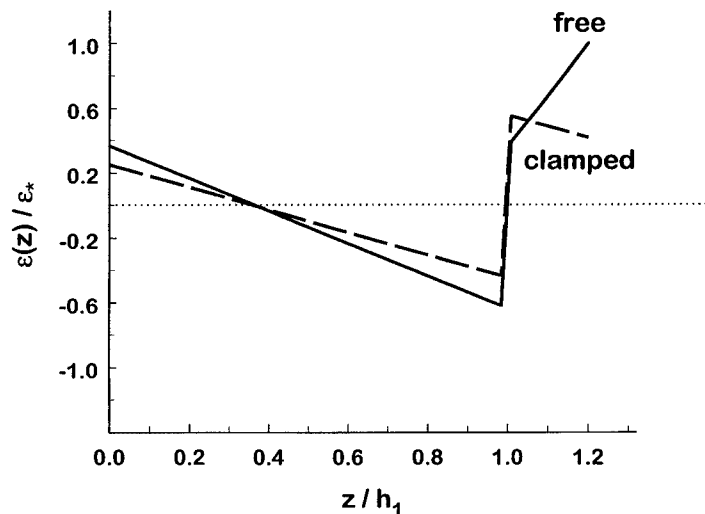
and the corresponding curvature is

Fig. 9. Comparison of the distribution of total elastic strain in the film for total thickness $h = 1.2h_1$ for the clamped case from Fig. 7 and the free case from Fig. 8.

$$\kappa(h) = 3\frac{h_1}{h}\left(1 - \frac{h_1^2}{h^2}\right). \tag{29}$$

The mismatch strain distribution and the dependence of curvature on thickness for this case are also shown in Figs 6 and 7 in the curves labeled "clamped against bending".

ACKNOWLEDGMENT

REFERENCES

Baldwin, W. M., Boardman, H. C., Halgren, J. A., Mattson, R. L. and McKloskey, A. S. (1955) Residual Stresses. *Metals Handbook* (Supplement), pp. 89–96. American Society for Metals, Cleveland.

Boley, B. and Weiner, J. H. (1960) *Theory of Thermal Stresses*, p. 277. Wiley, New York.

Eshelby, J. D. (1957) The determination of the elastic field of an ellipsoidal inclusion, and related problems. *Proc. Royal Soc. (London)* **A252,** 376–396.

Flinn, P. A. (1989) Principles and applications of wafer curvature techniques for stress measurements in thin films. *Thin Films: Stresses and Mechanical Properties* (ed. J. C. Bravman, W. D. Nix, D. M. Barnett and D. A. Smith), pp. 41–51. Materials Research Society, Pittsburgh.

Freund, L. B. (1993) The stress distribution and curvature of a general compositionally graded semiconductor layer. *J. Crystal Growth* **132,** 341–344.

Kroupa, F., Knesl. Z. and Valach, J. (1993) Residual stresses in graded thick coatings. *Acta Technica CSAV* **38**, 29–74.

Nakajima, K. (1991) Calculation of stresses in $In_{0.12}Ga_{0.88}As$ ternary bulk crystals with compositionally graded $In_{1-x}Ga_xAs$ layers on GaAs seeds. *J. Crystal Growth* **113**, 477–484.

Nakajima, K. (1992) Calculation of stresses in GaAs/Si strained heterostructures. *J. Crystal Growth* **121**, 278–296.

Spaepen, F. (1996) Substrate curvature resulting from the capillary forces of a liquid drop. *J. Mech. Phys. Solids* **44**, 675–681.

Stoney, G. G. (1909) The tension of metallic films deposited by electrolysis. *Proc. Royal Soc. (London)* **A82**, 172–175.

THE INFLUENCE OF MICROSTRUCTURAL SCALE ON THE COMBINATION OF STRENGTH AND ELECTRICAL RESISTIVITY IN COPPER BASED COMPOSITES

J. T. WOOD,[†] A. J. GRIFFIN Jr,[‡] J. D. EMBURY,[†] R. ZHOU,[‡]
M. NASTASI[‡] and M. VERON[†]

[†] Department of Materials Science and Engineering, McMaster University, 1280 Main Street West, Hamilton, Ontario, Canada L8S 4L7
[‡] Centre for Materials Science, Los Alamos National Laboratory, Los Alamos, New Mexico, U.S.A.

ABSTRACT

In many engineering applications materials are required to satisfy two or more selection criteria. An example is the provision of wire for the winding of high field magnets, and a methodology is proposed here that links these design criteria to the processing of fine scale composites. In developing the descriptions of the dependence of both mechanical strength and resistivity on the microstructural scale of the composite the modelling reveals the importance of new processes such as interface scattering and energy storage mechanisms at the interface that give new insights into the behaviour of fine scale structures. Finally from consideration of the scaling laws for strength and conductivity, it is possible to develop a comparison between the efficiencies of microscale, and macroscale composites for high field magnet applications.

INTRODUCTION

There are many engineering applications in which composite materials are required to satisfy two or more criteria regarding physical and mechanical properties. An example is the development of two-phase wires or tapes for the fabrication of coils for high field magnets (Wood *et al.*, 1995). Simple diagrammatic representations can be developed which display the combinations of properties for a variety of materials in relation to design requirements. An example of such a diagram is shown in Fig. 1.

For a simple solenoid, these diagrams are based on the development of functions to describe the response of the material in terms of the strength required to resist the Lorentz force and the conductivity required to minimize the ohmic heating in a given pulse of time Δt. Thus on this diagram we can indicate minimum acceptance criteria either in terms of the strength of the magnet in Teslas as horizontal lines or diagonal lines indicating maximum pulse durations. In general, materials for this application will be metallic composites or dispersion strengthened materials.

Further insight into the selection of materials can be gained by considering whether the properties of the composite are described by a suitable rule of mixtures or whether the scale and distribution of the phases in the composite must be considered.
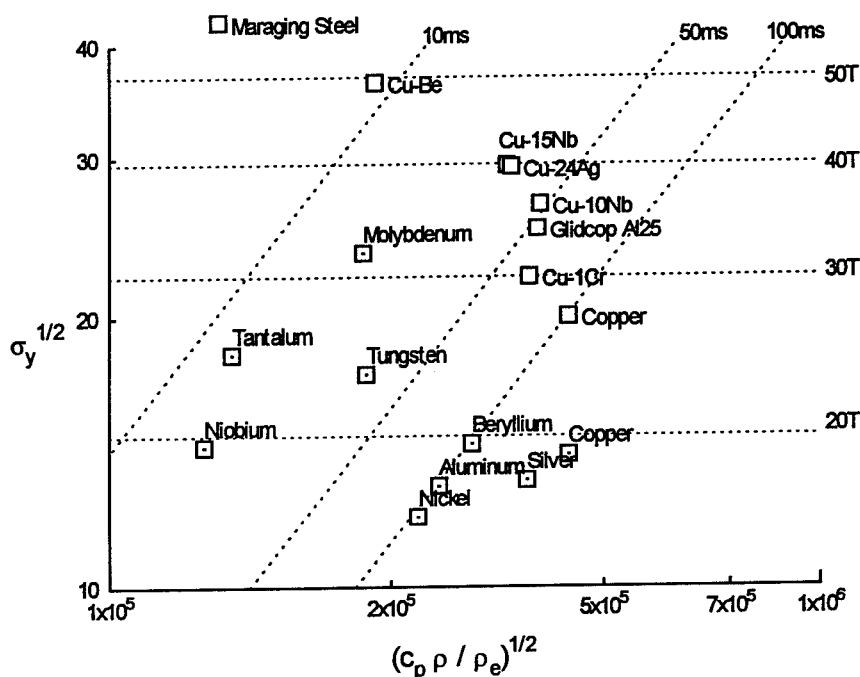
Fig. 1. Materials selection chart for the windings of high-field, pulsed magnets.

In this overview, consideration will be given first to drawn, filamentary composites in which attention must be given to the scale of the microstructure in relation to both the strength and the electrical conductivity. The results obtained on drawn, filamentary composites raise important fundamental questions regarding both the role of interphase interfaces in electron scattering and the magnitude and influence of internal stresses produced by co-deformation.

These concerns, particularly those related to electrical conductivity, can be addressed by reference to model systems of multilayers of copper and niobium prepared by vapour deposition. This portion of the study is based on the work of Dr A. J. Griffin Jr. and Dr M. Nastasi of the Los Alamos National Laboratory.

The final section of the overview will compare methods of using the appropriate laws of mixtures to develop fabrication methods for producing materials with suitable combinations of strength and electrical conductivity.

DRAWN FILAMENTARY COMPOSITES

Many two-phase materials containing plates or rods of the second phase can be deformed by wire drawing or rolling to yield fine-scale structures as shown in Fig. 2. The co-deformation of phases to produce fine-scale structures raises three fundamental issues: (a) the morphological stability of the embedded phase during large strain deformation (macroscopic aspects of this problem have been examined in detail
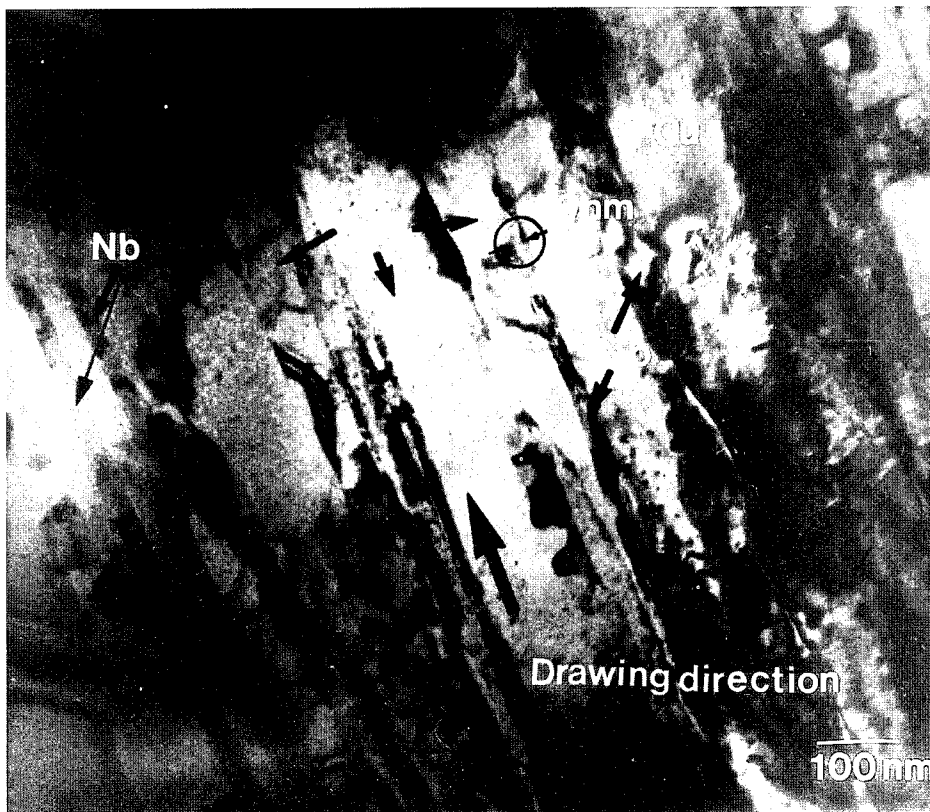
Fig. 2. A TEM micrograph of a longitudinal section of copper–niobium wire after drawing.
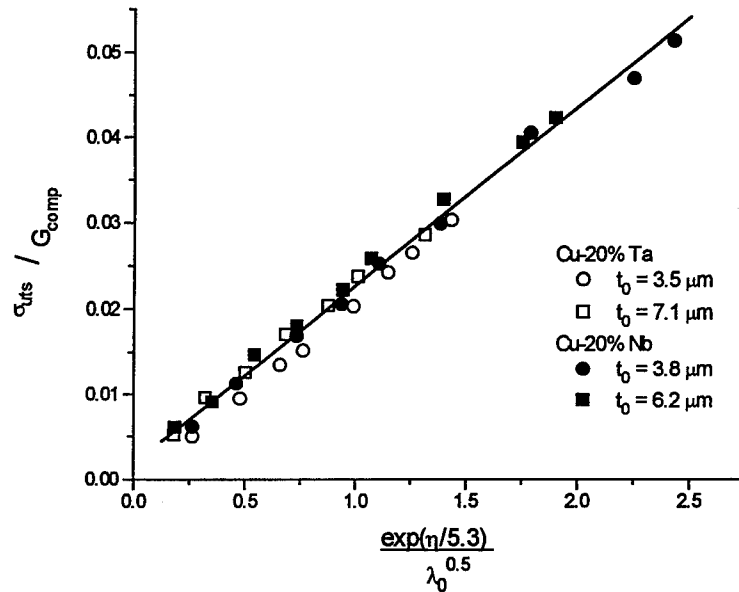
Fig. 3. Relationship between normalized strength and interphase spacing for drawn copper–niobium wires (Spitzif and Krotz, 1988).

by Steif, 1972); (b) the range of validity of strengthening relationships such as the Hall–Petch formulation for ultra-fine-scale structures (Christman, 1993); and (c) the mechanism of energy storage at large strains in two-phase systems.

In drawn, two-phase structures, the morphology of the phases can be very complex for the case where one phase is f.c.c. and one is b.c.c. due to the fibrous nature of the b.c.c. textures (Hosford, 1964). Thus prior to discussing the details of the validity of strengthening mechanisms and the energy storage processes, let us consider a simple description of the increase in strength due to imposed plastic strain in a system such as Cu–Nb.

If we assume that the strengthening is of the Hall–Petch type where the strength scales as $\lambda^{-1/2}$ where λ is the spacing of the second phase fibres, the data can be analyzed as shown in Fig. 3 (from Spitzig and Krotz, 1988). It can be seen that at fibre spacings of the order of 30 nm the strength level approaches 2 GPa. This is of the order of $E/80$ where E is the elastic modulus of copper.

A very simple model of electrical resistivity can be developed by assuming that at large strains the dominant contribution to electrical resistivity is scattering at the Cu–Nb interfaces as the spacing of fibres becomes of the order of the mean free path of the electrons.

Following the work of Dingle (1950) and Sondheimer (1952), the following relationships were proposed to predict the resistivity

$$\rho_f = \begin{cases} \rho_b \left[1 + \dfrac{3\bar{x}}{4\lambda}(1+p) \right] & \lambda \gg \bar{x} \\[2ex] \rho_b \left(\dfrac{1-p}{1+p} \right) \dfrac{\bar{x}}{\lambda} & \lambda \ll \bar{x} \end{cases} \tag{1}$$
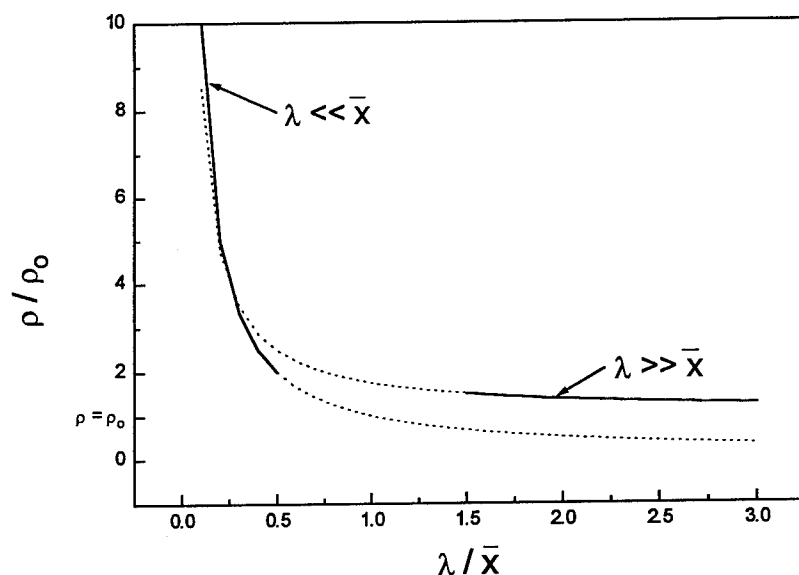
Fig. 4. Relationship between electrical resistivity and interphase spacing for fine-scale, two-phase micro-structures.

where ρ_f is the resistivity of the fibrous material, ρ_b is the resistivity of the bulk material, $\bar{x}$ is the mean free path of the electrons, λ is the interphase spacing and p is the probability of the electrons being scattered elastically. Typical values of p have been found experimentally to be in the range 0.10–0.15 (Frommeyer and Wassermann, 1975). The result of applying these equations is the prediction that, at large interphase spacings, the resistivity is that of the bulk material, whereas at spacings which are comparable to the mean free path, the scattering at interfaces will dominate and the resistivity will be higher than that of the bulk.

Using this type of model, the dependence of electrical conductivity on the scale of the drawn microstructure can be predicted as in Fig. 4. The physics of interface scattering has been discussed in detail by Skomski et al. (1992). The resistivity of well controlled, Cu–Nb layered structures is discussed in relation to the model proposed by Skomski et al. in a later section of this paper.

The simple laws for the dependence of strength and resistivity on the scale of the structure enables a basic initial framework to be developed to consider how these characteristics enter into the design of wire for magnets. Thus we can view the question of high-strength, high-conductivity composites from two viewpoints: (a) the concept of the design of structures based on the simplified models outlined above, and (b) detailed consideration of the strengthening and resistivity mechanisms in fine-scale structures.

FINE-SCALE COMPOSITES

If the strength of the composite increases as $\lambda^{-1/2}$ and the resistivity varies as λ^{-1}, then the combination of properties can be plotted on the design diagram as shown in
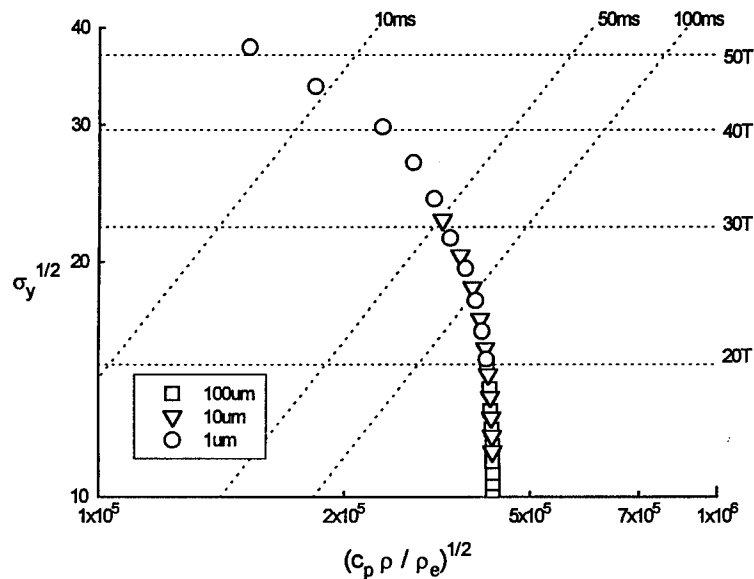
Fig. 5. Pulsed magnet materials selection chart showing the evolution of properties of *in-situ* composites with strain for various initial interphase spacings.

Fig. 5. The trajectory of increasing strength and decreasing conductivity will be determined by the initial scale of the structure, λ_0, and the magnitude of the imposed strain in the drawing process. The essential points of such a treatment are that structures with finer initial scale are advantageous because they can be processed with smaller imposed strains. However, the methodology has the drawback that both properties are linked to the same microstructural scaling parameter, namely the interphase interfacial spacing λ.

MACROSCOPIC COMPOSITES

The properties of strength and resistivity can be effectively decoupled by considering a macroscopic composite in which the scale of the conducting phase (in this case copper) remains in excess of the mean free path of the conducting electrons while the second phase is chosen such that it is able to work harden rapidly.

Typical cross sections for such macroscopic structures are shown in Fig. 6. Using this concept, we can use the fact that the copper stores dislocations as it work hardens but these contribute a resistivity of only 10^{-25} $\Omega \cdot m^3$ per unit length (Basinski and Saimoto, 1967) and hence the conductivity of heavily deformed copper is only reduced from the annealed copper standard by 1–2% in the absence of any other scattering mechanisms. The incorporated second phase can now co-deform with the copper but strain harden at a much higher rate than copper. Typical examples would be pearlitic steel or some stainless steels which undergo a martensitic transformation upon deformation. The appropriate law of scaling is then:
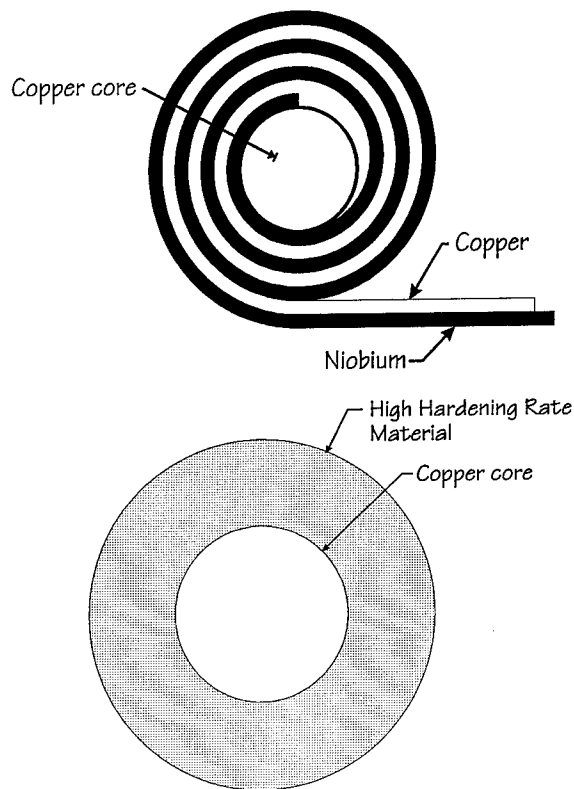
Fig. 6. Schematic representations of macroscopic composite structures.

$$\sigma_{\text{comp}} = \sigma_{\text{Cu}}V_{\text{Cu}} + \sigma_{\text{EP}}(\varepsilon)(1 - V_{\text{Cu}}), \tag{2}$$

where V_{Cu} is the volume fraction of the copper matrix and $\sigma_{\text{EP}}(\varepsilon)$ is the strength of the embedded phase after an imposed codeformation of ε. The resultant increase in strength predicted for copper containing 20% of various phases capable of work hardening to high imposed strains is shown in Fig. 7. It can be seen that this method
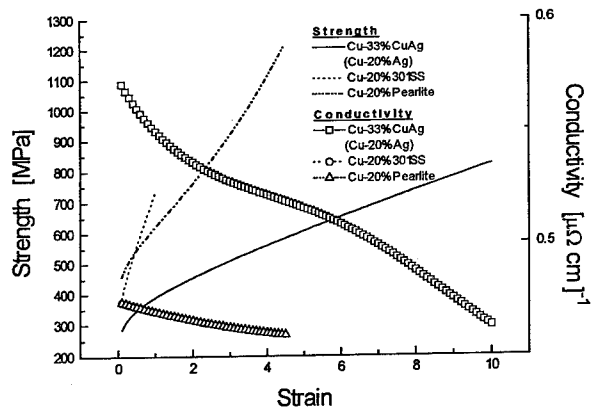

Fig. 7. Calculated evolution of strength and electrical conductivity with strain for various macroscopic composite systems. (The conductivity data for Cu-301SS and Cu–pearlite overlap.)
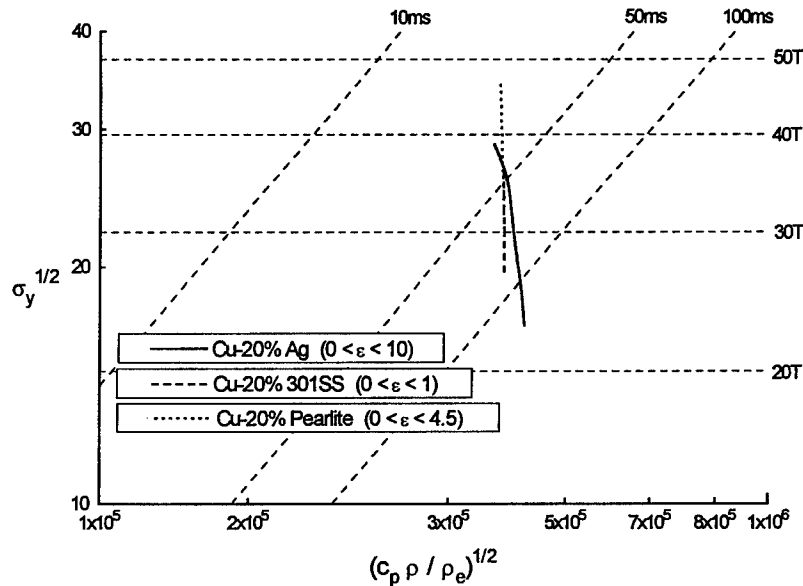
Fig. 8. Macroscopic composite data of Fig. 7 plotted on the pulsed magnet materials selection chart.

of decoupling the dependence of strength and electrical conductivity on the scale of the structure can be expressed as a new development trajectory on the design diagram as shown in Fig. 8.

FUNDAMENTAL ISSUES RELATING TO HEAVILY DEFORMED *IN SITU* COMPOSITES

Let us consider first the problem of microstructural scale and conductivity. The recent work of Skomski *et al.* (1992) considers the interface scattering in terms of the degree of substitutional disorder P_m and the interface thickness b as well as the scale of the microstructure λ. Thus

$$\rho(\lambda) = \tfrac{1}{2}(\rho_A + \rho_B)\frac{4bP_m}{\lambda}\tanh\left(\frac{\lambda}{4b}\right), \tag{3}$$

where ρ_A and ρ_B are the bulk resistivities of phases A and B.

The data obtained for vapour deposited layers of copper and niobium by Griffin *et al.* (1995) can be plotted in this form as shown in Fig. 9. Despite the difficulty of obtaining regular layered structures less than 10 nm in wavelength, the data show good agreement with the Skomski model providing an interface thickness of about 3–4 nm is assumed. A second interesting feature of this data is the observation that as the thickness of the vapour deposited niobium decreases the observed critical temperature for the superconducting transition in niobium is reduced as shown in Fig. 10. The most likely explanation of this observation is that, in the fine-scale structure, superconductive pairing of the electrons is disturbed by the proximity
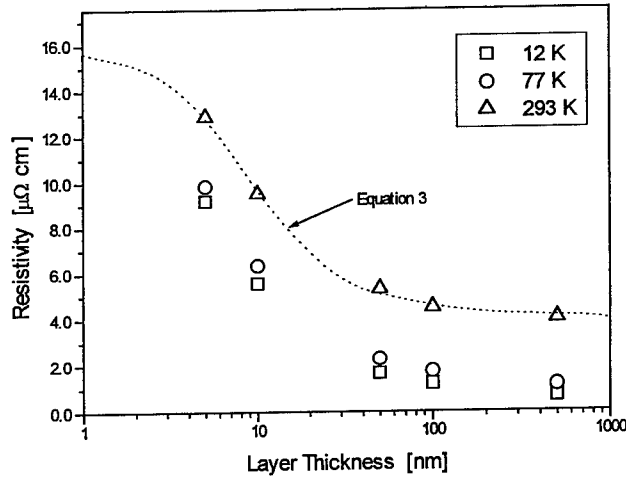
J. T. WOOD *et al.*

Fig. 9. Change in resistivity with layer thickness at various temperatures.

effect, resulting in a reduction of the critical temperature. However at very fine layer thicknesses the structures may be influenced by coherency stresses also, which may influence the conductivity.

Turning to the strengthening mechanisms in fine-scale structures, it is of importance to note that several studies (e.g. Wood and Embury, 1995) have shown direct evidence of large elastic stress in the niobium filaments after co-deformation. These elastic stresses need to be accounted for in the overall description of the detailed strengthening mechanism and it must be recognized that they cause the elastic–plastic transition to be rounded, making it difficult to define the yield stress and critical hardening rate. In addition to the elastic stress, the fine scale of the structure reduces the source length
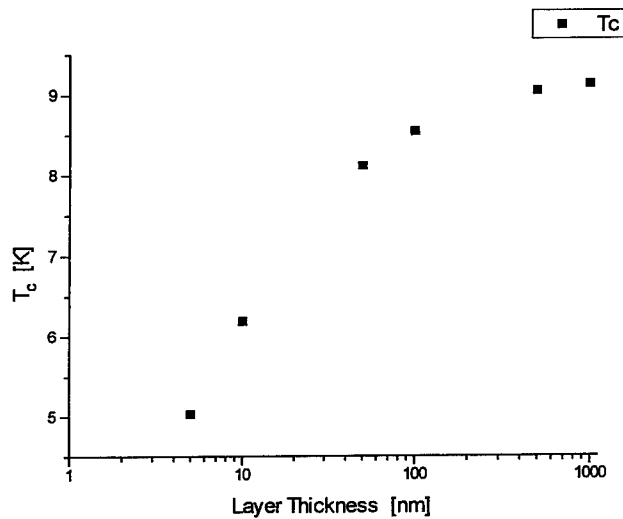

Fig. 10. Decrease of superconducting transition temperature of niobium with the decreasing niobium layer thickness.
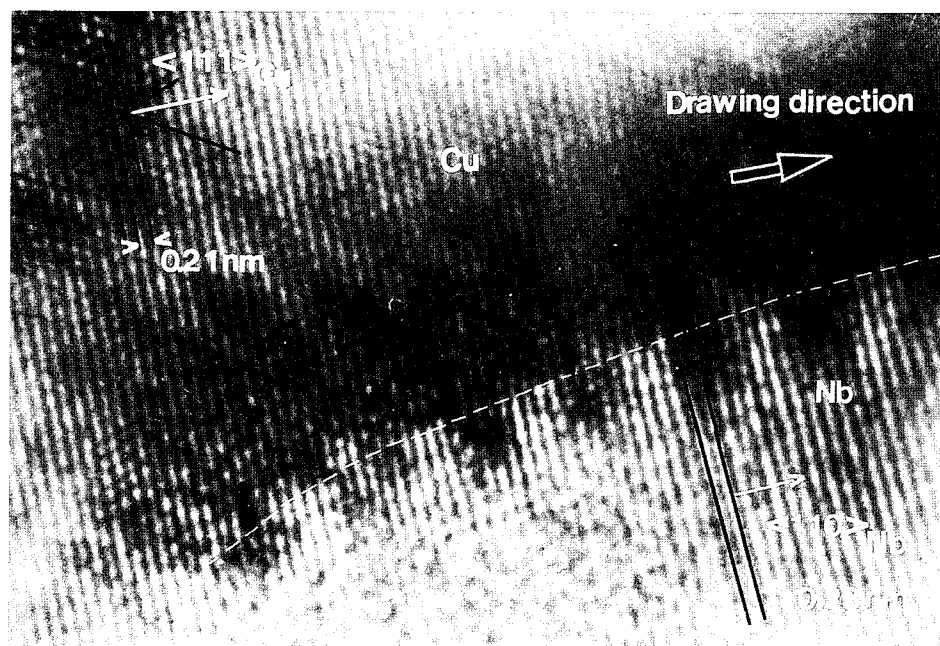
Fig. 11. A high resolution TEM image of the copper–niobium interface showing regularly spaced dislocations.

of the dislocations which may also contribute to the overall strength level. Also, it is important to note that the niobium phase is reduced in scale but that its cross-section remains essentially uniform. Thus, the scale of deformation during co-deformation at large plastic strains must be extremely fine and it is of value to ask how energy is stored in these structures. As few dislocations are observed in either the copper or niobium, it is probable that storage at the interphase interfaces becomes an important process. This concept has been examined previously in models suggested by Gil Sevillano *et al.* (1981) and Embury (1992). Direct evidence of the process can be seen in the high resolution electron micrograph shown in Fig. 11 where dislocations can be observed at spacings of the order of 7–10 atomic planes. Thus, as the scale of the structure is refined, the embedded phase eventually takes the form of whiskers which are developed by large strain co-deformation of the phases. In addition, large areas of interphase interfaces are created which are subject to tractions due to the compatibility of the phases and dislocation storage at the interface.

These observations strongly suggest that in fine-scale structures, new mechanisms of energy storage such as interfaces which are under traction due to the capture of dislocations must be examined in detail both by electron microscopy and by methods such as calorimetry and morphological and dimensional stability studies.

CONCLUSIONS

This paper emphasizes three essential aspects of fine scale composites:

(a) that the scale of these structures can be incorporated in simple scaling laws that have direct relevance to component design in areas such as high field magnets;

(b) that comparison of drawn *in situ* composites and macroscopic composites provide a useful way to decouple properties such as strength and conductivity which are normally linked to the same microstructural scale;

(c) at interface spacings below 50 nm, phenomena at the interphase interfaces influence a range of processes such as electron scattering, superconductivity, strengthening and energy storage and that systematic studies of these processes in relation to the specific combinations of materials represents a fruitful area for much future research.

ACKNOWLEDGEMENTS

REFERENCES

Basinski, Z. S. and Saimoto, S. (1967) Resistivity of deformed crystals. *Can. J. Phys.* **45**, 1167–1176.

J. T. WOOD *et al.*

Christman, (1993) Grain-boundary strengthening exponent in conventional and ultrafine microstructures. *Scripta Metall. Mater.* **28,** 1495–1500.

Dingle, R. B. (1950) The electrical conductivity of thin wires. *Proc. Roy. Soc.* **A201,** 545–560.

Embury, J. D. (1992) Micromechanical descriptions of heavily deformed materials. *Scripta Metall. Mater.* **27,** 981–986.

Frommeyer, G. and Wassermann, G. (1975) Anomalous properties of in-situ-produced silver-copper composite wires : I. Electrical conductivity. *Phys. Stat. Sol. A* **27,** 99–105.

Gil Sevillano, J., Van Houte, P. and Aernoudt, P. (1981) Large strain deformation and textures. *Prog. Mater. Sci.* **25,** 69–412.

Griffin Jr, A. J., Embury, J. D., Hundley, M. F., Jervis, T. R., Kung, H. H., Scarborough, W. K., Walter, K. C., Wood, J. T. and Nastasi, M. (1995) Residual stress, mechanical behaviour and electrical properties of Cu/Nb thin-film multilayers, in press.

Hosford Jr, W. F. (1964) Microstructural changes during deformation of [011] fiber-textured metals. *Trans. Met. Soc. AIME* **230,** 12–15.

Skomski, R., Enrech, M. and Coey, J. M. D. (1992) Resistance and structure of metallic multilayers. *Nanostructured Mater.* **1,** 337–345.

Sondheimer, E. H. (1952) The mean free path of electrons in metals. *Adv. Phys.* **1,** 1–42.

Spitzig, W. A. and Krotz, P. D. (1988) Comparison of the strengths and microstructures of Cu–20%Ta and Cu–2%Nb in situ composites. *Acta Metall.* **36** (7), 1709–1715.

Steif, P. J. (1972) On deformation instabilities in clad metals subjected to rolling. *J. Appl. Metalworking* **4,** 317–326.

Wood, J. T., Embury, J. D. and Ashby, M. F. (1995) An approach to materials selection for high-field magnet design, in press.

Wood, J. T. and Embury, J. D. (1995) The development of ultra-high strength wires by the deformation of in-situ composites. *Proc. of ICCM*-10 : *Vol. 2 : Metal Matrix Composites* (ed. A. Poursartip and K. N. Street), pp. 99–106.

Pergamon

PII S0022–5096(95)00026–9

RELIABILITY OF CERAMIC MULTILAYER ACTUATORS : A NONLINEAR FINITE ELEMENT SIMULATION

X. GONG and Z. SUO

Mechanical and Environmental Engineering Department, Materials Department,
University of California, Santa Barbara, CA 93106, U.S.A.

ABSTRACT

In a ceramic multilayer actuator, the abrupt end of an internal electrode concentrates the electric field, inducing stresses in the ceramic. Crack nucleation and growth have been observed experimentally, but have not been well modeled due to the complex material behaviors. We write a finite element program to solve this coupled electromechanical problem. The material is taken to be nonlinearly dielectric with electrostrictive strain quadratic in electric displacement. The program solves field distributions in a multilayer actuator, which are combined with fracture mechanics to obtain cracking condition. The calculations are compared with the existing analytical solution under the small-scale saturation conditions, and then extended to the large-scale saturation conditions. We show that the cracking condition established under the small-scale saturation conditions gives useful estimate even when the saturation zone is comparable to the actuator layer thickness.

1. INTRODUCTION

Ceramic multilayer actuators have found a wide range of applications owing to their small volumes, quick response, low energy consumption, and large generative forces (Uchino, 1993 ; Rogers, 1995). Various electrode configurations have been proposed (Yoshikawa and Shrout, 1993), one of which is shown in Fig. 1. An actuator often
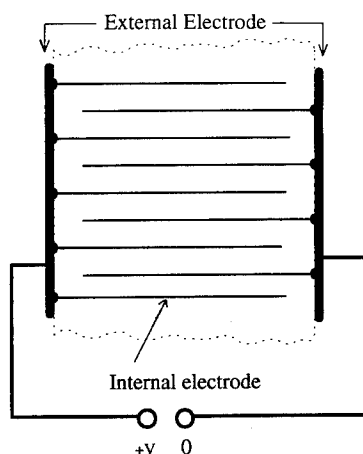

Fig. 1. A schematic picture of ceramic multilayer actuator.

consists of hundreds of ceramic layers, alternating with thin metal films (internal electrodes). Each metal film connects one edge to one of the external electrode strips, and terminates another edge inside the ceramic to maintain insulation. The terminated electrode edges raise a serious reliability problem. Cracks start in the ceramic around the electrode edges, grow and damage the device (Furuta and Uchino, 1993; Aburatani *et al.*, 1994; Schneider *et al.*, 1994).

Figure 2 illustrates a basic cracking mechanism (Suo, 1993). When a voltage V is applied to the multilayer actuator, an electric field $E_{appl} = V/H$ prevails in the region covered by two internal electrodes, where H is the individual ceramic layer thickness [Fig. 2(a)]. However, the electric field around a terminated electrode edge is non-uniform and much higher than E_{appl} [Fig. 2(b)]. Consequently, the ceramic around the electrode edge undergoes an incompatible deformation due to either ferroelectric switching or electrostriction [Fig. 2(c)]. The incompatible deformation, in its turn, induces a stress field that may activate flaws in the ceramic to grow.
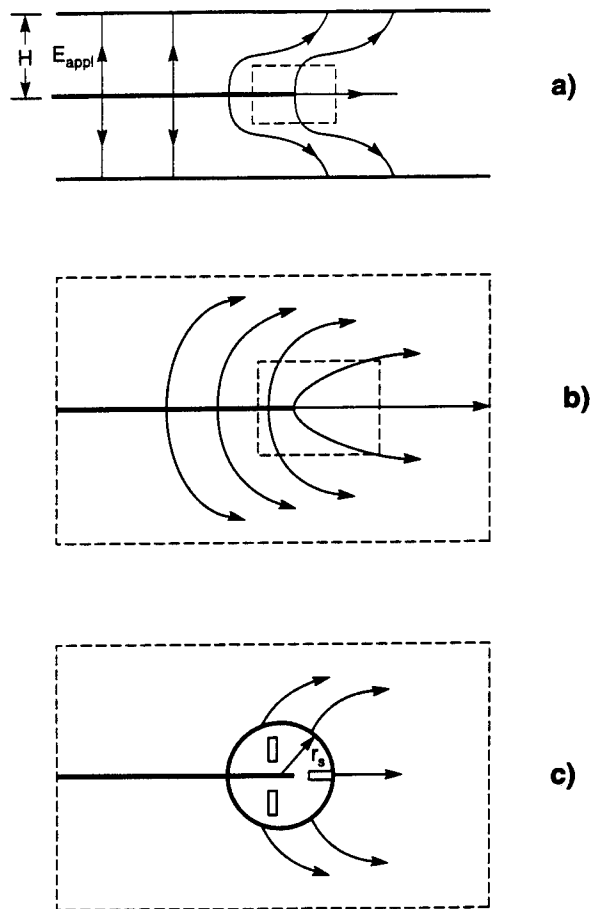

Fig. 2. A basic mechanism for cracking around an electrode edge.

Winzer *et al.* (1989) was the first to analyze the problem using finite element method. They determined the electric field in an actuator assuming that the ceramic is linearly dielectric, and then solved a linear elastic problem to determine the stress field induced by quadratic electrostriction. Yang and Suo (1994) studied the similar problems analytically, and showed that at a small distance r from an internal electrode edge, the stress field is $1/r$ singular. The strong singularity results from two idealizations: the electrode was taken to be a mathematical plane with no thickness, and the ceramic was linearly dielectric. In reality, as the electric field increases, the electric displacement saturates, resulting in a lower electrostrictive strain than that predicted from a linear dielectric. Yang and Suo (1994) proposed a step-like electrostriction model, and showed that the stress is no longer singular. For an electrostrictive ceramic with saturated electric displacement, Hom and Shankar (1995) and Hao *et al.* (1996) showed that the stress field around the electrode edge is only logarithmic singular.

The analytical solutions are only valid under the small-scale saturation conditions, and are obtained under the condition that the stress field does not affect the electric field. To analyze the problem, with realistic device geometries and nonlinear electro-mechanical coupling, one has to write a finite element program (Gong, 1994, 1995). Independent of our work, Hom and Shankar (1995) have formulated a finite element approach to the same problem. Their formulation differs from ours, but the two formulations give similar numerical results. The present paper builds upon the previous work and reports details of a finite element simulation. The conclusion is expected to be useful in actuator design. Section 2 formulates the coupled electro-mechanical field in a ceramic multilayer actuator as a boundary value problem. This problem is then solved by a finite element method outlined in Appendix A. Section 3 reviews the small-scale saturation model, and compares the solution with the finite element results. Section 4 extends the finite element analysis to the actuators under large-scale saturation conditions.

2. PROBLEM FORMULATION

We focus our attention on plane strain problems, which allow us to compare finite element results with existing analytical solutions. This section lists governing equations and boundary conditions for an actuator. Details of the finite element formulation specific to nonlinear electrostrictive ceramics are given in Appendix A. Once the stress field is solved, we apply fracture mechanics to obtain the stress intensity factor.

2.1. *Governing equations*

Subject a solid dielectric to a distribution of displacements u, v in the x, y directions, and electric potential ϕ. The strain tensor, γ, and the electric field vector $\mathbf{E}$, are the gradients

$$\gamma_{ij} = \tfrac{1}{2}(u_{i,j} + u_{j,i}), \quad E_i = -\phi_{,i}. \tag{2.1}$$

Across an interface, the stress tensor, σ, and the electric displacement vector, $\mathbf{D}$, jump by

$$n_i[\sigma_{ij}^+ - \sigma_{ij}^-] = t_j, \quad n_i[D_i^+ - D_i^-] = -\omega, \tag{2.2}$$

where **n** is the unit vector normal to the interface pointing from the $-$ side to the $+$ side, **t** is the traction, and ω is the charge per unit area, externally applied on the interface. If the material is free of space charge and body force, the stress tensor and the electric displacement vector are divergence-free, namely,

$$\sigma_{ij,j} = 0, \quad D_{i,i} = 0. \tag{2.3}$$

Suo (1991), and Hom and Shankar (1994) proposed a set of constitutive equations for nonlinear, isotropic electrostrictive ceramics on the basis of experimental observations and thermodynamic considerations. Under the plane strain conditions, the constitutive equations take the form

$$\gamma_{xx} = [(1-v^2)\sigma_{xx} - v(1+v)\sigma_{yy}]/Y + Q[(1-vq)D_x^2 - q(1+v)D_y^2] \tag{2.4a}$$

$$\gamma_{yy} = [(1-v^2)\sigma_{yy} - v(1+v)\sigma_{xx}]/Y + Q[(1-vq)D_y^2 - q(1+v)D_x^2] \tag{2.4b}$$

$$\gamma_{xy} = (1+v)\sigma_{xy}/Y + Q(1+q)D_x D_y \tag{2.4c}$$

$$E_x = -2Q[(1-vq)D_x\sigma_{xx} + (1+q)D_y\sigma_{xy}$$
$$\qquad -q(1+v)D_x\sigma_{yy} - q^2 D_x YQ(D_x^2 + D_y^2)] + f(D)D_x/D \tag{2.4d}$$

$$E_y = -2Q[(1-vq)D_y\sigma_{yy} + (1+q)D_x\sigma_{xy} - q(1+v)D_y\sigma_{xx}$$
$$\qquad -q^2 D_y YQ(D_x^2 + D_y^2)] + f(D)D_y/D. \tag{2.4e}$$

Here $D = (D_i D_i)^{1/2}$ is the magnitude of the electric displacement, v is Poisson's ratio, Y is Young's modulus, Q and q are the electrostrictive coefficients. The strains are linear in the stresses (elasticity) and quadratic in the electric displacements (electrostriction). The electric field is nonlinear in electric displacements (dielectric effects), and also depends on stresses (converse electrostrictive effects). The function, $E = f(D)$, is the dielectric response in the absence of stress. Experiments have shown that when the electric field increases, its ability to induce further electric displacement decreases, which finally saturates at a constant value D_s (Uchino and Nomura, 1983; Jang et al., 1989; Cao and Evans, 1993; Lynch et al., 1994; Lynch, 1995).

Figure 3 shows two D–E relations in the absence of stress. The relation used by Gong (1994), Hom and Shankar (1994) and Gong (1995) in the finite element analysis is written as

$$f(D) = \frac{E_s}{2} \ln\left(\frac{1 + D/D_s}{1 - D/D_s}\right). \tag{2.5}$$

Here D_s is the saturated electric displacement, E_s is a characteristic electric field. When E is small, D is linearly proportional to E, and the slope defines the dielectric permittivity ε. One can confirm that

$$E_s = D_s/\varepsilon. \tag{2.6}$$

The solid line in Fig. 3 is the D–E relation used by Hao et al. (1996). When $E < E_s$, the ceramic is linear. When $E > E_s$, D is maintained at the constant saturation value
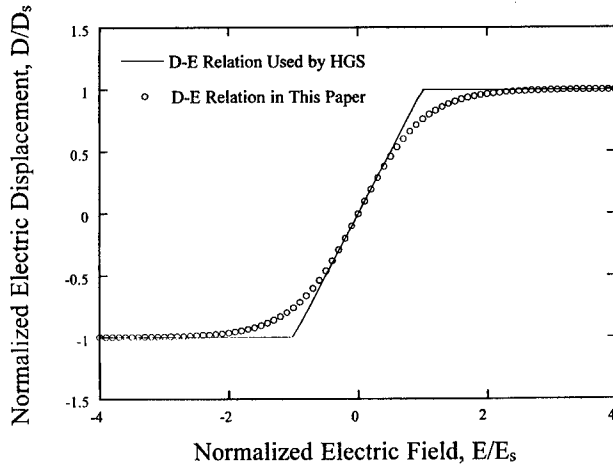
Fig. 3. The electric field and electric displacement relations used in the HGS solution and in this paper for finite element analysis.

D_s. The relationship (2.6) among the three parameters D_s, E_s and ε is the same for the two dielectric laws.

Notice that when the electric displacement saturates, the electrostrictive strain also saturates. This introduces another important parameter in actuator design

$$\gamma_s = QD_s^2, \tag{2.7}$$

which is the saturation strain along the electric field direction in the absence of stress. The saturation strain transverse to the electric field is $-qQD_s^2$.

2.2. Boundary conditions

Figure 4 shows the boundary conditions appropriate for a multilayer actuator. Place the origin of the Cartesian coordinate x–y at a terminated electrode edge. Because of the symmetry, only half of an individual layer needs to be analyzed. Along the upper electrode, the vertical displacement is constant

$$v(x, H) = \text{constant}. \tag{2.8a}$$

The value of the constant is to be determined as a part of the solution. The electric field potential equals the applied electric voltage,

$$\phi(x, H) = V_{\text{appl}}. \tag{2.8b}$$

When no external stress is applied on the actuator, the shear stress and the vertical resultant force vanish, namely

$$\sigma_{xy} = 0, \quad \int_{-L_2}^{L_1} \sigma_{yy}(x, H)\, dx = 0. \tag{2.8c}$$

The lower electrode is connected to the ground, so that

$$\phi(x, 0) = 0, \quad -L_2 \leqslant x \leqslant 0. \tag{2.8d}$$
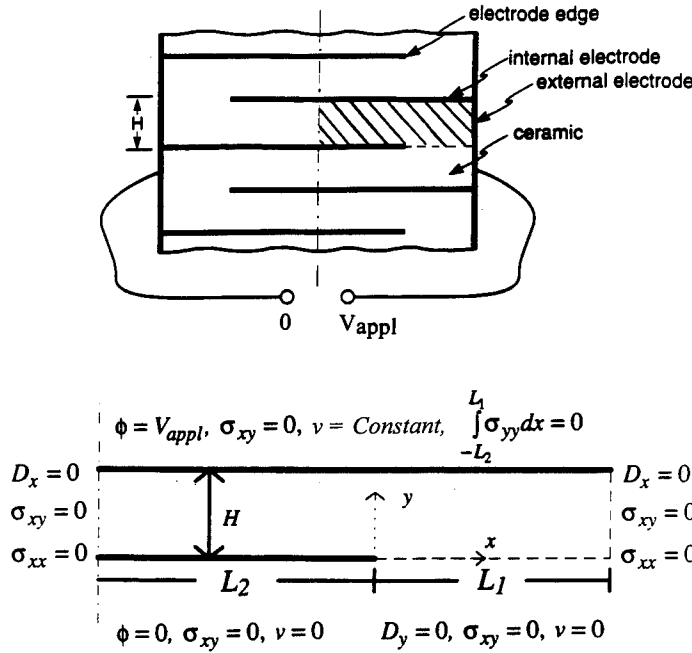
Fig. 4. Boundary conditions for a multilayer actuator.

The vertical displacement and the shear stress vanish on both the electrode and its front plane due to the symmetry

$$v(x,0) = 0, \quad \sigma_{xy} = 0, \quad -L_2 \leqslant x \leqslant L_1. \tag{2.8e}$$

In front of the lower electrode plane, due to symmetry, the vertical electric displacement vanishes

$$D_y(x,0) = 0, \quad 0 < x < L_1. \tag{2.8f}$$

At the end of the actuator and its vertical symmetric plane, tractions and horizontal electric displacement vanish

$$\sigma_{xx} = 0, \quad \sigma_{xy} = 0, \quad D_x = 0. \tag{2.8g}$$

To avoid rigid body motion, we constrain the horizontal motion at the left lower corner

$$u(-L_2,0) = 0. \tag{2.8h}$$

2.3. Stress far away from the electrode edge

We will use finite element program to analyze a special case that both L_1 and L_2 are much larger than H. Although this configuration is different from a typical actuator, it emphasizes the conditions around the electrode edge with minimum complications from the external boundaries. The more realistic complication $L_1 \ll L_2$, $L_1 \approx H$ will be studied elsewhere.

When $L_1 \gg H$ and $L_2 \gg H$, one can readily determine the stresses in the actuator far away from the electrode, where the electric field is uniform, vanishing in the inactive part and equal to the applied electric field in the active part. The only nonzero stress component is σ_{yy}, which is tensile ahead of the electrode edge, and compressive behind, due to the global mismatch between the active part and the inactive part. Denote the stress far ahead of the electrode edge by σ^+ and the stress far behind the electrode edge by σ^-. The resultant force vanishes

$$L_1 \sigma^+ + L_2 \sigma^- = 0. \tag{2.9a}$$

The vertical displacement is the same in both parts

$$\frac{1-v^2}{Y}\sigma^- + (1-vq)QD^2 = \frac{1-v^2}{Y}\sigma^+. \tag{2.9b}$$

These two equations solve the two stresses, giving

$$\sigma^+ = \frac{L_2}{L_1+L_2}\frac{1-vq}{1-v^2}YQD^2, \tag{2.10a}$$

$$\sigma^- = -\frac{L_1}{L_1+L_2}\frac{1-vq}{1-v^2}YQD^2. \tag{2.10b}$$

For example, taking $L_2 = L_1$, $Y = 10^{11}$ N/m^2, $QD^2 = 10^{-3}$, $v = q = 0.3$, one finds that the tensile stress $\sigma^+ = 50$ MPa. We emphasize that the stresses σ^+ and σ^- are valid far away from the electrode edge. The stress field in general must be determined by using the finite element analysis.

2.4. Computing the stress intensity factor

Once the stress field is obtained from the finite element calculation, the stress intensity factor can be evaluated by means of the fracture mechanics. Consider a crack-like flaw of length a, taken to be much smaller than the layer thickness, i.e. $a/H \ll 1$. The stress normal to the crack surface, σ_n, induces a stress intensity factor (Tada $et\ al.$, 1985)

$$K_I = \sqrt{\frac{2}{\pi a}}\int_0^a \sigma_n(x)\sqrt{\frac{x}{a-x}}\,dx. \tag{2.11}$$

We evaluate this integral numerically.

Introduce a dimensionless parameter

$$\alpha = \frac{QD_s Y\gamma_s}{E_s} = \frac{Y\gamma_s^2}{\varepsilon E_s^2}, \tag{2.12}$$

which is a material constant that measures the relative magnitude of mechanical and electrical energy. Its mathematical significance can be appreciated as follows. For a ceramic under uniaxial stress σ and electric displacement D, the longitudinal strain γ and electric field E are

$$\gamma = \frac{\sigma}{Y} + QD^2, \quad E = -2QD\sigma + \frac{E_s}{2}\ln\left(\frac{1+D/D_s}{1-D/D_s}\right). \tag{2.13}$$

Normalize the strain by γ_s, the stress by $Y\gamma_s$, the electric displacement by D_s, and the electric field by E_s, so that (2.13) takes a dimensionless form

$$\gamma = \sigma + D^2, \quad E = -2\alpha D\sigma + \frac{1}{2}\ln\left(\frac{1+D}{1-D}\right). \tag{2.14}$$

Similar relation for the multiaxial loading state can also be deduced from (2.4). Consequently, when $\alpha = 0$, the stresses do not affect electric fields. The approximation $\alpha = 0$ has been made in most previous publications, which we will verify in this paper.

The stress intensity factor takes the dimensionless form

$$\frac{K_I}{Y\gamma_s\sqrt{H}} = k\left(\frac{a}{H}, \frac{E_{appl}}{E_s}, \alpha, v, q\right). \tag{2.15}$$

Function k is to be determined from the finite element calculation.

3.   SMALL-SCALE SATURATION

This section summarizes the model for an actuator under the small-scale saturation conditions (Suo, 1993; Yang and Suo, 1994; Hao et al., 1996), and compares it with our finite element results.

3.1.   The small-scale saturation model

When the applied electric field is small compared to the characteristic electric field, $E_{appl} < E_s$, the electric field in the bulk of the actuator is linearly dielectric. The electric field a distance r ahead of the electrode edge is square-root singular

$$E = \frac{K_E}{\sqrt{2\pi r}}. \tag{3.1}$$

The electric field intensity factor K_E depends on the driving voltage and the device geometry, and can be solved from linear dielectric boundary value problems. Linearity and dimensional considerations dictate that the intensity factor should take the form

$$K_E = \Omega E_{appl}\sqrt{H}. \tag{3.2}$$

The dimensionless coefficient $\Omega = \sqrt{2}$ for the present actuator geometry.

Under the small-scale saturation conditions, the electric displacement saturates only within a small cylinder around the electrode edge. The radius of the saturated cylinder is

$$r_s = \frac{1}{2\pi}\left(\frac{K_E}{E_s}\right)^2. \tag{3.3}$$

The linear dielectric solution (3.1) is approximately valid in an annulus with its inner radius larger than the saturated cylinder and outer radius smaller than the individual ceramic layer thickness, i.e. $r_s < r < H$.

Around the electrode edge, the electric field generates an incompatible strain field, which, in its turn, induces a stress field. The high stress field is localized in a region scaled by the saturated cylinder. For a rapidly decaying stress field, the stress intensity factor, K_I, is small for both small and large flaws. Consequently K_I peaks for a flaw of some intermediate size scaled with r_s. The peak value takes the form

$$(K_I)_{max} = \Lambda \frac{Y\gamma_s K_E}{E_s}, \tag{3.4}$$

where the dimensionless number Λ depends on the detail of the material model. Substituting (3.2) into (3.4), one obtains that

$$(K_I)_{max} = \Lambda\Omega \frac{Y\gamma_s E_{appl} \sqrt{H}}{E_s}. \tag{3.5}$$

Consequently, under the small-scale saturation conditions, function k in (2.15) is linear in the loading parameter, E_{appl}/E_s.

No flaws, of any size and location, can grow if $(K_I)_{max} < K_{Ic}$, i.e.

$$\Lambda\Omega \frac{Y\gamma_s E_{appl} \sqrt{H}}{E_s} < K_{Ic}, \tag{3.6}$$

where K_{Ic} is the toughness of the electrostrictive ceramic material. Consequently, everything else being equal, there exists a critical layer thickness, given by

$$H_c = \left(\frac{K_{Ic} E_s}{\Lambda\Omega Y\gamma_s E_{appl}} \right)^2, \tag{3.7}$$

below which no flaw will grow.

The merit of the small-scale saturation approximation can be appreciated as follows. An actuator is made of a complex material with a complex geometry. Under the small-scale saturation conditions, the two complexities, material behavior and geometry effect, can be treated independently. The dimensionless details of a material law only affect the coefficient Λ defined by (3.4), which can be obtained either empirically or by analyzing a material model. The geometry details of the actuator only affect the coefficient Ω defined by (3.2), which can be obtained by analyzing a linear dielectric boundary value problem. The scheme will be particularly useful in evaluating several materials for a common actuator geometry, or several actuator geometries for a common material.

3.2. Comparison of the finite element calculation with the HGS solution

We compare the HGS (Hao et al., 1996) solution with the finite element results in this section. In all numerical calculations, we set $v = 0.26$, $q = 0.38$, and $L_1 = L_2 = 40H$. We use a small loading level $E_{appl}/E_s = 0.08$ to represent the small-
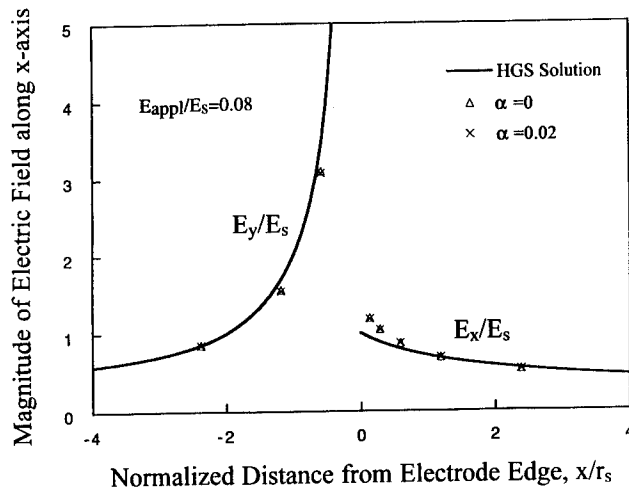
X. GONG and Z. SUO

Fig. 5. The electric field distributions along the x-axis under the small-scale saturation conditions.

scale saturation conditions. Figure 5 compares the electric field distribution along the x-axis. The solid line is the HGS solution; the electric field vector lies in the x-direction ahead of the electrode edge, and in the y-direction behind the electrode edge. The finite element results for $\alpha = 0$ and $\alpha = 0.02$ are indicated. As mentioned before, α defined in (2.12) affects the ability of the stress field to influence the electric field. In most existing analytical solutions, this parameter has been set to zero to simplify the analysis. Figure 5 shows that a realistic value $\alpha = 0.02$, does not change the electric field substantially, and both sets of results agree with the HGS solution.

Figure 6 compares the electric displacement distribution. Again, the two cases $\alpha = 0$ and $\alpha = 0.02$ give similar results. The difference between the finite element solutions and the HGS solution is caused by different D–E relations used in the calculations
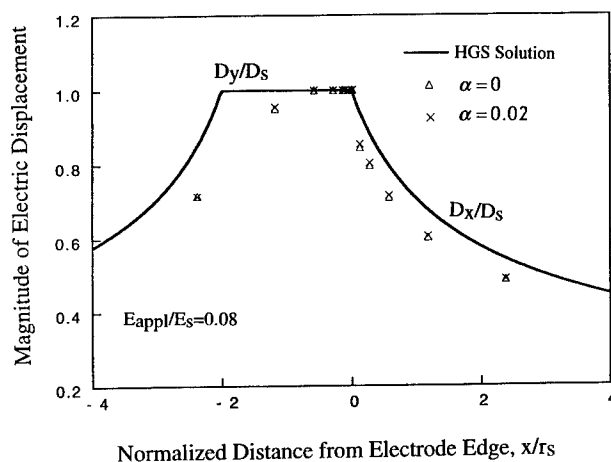

Fig. 6. The electric displacement distributions along the x-axis under the small-scale saturation conditions.
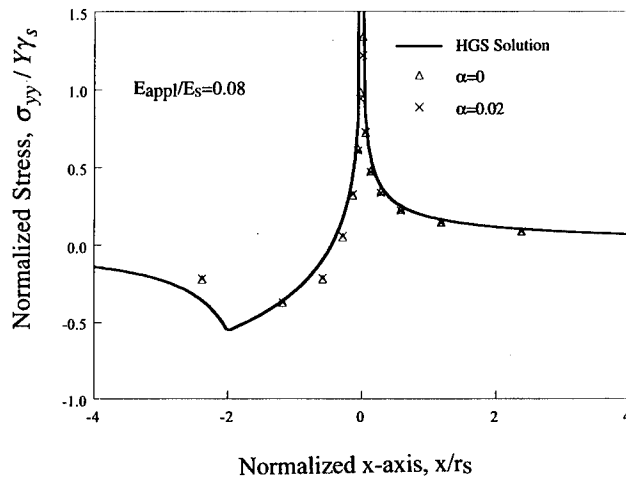
Fig. 7. The normal stress σ_{yy} in the electrode plane and in the plane directly ahead of the electrode edge.

(shown in Fig. 3). This is confirmed by comparing the finite element results with the existing analytical solutions in Appendix B.

Stress distributions along the x-axis are plotted in Figs 7 and 8. The small differences between the HGS solution and the finite element calculation suggest that the stress singularity does not change when using a slightly different D–E relations in Fig. 3. It also suggests that a similar stress intensity factor should be obtained. Consequently, details in the shape of the D–E relation plays little role as far as cracking condition is concerned.

Since the stress contributes negligibly to the electric field. Our finite element calculation under the large-scale saturation conditions will focus on the case $\alpha = 0$.
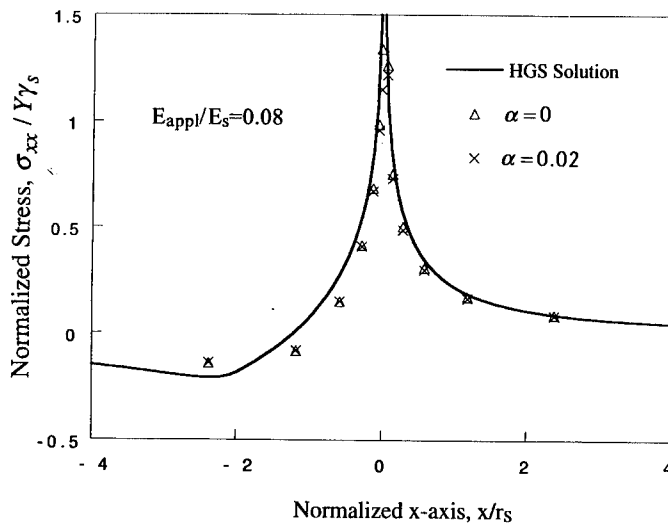

Fig. 8. The normal stress σ_{xx} in the electrode plane and in the plane directly ahead of the electrode edge.
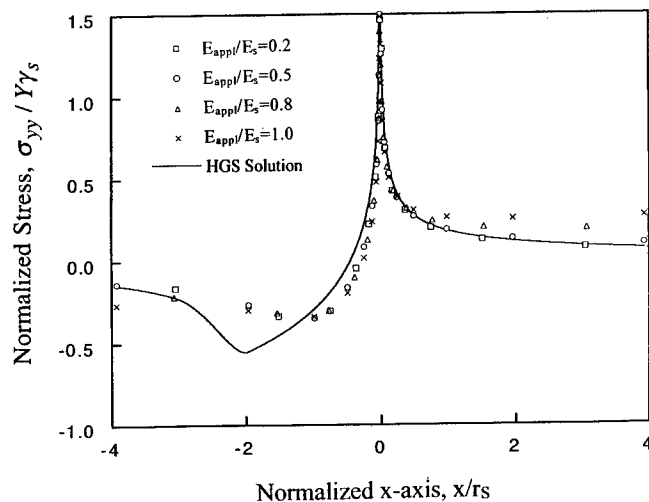
Fig. 9. The normal stress σ_{yy} in the electrode plane and in the plane directly ahead of the electrode edge for different applied electric fields.

4. LARGE-SCALE SATURATION

When the applied electric loading approaches the saturation electric field, the saturation zone size becomes comparable to the layer thickness. The electric field in the ceramic is no longer $r^{-1/2}$ distributed around the electrode edge. Consequently, the electric field intensity factor, K_E, is no longer meaningful, nor is the saturation cylinder radius, r_s. Nevertheless, we can normalize lengths in the similar manner as in the small-scale saturation case by a characteristic length, still written as r_s, but defined by

$$r_s = \frac{H E_{appl}^2}{\pi E_s^2}.$$ (4.1)

This definition is motivated by combining (3.2) and (3.3), although neither holds the original physical meaning. Figures 9 and 10 plot the stresses along x-axis at different applied electric fields. The solid lines are the stress distributions under the small-scale conditions. It may be instructive to think of the stress field as a combination of the local logarithmic singular stress field and the global uniform stress field. Near the electrode edge, the stress distributions are similar to those under the small-scale saturation conditions. Far away from the electrode edge, the stress is uniform, compressive behind the edge and tensile ahead of the edge (2.10).

Once the stress field is determined, the stress intensity factor K_I is evaluated for a small flaw from (2.11). The value of K_I depends on the position, orientation and size of the flaw introduced in the calculation. Such information on flaws is in general unavailable, or at the best, imprecise. We assume that the length of the crack-like flaw, a, is on the order of grain diameter, much smaller than the layer thickness, H. To be definite, we place the flaw along the x-axis, with one tip of the flaw at the point behind the electrode edge, where the normal stress changes from compression to
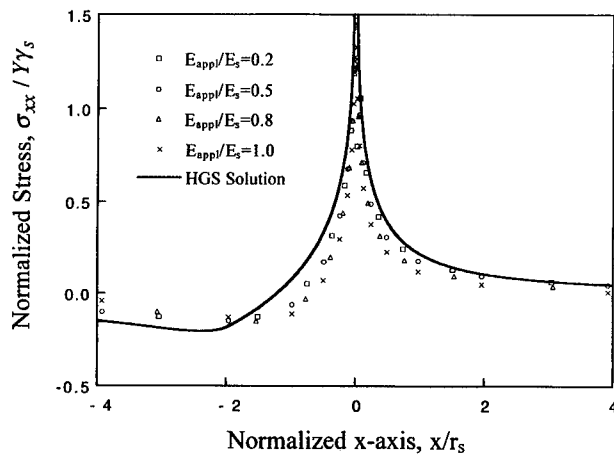
Fig. 10. The normal stress σ_{xx} in the electrode plane and in the plane directly ahead of the electrode edge for different applied electric fields.

tension. Figure 11 shows the calculated stress intensity factor at different applied electric fields. They all peak when the other flaw tip is at the electrode edge, and reaches similar value. The peak value of K_1 is written as

$$(K_1)_{\max} \cong 0.25 Y\gamma_s \sqrt{2H \frac{E_{\mathrm{appl}}}{E_s}}. \tag{4.2}$$

It is noted from Fig. 11 that the prefactor varies with the load level E_{appl}/E_s, but only
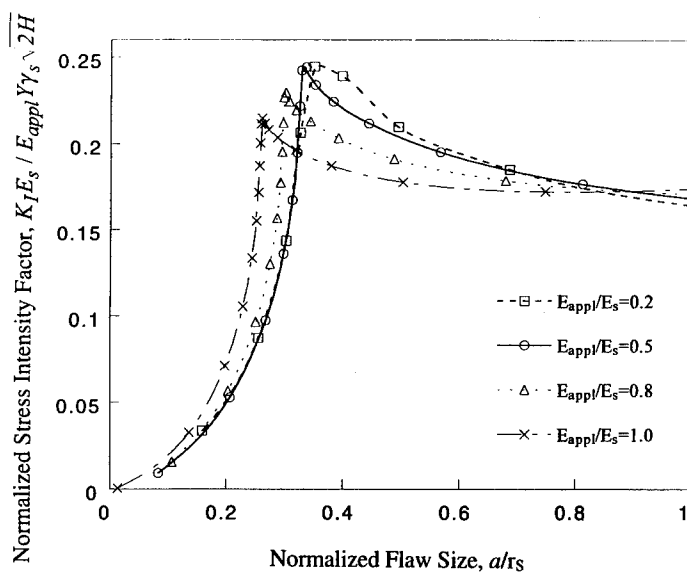

Fig. 11. The stress intensity factor for flaws under different loads.
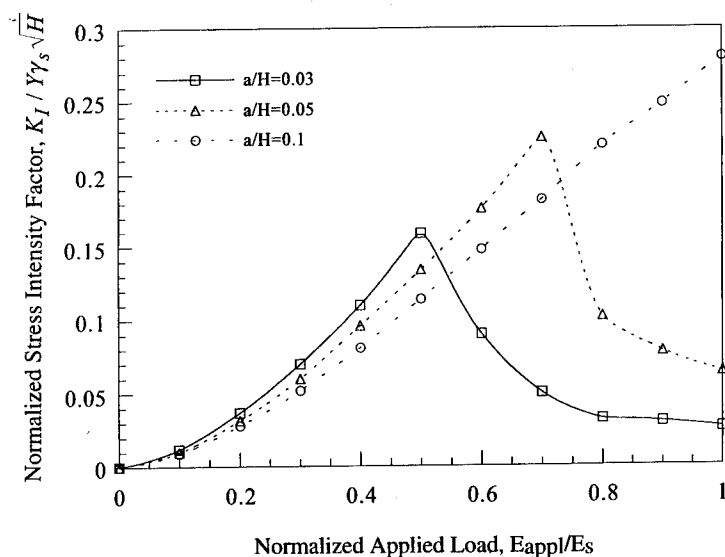
X. GONG and Z. SUO

Fig. 12. The stress intensity factor for fixed flaw sizes.

by a small amount. A larger value is chosen to write (4.2) for conservative design. No flaw will grow if $(K_I)_{max} < K_{Ic}$. Equation (4.2) defines a critical layer thickness

$$H_c = 8\left(\frac{K_{Ic}E_s}{Y\gamma_s E_{appl}}\right)^2.$$ (4.3)

No flaw will grow if every individual layer of the actuator is thinner than H_c. The form of the above expression is identical to the small-scale saturation approximation (3.7). The prefactor in (4.3), however, depends on the load level E_{appl}/E_s. The value used in (4.3) belongs to $E_{appl}/E_s = 0.2$, which serves as a conservative approximation, judging from Fig. 11.

The above cracking condition is derived under the assumption that small flaws are available in a size range, and the flaw that maximizes K_I is critical. Consequently, the cracking condition so derived does not depend on the flaw size. If, however, the flaw size a is known from processing, a different cracking condition can be formulated. Figure 12 shows crack driving force for three flaw sizes as a function of applied electric loads. For large flaws, K_I keeps increasing as the applied loading increases. For small flaws, K_I peaks at a certain applied load. The peak values are basically the same as one obtained from Fig. 11. Based on this behavior, we construct a maximum crack driving force versus normalized flaw sized curve in Fig. 13. Below this curve, flaws cannot grow at any electrical loads.

5. CONCLUDING REMARKS

The finite element calculation indicates that the crack nucleation condition deduced from the small-scale saturation is still approximately valid when the applied electric
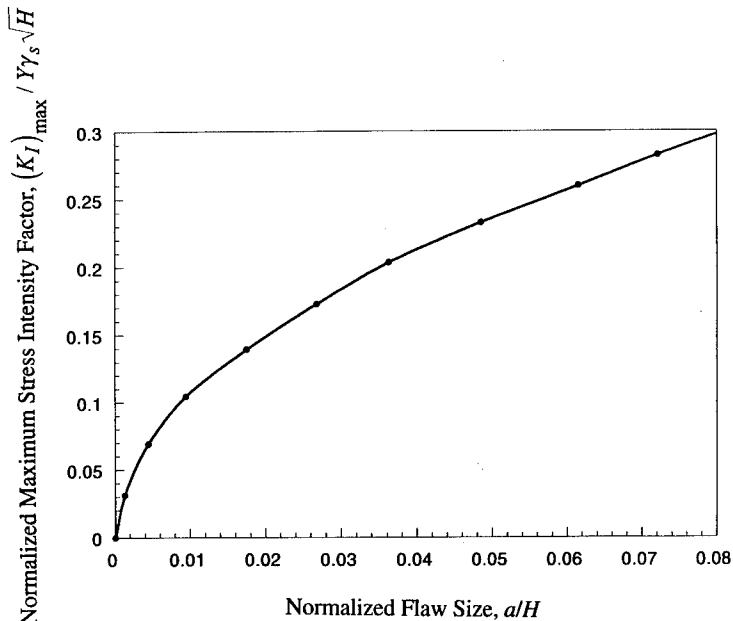
Fig. 13. The maximum stress intensity factor.

field approaches the saturation field. More accurate cracking conditions under the large-scale saturation conditions can also be obtained in similar forms, but with different numerical coefficients. Stress induced by electrostriction consists of two parts: a uniform stress induced by the overall strain mismatch far behind and far ahead of the electrode edge, and a nonuniform stress induced by the electric field concentration near the electrode end. For the particular geometry we have analyzed in the paper, the second part plays the dominant role in crack nucleation. For a typical actuator, where the gap between the internal electrode edge and the actuator end (L_1 in Fig. 4) is comparable to the layer thickness H, a further study on actuator geometry dependence of the cracking criterion is necessary.

ACKNOWLEDGEMENT

REFERENCES

Aburatani, H., Harada, S., Uchino, K. and Furuta, A. (1994) Destruction mechanism of ceramic multilayer actuators. *Japanese J. Appl. Phys.* **33**, 3091–3094.
Cao, H. C. and Evans, A. G. (1993) Nonlinear deformation of ferroelectric ceramics. *J. Am. Ceram. Soc.* **76**, 890–896.

Furuta, A. and Uchino, K. (1993) Dynamic observation of crack propagation in piezoelectric multilayer actuators. *J. Am. Ceram. Soc.* **76,** 1615–1617.

Gong, X. (1994) Stresses near the end of an internal electrode in multilayer electrostrictive ceramic actuators. *Mater. Res. Soc. Symp. Proc.* **360,** 83–88.

Gong, X. (1995) A finite element solution of failures in capacitor-type multilayer ferroelectric ceramic actuators. *Adaptive Material Systems, ASME,* 57–63.

Hom, C. L. and Shankar, N. (1994) A fully coupled constitutive model for electrostrictive ceramic materials. *J. Intelligence Mater. Sys. Struct.* **5,** 795–801.

Hom, C. L. and Shankar, N. (1995) A finite element method for electrostrictive ceramic devices. *Int. J. Solids Struct.,* in press.

Hao, T. H., Gong, X. and Suo, Z. (1996) Fracture mechanics for the design of ceramic multilayer actuators. *J. Mech. Phys. Solids* **44,** 23–48.

Lynch, C. S. (1995) The effect of uniaxial stress on the electro-mechanical response of 8/65/35 PLZT. Submitted to *Acta Metall. Mater.*

Lynch, C. S., Yang, W., Collier, L., Suo, Z. and McMeeking, R. M. (1994) Electric field induced cracking in ferroelectric ceramics. *Ferroelectrics* **166,** 11–30.

Rice, J. R. (1967) Stresses due to a sharp notch in a work-hardening elastic-plastic material loaded by longitudinal shear. *J. Appl. Mech.* **34,** 287–298.

Rogers, C. A. (1995) Intelligent materials. *Scientific American,* September Issue, 154–157.

Schneider, G. A., Rostek, A., Zickgraf, B. and Aldinger, F. (1994) Crack growth in ferroelectric ceramics under mechanical and electrical loading. *Proc. 4th, Int. Conf. Elect. Ceram. & Appl.* 1211–1216.

Suo, Z. (1991) Mechanics concepts for failure in ferroelectric ceramics. *Smart Structures and Materials* (ed. A. V. Srinvasan), pp. 1–6. ASME, New York.

Suo, Z. (1993) Models for breakdown resistant dielectric and ferroelectric ceramics. *J. Mech. Phys. Solids* **41,** 1155–1176.

Tada, H., Paris, P. C. and Irwin, G. R. (1985) *The Stress Analysis of Cracks Handbook.* Del Research, St. Louis, MO.

Uchino, K. (1993) Ceramic actuators: principles and applications. *MRS Bulletin,* April Issue, 42–48.

Uchino, K. and Nomura, S. (1983) Electrostriction in PZT-family antiferroelectrics. *Ferroelectrics* **50,** 191–196.

Winzer, S. R., Shankar, N. and Ritter, A. P. (1989) Designing cofired multilayer electrostrictive actuators for reliability. *J. Am. Ceram. Soc.* **72,** 2246–2257.

Yang, W. and Suo, Z. (1994) Cracking in ceramic actuators caused by electrostriction. *J. Mech. Phys. Solids* **42,** 649–663.

Yoshikawa, S. and Shrout, T. (1993) Multilayer piezoelectric actuators: structures and reliability. American Institute of Aeronautics and Astronauts (AIAA)-93-1711-CP.

Zienkiewicz, O. C. (1977) *The Finite Element Method.* McGraw-Hill Book Company.

APPENDIX A: FINITE ELEMENT METHOD FOR NONLINEAR ELECTROSTRICTIVE CERAMICS

We use eight-node quadratic isoparametric elements (Zienkiewicz, 1977). Divide the physical plane x–y into many (possibly curved) quadrilaterals, and map every element to a square with side length 2 in the calculation plane ξ–η according to

$$x = \sum_{i=1}^{8} x_i N_i(\xi, \eta), \quad y = \sum_{i=1}^{8} y_i N_i(\xi, \eta), \tag{A.1}$$

where (x_i, y_i) are the nodal position vectors, and $N_i(\xi, \eta)$ are the interpolation functions. Denote the nodal values of the displacements and electric potential by u_i, v_i, ϕ_i. Approximate the field $u(x, y), v(x, y),$ and $\phi(x, y)$ within an element in the same way as the position vectors, namely

$$u(x,y) = \sum_{i=1}^{8} u_i N_i(\xi,\eta), \quad v(x,y) = \sum_{i=1}^{8} v_i N_i(\xi,\eta), \quad \phi(x,y) = \sum_{i=1}^{8} \phi_i N_i(\xi,\eta). \quad (A.2)$$

Write all the nodal values of u, v, and ϕ on the mesh by a column, $\mathbf{a}$, and assemble the above interpolation in matrix form

$$\begin{bmatrix} u(x,y) \\ v(x,y) \\ \phi(x,y) \end{bmatrix} = \mathbf{N}\mathbf{a}, \qquad (A.3)$$

where $\mathbf{N}$ contains the interpolation functions for all the nodes of the entire mesh.

The basic field equations in Section 2 can be written as a weak statement

$$\int(\sigma_{ij}\,\delta\gamma_{ij} - D_i\,\delta E_i)\,\mathrm{d}v = \int(t_i\,\delta u_i - \omega\,\delta\phi)\,\mathrm{d}s. \qquad (A.4)$$

Here $\delta(\ )$ indicates small variations. Denote

$$\mathbf{\Sigma} = \begin{bmatrix} \sigma_x \\ \sigma_y \\ \tau_{xy} \\ D_x \\ D_y \end{bmatrix}, \quad \mathbf{\Gamma} = \begin{bmatrix} \gamma_x \\ \gamma_y \\ 2\gamma_{xy} \\ -E_x \\ -E_y \end{bmatrix}, \quad \mathbf{T} = \begin{bmatrix} t_x^0 \\ t_y^0 \\ -\omega^0 \end{bmatrix}. \qquad (A.5)$$

Here $\mathbf{t}^0$ is the traction prescribed on part of the boundary S_t, and ω^0 is the charge per unit area prescribed on part of the boundary S_ω. Taking gradients of the displacements and the electric potential according to (A.3) and (2.1), one obtains that

$$\delta\mathbf{\Gamma} = \mathbf{B}\,\delta\mathbf{a}, \qquad (A.6)$$

where $\mathbf{B}$ is the matrix resulting from the differentiation. In the discretized form (A.4) becomes

$$\delta\mathbf{a}^T\int_v \mathbf{B}^T\mathbf{\Sigma}\,\mathrm{d}v = \delta\mathbf{a}^T\int_{S_t+S_\omega} \mathbf{N}^T\mathbf{T}\,\mathrm{d}S. \qquad (A.7)$$

The superscript T stands for the transpose of a matrix. Since (A.7) holds true for arbitrarily chosen $\delta\mathbf{a}$, one concludes that

$$\int_v \mathbf{B}^T\mathbf{\Sigma}\,\mathrm{d}v = \int_{S_t+S_\omega} \mathbf{N}^T\mathbf{T}\,\mathrm{d}S. \qquad (A.8)$$

Notice $\mathbf{\Sigma}$ is a function of $\mathbf{\Gamma}$, and therefore a function of $\mathbf{a}$. Equation (A.8) is a set of nonlinear equations for a nodal variables $\mathbf{a}$. They are solved incrementally by linear equations

$$\mathbf{K}\,\Delta\mathbf{a} = \Delta\lambda\mathbf{R}. \qquad (A.9)$$

Here $\Delta\mathbf{a}$ is the increment, $\Delta\lambda$ is a parameter that controls the loading increment, $\mathbf{K}$ is the tangential stiffness matrix

$$\mathbf{K} = \int_v \mathbf{B}^T\mathbf{C}^{-1}\mathbf{B}\,\mathrm{d}v, \qquad (A.10)$$

and $\mathbf{R}$ is the equivalent load

$$\mathbf{R} = \int_{S_t+S_\omega} \mathbf{N}^T\mathbf{T}\,\mathrm{d}S. \qquad (A.11)$$

The matrix $\mathbf{C}$ contains the differential coefficients of the constitutive equations, namely

$$d\Gamma = \mathbf{C}\,d\Sigma. \tag{A.12}$$

The matrix $\mathbf{C}$ is symmetric, but in general not positive-definite.

APPENDIX B: ELECTRIC FIELD NEAR ELECTRODE EDGE

When the effect of stress on the electric field is negligible, the governing equations for the electric field around an electrode edge take the same form as the governing equations for the
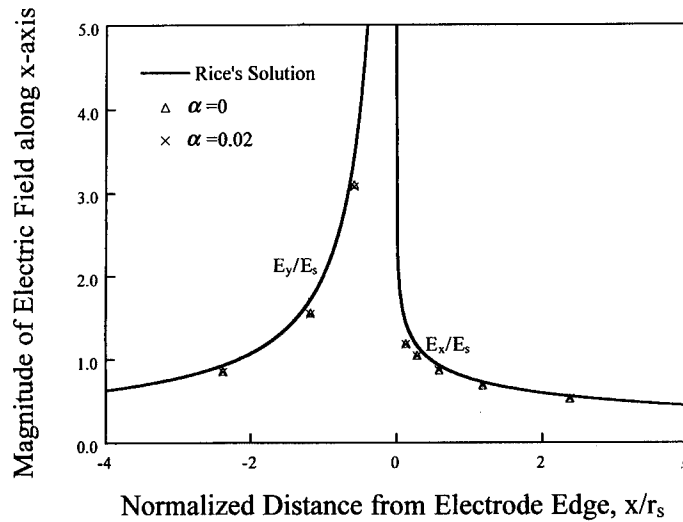

Fig. B1. Comparison of the electric field distribution along the x-axis between finite element solution and the analytic solution.
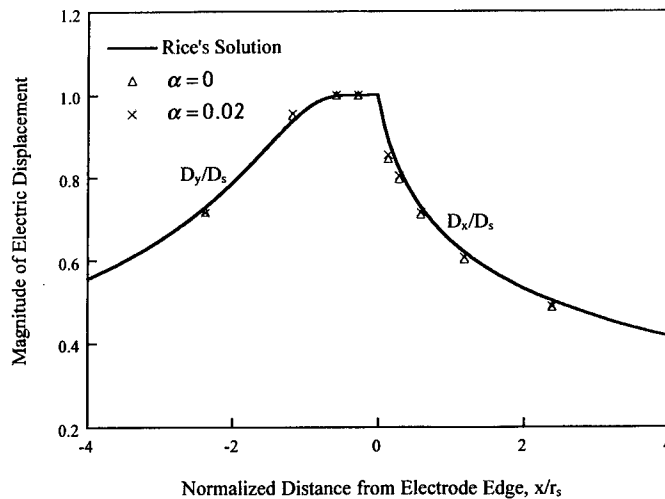

Fig. B2. Comparison of the electric displacement distribution along the x-axis between finite element solution and the analytic solution.

stress field around a mode III crack tip. We now interpret Rice's (1967) solution of a mode III crack in a nonlinearly elastic solid for an electrode in a nonlinearly dielectric solid. Let D, E be the magnitude of electric displacement and electric field, φ be the angle between the direction of the electric field and the x-direction, measured positive counterclockwise. Write

$$X(E) = \frac{K_E^2}{2\pi E_s^2} \left[2 \int_E^\infty \frac{du}{u^2 D(u)} - \frac{1}{ED(E)} \right], \tag{B.1}$$

$$R(E) = \frac{K_E^2}{2\pi E_s^2 ED(E)}, \tag{B.2}$$

where K_E is the electric field intensity factor of an asymptotic approach to the linear D–E interaction. For a given electric field magnitude E, the position coordinates are

$$x = -X(E) - R(E)\cos 2\varphi, \quad y = R(E)\sin 2\varphi. \tag{B.3}$$

This solution for the dielectric law (2.5) is plotted and compared with the finite element solution for small scale saturation in Fig. A1 and Fig. A2.

Pergamon

PII S0022–5096(96)00002–6

THE INTERFACE CRACK PROBLEM FOR A NONHOMOGENEOUS COATING BONDED TO A HOMOGENEOUS SUBSTRATE

Y. F. CHEN and F. ERDOGAN

Department of Mechanical Engineering and Mechanics, Lehigh University, Bethlehem, PA 18015, U.S.A.

ABSTRACT

The debonding problem for a composite layer that consists of a homogeneous substrate and a non-homogeneous coating is considered. It is assumed that the problem is one of plane strain or generalized plane stress and the elastic medium contains a crack along the interface. It is further assumed that the thermomechanical properties of the medium are continuous functions of the thickness coordinate with discontinuous derivatives and the kink line of the property distributions corresponds to the "interface". The mixed-mode crack problem is formulated for arbitrary crack surface tractions and sample results are given for uniform normal and shear tractions. The main variables in the problem are two dimensionless length parameters and a nonhmogeneity constant. Calculated results consist of primarily the stress intensity factors and the strain energy release rate and are partly intended to provide benchmark solutions for further numerical studies.

1. INTRODUCTION

In many high temperature applications such as advanced turbine systems and earth-to-orbit winged planes, to achieve higher efficiencies and higher velocities the use of structural ceramics is becoming almost a necessity for the protection of hot section components. For example, in large natural gas-fired stationary turbines currently in service, with 1260°C rotor inlet temperature the lower heating value plant efficiency is approximately 54%. With some innovations in design and changes in materials and cooling systems, a goal of increasing the plant efficiency to 60% does not seem to be unrealistic. This, in turn, requires raising the inlet temperature to well over 1400°C and the development and use of new materials and coatings. The homogeneous ceramic coatings used for this purpose seem to have some reliability and durability problems that need to be addressed. The problems arise from relatively high residual and thermal stresses caused by the mismatch in thermal expansion coefficients, generally poor bonding of ceramic layers to metal substrates, very low resistance of most refractory ceramics used as coatings to oxygen diffusion, and low toughness of ceramics. Homogeneous coatings, therefore, tend to be highly susceptible to cracking and spallation.

An alternative concept that may be used to overcome some of the shortcomings of

the homogeneous ceramic coatings would be the introduction of an interfacial zone with graded thermomechanical properties between the coating and the substrate or the replacement of the coating by a composite layer with a volume fraction varying between 0% ceramic and 100% metal on the interface and 100% ceramic and 0% metal near and at the surface. Such particulate composites with continuously varying volume fractions are called functionally graded materials (FGM) [for review and extensive references see Yamanouchi *et al.* (1990) and Holt *et al.* (1993)]. The use of functionally graded layers seems to reduce the magnitude of the residual and thermal stresses (Lee and Erdogan, 1994), significantly increase the coating/substrate bonding strength (Kurihara *et al.*, 1990) and, by increasing the fracture toughness in thickness direction, provide the composite medium with a natural R-curve behaviour (Saito and Takahashi, 1990). By controlling not only the composition profile but also the microstructure, the concept of functionally graded materials provides a great deal of flexibility in material design. As the processing techniques improve, the potential for the high technology oriented applications of the concept appears to be unlimited. However, in the near future the primary use of these new materials will most likely be limited to thermal barrier coatings (mainly in gas turbines), wear-resistant coatings in bearings, gears, cams and machine tools, and interfacial zones to bond basically incompatible materials such as diamond films and metal substrates (Kurihara *et al.*, 1990).

Aside from the intentionally graded materials, there are also other materials in which thermomechanical properties vary continuously as a natural consequence of processing. For example, in the case of ion plating, the impact of charged particles causes considerable mixing of the two materials through sputtering, resulting in a coating that has a gradual change in its composition (Spalvins, 1985). Similarly, the electron microprobe analysis shows that in most diffusion bonding processes the atomic compositions of the two materials vary continuously across the nominal interface (Shiau *et al.*, 1988, Brennan, 1991). At a greater length scale such materials as bones, sea shells, bamboo stems and shale/sandstone interfaces are examples of natural functionally graded materials. From a viewpoint of mechanics, the field in which material nonhomogeneity was first recognized and studied appears to be soil mechanics where generally the stiffness variation resulting from the change in over-burden pressure is too significant to ignore (Olszak, 1958).

In layered structures such as ceramic-coated metal substrates, there are mainly three groups of fracture problems, namely surface cracking and crack penetration, debonding, and edge delamination. In trying to obtain analytical benchmark solutions, the problems are usually treated as being plane strain or axisymmetric. In this study we consider the problem of debonding in a composite layer which consists of a homogeneous substrate and a nonhomogeneous coating. It is assumed that the problem is one of plane strain or generalized plane stress, and the elastic medium contains a crack along the interface (Fig. 1). The coating is processed in such a way that the thermomechanical properties of the medium are continuous with discontinuous derivatives and the kink line of the property distribution corresponds to the "interface". In addition to the parameter describing the degree of nonhomogeneity in the coating, the main variables in the problem are the dimensionless constants h_1/a and h_2/a where $2a$, h_1 and h_2 are, respectively, the crack length, the substrate thickness and the coating
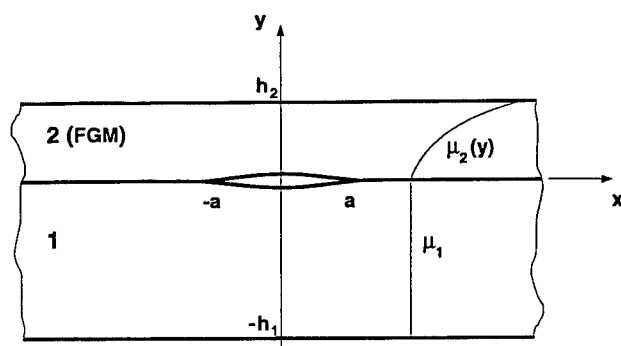
Fig. 1. Geometry of the interface crack for a functionally graded coating bonded to a homogeneous substrate.

thickness. The crack surface tractions are assumed to be the only nonzero external loads.

In similar studies considered previously it was generally assumed that the non-homogeneous medium consists of infinite or semi-infinite planes. The mode I and mixed mode plane strain crack problems were studied by Delale and Erdogan (1983) and Konda and Erdogan (1994), respectively. The corresponding axisymmetric problem was considered by Ozturk and Erdogan (1993). The interface crack problem shown in Fig. 1 with $h_1 = \infty$, $h_2 = \infty$ was studied by Delale and Erdogan (1988).

2. FORMULATION

In the plane elasticity problem shown in Fig. 1, it is assumed that the substrate is homogeneous with elastic constants μ_1, κ_1, the coating is nonhomogeneous with elastic parameters $\mu_2(y)$, $\kappa_2(y)$, and μ_2 is approximated by

$$\mu_2(y) = \mu_1 e^{y\gamma}, \tag{1}$$

where μ_i is the shear modulus, $\kappa_i = 3 - 4v_i$ for plane strain and $\kappa_i = (3 - v_i)/(1 + v_i)$ for generalized plane stress, v_i being the Poisson's ratio ($i = 1, 2$). In previous studies it was shown that the influence of the variation in Poisson's ratio on stress intensity factors is rather insignificant and, therefore, κ may be assumed to be constant throughout the medium. Thus, by substituting from the stress/displacement relations

$$\sigma_{xx} = \frac{\mu}{\kappa - 1}\left[(\kappa + 1)\frac{\partial u}{\partial x} + (3 - \kappa)\frac{\partial v}{\partial y}\right],$$

$$\sigma_{yy} = \frac{\mu}{\kappa - 1}\left[(3 - \kappa)\frac{\partial u}{\partial x} + (\kappa + 1)\frac{\partial v}{\partial y}\right],$$

$$\sigma_{xy} = \mu\left(\frac{\partial u}{\partial y} + \frac{\partial v}{\partial x}\right) \tag{2a–c}$$

into the equilibrium equations and by using (1), for the medium 2, i.e. for $0 < y < h_2$ we obtain

$$(\kappa+1)\frac{\partial^2 u_2}{\partial x^2} + (\kappa-1)\frac{\partial^2 u_2}{\partial y^2} + 2\frac{\partial^2 v_2}{\partial x \partial y} + \gamma(\kappa-1)\left(\frac{\partial u_2}{\partial y} + \frac{\partial v_2}{\partial x}\right) = 0,$$

$$(\kappa-1)\frac{\partial^2 v_2}{\partial x^2} + (\kappa+1)\frac{\partial^2 v_2}{\partial y^2} + 2\frac{\partial^2 u_2}{\partial x \partial y} + \gamma(3-\kappa)\frac{\partial u_2}{\partial x} + \gamma(\kappa+1)\frac{\partial v_2}{\partial y} = 0. \quad \text{(3a,b)}$$

Equations similar to (3) with $\gamma = 0$ are satisfied by the displacements u_1 and v_1 for medium 1, $-h_1 < y < 0$.

By using standard Fourier transforms, for the nonhomogeneous layer 2 (Fig. 1) it can be shown that

$$u_2(x,y) = \frac{1}{2\pi}\int_{-\infty}^{\infty} \sum_1^4 C_k(\alpha)e^{n_k y}e^{i\alpha x}\,d\alpha,$$

$$v_2(x,y) = \frac{1}{2\pi}\int_{-\infty}^{\infty} \sum_1^4 m_k(\alpha)C_k(\alpha)e^{n_k y}e^{i\alpha x}\,d\alpha \qquad \text{(4a,b)}$$

where $C_1, \ldots, C_4$ are unknown functions of α, $n_1, \ldots, n_4$ are the roots of the characteristic equation

$$n^4 + 2\gamma n^3 - (2\alpha^2 - \gamma^2)n^2 - 2\alpha^2\gamma n + \frac{3-\kappa}{1+\kappa}\alpha^2\gamma^2 + \alpha^4 = 0, \qquad \text{(5)}$$

and $m_1, \ldots, m_4$ are given by

$$m_k(\alpha) = \frac{-i\alpha[2n_k + \gamma(3-\kappa)]}{(\kappa+1)n_k^2 + \gamma(\kappa+1)n_k - (\kappa-1)\alpha^2}, \quad k = 1,\ldots,4. \qquad \text{(6)}$$

Solving (5) we find

$$n_1 = \bar{n}_2 = \tfrac{1}{2}(-\gamma + Re^{i\theta}), \quad n_3 = \bar{n}_4 = -\tfrac{1}{2}(\gamma + Re^{-i\theta}), \qquad \text{(7)}$$

$$R = \left[(\gamma^2 + 4\alpha^2)^2 + 16\alpha^2\gamma^2\left(\frac{3-\kappa}{1+\kappa}\right)\right]^{1/4},$$

$$\theta = \tfrac{1}{2}\tan^{-1}\left[\frac{4\alpha\gamma}{\gamma^2 + 4\alpha^2}\left(\frac{3-\kappa}{1+\kappa}\right)^{1/2}\right], \qquad \text{(8a,b)}$$

where the bar stands for complex conjugate.

Similarly, for medium 1, $-h_1 < y < 0$, $\gamma = 0$ and from (5) it may be seen that $n = \mp\alpha$ are double roots. Thus, the solution of (3) with $\gamma = 0$ may be expressed as

$$u_1(x,y) = \frac{1}{2\pi}\int_{-\infty}^{\infty} [(A_1 + A_2 y)e^{|\alpha|y} + (A_3 + A_4 y)e^{-|\alpha|y}]e^{i\alpha x}\,d\alpha,$$

$$v_1(x,y) = \frac{1}{2\pi}\int_{-\infty}^{\infty} [(B_1 + B_2 y)e^{|\alpha|y} + (B_3 + B_4 y)e^{-|\alpha|y}]e^{i\alpha x}\,d\alpha, \qquad \text{(9a,b)}$$

$$B_1 = -\frac{i\alpha}{|\alpha|}A_1 + \frac{i\kappa}{\alpha}A_2, \quad B_2 = -\frac{i\alpha}{|\alpha|}A_2,$$

$$B_3 = \frac{i\alpha}{|\alpha|}A_3 + \frac{i\kappa}{\alpha}A_4, \quad B_4 = \frac{i\alpha}{|\alpha|}A_4 \tag{10a–d}$$

where $A_1, \ldots, A_4$ are again unknown functions of α.

The unknowns C_k and A_k $(k = 1, \ldots, 4)$ are obtained from the following boundary and continuity conditions

$$\sigma_{2yy}(x, h_2) = 0, \quad \sigma_{2xy}(x, h_2) = 0, \quad -\infty < x < \infty, \tag{11a,b}$$

$$\sigma_{1yy}(x, -h_1) = 0, \quad \sigma_{1xy}(x, -h_1) = 0, \quad -\infty < x < \infty, \tag{12a,b}$$

$$\sigma_{2yy}(x, +0) = \sigma_{1yy}(x, -0), \quad \sigma_{2xy}(x, +0) = \sigma_{1xy}(x, -0), \quad -\infty < x < \infty, \tag{13a,b}$$

$$\sigma_{1yy}(x, -0) = p_1(x), \quad \sigma_{1xy}(x, -0) = p_2(x), \quad -a < x < a, \tag{14a,b}$$

$$u_2(x, +0) - u_1(x, -0) = 0, \quad v_2(x, +0) - v_1(x, -0) = 0, \quad |x| > a, \tag{15a,b}$$

where the crack surface tractions p_1 and p_2 are known functions. The homogeneous equations (11)–(13) may be used to eliminate six of the eight unknowns A_k, C_k $(k = 1, \ldots, 4)$ and the mixed boundary conditions (14) and (15) would give a pair of dual integral equations to determine the remaining two.

3.   THE INTEGRAL EQUATIONS

Replacing the mixed boundary conditions (14) and (15) by

$$\frac{\partial}{\partial x}[v_2(x, +0) - v_1(x, -0)] = f_1(x), \quad -\infty < x < \infty,$$

$$\frac{\partial}{\partial x}[u_2(x, +0) - u_1(x, -0)] = f_2(x), \quad -\infty < x < \infty, \tag{16a,b}$$

it is seen that all eight unknown functions $A_k(\alpha)$ and $C_k(\alpha)$, $(k = 1, \ldots, 4)$ may be determined in terms of f_1 and f_2 by using (11)–(13) and (16). It is also seen that (15) would be satisfied if we require

$$f_j(x) = 0, \quad |x| > a, \quad j = 1, 2, \tag{17}$$

$$\int_{-a}^{a} f_j(x)\, dx = 0, \quad j = 1, 2. \tag{18}$$

The new unknown functions f_1 and f_2 would then be determined by using the conditions (14). Referring to Chen (1990) for details, (14) may be expressed as follows

$$\frac{1}{\pi}\int_{-a}^{a}\sum_{1}^{2}K_{ij}(x,t)f_j(t)\,\mathrm{d}t = \frac{1+\kappa}{2\mu_1}p_i(x), \quad i = 1,2, \quad -a < x < a, \tag{19}$$

where the kernels K_{ij} $(i,j = 1,2)$ are known functions.

In the crack problem under consideration the singular behaviour of the stress state near the crack tips will be dependent on that of the density functions f_1 and f_2, which, in turn, is controlled by the singularities of the kernels K_{ij}. For a crack embedded in a homogeneous medium the kernels have the form

$$K_{ij}(x,t) = \frac{\delta_{ij}}{t-x} + g_{ij}(x,t), \quad (i,j = 1,2), \tag{20}$$

where the terms g_{ij} are square integrable in $-a \leqslant (x,t) \leqslant a$ and do not contribute to the singular nature of the solution. The Cauchy kernel shown in (20) leads to the conventional square-root singularity for f_1 and f_2 and, indirectly, for the stresses. In piecewise homogeneous materials containing an interface crack (along the x axis) the kernels K_{ij} are of the form (Erdogan and Gupta, 1971)

$$K_{11}(x,t) = \frac{\gamma_1}{t-x} + h_{11}(x,t), \quad K_{12}(x,t) = \gamma_2\,\delta(t-x) + h_{12}(x,t),$$

$$K_{21}(x,t) = -\gamma_2\,\delta(t-x) + h_{21}(x,t), \quad K_{22}(x,t) = \frac{\gamma_1}{t-x} + h_{22}(x,t), \tag{21}$$

where γ_1 and γ_2 are bimaterial constants and the square-integrable kernels h_{ij} depend on the part/crack geometry as well as the material constants. With the kernels as given by (21) the integral equations (19) become one of the second kind, giving the well-known stress and displacement oscillations at the crack tips.

In the present problem the kernels K_{ij} which appear in (19) may be expressed as follows (Chen, 1990)

$$K_{ij}(x,t) = \lim_{y\to-0}\left(\frac{\kappa+1}{4}\right)\int_{-\infty}^{\infty} F_{ij}(y,\alpha)\mathrm{e}^{|\alpha|y+i\alpha(x-t)}\,\mathrm{d}\alpha + K_{ij}^0(x,t), \tag{21}$$

where $K_{ij}^0(x,t)$ are known, square-integrable functions. The singular behaviour of K_{ij} at $x = t$ is determined by the asymptotic values of F_{ij} for $|\alpha| \to \infty$. The leading terms of asymptotic expansions of $F_{ij}(y,\alpha)$ for $|\alpha| \to \infty$ are shown to be (Chen, 1990)

$$F_{11}^\infty(y,\alpha) = \frac{2i\alpha}{(\kappa+1)|\alpha|} - \frac{2i\alpha y}{\kappa+1}, \quad F_{12}^\infty(y,\alpha) = \frac{2|\alpha|y}{\kappa+1},$$

$$F_{21}^\infty(y,\alpha) = \frac{2|\alpha|y}{\kappa+1}, \quad F_{22}^\infty(y,\alpha) = \frac{2i\alpha}{(\kappa+1)|\alpha|} + \frac{2i\alpha y}{\kappa+1}. \tag{22}$$

Thus, by using the relations

$$\lim_{y \to -0} \int_0^\infty e^{\alpha y} \sin \alpha(t-x) \, d\alpha = \frac{1}{t-x},$$

$$\lim_{y \to -0} \int_0^\infty \alpha y e^{\alpha y} \sin \alpha(t-x) \, d\alpha = 0, \qquad (23a,b)$$

from (21) and (22) it may easily be shown that

$$K_{ij}(x,t) = \frac{\delta_{ij}}{t-x} + k_{ij}(x,t),$$

$$k_{ij}(x,t) = K_{ij}^0(x,t) + \frac{\kappa+1}{4} \int_{-\infty}^\infty [F_{ij}(0,\alpha) - F_{ij}^\infty(0,\alpha)] e^{i\alpha(x-t)} \, d\alpha. \qquad (24a,b)$$

The functions k_{ij} are now square integrable and are treated as Fredholm kernels. From (24) and (19) it is clear that at the crack tips $x = \mp a$ the unknown functions f_1 and f_2 and consequently the stress state would have the conventional square-root singularity. For the crack geometry given by Fig. 1 the modes I and II stress intensity factors may then be defined and evaluated from

$$k_1(a) = \lim_{x \to a} \sqrt{2(x-a)} \sigma_{yy}(x,0) = -\lim_{x \to a} \frac{2\mu_1}{\kappa+1} \sqrt{2(a-x)} f_1(x),$$

$$k_2(a) = \lim_{x \to a} \sqrt{2(x-a)} \sigma_{xy}(x,0) = -\lim_{x \to a} \frac{2\mu_1}{\kappa+1} \sqrt{2(a-x)} f_2(x). \qquad (25a,b)$$

The integral equations (19) are solved under the single-valuedness conditions (18).

4. ON THE SOLUTION OF INTEGRAL EQUATIONS

To solve the integral equations (19), first the following normalized quantities are defined

$$s = t/a, \quad r = x/a, \quad k_{ij}^*(r,s) = a k_{ij}(x,t),$$

$$f_i^*(s) = f(t) \quad p_i^*(r) = p_i(x), \quad (i,j) = (1,2), \qquad (26)$$

giving

$$\int_{-1}^1 \sum_{j=1}^2 \left[\frac{\delta_{ij}}{s-r} + k_{ij}^*(r,s) \right] f_j^*(s) \, ds = \frac{\pi(\kappa+1)}{2\mu_1} p_i^*(r), \quad (i = 1,2), \quad |r| < 1. \qquad (27)$$

The fundamental solution of (27) is $(1-s^2)^{-1/2}$ and hence, the unknown functions are of the form

$$f_i^*(s) = F_i(s)/(1-s^2)^{1/2}, \quad -1 < s < 1, \quad (i = 1,2). \qquad (28)$$

The new unknown functions F_1 and F_2 are bounded and, therefore, may be expressed as

$$F_i(s) = \sum_0^\infty B_{ij}T_j(s), \quad (i = 1, 2),$$ (29)

where the orthogonal functions $T_0, T_1, \ldots$ are Chebyshev polynomials of the first kind and are associated with the weight function $(1-s^2)^{-1/2}$. The singular integral equations (27) are regularized by using (28), (29) and

$$\frac{1}{\pi} \int_{-1}^1 \frac{T_j(s)\,ds}{(s-r)\sqrt{1-s^2}} = \begin{cases} 0, & j = 0, \quad |r| < 1, \\ U_{j-1}(r), & j > 0, \quad |r| < 1, \\ -\left(r - \frac{|r|}{r}\sqrt{r^2-1}\right)^j \Big/ \left(\frac{|r|}{r}\sqrt{r^2-1}\right), & j \geqslant 0, \quad |r| > 1, \end{cases}$$ (30)

where $U_n(r)$ $(n = 0, 1, \ldots)$ is the Chebyshev polynomial of the second kind. By substituting from (28)–(30) into (27), truncating the series at $j = n$ and using a suitable collocation technique (27) may be reduced to a system of linear algebraic equations in the unknown coefficients B_{ij} $(i = 1, 2, j = 0, 1, \ldots)$. By using the orthogonality of T_j and the single-valuedness conditions (18), it may be seen that

$$B_{io} = 0, \quad (i = 1, 2).$$ (31)

After determining B_{ij}, from (25), (28), (29) and (31) the stress intensity factors may be obtained as

$$k_1(a) = -\frac{2\mu_1}{\kappa+1}\sqrt{a}\sum_1^\infty B_{1j}, \quad k_2(a) = -\frac{2\mu_1}{\kappa+1}\sqrt{a}\sum_1^\infty B_{2j}.$$ (32)

Similarly, by substituting from (26), (28) and (29) into (16), the crack opening displacements may be evaluated as follows

$$v_2(x,+0) - v_1(x,-0) = -\sqrt{a^2-x^2}\sum_1^\infty \frac{1}{j}B_{1j}U_{j-1}(x/a), \quad |x| < a,$$

$$u_2(x,+0) - u_1(x,-0) = -\sqrt{a^2-x^2}\sum_1^\infty \frac{1}{j}B_{2j}U_{j-1}(x/a), \quad |x| < a.$$ (33a,b)

By using (28)–(30), in (27) the integrals involving the Cauchy kernel are evaluated in closed form and the remaining integrals are Gaussian with the weight $(1-s^2)^{-1/2}$. Such integrals can be evaluated quite accurately provided the functions k_{ij}^* are bounded and continuous. However, by examining (24b), it was shown that at $x = t$ (or $r = s$) the Fredholm kernels k_{ij} had discontinuities which could be separated through asymptotic analysis (Chen, 1990). It was also shown that the accuracy of the integrals in (27) involving k_{ij}^* is significantly influenced by the manner in which these discontinuities are handled in numerical analysis. The leading terms giving the discontinuities in k_{ij}^* are as follows (Chen, 1990)

$$(k_{11}^*(r,s), k_{22}^*(r,s)) \sim \int_0^\infty \frac{\sin \alpha a(s-r)}{\alpha} \, d\alpha = \frac{\pi}{2} \frac{|s-r|}{s-r}, \qquad (34)$$

$$(k_{12}^*(r,s), k_{21}^*(r,s)) \sim \int_A^\infty \frac{\cos \alpha a(s-r)}{\alpha} \, d\alpha = -\gamma_0 - \log|Aa(s-r)|$$

$$-\int_0^{|Aa(s-r)|} \frac{\cos \alpha s - 1}{\alpha} \, d\alpha, \qquad (35)$$

where A is a positive constant and γ_0 is the Euler's constant, $\gamma_0 = 0.57721566490$. It was observed that a direct application of Gaussian integration methods to evaluate the integrals of discontinuous functions in (27) could give erroneous results. In the numerical analysis the discontinuous kernels shown in (34) and (35) were separated and the resulting integrals were evaluated in closed form by using

$$\int_{-1}^1 \frac{T_n(s)}{\sqrt{1-s^2}} \frac{|s-r|}{s-r} \, ds = \frac{2}{\pi} U_{n-1}(r) \sqrt{1-r^2}, \quad n \geqslant 1, \qquad (36)$$

$$\int_{-1}^1 \frac{T_n(s)}{\sqrt{1-s^2}} \log|s-r| \, ds = -\frac{\pi}{n} T_n(r), \quad n \geqslant 1. \qquad (37)$$

After obtaining the stress intensity factors from (32), by using the asymptotic behavior of stresses and crack opening displacements given by (25) and the concept of crack closure energy, the strain energy release rate at the crack tip $x = a$ may be evaluated as follows

$$\mathbf{G}(a) = \frac{\pi(\kappa+1)}{8\mu_1} [k_1^2(a) + k_2^2(a)]. \qquad (38)$$

5. RESULTS

In some ceramic coatings and in, for example, dry film lubrication, the stiffness of the coating would be less than that of the substrate. In many other cases involving contact problems and some thermal barrier coatings, usually the coating is stiffer than the substrate. Therefore, in all examples given in this study the normalized nonhomogeneity constant γa is varied between -3 and 3, which covers nearly all cases that may arise in practice. The calculated results are the stress intensity factors k_1, k_2 and the strain energy release rate $\mathbf{G}$ obtained for two loading conditions, namely $p_1(x) = -\sigma_0, p_2(x) = 0$ and $p_1(x) = 0, p_2(x) = -\tau_0$. Three sets of results are obtained and presented by Chen (1990). In the first the effect of Poisson's ratio is examined by varying v between 0.01 and 0.499 for a fixed geometry $h_1/a = 100$, $h_2/a = 1$. In the second for fixed $v = 0.3$ and $h_1/a = 100$ the results are given for $h_2/a = 100, 10, 2, 1$, $0.5, 0.25$. The third set of results are obtained for fixed $v = 0.3$, $h_2/a = 1$, and $h_1/a = 10$, $4, 2, 1$. In this article only some sample results are presented. The results obtained for
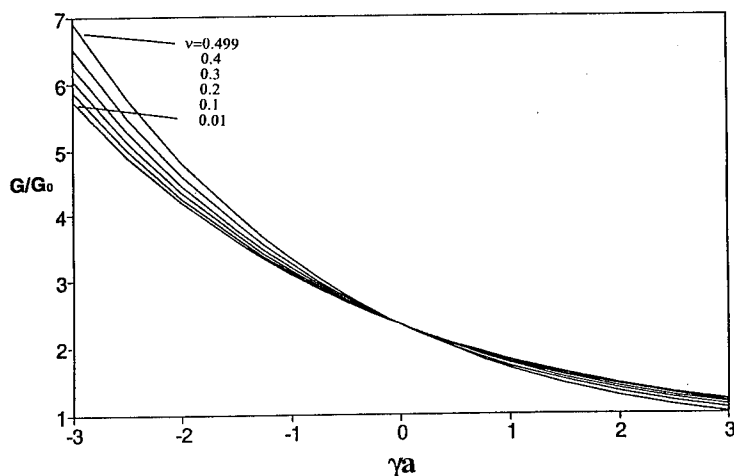
Y. F. CHEN and F. ERDOGAN

Fig. 2. The influence of the Poisson's ratio on the strain energy release rate; loading: uniform crack surface pressure, σ_0.

$h_1/a = h_2/a = 100$ are very nearly the same as that obtained by Delale and Erdogan (1988) for two semi-infinite media.

Figure 2 shows the effect of Poisson's ratio v on the normalized strain energy release rate $\mathbf{G}/\mathbf{G_0}$ for uniform normal tractions $p_1 = -\sigma_0$, $p_2 = 0$ where

$$\mathbf{G_0} = \frac{\pi(\kappa+1)}{8\mu_1}\sigma_0^2 a \qquad (39)$$

is the corresponding value for a homogeneous infinite medium with elastic constants μ_1 and κ. Note that the influence of v may be significant only for large negative values of γa. Also, for $\gamma = 0$ the medium is homogeneous, the Fredholm kernels k_{ij}^* in (27) are independent of the Poisson's ratio v and consequently the normalized strain energy release rate and the stress intensity factors would be independent of v.

In the next set of results given in Figs 3–8 it is assumed that $v = 0.3$, $h_1/a = 100$ and $h_2/a = 1$, 0.5, 0.25. The figures show essentially the effect of the length of an interface crack on $\mathbf{G}$, k_1 and k_2 for a relatively thin FGM coating bonded to a homogeneous substrate. In these and the subsequent figures the normalizing quantities for the strain energy release rate and stress intensity factors are

$$\mathbf{G_0} = \frac{\pi(\kappa+1)}{8\mu_1}p_0^2 a, \quad k_0 = p_0 \sqrt{a}, \quad (p_0 = \sigma_0 \text{ or } \tau_0), \qquad (40)$$

respectively. It may be observed that generally the magnitudes of $\mathbf{G}$, k_1 and k_2 decrease as the stiffness of the coating increases, that is, as the relative thickness h_2/a and the nonhomogeneity constant γa increase.

Figures 9–12 show the effect of the substrate thickness h_1/a on the normalized stress intensity factors for fixed values of $v = 0.3$ and $h_2/a = 1$. It may be observed that for $h_1/a = 10$ and $h_1/a = 4$ the results are very nearly identical. In the homogeneous case of $\gamma = 0$, for $h_1 = h_2$, because of symmetry, the problem uncouples and consequently
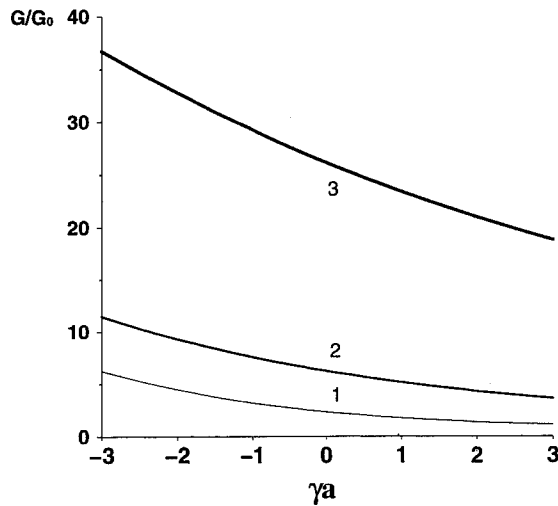
Fig. 3. The influence of h_2/a on the normalized strain energy release rate; loading: uniform crack surface pressure σ_0, $\nu = 0.3$, $h_1/a = 100$, (1) $h_2/a = 1$, (2) $h_2/a = 0.5$, (3) $h_2/a = 0.25$.
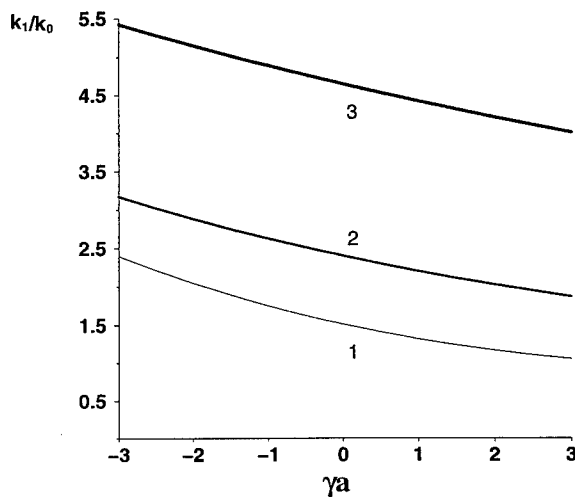

Fig. 4. The influence of h_2/a on mode I stress intensity factor k_1, loading: σ_0, $\nu = 0.3$, $h_1/a = 100$, (1) $h_2/a = 1$, (2) $h_2/a = 0.5$, (3) $h_2/a = 0.25$.

we have $k_2 = 0$ for mode I loading ($p_1 = -\sigma_0, p_2 = 0$) and $k_1 = 0$ for mode II loading ($p_1 = 0, p_2 = -\tau_0$). Under mode I loading the sign of k_2 generally depends on the relative stiffnesses of the layers on the two sides of the interface crack. As seen in Fig. 10, the relative stiffness is, in turn, controlled by γa and h_2/h_1.

The mixed mode stress intensity factors k_1 and k_2 may be used to determine the probable crack growth angle θ_0 at the crack tip which is measured from the positive x axis and is calculated from $\partial\sigma_{\theta\theta}(r, \theta)/\partial\theta = 0$, $\sigma_{\theta\theta}(r, \theta_0) > 0$ (Erdogan and Sih, 1963) or
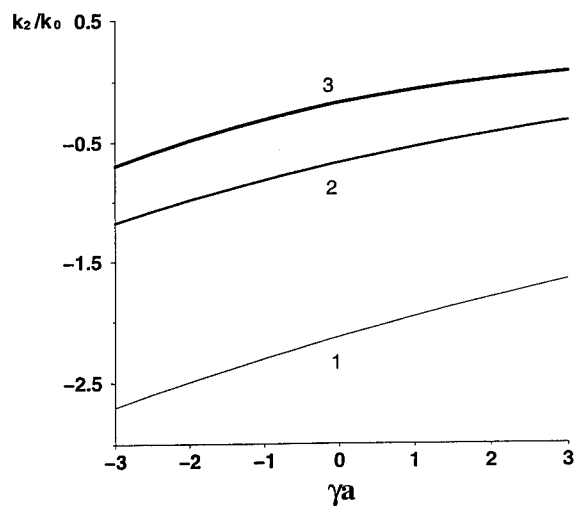
Fig. 5. The influence of h_2/a on mode II stress intensity factor k_2, loading: σ_0, $v = 0.3$, $h_1/a = 100$, (1) $h_2/a = 0.25$, (2) $h_2/a = 0.5$, (3) $h_2/a = 1$.
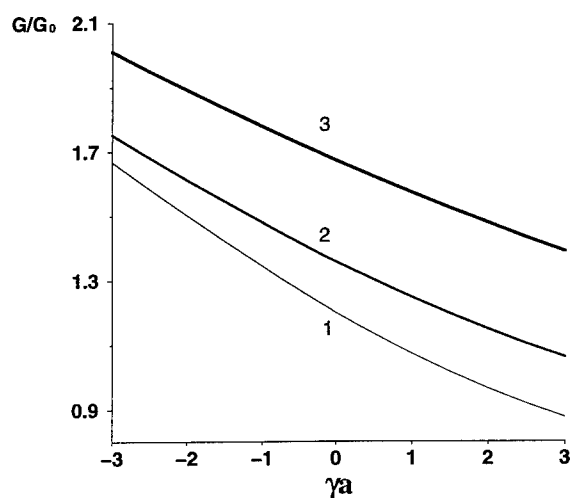

Fig. 6. The influence of h_2/a on $\mathbf{G}$, loading: uniform crack surface shear τ_0, $v = 0.3$, $h_1/a = 100$, (1) $h_2/a = 1$, (2) $h_2/a = 0.5$, (3) $h_2/a = 0.25$.

$$k_1 \sin \theta_0 + k_2(3\cos \theta_0 - 1) = 0,$$

$$k_1 \cos^2 \frac{\theta_0}{2} - \frac{3}{2}k_2 \sin \theta_0 > 0. \tag{41}$$

Some calculated values of θ_0 for $v = 0.3$, $h_1/a = 100$, $h_2/a = 0.25, 0.5, 1, 2, 10$ and for uniform tractions $p_1 = -\sigma_0$, $p_2 = 0$ are shown in Fig. 13. The figure indicates that if the medium is isotropic with regard to the crack growth resistance $\mathbf{G_c}$ near the crack tip, maximum energy release and, as a result, further crack growth would take place
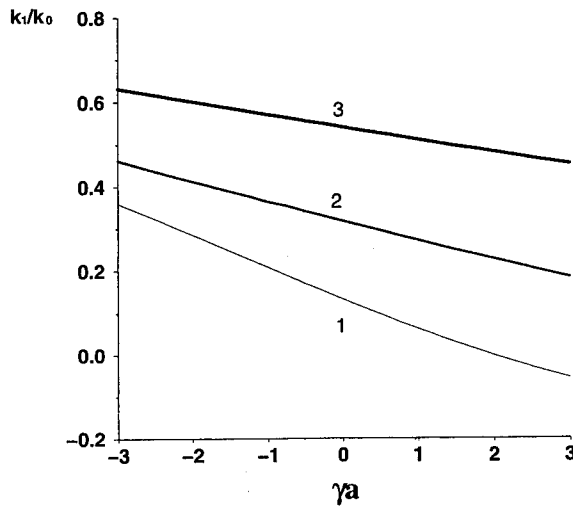
Fig. 7. The influence of h_2/a on k_1, loading: τ_0, $v = 0.3$, $h_1/a = 100$, (1) $h_2/a = 1$, (2) $h_2/a = 0.5$, (3) $h_2/a = 0.25$.
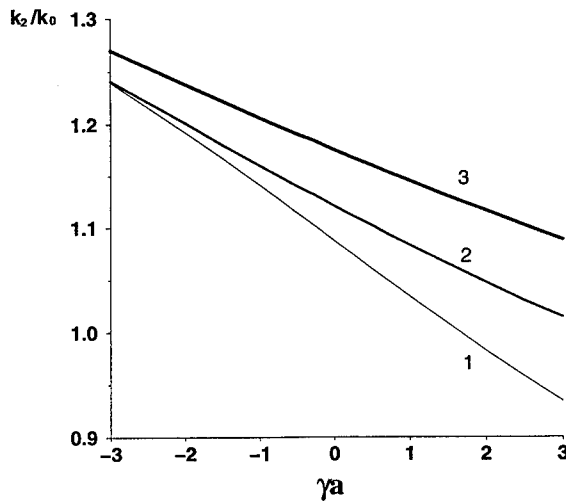

Fig. 8. The influence of h_2/a on k_2, loading: τ_0, $v = 0.3$, $h_1/a = 100$, (1) $h_2/a = 1$, (2) $h_2/a = 0.5$, (3) $h_2/a = 0.25$.

in a direction toward the less stiff material. On the other hand, if $\mathbf{G}_c$ is θ dependent, then the crack growth direction θ_0 would be determined by maximizing $\mathbf{G}(\theta)/\mathbf{G}_c(\theta)$, $\mathbf{G}(\theta)$ being the strain energy release rate for a small radial crack extension in the direction of θ.

It should be observed that in formulating the problem, the crack surface tractions p_1 and p_2 are assumed to be arbitrary functions of x. Therefore, the technique presented may be used to solve any quasi-static interface crack problem involving FGM coatings after properly separating the solution for the uncracked medium. Also, for the validity of the solution it is essential that the normal crack opening $v_2^+ - v_1^-$ be positive;
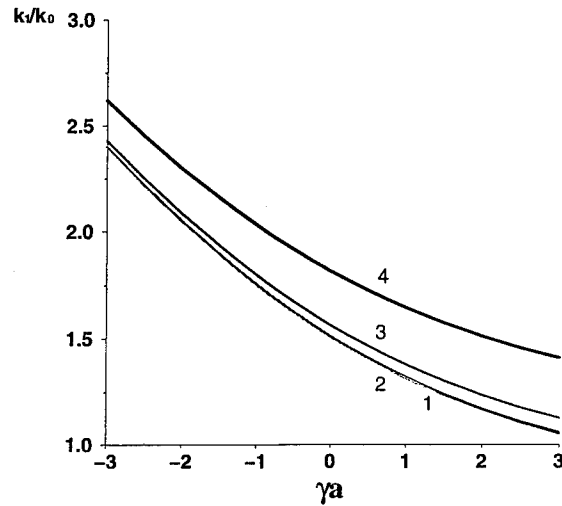
784   Y. F. CHEN and F. ERDOGAN

Fig. 9. The influence of h_1/a on k_1, loading: σ_0, $v = 0.3$, $h_2/a = 1$, (1) $h_1/a = 10$, (2) $h_1/a = 4$, (3) $h_1/a = 2$, (4) $h_1/a = 1$.
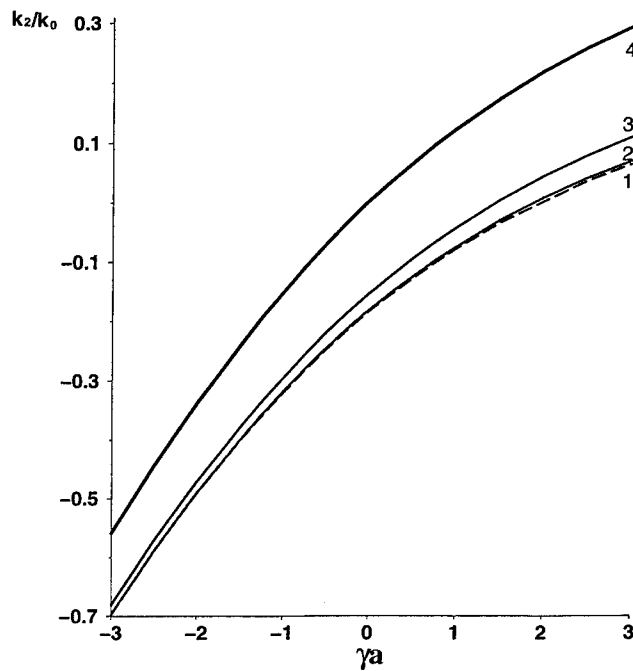

Fig. 10. The influence of h_1/a on k_2, loading: σ_0, $v = 0.3$, $h_2/a = 1$, (1) $h_1/a = 10$, (2) $h_1/a = 4$, (3) $h_1/a = 2$, (4) $h_1/a = 1$.

otherwise the problem must be treated as a crack/contact problem (Erdogan and Wu, 1996). For example, under pure shear loading $p_1 = 0$, $p_2 = -\tau_0$, $v_2^+ - v_1^-$ is an odd function of x and consequently the crack would remain partially closed (Chen, 1990).
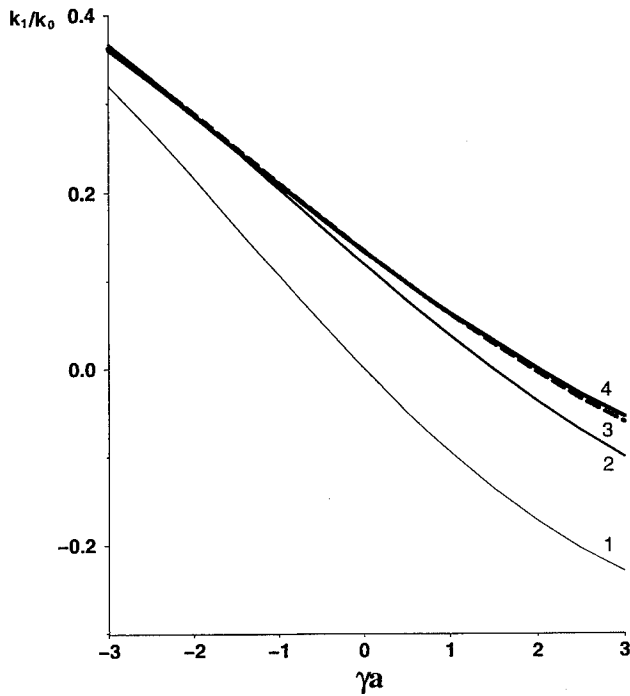
Fig. 11. The influence of h_1/a on k_1, loading: τ_0, $v = 0.3$, $h_2/a = 1$, (1) $h_1/a = 1$, (2) $h_1/a = 2$, (3) $h_1/a = 4$, (4) $h_1/a = 10$.
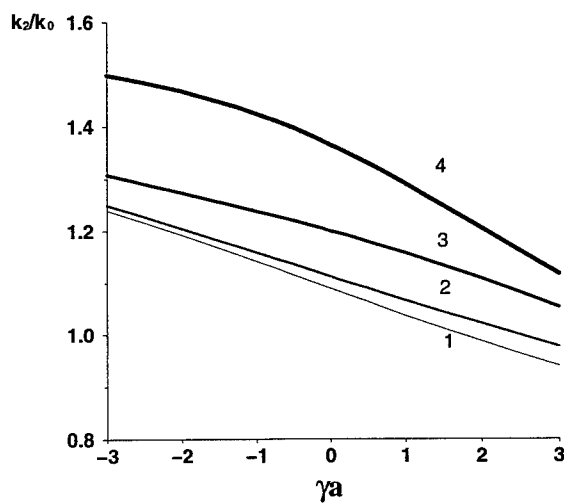

Fig. 12. The influence of h_1/a on k_2, loading: τ_0, $v = 0.3$, $h_2/a = 1$, (1) $h_1/a = 10$, (2) $h_1/a = 4$, (3) $h_1/a = 2$, (4) $h_1/a = 1$.

Hence, such a solution can be used only in superposition with other solutions that would give $v_2^+ - v_1^- > 0$ for $-a < x < a$.
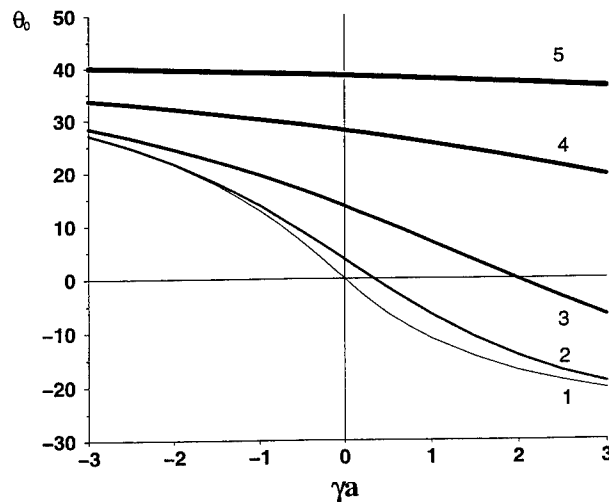
Fig. 13. The effect of the coating thickness h_2/a and the nonhomogeneity constant γ on the probable crack growth direction θ_0, loading: σ_0, $v = 0.3$, $h_1/a = 100$, (1) $h_2/a = 10$ and 100, (2) $h_2/a = 2$, (3) $h_2/a = 1$, (4) $h_2/a = 0.5$, (5) $h_2/a = 0.25$. (The angle θ_0 is measured at the crack tip a from the positive x axis.)

ACKNOWLEDGEMENT

REFERENCES

Brennan, J. J. (1991) Interfacial studies of refractory glass-ceramic matrix/advanced SiC fiber reinforced composites. Annual Report, ONR Contract N00014-87-C-0699 United Technologies Research Center.

Chen, Y. F. (1990) The interface crack problem in nonhomogeneous bonded materials of finite thickness. Ph.D. dissertation, ME-MECH Department, Lehigh University.

Delale, F. and Erdogan, F. (1983) The crack problem for a nonhomogeneous plane. *ASME J. Appl. Mech.* **50**, 609–614.

Delale, F. and Erdogan, F. (1988) Interface crack in a nonhomogeneous elastic medium. *Int. J. Engng Sci.* **28**, 559–568.

Erdogan, F. and Gupta, G. D. (1971) Layered composites with an interface flaw. *Int. J. Solids Structures* **7**, 39–61.

Erdogan, F. and Sih, G. C. (1963) On the crack extension in plates under plane loading and transverse shear. *J. Basic Engng, Trans. ASME* **85**, 519–525.

Erdogan, F. and Wu, B. H. (1996) Crack problems in FGM layers under thermal stresses, to appear in *J. Thermal Stresses*.

Holt, J. B., Koizumi, M., Hirai, T. and Munir, Z. A. (eds) (1993) *Ceramic Transactions—Functionally Gradient Materials*, Vol. 34. American Ceramic Society, Westerville, OH.

Konda, N. and Erdogan, F. (1994) The mixed-mode crack problem in a nonhomogeneous elastic medium. *Engng Fracture Mech.—An Int. J.* **47**, 533–545.

Kurihara, K., Sasaki, K. and Kawarada, M. (1990) Adhesion improvement of diamond films. *FGM-90, Proc. 1st Int. Symp. on Functionally Gradient Materials* (eds M. Yamanouchi, M. Koizumi, T. Hirai and I. Shiota). FGM Forum, Sendai, Japan.

Lee, Y. D. and Erdogan (1994) Residual stresses in FGM and laminated thermal barrier coatings. *Int. J. Fracture* **69,** 145–165.

Olszak, W. (ed.) (1958) *Nonhomogeneity in Elasticity and Plasticity*, Proc. IUTAM Symposium, Warsaw. Pergamon Press.

Ozturk, M. and Erdogan, F. (1993) The axisymmetric crack problem in a nonhomogeneous medium. *ASME J. Appl. Mech.* **60,** 406–413.

Spalvins, T. (1985) The structure of ion-plated films in relation to coating properties. *Proc. Ion Plating and Implantation Applications.* American Society of Metals.

Shiau, F. Y., Zuo, Y., Zeng, X. Y., Lin, J. C. and Chang, Y. A. (1998) Interfacial reaction between copper and GaAs. *Adhesion in Solids, Materials Research Society Symposium Proc.*, Vol. 119 (eds D. M. Mattox, J. E. E. Baglin, R. J. Gottshall and C. D. Batich). MRS, Pittsburgh, PA.

Yamanouchi, M., Koizumi, M., Hirai, T. and Shiota, I. (eds) (1990) *FGM*-90, *Proc. 1st Int. Symp. on Functionally Gradient Materials.* FGM Forum, Sendai, Japan.

ON THE TOUGHNESS OF DUCTILE ADHESIVE JOINTS

VIGGO TVERGAARD

Department of Solid Mechanics, Technical University of Denmark, Lyngby, Denmark

and

JOHN W. HUTCHINSON

Division of Applied Sciences, Harvard University, Cambridge, Massachussetts, U.S.A.

ABSTRACT

Crack propagation along one of the interfaces between a thin ductile adhesive layer and the elastic substrates it joins is considered. The layer is taken as being elastic–plastic, and the fracture process of the interface is modeled by a traction–separation law, characterized by the peak separation stress $\hat{\sigma}$ and the work of separation per unit area Γ_0. Crack growth resistance curves for mode I loading of the adhesive joint are computed, with emphasis on steady-state toughness, as a function of three extrinsic effects: layer thickness, layer–substrate modulus mismatch, and initial residual stress in the layer. Conditions under which separation first occurs well ahead of the initial crack tip are discussed.

1. SPECIFICATION OF THE MODEL

This paper continues the study begun by Tvergaard and Hutchinson (1994) in which an embedded fracture zone model is applied to the mode I fracture of an adhesive joint comprised of a thin elastic–plastic metal layer joining two elastic substrates. The present work employs the model to investigate the influence on joint toughness of both the elastic mismatch between the layer and the substrates and the residual stress in the layer. As in the earlier study, the thickness of the ductile layer is another extrinsic variable which comes into play.

The approach adopted was first introduced by Needleman (1987) to study particle debonding in metal matrices and subsequently by Tvergaard and Hutchinson (1992, 1993) to model crack growth resistance in homogeneous solids and along interfaces. A traction–separation law simulating the fracture process is embedded within an elastic–plastic continuum as a boundary condition along the line extending ahead of the crack. In the case of an interface joining dissimilar materials, the separation law necessarily involves both the normal and shear tractions and the two associated relative displacements of the surfaces across the interface.
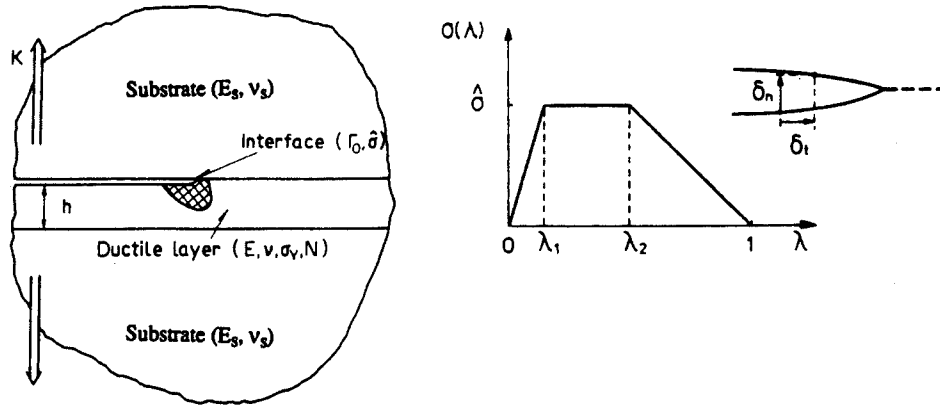
Fig. 1. Geometry of system and traction–separation relation for interface.

1.1. Traction–separation law for the interface

Following the notation for the law introduced in Tvergaard and Hutchinson (1993, 1994) let δ_n and δ_t be the normal and tangential components of the relative displacement of the crack faces across the interface in the zone where the fracture processes are occurring, as indicated in Fig. 1. Let δ_n^c and δ_t^c be critical values of these displacement components, and define a single nondimensional separation measure as

$$\lambda = \sqrt{(\delta_n/\delta_n^c)^2 + (\delta_t/\delta_t^c)^2} \qquad (1.1)$$

such that the tractions drop to zero when $\lambda = 1$. With $\sigma(\lambda)$ displayed in Fig. 1, a potential from which the tractions are derived is defined as

$$\Phi(\delta_n, \delta_t) = \delta_n^c \int_0^\lambda \sigma(\lambda')\,d\lambda'. \qquad (1.2)$$

The normal and tangential components of the traction acting on the interface in the fracture process zone are given by

$$T_n = \frac{\partial\Phi}{\partial\delta_n} = \frac{\sigma(\lambda)}{\lambda}\frac{\delta_n}{\delta_n^c}, \quad T_t = \frac{\partial\Phi}{\partial\delta_t} = \frac{\sigma(\lambda)}{\lambda}\frac{\delta_t}{\delta_t^c}\frac{\delta_n^c}{\delta_t^c}. \qquad (1.3)$$

The traction law under a purely normal separation $(\delta_t = 0)$ is $T_n = \sigma(\lambda)$ where $\lambda = \delta_n/\delta_n^c$. Under a purely tangential displacement $(\delta_n = 0)$, $T_t = (\delta_n^c/\delta_t^c)\sigma(\lambda)$ where $\lambda = \delta_t/\delta_t^c$. The peak normal traction under pure normal separation is $\hat{\sigma}$, and the peak shear traction is $(\delta_n^c/\delta_t^c)\hat{\sigma}$ in a pure tangential "separation". The work of separation per unit area of interface is given by (1.2) with $\lambda = 1$. For the separation function $\sigma(\lambda)$ specified in Fig. 1,

$$\Gamma_0 = \tfrac{1}{2}\hat{\sigma}\,\delta_n^c[1 - \lambda_1 + \lambda_2]. \qquad (1.4)$$

The parameters governing the separation law of the interface are the work of the fracture process Γ_0, the peak stress quantity $\hat{\sigma}$, and the critical displacement ratio δ_n^c/δ_t^c, together with the factors λ_1 and λ_2 governing the shape of the separation

function. Note that use of the potential ensures that the work of separation is Γ_0 regardless of the combination of normal and tangential displacements taking place in the process zone. Experience gained in the earlier studies suggests that the details of the shape of the separation law are relatively unimportant. The loading in the present ductile layer problem is mode I. Nevertheless, the asymmetry introduced by the existence of the crack on one interface and not the other gives rise to some tangential separation. However, the separation displacements are predominantly normal, such that the choice of the ratio δ_n^c/δ_t^c also has relatively little influence on the predictions of the macroscopic toughness. The two most important parameters characterizing the fracture process in this model are Γ_0 and $\hat{\sigma}$.

1.2. *Continuum properties of the ductile adhesive and the elastic substrates*

The layer has thickness h and is assumed to be elastically isotropic with Young's modulus E and Poisson's ratio v. The residual stress state in the unloaded layer is assumed to be equibiaxial, acting parallel to the plane of the layer, of magnitude σ_R. Commonly, when a metal layer joins two ceramic substrates, a residual tensile stress in the thin metal layer develops due to thermal expansion mismatch and the consequence of cooling from a high bonding temperature. The plastic response of the layer material is characterized by J_2 flow theory, i.e. the standard isotropic hardening incremental plasticity theory based on the Mises invariant. The tensile curve of true stress versus true strain for the layer material is taken to be

$$
\begin{aligned}
\varepsilon &= \sigma/E & &\text{for} \quad \sigma \leqslant \sigma_Y \\
\varepsilon &= (\sigma_Y/E)(\sigma/\sigma_Y)^{1/N} & &\text{for} \quad \sigma > \sigma_Y
\end{aligned}
\tag{1.5}
$$

where σ_Y is the tensile yield stress and N is the strain hardening exponent. The primary effect of the residual stress is its influence on the onset of yield when the joint is loaded.

The two elastic substrates joined by the adhesive layer are assumed to be identical and isotropic with Young's modulus E_s and Poisson's ratio v_s.

1.3. *Mode I loading for long cracks and definition of steady-state toughness*

The focus in this paper is on symmetrically loaded joints containing interface cracks that are long compared to the extent of the plastic zones induced in the layer. Under this condition, the asymptotic problem indicated in Fig. 1 applies, wherein the crack is taken to be semi-infinite and is loaded remotely by the symmetric mode I stress field with amplitude given by the stress intensity factor K. Irwin's relation between the energy release rate G and the stress intensity factor K for a mode I, plane strain crack in an elastic solid is

$$
G = \frac{(1 - v_s^2)}{E_s} K^2.
\tag{1.6}
$$

This relation applies to the asymptotic problem of Fig. 1 with G interpreted as the remote, or applied, energy release rate. The crack growth resistance Γ is identified with G under conditions of crack advance. There is one material length quantity, R_0,

in the model, which was introduced in the study of mixed mode interface fracture by Tvergaard and Hutchinson (1993)

$$R_0 = \frac{2}{3\pi(1-\beta^2)}\left[\frac{(1-v^2)}{E} + \frac{(1-v_s^2)}{E_s}\right]^{-1}\frac{\Gamma_0}{\sigma_Y^2} \qquad (1.7)$$

where β is the second Dundurs elastic mismatch parameter

$$\beta = \frac{1}{2}\frac{\mu(1-2v_s)-\mu_s(1-2v)}{\mu(1-v_s)+\mu_s(1-v)} \qquad (1.8)$$

and μ and μ_s are the shear moduli. In the absence of elastic mismatch (1.7) reduces to

$$R_0 = \frac{1}{3\pi(1-v^2)}\frac{E\Gamma_0}{\sigma_Y^2}. \qquad (1.9)$$

The length quantity R_0 can be thought of as an estimate of the size of the plastic zone of the interface crack when $\Gamma = \Gamma_0$ and $h \gg R_0$.

The model has been used to compute the history of Γ as a function of crack advance Δa as dependent on the parameters of the system. From this resistance curve data, one can identify a toughness level characterizing initiation of crack growth and an asymptote, denoted by Γ_{ss}, characterizing the steady-state condition wherein the crack advances under constant Γ. Typically, this asymptote is attained after a crack advance on the order of several times R_0. The steady-state toughness, Γ_{ss}, provides the most meaningful measure of the joint toughness, and it will be this quantity which will be featured in the sequel. The nondimensional relation between the steady-state toughness and the parameters of the model is

$$\frac{\Gamma_{ss}}{\Gamma_0} = F\left(\frac{\hat{\sigma}}{\sigma_Y}, N, \frac{h}{R_0}, \frac{E_s}{E}, \frac{\sigma_R}{\sigma_Y}\right). \qquad (1.10)$$

There is also a weak dependence on δ_t^c/δ_n^c, v, v_s, σ_Y/E, λ_1 and λ_2. Given the large number of parameters in the model, it is not possible to present or even compute the full parametric dependence. In this paper, attention is directed to the parameters shown explicitly in (1.10), with the exception of N, which is fixed at 0.1 in all the computations corresponding to a typical strain hardening level. Each value of Γ_{ss}/Γ_0 is obtained by computing the full resistance curve, starting from initiation to a level of a crack advance, Δa, such that Γ approximately attains the asymptote, and, consequently, extensive numerical computation lies behind the results reported in Section 3.

2. NUMERICAL METHOD

The problem considered is an extension of the problem analyzed by Tvergaard and Hutchinson (1994), and the numerical method employed is essentially the same as that presented in that earlier paper. The method exploits the fact that the plastic

deformation takes place only in the thin layer of thickness h, while the solids on either side of the layer remain elastic. The region analyzed numerically is divided into three sub-regions, where the outer regions comprising the elastic substrates are semi-circular with radius A_0, and region occupied by the layer is rectangular with dimensions h by $2A_0$. The finite element mesh consists of quadrilaterals, each built up of four triangular, linear-displacement elements. The meshes used for the substrate region are identical to those employed in the earlier reference. In the layer the quadrilaterals are rectangular with edge nodes located so that they fit the edge nodes of the adjacent region. The initial crack tip is located at $x_1 = x_2 = 0$, and a uniform mesh region of length B_0 is used in front of the initial crack tip to model crack growth. The length of one square element in this uniformly meshed region is denoted by Δ_0.

On the circular edges of the substrate regions loads corresponding to the tractions of the mode I stress field are applied, with amplitude K. At the two ends of the thin layer the edge loads are neglected, which introduces a very small error as long as h/A_0 is small. At the interface between the lower substrate and the layer, the conditions to be satisfied are

$$u^1(\eta_+) = u^1(\eta_-), \quad u^2(\eta_+) = u^2(\eta_-) \tag{2.1}$$

$$T^1(\eta_+) = -T^1(\eta_-), \quad T^2(\eta_+) = -T^2(\eta_-) \tag{2.2}$$

where η is the coordinate along the interface and the " $+$ " denotes a value just above the interface and the " $-$ " denotes a value just below. Along the upper interface, the initial crack surfaces for $x_1 < 0$ are traction-free, while for $x_1 > 0$ the displacements and tractions are related by the traction separation law of the interface of Section 1.1. Thus, for $x_1 > 0$

$$u^1(x_{1+}) - u^1(x_{1-}) = \delta_t(x_1), \quad u^2(x_{1+}) - u^2(x_{1-}) = \delta_n(x_1) \tag{2.3}$$

$$T^1(x_{1+}) = -T^1(x_{1-}) = T_t(x_1), \quad T^2(x_{1+}) = -T^2(x_{1-}) = T_n(x_1). \tag{2.4}$$

For the upper substrate region, the linear elastic equations are solved once at the start to obtain linear relations between the nodal displacements along $x_1 > 0$, the corresponding nodal forces, and the load amplitude K, using a Rayleigh–Ritz finite element method. Similar linear relations are obtained between nodal displacements on the lower interface boundary, the corresponding nodal forces, and the amplitude K. In the layer, elastic–plastic deformations take place following a finite strain generalization of J_2 flow theory, as has been described in more detail in Tvergaard and Hutchinson (1992). Thus, solutions in the layer have to be obtained incrementally, and in each increment linear relations are obtained between nodal displacement increments and the corresponding nodal force increments on the upper and lower edges of the layer.

The relations for the three sub-regions are finally assembled using (2.1)–(2.4) to obtain a set of linear algebraic equations for the increment in the load amplitude K and the nodal displacement increments along the layer edges. On the initial part of the resistance curve, an increment in K is prescribed, but this procedure is unstable when K approaches its asymptote. Then, the Rayleigh–Ritz method is used to control a monotonic increase of displacement differences at the crack tip.

In all of the computations, the properties of the elastic–plastic layer are specified by the parameters $\sigma_Y/E = 0.003$, $v = \frac{1}{3}$, and $N = 0.1$. Different levels of elastic modulus mismatch between the layer and the substrates are considered ($E_s/E = 1, 3, 6$ and 12), all with $v_s = v = \frac{1}{3}$. The separation law is specified using $\delta_n^c/\delta_t^c = 1$, $\lambda_1 = 0.15$ and $\lambda_2 = 0.5$ with $\hat{\sigma}/\sigma_Y$ varied. The preceding paper established that the predictions for the present class of problems are not strongly sensitive to δ_n^c/δ_t^c, λ_1 or λ_2.

Let Δ_0 denote the length of one of the small elements in the uniform mesh along the interface in the crack growth region. Most of the computations have been carried out for a region size specified by $A_0 = 44{,}000 \, \Delta_0$ and $B_0 = 40 \, \Delta_0$. Mesh refinements have been carried out to test convergence. Based on these trials the computations for the elastic mismatches with $E_s/E = 3$, 6 and 12 were performed with $\Delta_0 = 10 \, \delta_n^c$, whereas the computations with no modulus mismatch were computed with $\Delta_0 = 5 \, \delta_n^c$. For the larger values of the layer thickness h, compared to Δ_0, the mesh size is stretched across the layer in such a way that the row of quadrilateral elements along the crack plane are square. In each of the semi-circular elastic regions the number of triangular elements is 6248 and the number of nodal points is 3203. In the thin elastic–plastic layer the number of triangular elements is 8800 and the number of nodal points is 4531.

3. STEADY-STATE TOUGHNESS

The full set of numerical results for Γ_{ss}/Γ_0 as a function of $\hat{\sigma}/\sigma_Y$, h/R_0, E_s/E and σ_R/σ_Y are shown in the four parts of Fig. 2. Parts (a)–(d) correspond to values of E_s/E of 1, 3, 6, and 12, respectively. Figure 2(a) and (c) display results for $\sigma_R = 0$ (the solid-line curves), as well as for a biaxial tensile residual stress in the layer nearly at yield, $\sigma_R/\sigma_0 = 0.95$ (the dashed-line curves). The solid-line curves for the case of no elastic mismatch in Fig. 2(a) were presented earlier by Tvergaard and Hutchinson (1994).

The main qualitative trends evident in Fig. 2 can be summarized as follows. (i) Normalized steady-state toughness increases strongly with $\hat{\sigma}/\sigma_Y$, with all other parameters held fixed. This dependence has been discussed in some detail in the authors' earlier papers on the model. (ii) Very thin layers, in the sense that $h/R_0 \ll 1$, have almost no enhancement of toughness due to plastic deformation, i.e. $\Gamma_{ss} \cong \Gamma_0$. This limit, in which the layer thickness is small compared to the size of the unconstrained plastic zone, will be discussed further in Section 4. (iii) At the other limit, when the layer thickness is larger than the plastic zone ($h/R_0 \gg 1$), Γ_{ss}/Γ_0 becomes independent of h, because the interaction of the plastic zone with substrate on the other side of the uncracked interface becomes negligible. The value of h/R_0 at which the toughness becomes independent of the layer thickness is a function of $\hat{\sigma}/\sigma_Y$ because the plastic zone size increases with this parameter. (iv) The ratio of the substrate elastic modulus to that of the layer, E_s/E, has a fairly significant effect such that joints with relatively stiff substrates have higher toughnesses, all other parameters remaining the same. (v) The residual stress in the layer σ_R has a major effect on joint toughness. Tensile residual stresses lower the joint toughness, while compressive stresses raise the toughness.

The influence of E_s/E on the normalized steady-state toughness is isolated in Fig.
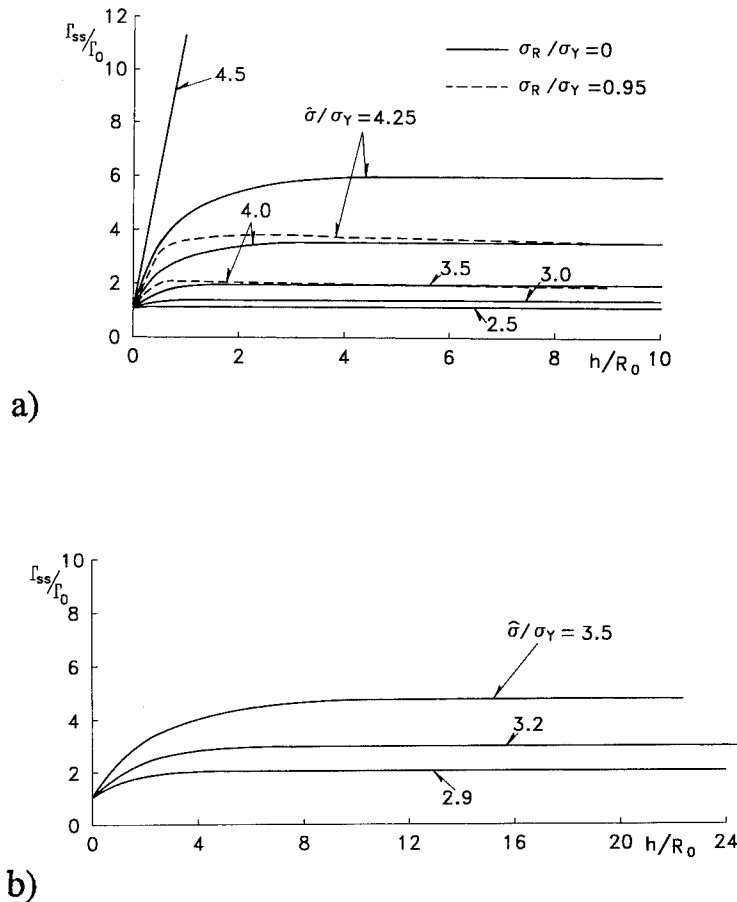
a)

b)

Fig. 2. Normalized steady-state toughness of the joint as a function of layer thickness for various values of $\hat{\sigma}/\sigma_Y$. (a) $E_s/E = 1$, (b) $E_s/E = 3$, (c) $E_s/E = 6$, and (d) $E_s/E = 12$. The other parameters are specified in the text.

3, where curves of Γ_{ss}/Γ_0 as a function of $\hat{\sigma}/\sigma_Y$ are plotted for large values of h/R_0 chosen to ensure that the toughness is independent of h. In the range of $\hat{\sigma}/\sigma_Y$ for which the toughness is magnified above Γ_0, an increase in E_s/E leads to an increase in Γ_{ss}/Γ_0. Judging from the results in Fig. 3, it appears that the full effect is achieved for modulus mismatches satisfying $E_s/E > 10$. It seems likely that the toughness enhancement is related to the ability of stiffer substrates to better shield the layer near the tip, thereby lowering the peak normal stress on the interface ahead of the tip.

A cross-plot of Γ_{ss}/Γ_0 as a function of σ_R/σ_Y is shown for one set of parameters in Fig. 4. The case shown has $E_s/E = 6$, $\hat{\sigma}/\sigma_Y = 3$, with $\sigma_Y/E = 0.003$ and $N = 0.1$. The calculations were carried out using $h/R_0 = 13.46$, and thus these results are also in the range where the plastic zone does not extend across the layer and the joint toughness is independent of h. The role of residual stress is clearly significant. Qualitatively, the residual stress effect can be thought of as raising (when $\sigma_R > 0$) or lowering (when
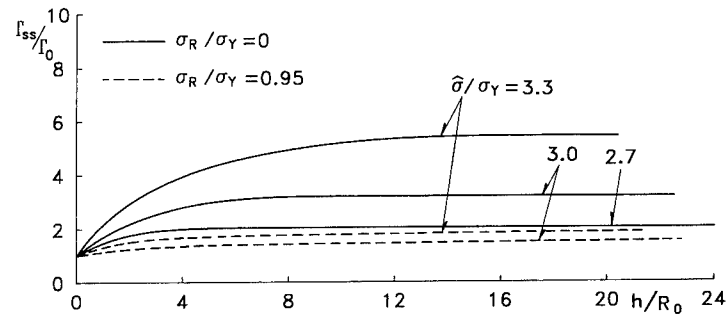
c)
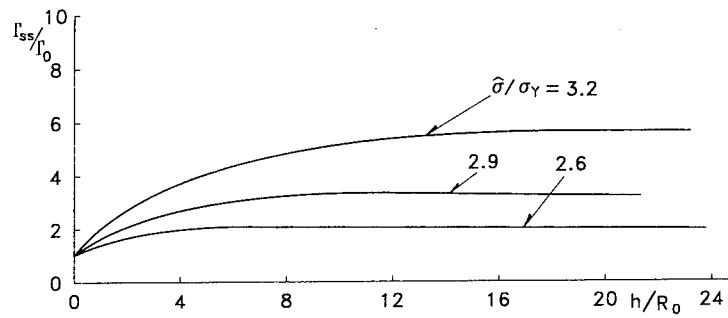
d)

Fig. 2. *Continued.*

$\sigma_R < 0$) the additional effective stress needed to cause yield, thereby suppressing or enhancing plastic deformation. To understand this, note that, with respect to plastic yielding, a residual biaxial stress σ_R acting parallel to the plane of the layer is equivalent to a uniaxial stress $-\sigma_R$ acting normal to the plane of the layer. (This follows from superposition of a hydrostatic stress state $-\sigma_R \delta_{ij}$, which has no effect on the yield condition.) Thus, the onset of plastic yielding at any point in the layer near the tip will be delayed (or advanced) to a higher (or lower) local stress normal to the interface resulting from the applied K, depending on whether $\sigma_R > 0$ (or $\sigma_R < 0$). The effect is roughly equivalent to decreasing or increasing $\hat{\sigma}$.

In the examples shown in Figs 2–4, the peak interface stress $\hat{\sigma}$ is attained immediately ahead of the crack tip such that debonding links back to the crack tip as crack advance occurs. The stress distribution in a thin metal layer ahead of the crack tip in the layer–substrate geometry considered here has also been studied by Varias *et al.* (1991) for the stationary crack without any debonding. The constraint imposed on the layer by the elastic substrates gives rise to a large component of hydrostatic tension in the
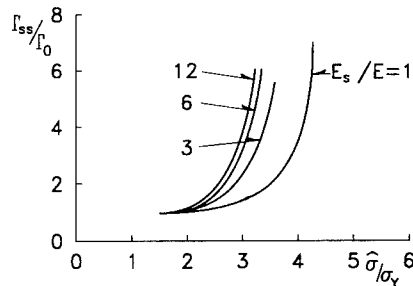
Fig. 3. Dependence of steady-state toughness of the joint on $\hat{\sigma}/\sigma_Y$ for various E_s/E, all for the limit of large h/R_0 for which the layer thickness exceeds the height of the plastic zone.
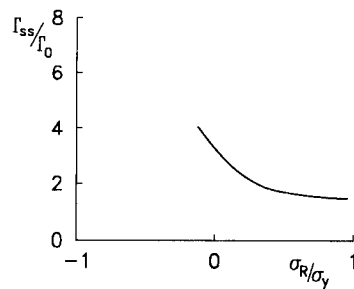

Fig. 4. Effect of residual stress on the steady-state toughness for the limit in which $h/R_0 \gg 1$. In this example, $\hat{\sigma}/\sigma_Y = 3$ and $E_s/E = 6$.

layer such that the peak in the interface stress occurs at a distance ahead of the tip. This is the location where the interface stress first attains $\hat{\sigma}$. If $\hat{\sigma}/\sigma_Y$ is sufficiently large and if the layer is sufficiently thin, then the peak stress on the interface is attained so far ahead of the tip that debonded patches occur which are unconnected to the crack tip. An example for which this occurs is shown in Fig. 5 for the case where $\hat{\sigma}/\sigma_Y = 5$, $E_s/E = 1$ and $h/R_0 = 0.186$. The figure displays the deformed mesh and crack opening profile at three levels of applied load corresponding to $\Gamma/\Gamma_0 = 2.06, 2.90$, and 3.73. At the lowest of the three load levels, the peak stress has just been attained and debonding of the interface has begun at a distance of approximately $2h$ ahead of the blunted crack tip. At the two higher load levels, an isolated debonded patch opens and expands. Of course, the present calculations are two dimensional, while the actual process will be three dimensional. Debonding in roughly equiaxed patches well ahead of the crack tip has been observed and documented for Au/Al_2O_3 interfaces by Reimanis et al. (1991) and Turner and Evans (1996) and has been studied theoretically by He et al. (1996).

4. APPROXIMATE ANALYSIS OF MODEL FOR LARGE $\hat{\sigma}/\sigma_Y$

In this section an approximate analysis of the model will be carried out under the assumption that $\hat{\sigma}/\sigma_Y$ is sufficiently large that interface debonding starts at a point $\hat{x}$ at least several layer thicknesses ahead of the tip. Thus, the focus will be on initiation

Γ/Γ_0=2.06
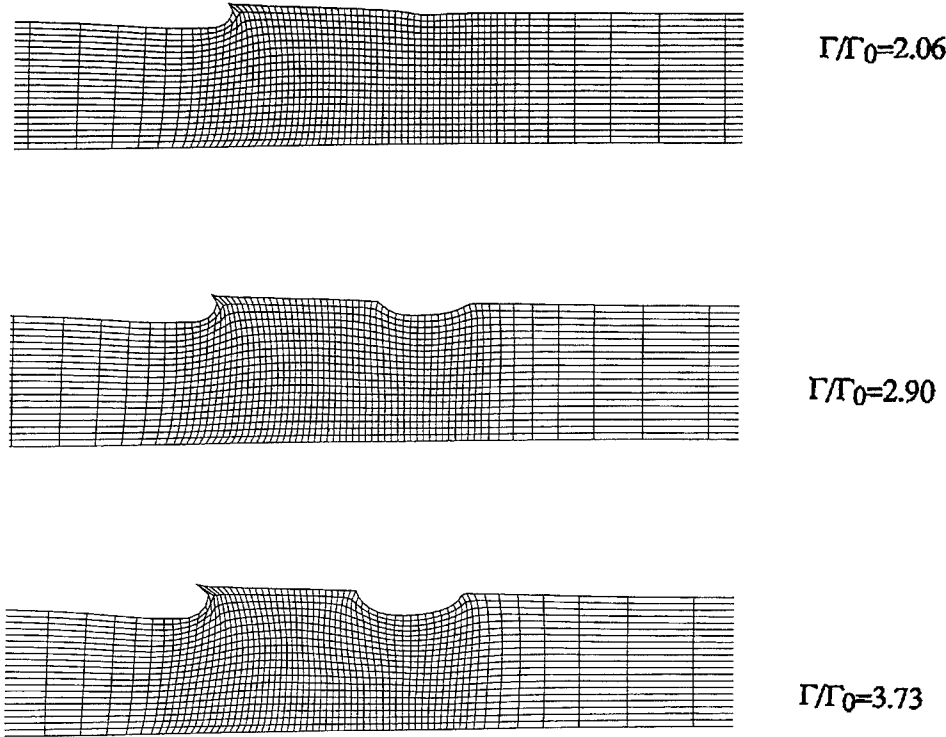
Γ/Γ_0=2.90

Γ/Γ_0=3.73

Fig. 5. An example illustrating debonding of a patch unconnected to the crack tip at three levels of load. For this example, $\hat{\sigma}/\sigma_Y = 5$, $E_s/E = 1$ and $h/R_0 = 0.186$.

of debonding in the regime discussed above where debonding starts in the form of isolated patches ahead of the tip. While highly approximate, the analysis does capture the qualitative dependencies on some of the most important parameters and informs aspects of behavior in the regime where debonding extends back to the tip.

Assume there is no residual stress in the layer and the layer material is elastic–perfectly plastic. When the layer is very thin, the elastic stress distribution for the limit of zero layer thickness will be used to estimate the stress acting on the interface at the point where the peak stress is attained. That is, from $\sigma_{22} = K/\sqrt{2\pi x_1}$, it follows that if $\hat{K}$ is the value of the stress intensity factor at which debonding starts

$$\hat{\sigma} = \hat{K}/\sqrt{2\pi\hat{x}}. \tag{4.1}$$

In the portion of the layer between the tip and the point of initial debonding, i.e. $0 < x_1 < \hat{x}$, the x_1 component of stress increases linearly according to $d\sigma_{11}/dx_1 = (2/\sqrt{3})\sigma_Y/h$. This follows from simple equilibrium and the fact that the layer undergoes plastic shearing along its top and bottom surfaces (Hill, 1950; Varias et al., 1991). The well-known stress state at the tip of a crack in an elastic–perfectly plastic material applies such that, at $x_1 = 0$, $\sigma_{11} \cong 2\sigma_Y$. Therefore, at the location of the peak stress,

$\sigma_{11} \cong 2\sigma_Y + (2/\sqrt{3})\sigma_Y(\hat{x}/h)$. The state of stress at the location of the peak satisfies yield and is approximately a state of hydrostatic tension superimposed on a state of uniaxial tension, with $\sigma_{22} \cong \sigma_{11} + \sigma_Y$. Thus, a second approximate relation between the peak debonding stress and the location of the onset of debonding is

$$\hat{\sigma} \cong 3\sigma_Y + (2/\sqrt{3})\sigma_Y(\hat{x}/h). \tag{4.2}$$

Eliminate $\hat{x}$ from (4.1) and (4.2), using (1.6), to obtain the estimate of $\hat{\Gamma}$ at which the debonding condition is first attained

$$\hat{\Gamma} = \sqrt{3}\pi(1 - v_s^2)\left(\frac{\hat{\sigma}}{\sigma_Y}\right)^2\left(\frac{\hat{\sigma}}{\sigma_Y} - 3\right)\frac{h\sigma_Y^2}{E_s}. \tag{4.3}$$

The location of the point of first debond is

$$\frac{\hat{x}}{h} = \frac{\sqrt{3}}{2}\left(\frac{\hat{\sigma}}{\sigma_Y} - 3\right). \tag{4.4}$$

Note that $\hat{\Gamma}$ does not depend on Γ_0; it is associated with the attainment of a critical stress at some point on the interface ahead of the crack tip. Application of the above formulas is limited to values of $\hat{\sigma}/\sigma_Y$ sufficiently large such that $\hat{x}/h \geqslant 2$, i.e. roughly $\hat{\sigma}/\sigma_Y \geqslant 5$. Finally, normalize the estimate in (4.3) by Γ_0, using (1.7), to obtain

$$\frac{\hat{\Gamma}}{\Gamma_0} = \frac{(1 - v_s^2)}{\sqrt{3}}\left(\frac{\hat{\sigma}}{\sigma_Y}\right)^2\left(\frac{\hat{\sigma}}{\sigma_Y} - 3\right)\frac{E^*}{E_s}\frac{h}{R_0} \tag{4.5}$$

where

$$\frac{1}{E^*} = \frac{(1 - \beta^2)}{2}\left(\frac{1 - v^2}{E} + \frac{1 - v_s^2}{E_s}\right). \tag{4.6}$$

Formulas (4.3) and (4.5) reveal the exceptionally strong dependence on $\hat{\sigma}/\sigma_Y$, which is also evident in the other regime in the plots of steady-state toughness in Fig. 2. Note that the trend of $\hat{\Gamma}/\Gamma_0$ with E_s/E implied by (4.5) is opposite to that for Γ_{ss}/Γ_0 in Fig. 3 in the range $h/R_0 \gg 1$. Numerical calculations for $\hat{\Gamma}/\Gamma_0$ as a function of E_s/E in the range of small h/R_0 with large $\hat{\sigma}/\sigma_Y$ have not been carried out.

Finally, a connection is noted between the approximate results for the onset of debonding and the numerical results for steady-state toughness in Fig. 2. From the plots in Fig. 2, it can be seen that in the range of small h/R_0 (e.g. $h/R_0 < 1/2$) the normalized joint toughness varies approximately linearly with layer thickness according to

$$\frac{\Gamma_{ss}}{\Gamma_0} \cong 1 + C\frac{h}{R_0} \tag{4.7}$$

or

$$\Gamma_{ss} \cong \Gamma_0 + C\frac{h\Gamma_0}{R_0} = \Gamma_0 + 3\pi C\frac{h\sigma_Y^2}{E^*} \tag{4.8}$$

where C depends on $\hat{\sigma}/\sigma_Y$ and N but not on Γ_0. In this range, the enhancement of joint toughness above the work of separation of the interface is independent of Γ_0, as is the case for the result in (4.3). In fact, it can be noted that the enhancement in steady-state toughness in (4.8) has precisely the same parametric dependence as (4.3). Qualitatively, the trend of $\hat{\Gamma}$ with $\hat{\sigma}$ given by (4.3) reflects the trends shown in Fig. 2 in the range of small h/R_0.

ACKNOWLEDGEMENT

REFERENCES

He, M. Y., Evans, A. G. and Hutchinson, J. W. (1996) Interface cracking phenomena in constrained metal layers. *Acta Metall. Mater.*, in press.

Hill, R. (1950) *The Mathematical Theory of Plasticity*. Clarendon Press, Oxford.

Needleman, A. (1987) A continuum model for void nucleation by inclusion debonding. *J. Appl. Mech.* **54**, 525–531.

Reimanis, I. E., Dalgleish, B. J. and Evans, A. G. (1991) The fracture resistance of a model metal/ceramic interface. *Acta Metall. Mater.* **39**, 3133–3141.

Turner, M. R. and Evans, A. G. (1996) An experimental study of the mechanisms of crack extension along an oxide/metal interface. *Acta Metall. Mater.*, in press.

Tvergaard, V. and Hutchinson, J. W. (1992) The relation between crack growth resistance and fracture process parameters in elastic–plastic solids. *J. Mech. Phys. Solids* **40**, 1377–1397.

Tvergaard, V. and Hutchinson, J. W. (1993) The influence of plasticity on mixed mode interface toughness. *J. Mech. Phys. Solids* **41**, 1119–1135.

Tvergaard, V. and Hutchinson, J. W. (1994) Toughness of an interface along a thin ductile layer joining elastic solids. *Phil. Mag. A* **70**, 641–656.

Varias, A. G., Suo, Z. and Shih, C. F. (1991) Ductile failure of a constrained metal foil. *J. Mech. Phys. Solids* **39**, 963–986.

Pergamon

PII S0022–5096(96)00024–S

CRACKING PATTERNS IN METAL–CERAMIC LAMINATES: EFFECTS OF PLASTICITY

M. C. SHAW,[†‡] T. W. CLYNE,[†] A. C. F. COCKS,[‡] N. A. FLECK[‡]
and S. K. PATERAS[†]

† Department of Materials Science & Metallurgy, Pembroke Street, Cambridge University,
Cambridge CB2 3QZ, U.K.
‡ Department of Engineering, Trumpington Street, Cambridge University,
Cambridge CB2 1PZ, U.K.

ABSTRACT

Multilayered metal–ceramic composites exhibit unique fracture characteristics that result from the need to reinitiate cracks in adjacent ceramic layers across intact metal layers. Quantitative knowledge of the stress and strain fields around cracked brittle layers is required to predict the fracture modes of such composites. In this paper, two competing fracture modes are analysed for a laminate containing a precrack that spans several layers: fracture is either by co-planar crack growth within the ceramic layers ahead of the initial crack, or, by multiple cracking within the ceramic layers. The appropriate boundary conditions employed in the numerical modelling are determined by comparing finite element predictions with experimental observations of elastic and plastic strain distributions around single cracks in Al/Al_2O_3 laminates using moiré interferometry. It is found that plastic yielding of the metal layers encourages single, co-planar crack growth instead of multiple cracking. This competition between single and multiple cracking is summarised in the form of a fracture map.

1. INTRODUCTION

Before brittle–ductile multilayered composites, or laminates, can be used in engineering components, the relationship between their microstructure and fracture modes must be assessed quantitatively. Of particular importance is the capability to predict whether fracture occurs by the propagation of a low-energy single dominant crack or by high energy multiple cracking within each brittle layer (Fig. 1) (Shaw *et al.*, 1993; Huang *et al.*, 1994; Huang and Zhang 1995; Pateras *et al.*, 1995).

In both cases, it has been shown that tensile and flexural loading of pre-cracked laminates causes nucleation of cracks in intact ceramic layers near the crack tip. Although yielding of the metallic layers lowers the stresses in the intact ceramic layers ahead of the crack tip as compared to a fully elastic system (Chan *et al.*, 1993), the magnitude of the stress relaxation tends to be minor, even with metals of low yield stress, such as aluminium. The most important factor affecting such stress concentrations is the thickness of the metal layer, primarily as a consequence of the increased distance between the crack tip and the next ceramic layer. Although this effect has been confirmed for low-metal volume fraction materials (Shaw *et al.*, 1993),

the situation has not yet been quantitatively assessed for cases where the thickness of the metal layers is greater than that of the ceramic layers.
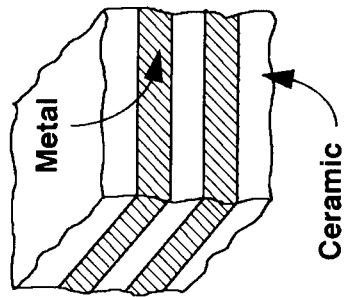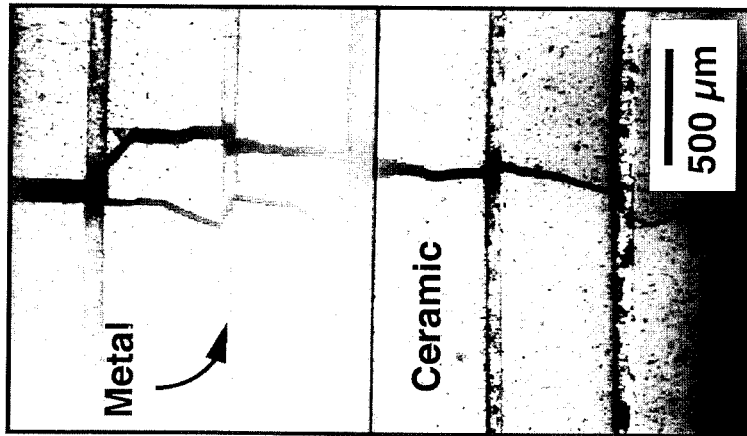
After cracking of the ceramic layers total failure of the laminate occurs by rupture of the intervening metal layers. Whether or not this involves multiple cracking of individual ceramic layers depends in part on how stress is transferred from the cracked ceramic layers into the remainder of the material (Shaw *et al.*, 1993; Huang *et al.*, 1994; Huang and Zhang, 1995). The present paper represents a first step towards the solution of this problem by treating the limiting case of an initially unloaded, precracked system (Fig. 2) with ceramic layers of deterministic strength. The effects of local variations in the strength of the ceramic layers is treated elsewhere (Shaw, 1995).

2. PROBLEM SPECIFICATION

Consider a laminate geometry that contains two cracks: one of length, a_0 (the precrack), and a second crack, which is considered to have reinitiated in the ceramic layer adjacent to the precrack tip, layer C1 [Fig. 2(a)]. A Cartesian co-ordinate system, (x, y), is defined with its origin at the tip of the precrack; see Fig. 2(a). Previous analyses of this problem have shown that the maximum value of the axial component of stress, σ_{yy}, occurs either ahead of the second renucleated crack, i.e. in ceramic layer C2, which is uncracked [Fig. 2(a)], or above and below the renucleated crack in layer C1 (Shaw *et al.*, 1993; Huang *et al.*, 1994; Huang and Zhang, 1995). The location of this peak stress is dictated by the importance of two roles played by the bridging metal ligament. The first role is to decrease the axial stress in layer C2 by crack bridging, and the second is to increase the stress in layer C1 (Shaw *et al.*, 1993; Huang *et al.*, 1994; Huang and Zhang, 1995). Microstructural parameters affecting the relative magnitudes of the crack tip and wake stresses include the relative thickness of the layers (Shaw *et al.*, 1993; Huang *et al.*, 1994; Huang and Zhang, 1995), and the yield stress of the metal (Huang *et al.*, 1994; Huang and Zhang, 1995). The effect of the length of the precrack, however, is as yet unknown.

Plastic yielding of metal layers M1 (the one that bridges the cracked ceramic layers) and M2 (that separates the tip of the renucleated crack from layer C2) strongly influences the location of the peak axial stress. Plastic flow in layer M1 decreases the crack wake stresses by reducing the magnitude of the surface traction acting on the crack face, and increases the stress in layer C2 due to a loss of crack shielding. Plastic flow in layer M2, however, reduces the stress in layer C2, as described earlier. The ratio of the cracking stress of the ceramic, σ_c, to the flow stress of the metal, σ_y, is therefore an important parameter in determining the location of the peak axial stress (Huang and Zhang, 1995). For example, raising this ratio for cases with an infinite precrack and where the peak axial stress is in the cracked ceramic layer is predicted to shift the location of peak stress to the intact ceramic layer ahead of the crack tip (Huang and Zhang, 1995). However, since there is interest in initial precracks as short as a single ceramic layer thickness, one goal of the present investigation is to determine the effect of such short cracks on the fracture mode. Finally, a primary aim of the present investigation is to examine the validity of finite element analyses by comparing
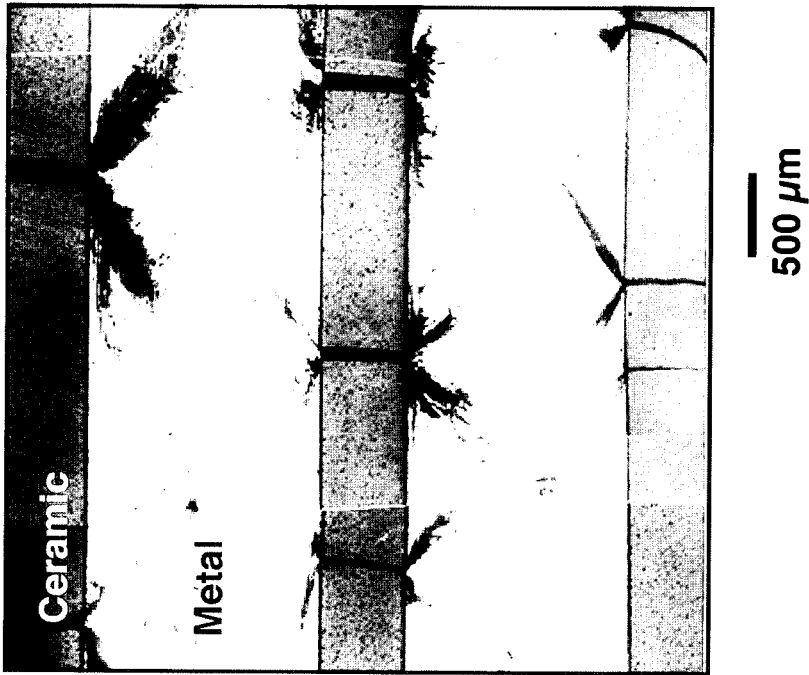
Fig. 1. Optical micrographs of Al/Al$_2$O$_3$ laminates exhibiting (a) co-planar, dominant cracking and (b) multiple cracking.
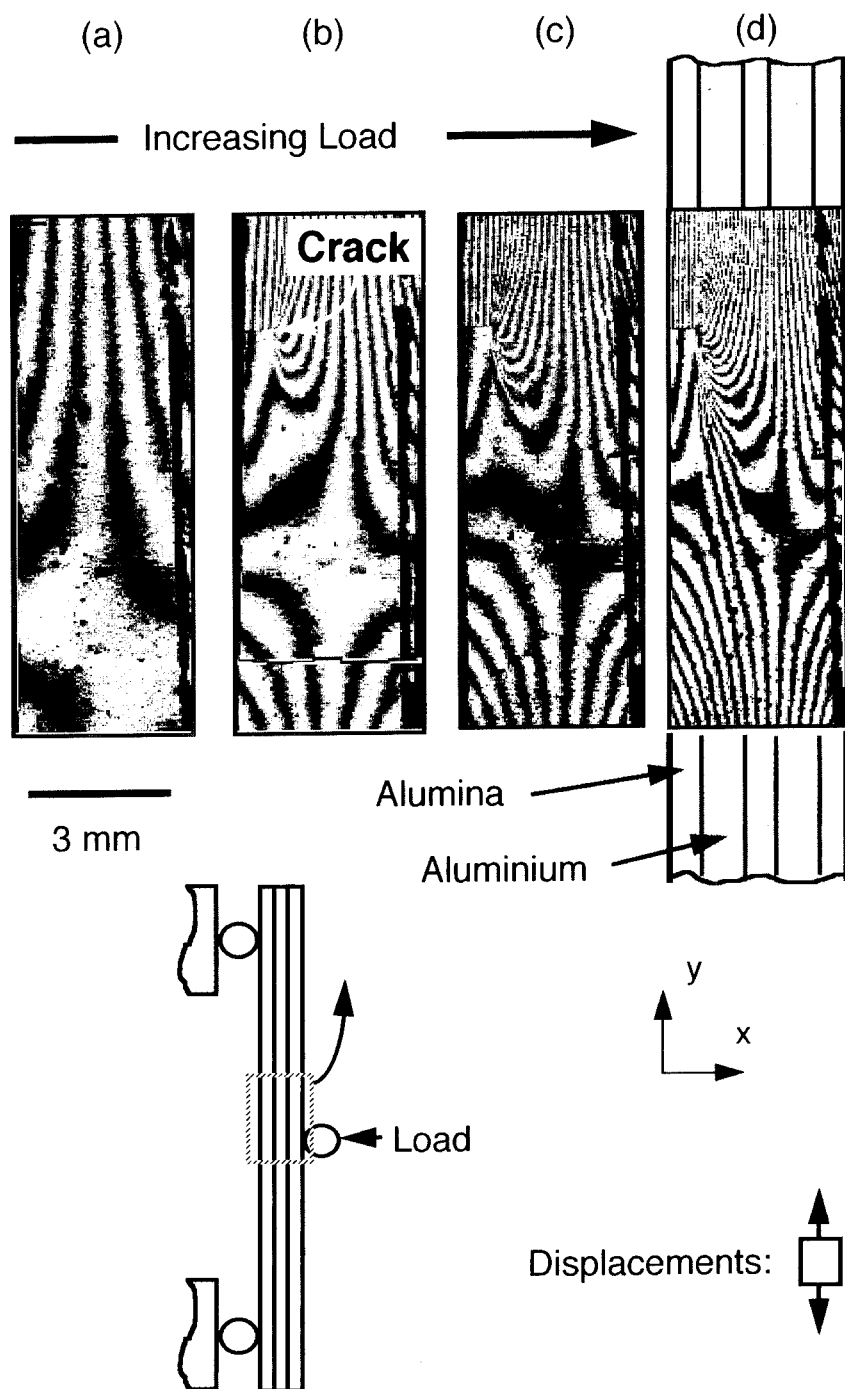
M. C. SHAW *et al.*

Fig. 3. Moiré interferographs showing longitudinal displacement fields accompanying a flexural experiment described in the text. No cracks are present in (a), whereas a crack has formed in the left ceramic layer in (b) through (d). The fringes correspond to contours of constant displacement in the vertical (y) direction, with a separation of 0.42 μm/fringe.
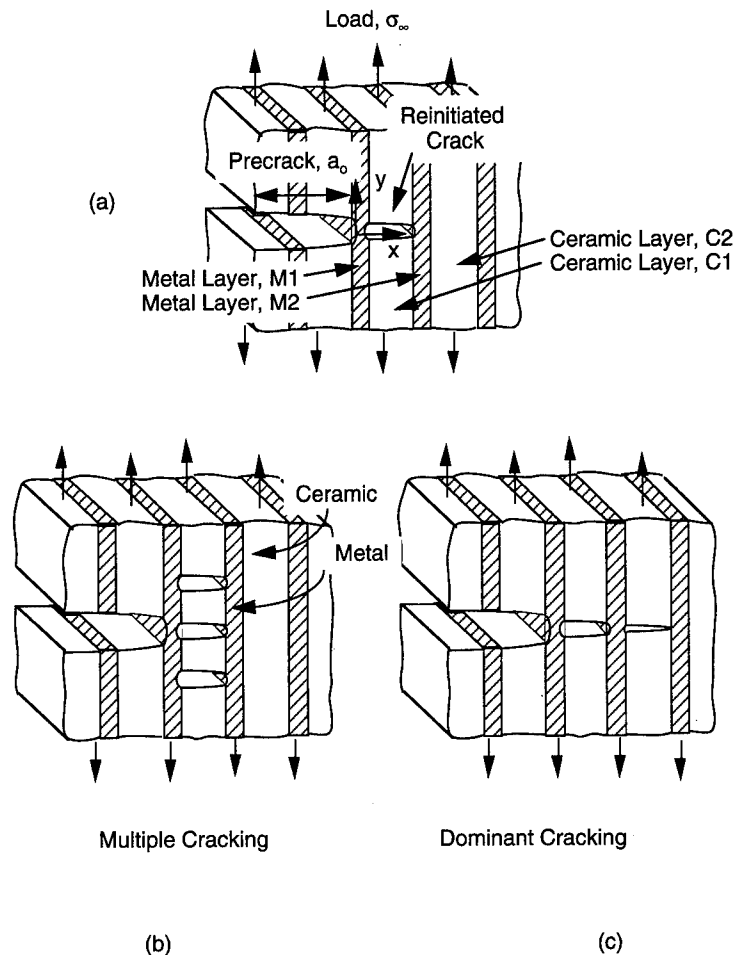
Fig. 2. Schematics illustrating (a) the initial geometry and (b), (c) subsequent cracking modes. The cracking sequence in (b) corresponds to multiple cracking and in (c) corresponds to co-planar dominant cracking.

predictions for crack tip strain fields obtained by finite element analysis with those obtained experimentally by moiré interferometry.

3.   STRESS ANALYSIS OF CRACKED, LAYERED GEOMETRIES

In this section we employ the finite element method to determine the stress and strain fields within the different layers of a cracked geometry. Two situations are examined in detail. In Section 3.1, the underlying assumptions of the finite element model are examined by comparing predicted strain fields around a single crack in an Al/Al_2O_3 laminate subject to three point flexural loading with data obtained by moiré interferometry. Particular attention is paid to modelling the crack tip that impinges on the metal layer and the nature of the interfacial bond between the metal and

ceramic layers. In Section 3.2 of the finite element analysis, the stress fields in the vicinity of the precrack tip are determined subject either to remote tensile loading or the asymototic crack-tip displacement field, assuming small-scale yielding. A range of layer thickness ratios, precrack lengths and remote loads are investigated and the results are used to assist in the construction of a fracture map (Section 4).

All the finite element analyses incorporated the following features: (i) only the upper half of the laminate specimen geometry was modelled, by symmetry considerations, (ii) the lateral faces of the mesh are traction-free, (iii) the crack faces are traction-free, (iv) the lower surface of the bridging metal layer, and the uncracked parts of the specimen were constrained against displacement in the vertical (y) direction, but not the horizontal (x) direction. The analyses were conducted using plane strain conditions and a mixture of 8-noded quadrilateral and 6-noded triangular elements. Large deformation analyses with hybrid elements were used with perfect bonding between the layers.

3.1. *Single crack geometry: flexural loading*

3.1.1. *Flexural loading: moiré interferometry experiments.* High-resolution strain mapping experiments were conducted around a single crack in Al/Al_2O_3 laminates subject to three-point flexural loading using moiré interferometry (Post, 1987). A description of the experimental procedure is summarised in the Appendix. Experiments were conducted using aluminium/alumina laminates containing three ceramic layers and two metal layers in three point flexure. The dimensions of the beams used are summarised in Table 1. During initial loading, the beams exhibited a fringe pattern consistent with simple flexure [Fig.3 (a)]. For the case illustrated in Fig. 3, when the strain in the outer ceramic layer reached the value of 8×10^{-4}, a crack initiated in the outer ceramic layer. This crack tunnelled through the layer and arrested at the interface between the ceramic and metal layers. A convergence of fringes was observed in the metal layer in the vicinity of the crack tip, corresponding to a strain intensification within the metal layer associated with the presence of the crack [Fig. 3(b–d)]. As the level of the remote flexural load was increased, the number of fringes increased [Fig. 3(b–d)]. The distribution of axial strain, ε_{yy}, along longitudinal trajectories within the metal and uncracked ceramic layers were determined from the interferographs for comparison with the numerical predictions.

Typical distributions of the axial strain component, ε_{yy}, in the metal layer are

Table 1. *Dimensions of mechanical test specimens (moiré interferometry)*

Outer roller (mm)	40
Specimen height, h (mm)	3.5
Specimen width, b (mm)	4
Number of ceramic layers	3
Number of metal layers	2
Ceramic layer thickness (mm)	0.5
Metal layer thickness (mm)	1.0

plotted as a function of vertical distance from the crack plane in Fig. 4. Results are shown for three trajectories located at positions from the crack tip of 1/4, 1/2 and 3/4 of the metal layer thickness, at a fixed bending moment of 1.5 Nm. These are denoted as trajectories A, B and C, respectively. The strains were not measured experimentally within ~ 50 μm of the crack tip (0.05 h_m), as a result of disintegration of the epoxy diffraction grating within this region. The axial strains in trajectory A were the highest, and decreased for trajectories B and C, which were located further from the crack tip. In all three trajectories, a peak in strain was observed at a distance from the crack plane corresponding to approximately one ceramic layer thickness. The peak axial strain in trajectory A was $\sim 1.3 \times 10^{-3}$. For all three trajectories, the strain then decreased with further distance from the crack plane, until a far-field axial strain was
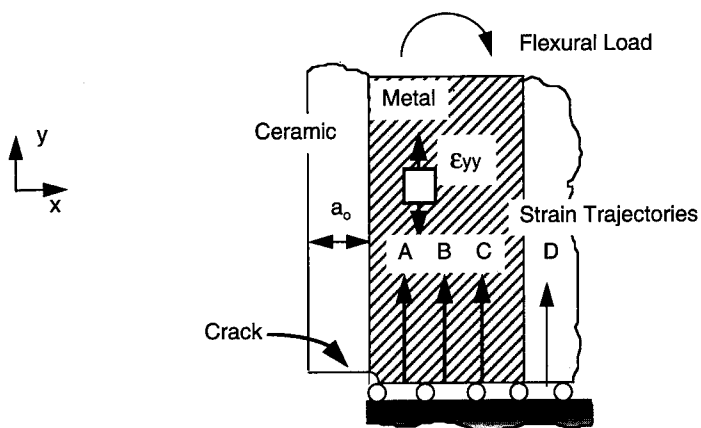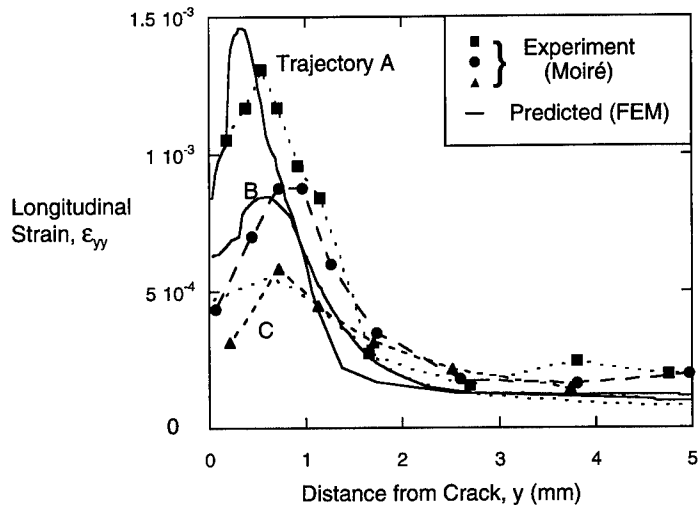

Fig. 4. Distributions of longitudinal strain, ε_{yy}, vs distance from the crack plane, y, within the metal layer along three different trajectories. The applied bending moment is 1.5 Nm. Both experimental measurements and numerical predictions are shown.

M. C. SHAW *et al.*

reached at a distance of ~ 2 mm (twice the metal layer thickness). The magnitudes of the steady-state far-field strains were well below the yield strain of the metal and the cracking strain of the ceramic.

The axial strains are plotted in Fig. 5 for two different magnitudes of applied bending moment (1.5 and 2.0 Nm) for trajectory B. The strain distribution for the low load case is the same as in Fig. 4. The magnitude of the peak axial strain within the metal increased by over 100%, from 9×10^{-4} to 2.1×10^{-3}. The distance from the
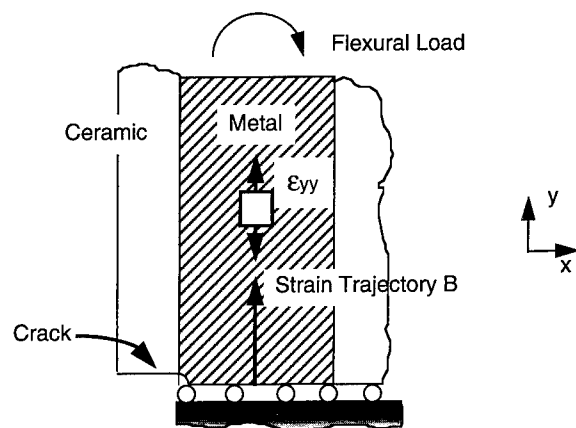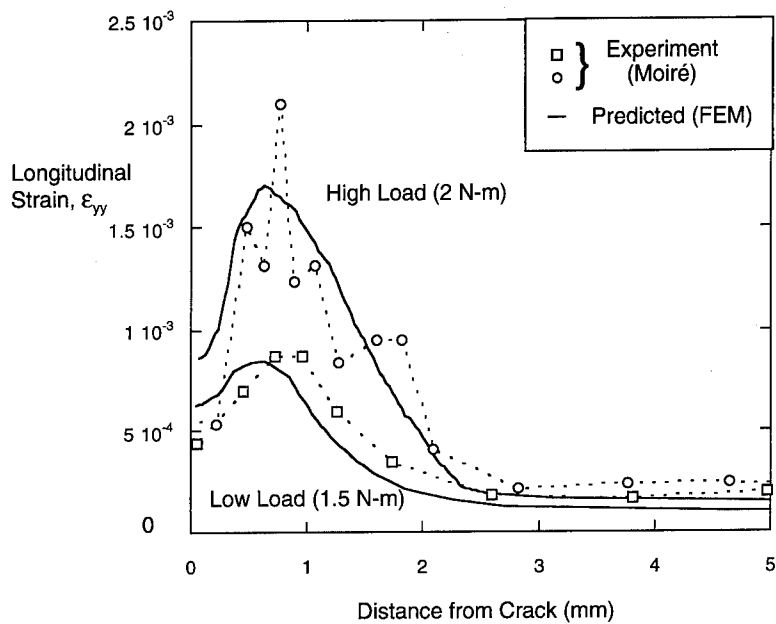

Fig. 5. Distributions of longitudinal strain, ε_{yy}, vs distance from the crack plane, y, along the *middle* of the metal layer for applied bending moments of 1.5 and 2 Nm. Both experimental measurements and numerical predictions are shown.

crack plane over which the strains were increased relative to the remote strains was also greater for the case of a higher remote load.

Finally, the distribution of axial strain along a line ~ 50 μm from the interface within the intact ceramic layer opposite the crack (trajectory D in Fig. 4) is shown in Fig. 6 for two applied bending moments of 2 and 2.8 Nm. Here, the magnitude of the remote axial strains increased as a result of the increased remote load from 1.3×10^{-4} to 2×10^{-4}, and the magnitude of the peak strain within the ceramic increased from 5×10^{-4} to 9×10^{-2}, both approximately by a factor of two.
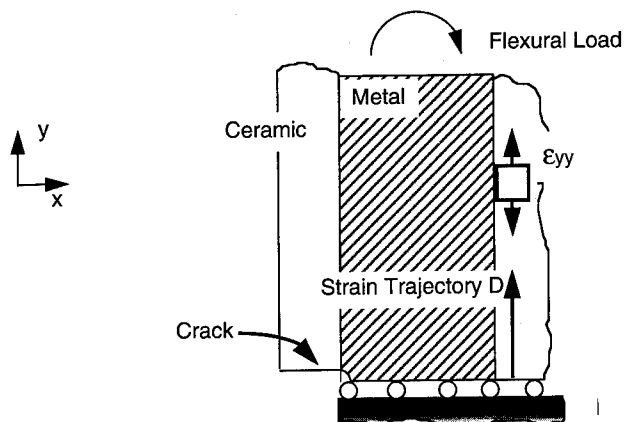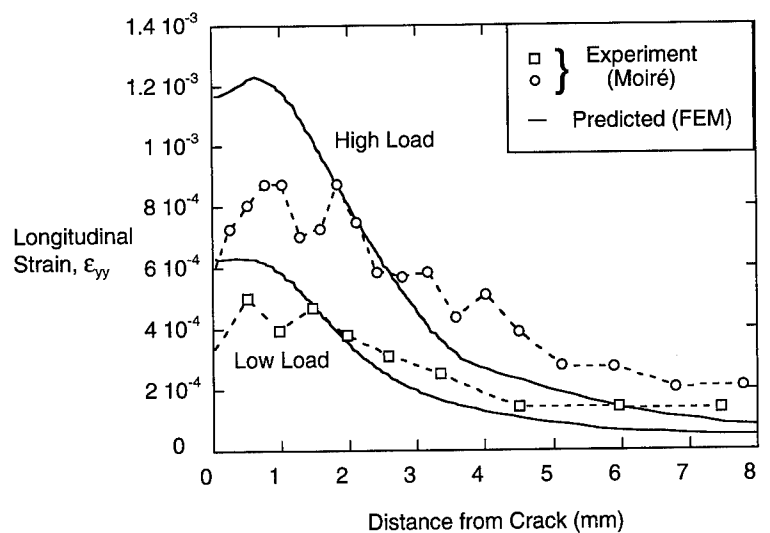

Fig. 6. Distributions of longitudinal strain, ε_{yy}, vs distance from the crack plane, y, within the intact ceramic layer ahead of the crack for applied bending moments of 1.5 and 2 Nm. Both experimental measurements and numerical predictions are shown.

3.1.2. *Flexural loading : finite element analysis.* The laminate specimen examined by moiré interferometry was modelled by finite element methods to allow direct comparison of the strain fields. The model geometry (dimensions and number of layers), material properties and boundary conditions were selected to agree with those of the specimens used for the moiré experiments described in Section 3.1.1. Specifically, the elastic moduli of the two materials were incorporated into the analyses (Table 2). An elastic–perfectly plastic constitutive law was ascribed to the metal layers in the model, with yield stress, σ_Y. In practice it is difficult to independently determine an appropriate value of σ_Y for the aluminium layers used in the experiments of Section 3.1.1. A value of σ_Y was therefore chosen to provide the best fit with experimentally determined strain fields. A single crack in the outermost ceramic layer directly opposite the middle roller was introduced. The crack tip was extended into the metal layer to a distance of 1/40 of the metal thickness, h_m, from the metal–ceramic interface with a finite crack tip radius of 1/40 h_m [Fig.7(a)]. This choice of crack tip geometry was based on experimental observations of crack tip profiles [Fig. 7(b)].

Flexural loading was applied to the finite element model by imposing a point load at the position of the upper load point in a horizontal direction. The magnitudes of the loads were chosen to coincide with those used during the moiré interferometry experiments. For each load level contour maps of the axial strain fields around the crack tip were determined. A typical contour map of the predicted axial strain is shown in Fig. 8 for an applied bending moment of 1.5 Nm and a metal yield strength of 50 MPa, which is typical of that for pure aluminium in the fully annealed condition as used experimentally (Appendix). The results indicate a localisation of axial strain near the tip of the precrack, with significant strain concentration extending in a direction perpendicular to the crack plane to a distance of several times the ceramic layer thickness. The strain distributions were determined along several different trajectories within this contour map. The results are compared with experimental distributions of strain obtained by moiré interferometry in Figs 4–7. Clearly, there is excellent agreement between the predicted and measured axial strain distributions. The agreement includes both the magnitudes of the strains and the distribution of strain around the crack tip at different loads.

The good agreement between the experimental and predicted ε_{yy} strain distributions in the layers near the tip of the crack (Figs 4–7) has several important implications. First, the assumption of a perfectly bonded interface must be valid. Second, plane strain conditions must be applicable. Third, the constitutive relationships of the materials, including an elastic–perfectly plastic response of the metal with a yield strength of 50 MPa appear to be well-represented. Finally, the crack tip geometrical

Table 2. *Properties of materials*

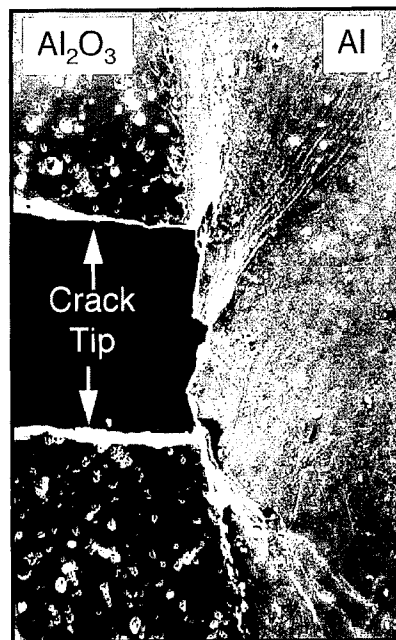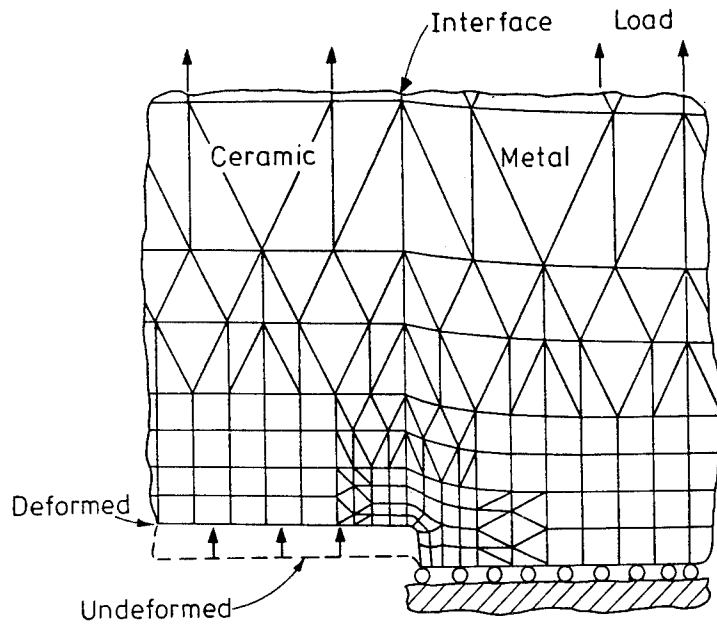| Material	Young's modulus, E (GPa)	Yield stress, σ_Y (MPa)	Poisson's ratio, v
Alumina	380	—	0.2
Aluminium	70	50	0.3

Fig. 7. An example of the crack tip mesh used in the finite element analyses. A high magnification scanning electron micrograph of a crack tip in an Al/Al$_2$O$_3$ laminate after a single load–unload cycle is shown for comparison.
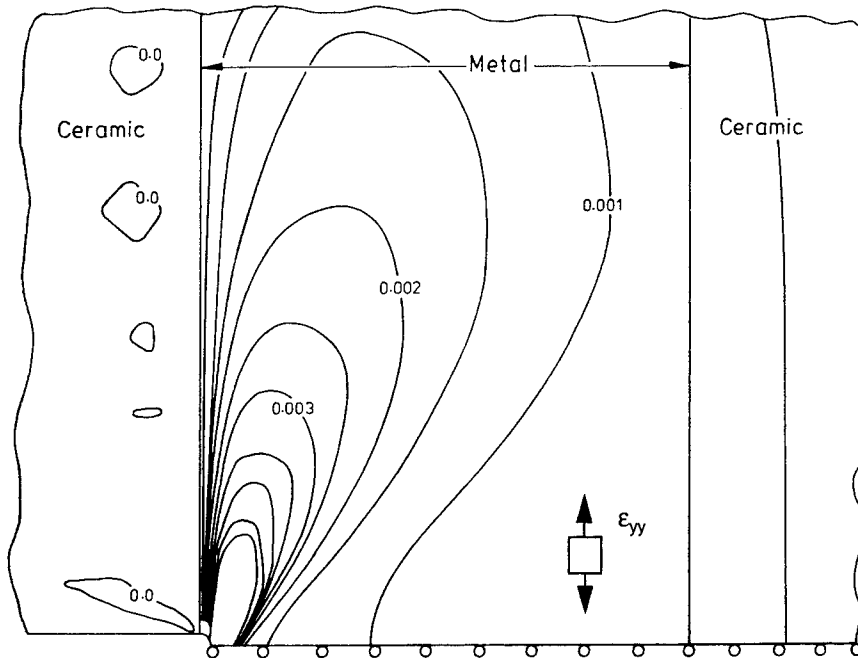
Fig. 8. A contour map of the predicted distribution of strain, ε_{yy}, in the vicinity of the crack tip showing a localisation of strain.

boundary conditions imposed appear to constitute a good approximation in this case. These conclusions then enabled the application of this modelling approach to the analysis of the precracked laminate geometry.

3.2.   *Multiple crack geometry-remote tensile loading*

The distributions of stress near the cracks in the precracked geometry shown in Fig. 2(a) were investigated by finite element analysis using the unconstrained crack tip mesh geometry shown in Fig. 7(a). Tensile loads were applied by imposing a vertical displacement to the upper boundary of the model, which was constrained to remain straight. In other cases, the elastic crack tip displacement field was applied as a loading parameter by imposing the appropriate displacement boundary conditions to the perimeter of the precracked geometry. Stress components that were investigated included both the opening stress component, σ_{yy}, and the maximum principal stress, σ_1. The range of metal–ceramic layer thickness and precrack lengths used during the analyses are summarised in Table 3, whereas the material properties investigated were

Table 3. *Geometries of laminate microstructures analysed for*
fracture map

Precrack length, a_0/h_c	1, 2, 5, 20, ∞
Metal–ceramic layer thickness ratio, h_m/h_c	1, 2, 4

the same as those for the flexural beam, except that now Young's modulus of both the ceramic and metal layers were assumed to be the same. For the analyses involving tensile loading, a range of remote tensile load, σ_∞, was applied, typically from $0 < \sigma_\infty < 2\sigma_Y$. Nodal displacements, strains and stresses were recorded at increments of $0.2\,\sigma_Y$.

In all cases, at low remote loads (e.g. $\sigma_\infty \sim 0.2\sigma_Y$), the entire system remained elastic, with the exception of small regions of the metal located near the tips of the cracks that exhibited plastic yielding. However, as the level of remote load was raised, plastic yielding of layers M1 and M2 resulted in a change in the distribution of axial stress, σ_{yy}, around the cracks. In some cases, this resulted in the location of peak axial stress moving from layer C1 to layer C2. This effect has strong implications for the predicted fracture response of these materials, as elaborated below.

An example of such a transition is shown in Fig. 9(a) and (b), where contour maps of the axial component of stress, σ_{yy}, obtained at two different loads ($\sigma_\infty/\sigma_Y = 0.2$ and 1, respectively), are presented from a laminate with equal thickness metal and ceramic layers and a precrack length of five ceramic and four metal layer thicknesses. In Fig. 9(a), the maximum axial stress in layer C2 is only of the order of $\sigma/\sigma_\infty \sim 1.2$, whereas for layer C1 the maximum axial stress reaches at least $\sigma/\sigma_\infty \sim 1.3$. Therefore, provided the ceramic layers exhibit a deterministic strength and provided the next crack will form at this level of remote load ($\sigma_\infty/\sigma_Y = 0.2$), a multiple cracking response is predicted since the location of the maximum stress occurs in layer C1. This might be expected to apply when the ratio of ceramic strength to metal flow stress is low (~ 1), for this layer thickness ratio and precrack length.

However, raising the magnitude of the remote load, such that significant plastic deformation of the metal layers occurred, led to a major redistribution of axial stress around the crack tip. This may be seen in Fig. 9(b), where a contour map of the same region shown in Fig 9(a) is illustrated, but for a remote load $\sigma_\infty/\sigma_Y \sim 1$. In Fig. 9(b), the location of peak axial stress now occurs in layer C2, which experiences a peak axial stress in excess of $\sigma_{yy}/\sigma_\infty = 2$. In contrast, the maximum axial stress in layer C1 is only of the order of $\sigma_{yy}/\sigma_\infty \sim 1.3$. The fact that the peak stress now occurs in layer C2 implies that fracture at this level of remote load ($\sigma_\infty/\sigma_Y \sim 1$) would proceed by dominant, single cracking, rather than the multiple cracking response predicted for the same geometry but at the lower load ($\sigma_\infty/\sigma_Y = 0.2$).

3.2.1. *Yielding of the bridging metal layer.* The observation that the location of peak axial stress depends on the ratio of the remote load to the yield stress of the metal is a direct result of plastic yielding of the bridging metal layer. Such yielding with increasing crack opening is well documented for constrained metal layers (Bannister and Ashby, 1991). Evidence of this phenomenon is shown in Fig. 10, which shows a plot of the average traction stress, $\bar{T}$, at the crack plane, in layer M1, against the average crack opening displacement, $\bar{u}$. The value of $\bar{T}$ is defined by

$$\bar{T} = \frac{1}{h_m} \int_0^{h_m} \sigma_{yy}(x,0)\,dx. \tag{1}$$

Two broad regimes of the stress–displacement response of the metal layer may be distinguished. In the first stage, the metal layer acts essentially as a linear spring, such
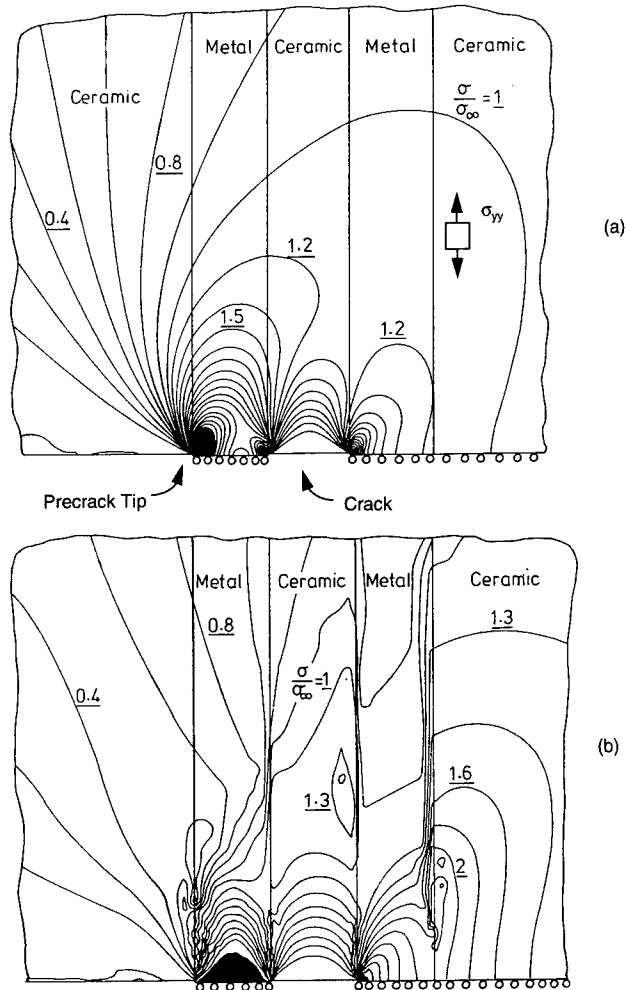
Fig. 9. Contour maps of the distributions of strain for a laminate containing equal thickness metal and ceramic layers and a normalised precrack of length of five. In (a), negligible plastic yielding has occurred, resulting in a maximum axial stress, σ_{yy}, occurring in layer C1. In (b), extensive plastic yielding has resulted in a shift in location of peak axial stress to layer C2.

that the increase in bridging traction is linear with average crack opening. In the second regime, however, significant plastic flow of the metal layer occurs and results in a sharp decrease in the rate of increase in bridging stress with crack opening. Furthermore, the magnitude of the normalised average crack opening displacement at which this transition occurs is dependent on the length of the precrack, a_0: longer precracks tend to result in higher stresses within the metal layer.

This effect, as well as the general observation of the bridging stress rising above the uniaxial yield stress, σ_Y, results from the high degree of plastic constraint imposed on the metal layers near the crack tip. This effect, in turn, is well known, and results from the presence of the stiff ceramic that is well bonded to either side of the metal layer
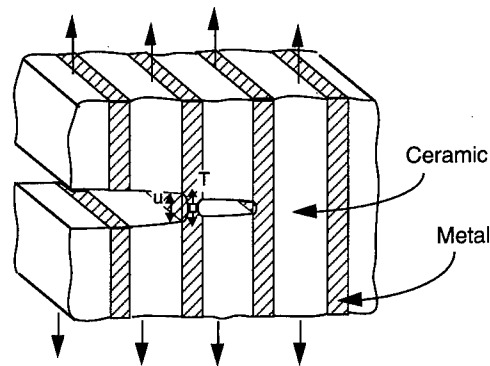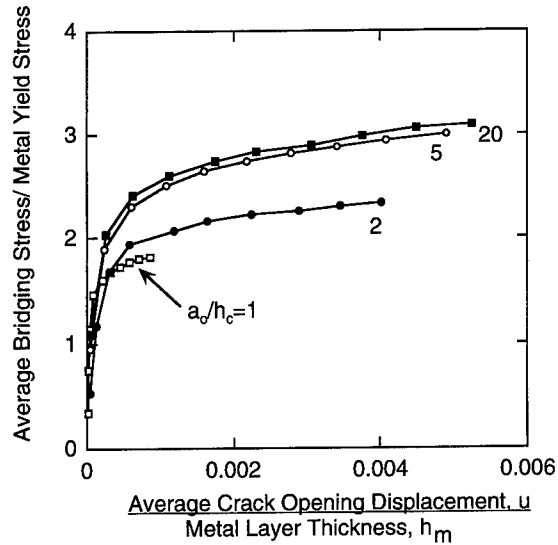
Fig. 10. Plot of the normalised average bridging stress, $\bar{T}/\sigma_Y$, vs average crack opening, $\bar{u}/h_m$ for several different precrack lengths.

(Hill, 1950). As a result, the magnitude of the applied stress required to bring the metal layer to the point of plastic yielding is raised, relative to the case with no constraint. The observation that the bridging stress is lower for shorter precracks now can be explained.

The high triaxiality near the crack tip results from transverse tensile stresses acting on the metal layer in directions parallel to the crack plane. These stresses originate (a) from the inability of the ceramic material on either side of the deforming metal layer near the crack tip to strain sufficiently in the x direction and (b) from the through thickness stresses generated by the plane strain condition. For materials with relatively short precracks, however, the magnitudes of the transverse, σ_{xx}, stresses that can build up within the cracked ceramic material are limited by the proximity of the free surface, as compared to the case of longer precracks. This effect then leads to

a decrease in the magnitude of the crack tip hydrostatic stress and consequent attainment of yield within the metal layer at lower applied stress, i.e. smaller crack openings. Thus, the maximum axial stress that can be carried by bridging metal layers is lower in systems with short precracks.

Yielding within layer M1 decreases the ratio of maximum wake stress to tip stress in two ways. First, the elastic contribution to the wake stress that arises from the surface tractions, $\bar{T}$, is linearly related to the magnitude of the traction stress (Roark, 1954). Once $\bar{T}$ reaches a maximum, a limit is placed upon the contribution to the wake stress from the corresponding traction on the crack flanks. Secondly, the crack tip stress intensity factor, as modified by the presence of the bridging metal layer is (Marshall *et al.*, 1985)

$$K_{\text{tip}} = 2\sqrt{\frac{a}{\pi}} \int_0^1 \frac{\sigma_\infty - T(X)}{\sqrt{(1 - X^2)}} \, dX, \tag{2}$$

where X is the relative position along the crack flanks, $X = x/a_0$. Therefore, if the magnitude of T decreases relative to σ_∞, the increase in crack tip stress intensity factor will lead to an increase in the stress layer C2. Although (2) applies to semi-infinite half-space geometries with infinite cracks, these general trends should apply to the present situation.

Yielding within layer M2 does not significantly reduce the stress layer in C2, consistent with the findings of earlier analyses (Chan *et al.*, 1993). This conclusion was confirmed by comparing the results of an analysis with an elastic layer M2 ($\sigma_Y = \infty$) and elastic–plastic M1, to those of a similar analysis with elastic–plastic layers M1 and M2. No significant change in the distribution of stress within layer C2 was observed accompanying yielding of layer M1, between the two cases. This result indicates that the transition in fracture behaviour results primarily from a plateau in crack wake stress due to yielding of metal layer M1, as described above.

4. FRACTURE MAP FORMULATION

The stress distributions obtained from the finite element analyses at different loads have been used to formulate a fracture map for the failure mode of the composites. The maximum stress in the wake (σ_B^*) and in front of the crack (σ_A^*) were determined first from the distributions of stress within the layers at different increments of remote load for each composite system. These maxima were then normalised by the yield stress of the metal, σ_Y, and plotted against the normalised applied load (e.g. Fig. 11). In those cases when increasing the remote load caused the peak stress to shift from the crack wake to the region in front of the crack, the magnitude of the quantities were noted at this point (e.g. $\sigma_A^*/\sigma_Y = \sigma_B^*/\sigma_Y \sim 1.3$ in Fig. 11). These values were then plotted as the ordinate of a fracture map, with the corresponding metal to ceramic layer thickness ratio as the abscissa (Fig. 12).

This has the following physical interpretation: *if* the ratio of the fracture stress of the ceramic, σ_C, to the yield stress of the metal is fairly low (e.g. $\sigma_C/\sigma_Y < 0.7$ in Fig. 11), then the next crack that will form will do so when the level of the remote load is
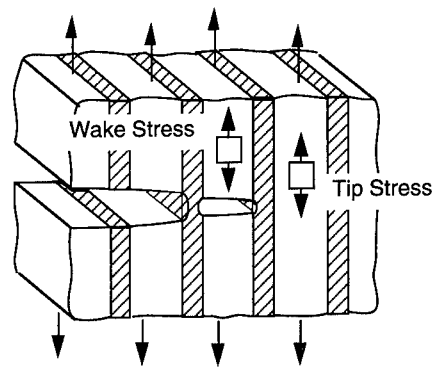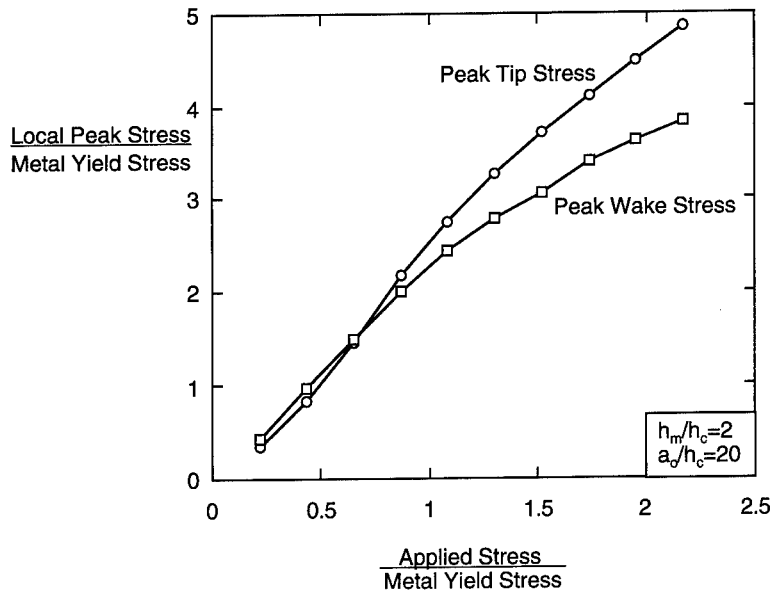
Fig. 11. Plot of the normalised peak axial stress in layers C1 (crack wake) and C2 (crack tip) vs the normalised applied stress.

such that insignificant yielding of the metal layer has occurred. Therefore, the appropriate stress distribution to be analysed is that corresponding to a nearly elastic system [Fig. 9(a)]. However, if the cracking stress to metal yield stress ratio is higher (e.g. $\sigma_C/\sigma_Y > 0.7$ in Fig. 11), then the remote load needed for further cracking is also higher, for given σ_Y, leading to a change from wake to frontal cracking in some cases [Fig. 9(b)]. These results are summarised in Fig. 12, which shows the results obtained from several different cases with different metal layer thickness and precrack lengths. Furthermore, this conclusion was valid if either the σ_1 or σ_{yy} component of stress was considered; there was less than 5% difference in the critical ratio of σ_C/σ_Y for either stress component.
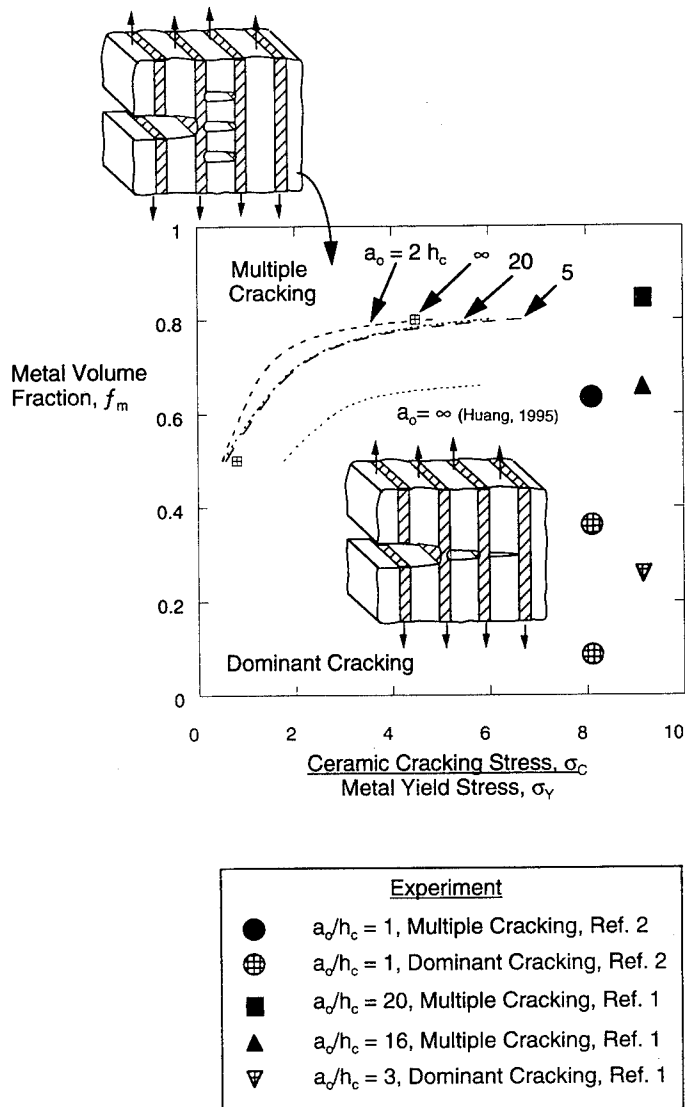
Fig. 12. Map of the predicted fracture mode for multilayers with different ratios of layer thickness and ceramic cracking stress to metal yield stress, σ_C/σ_Y.

It should be noted, however, that for laminates containing a precrack of length equal to one ceramic layer thickness, the location of maximum stress always occurred in the intact ceramic layer ahead of the crack tip, regardless of the level of remote load. In no instance was the maximum stress found to occur in the ceramic layer that already contained the crack. Therefore, in systems that do not contain a precrack of significant length, i.e. one that spans several layers, dominant cracking is the predicted failure mechanism. This prediction was found to apply to systems with the three layer thickness ratios that were investigated ($1 < h_m/h_c < 4$).

Comparison of the predicted fracture mode with experiment indicated good agreement for systems with long precracks and low and high metal volume fractions, and for systems with short precracks and low metal volume fractions but the prediction of an incorrect failure mode for systems with short precracks and high metal volume fractions. This can be seen in Fig. 12 where experimentally observed fracture modes (Shaw *et al.*, 1993; Pateras *et al.*, 1995) are included on the fracture diagram. Although the reasons for this discrepancy are not yet clear, it may be a consequence of the stochastic nature of brittle fracture. Further work to clarify this point is in progress (Shaw, 1995). Furthermore, these predictions for the mechanism boundary obtained by the finite element method differ from that identified by an elastic–plastic shear lag approach (Fig. 12) (Huang and Zhang 1995). The present analysis indicated that multiple cracking in systems with precracks of finite length will occur over a smaller range of layer thickness ratios. The cause of this discrepancy is not clear, although most likely arises in the different approaches used to conduct the analyses. This trend, however, is consistent with the general conclusion of the present investigation that wake stresses are decreased as a result of finite crack lengths, leading to a propensity towards dominant cracking.

5. CONCLUSIONS

A finite element model has been developed for investigating the fracture of ceramic–metal laminates. Moiré interferometry was used to investigate experimentally the distribution of strain surrounding cracks in aluminium/alumina laminates. Good agreement has been observed between the predicted and experimentally observed crack-tip strain fields. The finite element calculations were used to predict the fracture sequence of laminate specimens with precracks of varying lengths. These results have been used to develop a fracture map for prediction of the cracking patterns as a function of layer thickness, initial crack length and the ratio of ceramic strength to metal yield stress, σ_C/σ_Y. We find that fracture will tend to occur by dominant cracking for materials with relatively high ratios of σ_C/σ_Y. Experimental observations of crack patterns are in partial agreement with this prediction, although multiple cracking patterns have been observed at lower metal contents than predicted.

ACKNOWLEDGEMENTS

REFERENCES

Bannister, M. and Ashby, M. F. (1991) The deformation and fracture of constrained metal sheets. *Acta Metall. Mater* **39**, 2575–2582.
Chan, K. S., He, M. Y. and Hutchinson, J. W. (1993) Cracking and stress redistribution in ceramic/metal layered composites. *Mater. Sci. Engng* **A167**, 57–64

Hill, R. (1950) *The Mathematical Theory of Plasticity*. Oxford University Press, London.

Huang, Y., Zhang, H. W. (1995) The role of metal plasticity and interfacial strength in the cracking of metal/ceramic laminates. *Acta Metall. Mater.* **43**, 1523–1530.

Huang, Y., Zhang, H. W. and Wu, F. (1994). *Int. J. Solids Struct.* **31**, 2753.

Marshall, D. B., Cox, B. N. and Evans, A. G. (1985), The mechanics of matrix cracking in a brittle-matrix fiber composite. *Acta Metall. Mater.* **33**, 2013–2021.

Pateras, S. K., Shaw, M. C. *et al.* (1995) The effect of metal layer thickness on the fracture energy of metal/ceramic multilayers. *ICCM Conference Proceedings*, submitted.

Post, D. (1987) *Handbook on Experimental Mechanics*, pp. 314–387. Prentice-Hall.

Rasband, W. (1995) NIH Image, Anonymous FTP.

Shaw, M. C. (1995) The effects of strength probalistics on the fracture of metal/ceramic multilayers. *Acta Metall. Mater.*, submitted.

Shaw, M. C., Marshall, D. B., Dadkhah, M. S. *et al.* (1993) Cracking and damage mechanisms in ceramic/metal multilayers. *Acta Metall. Mater* **41**, 3311–3320

Roark, T. J. (1954) *Formulas for Stress and Strain*. McGraw-Hill, New York.

APPENDIX: MOIRÉ INTERFEROMETRY EXPERIMENTAL PROCEDURE

Bulk specimens were prepared by vacuum diffusion bonding stacks of commercially available alumina† and aluminium‡ sheets. The sheets were cleaned with acetone prior to bonding. Diffusion bonding was conducted in a vacuum of $\sim 10^{-5}$ Torr using an applied pressure of ~ 5 MPa at a temperature of 610°C for a time of 4 h. Beam specimens for the moiré interferometry experiments were cut from the diffusion bonded specimens using a water-cooled diamond abrasive cut-off saw. The dimensions of the beam were $\sim 5 \times h \times 100$ mm, where h depended on the metal layer thickness (Table 1). One side of the beams was polished using diamond metallographic compounds and a linear diffraction grating with 1200 lines/mm was reproduced on this side surface using epoxy resin. Three-point flexural testing of the laminate beams was conducted in displacement control. Loads were measured using an Entran 1 kN load cell with a load resolution of 1.8 N.

The surface strain states of the laminates were monitored during the experiment using moiré interferometry (Post, 1987). Two-beam interferometry was used with a 632 nm wavelength HeNe laser and an output power of 30 mW. This arrangement yielded moiré interferographs with a displacement sensitivity of 0.42 μm/fringe, with a possible strain resolution of $\sim 10^{-5}$. A typical experiment involved incrementally increasing the displacement of the loading points, followed by a pause during which the load was recorded and the interferographs were exposed and developed. The interferographs were digitised and the longitudinal fringe spacing, $L_0(y)$, were determined from the digitised images along longitudinal trajectories of interest using the public domain NIH Image program (Rasband, 1995). These fringe spacing were then used to calculate the longitudinal strains (ε_{yy}) (Post, 1987)

$$\varepsilon_{yy}(y) = \frac{1}{2vL_o}, \tag{A.1}$$

where $v =$ the number of lines/mm in the diffraction grating.

† Hoescht alumina.
‡ Johnson-Matthey 99.999% aluminium.

SUMMARY

J. D. EMBURY,† L. B. FREUND,‡ A. NEEDLEMAN,‡ C. F. SHIH,‡
F. SPAEPEN§ and S. SURESH¶

† Department of Materials Science and Engineering, McMaster University, Hamilton, Ontario,
Canada, L8S 4L7
‡ Division of Engineering, Brown University, Providence RI 02912, U.S.A.
§ Division of Applied Sciences, Harvard University, Cambridge, MA 02138, U.S.A.
¶ Department of Materials Science and Engineering, Massachusetts Institute of Technology,
Cambridge, MA 02139, U.S.A.

This volume contains the texts of ten keynote lectures of the Engineering Foundation Conference on Mechanics and Physics of Layered and Graded Materials, held in Davos, Switzerland, 21–25 August 1995. A discussion session at the end of the Conference provided a perspective on the current state of the subject and key issues for further investigation. It is that discussion that we summarize here.

The interest in the subject stems from the fact that mechanical properties of multi-phase materials are, to a large extent, determined by the deformation and failure mechanisms at the interfaces. There is, therefore, great interest in controlling interface behavior by layering and grading of composition–microstructure. Current or potential engineering applications include case-hardening of steels for tribological protection, thermally-sprayed zirconia-metal graded coatings for thermal-barrier protection in ground-vehicle engines, and SiGe and InGaAs graded layers in microelectronics and optoelectronics.

What can be gained by grading interfaces? In semiconductors, synthesized by any of several physical or chemical vapor deposition techniques, grading can be used to control the population, distribution or kinetics of misfit and threading dislocations in heteroepitaxial structures. Graded interfaces can significantly reduce the stress concentrations that arise from the mismatch in mechanical properties across an interface, thereby improving the tolerance to the onset of cracking. Compositional gradation can also be used to markedly alleviate the spread of plastic flow in ductile layers. Similarly, a compositionally graded interlayer between solids with a large thermal expansion mismatch smooths the distribution of thermal stresses across the thickness of the layer and can be used to diminish the magnitude of thermal stresses at critical locations. Indeed, an interface with a gradual change in composition is sometimes essential for maintaining the mechanical integrity of the joint between dissimilar solids, e.g. metals and ceramics, in the presence of large fluctuations in temperature, provided that the microstructure of the graded interface is thermally stable.

In order to guide the design of graded interfaces so that their potential benefits are fully realized, a basic understanding of the mechanics and physics of deformation and transport processes in graded structures is needed.

When the range of possible applications is considered, the issue of size scale becomes immediately apparent. The operative mechanisms can be very different when the interface extends over nanometers from when the interface extends over tens of micrometers. Indeed, the characterization of graded and layered systems necessarily involves parameters that have a characteristic dimension of length including, for example, quantities such as the modulus gradient, the thermal conductivity gradient, the fracture toughness and a Burgers vector associated with the misfit dislocations. Ratios of surface energy and surface stress to the volumetric stored energy provide additional length parameters. From these, a variety of characteristic lengths can be constructed, e.g. the Burgers vector divided by plastic strain, surface energy divided by elastic mismatch energy, fracture toughness divided by modulus gradient to the three halves power and thermal conductivity gradient divided by the average thermal conductivity. It is the ratio of layer thickness, curvature and size of microstructural features to these characteristic lengths that determines regimes of behavior. The appropriate framework, continuum or atomistic, for modeling will depend on which regime plays the dominant role in determining behavior. At any size scale, a question of interest is how small, relative to the total interface thickness, stepwise variations have to be before they have the advantages of a smooth variation, because processing almost inevitably gives rise to a layered rather than a graded structure.

When characteristic lengths are small, of the order of 1–100 nm, as they are in many systems of technological importance, the characterization of basic properties can be quite different from that of corresponding bulk materials, and provides challenges for both theory and experiment. For example, experimental characterizations of the wavelength of internal stresses, of interface roughness, of elastic–plastic transition mechanisms and of the development of texture in circumstances where the usual choices of slip systems are not appropriate are needed. Understanding the basic atomic and electronic structure at the interface between very dissimilar phases is one basic challenge for theory. Thermodynamic properties, such as solubilities and segregation, on a size scale of 10 nm and smaller are another challenge. A further set of fundamental questions concerns stability, both chemical and morphological, of layered and graded structures. There is also the potentially strong effect of a high interfacial area on atomic transport or creep.

Consideration of plasticity in thin layers poses special challenges. Are the deformation modes the same as in bulk samples or does the size scale of the layers, together with the increased surface to volume ratio, bring new deformation mechanisms into play? What sort of constitutive relations are appropriate for characterizing plasticity on this scale? Do the high internal stresses that arise from thermal mismatch strains that occur during processing lead to slip taking place in a regime that is not ordinarily encountered in bulk materials, for example, the regime where pressure effects on dislocation motion play a significant role? How does the microstructure of such materials evolve during fabrication or during plastic flow?

Fundamental issues remain concerning the characterization of toughness for solids with layered and graded interfaces. In particular, the design of experiments to obtain

the relevant and "valid" fracture parameters, which unambiguously describe the "intrinsic" resistance of the layered structure to fracture over a broad range of mode mixities and monotonic and cyclic variations in stress–temperature gradients, poses a basic challenge.

It is hoped that the conference itself, and the timely publication of these proceedings, will serve to stimulate further research and discussion on the behavior of layered and graded materials, an area which is rich in both scientific research opportunities and technological potential.